Fachbereich Mathematik und Naturwissenschaften
Fachgruppe Physik
Bergische Universität Wuppertal

# Simulation of the phase behavior in polar model liquids.

**Dissertation**
**by**
**Heiko Braun**

August 2015

Die Dissertation kann wie folgt zitiert werden:

urn:nbn:de:hbz:468-20151210-114928-0
[http://nbn-resolving.de/urn/resolver.pl?urn=urn%3Anbn%3Ade%3Ahbz%3A468-20151210-114928-0]

# Contents

# List of Tables

# List of Figures

# Abbreviations

Table 0.1.: Abbreviations used in the text

| Abbreviation | Explanation |
|---|---|
| 2CLJ | two-centre Lennard-Jones |
| CHD | charged hard dumbbell |
| CSD | charged soft dumbbell |
| DHS | dipolar hard sphere |
| DSS | dipolar soft sphere |
| FCC | face-centered cubic |
| g-l | gas-liquid |
| GEMC | Gibbs ensemble Monte Carlo |
| LAMMPS | large-scale atomic/molecular massively parallel simulator |
| LJ | Lennard-Jones |
| MC | Monte Carlo |
| MD | molecular dynamics |
| PPPM | particle-particle particle-mesh |
| RDF | radial distribution function |
| RPM | restricted primitive model |
| ST | Stockmayer |
| TIP4P | transferable intermolecular potential 4 point |

# 1. Introduction

What makes a liquid a liquid? This question can be answered by the van der Waals theory, which states that attraction between molecular particles is necessary for a gas-liquid phase transition [1]. So let us take an example, the well-known Lennard-Jones potential [2], which has the form

$$u_{LJ}(r) = 4\left[\left(\frac{1}{r}\right)^{12} - \left(\frac{1}{r}\right)^{6}\right] \quad , \tag{1.0.1}$$

where $u_{LJ}$ is the potential energy and $r$ the intermolecular separation in reduced units. Due to the $r^{-6}$ dispersion attraction, the Lennard-Jones model exhibits a gas-liquid phase transition (e.g. Ref. [3, 4]) and can in the meantime be considered as a kind of warm-up exercise for anyone getting started with computer simulations in the field of soft matter physics.
But what about polar models, where the attractive interaction is not as apparent as in the case of the Lennard-Jones model? Or, in the words of van Leeuwen and Smit *What makes a polar liquid a liquid* [5]? The interaction of two point dipoles can be attractive or repulsive, depending on their orientation to each other. For a gas of dipole moments $\mu$ it can be shown that the thermal average at temperature $T$ results in the overall attractive dipole-dipole potential $u_{DD}(r) = -\frac{2}{3}\frac{\mu^4}{Tr^6}$ [6]. This indicates the existence of gas-liquid coexistence. But the aforementioned conclusion is not as clear as it looks. The existence of gas-liquid coexistence in dipolar fluids with no other contribution to attractive interaction than dipole-dipole interaction is a basic and open question in the theory of fluids and has created significant interest. It is perhaps comparable to the freezing transition in the hard sphere fluid discovered in early computer simulation work by Alder and Wainwright in the late fifties [7]. In the studies of dipolar fluid systems, two simple and often used representations are the dipolar soft sphere model, where the dispersion attraction in the Lennard-Jones potential is replaced by the interaction energy of a point dipole, and the dipolar hard sphere model, where the soft sphere repulsion in the dipolar soft sphere model is replaced by a spherical hard core potential [8–11]. About twenty years ago, a number of theoretical papers concluded the absence of a gas-liquid critical point for those systems due to the formation of reversible chains, which essentially possess no mutual interaction [12–15]. Those theoretical results are supported by different computer simulations done for dipolar systems. Dipolar hard spheres were analyzed for a gas-liquid phase separation by Calliol [16] using Monte Carlo simulations in the isothermal-isobaric

ensemble (NPT ensemble, constant particle number $N$, pressure $P$, and temperature $T$) and in the Gibbs ensemble. He came to the conclusion that in the analyzed region of the phase diagram no gas-liquid transition exists. This is in contradiction to an earlier work of Ng *et al.* [17], who observed a gas-liquid transition for a system of 32 dipolar hard spheres using Monte Carlo simulations. Van Leeuwen and Smit [5] introduced a factor $\lambda$ to allow an independent control of the dispersion attraction from the dipolar interaction in the Stockmayer fluid (Lennard-Jones plus dipole-dipole potential). They studied a range of $\lambda$ with the focus on the limit $\lambda \to 0$, where the system is equivalent to dipolar soft spheres. For $\lambda < 0.3$ they could not detect gas-liquid criticality in their simulations due to chain formation, which is not observed for higher $\lambda$. The pure dipolar soft sphere fluid in an applied field was studied by Stevens and Grest [18] using Gibbs ensemble Monte Carlo. They determined the critical parameters as a function of the applied field and conclude in the zero field case that coexistence most likely does not occur. Thermodynamics and structural properties of the dipolar Yukawa hard sphere fluid were studied by Szalai *et al.* [19]. They found that at high dipole moments the gas-liquid phase transition disappears, while chainlike structures appear in the low-density fluid phase. More recent molecular dynamics simulations of the Stockmayer fluid performed by Bartke and Hentschke [20, 21], which can be mapped onto the system studied by van Leeuwen and Smit, show that the threshold found in Ref. [5] does not exist. The conclusion that chain formation indeed leads to the disappearance of gas-liquid criticality in the dipolar soft sphere limit still appears to be valid. Sindt and Camp used an effective many-body isotropic interaction able to mimic the dipolar soft sphere model and clearly linked the transition disappearance to chain formation [22]. Rovigatti *et al.* [23, 24] observes self-assembly of dipolar hard spheres into closed rings and concludes that this excludes the possibility of critical phenomena. In a further study on a model of particles with dissimilar patches they support the conclusion that the absence of gas-liquid separation in DHS could be a consequence of extensive ring formation [25]. To shed more light on the gas-liquid transition debate they suggest further studies on the structural transition from chains to branched network for the dipolar hard sphere model [26]. Again, ring formation suggests a similar result from Rovigatti and Dussi *et al.* [27] where they investigated the charged soft dumbbell model we also use in our work. The charged soft dumbbell model consists of two oppositely charged soft sphere sites, displaced through an axis of length $d$, and allows to approach the dipolar soft sphere limit $d \to 0$. In their Monte Carlo simulations they were able to locate the gas-liquid critical point for dumbbells, but they were not able to track it down to the smallest dumbbell length due to the formation of rings.

Despite the abundant evidence for the absence of a gas-liquid phase transition for purely dipolar systems, there are also researchers who come to the opposite conclusion. First of all, the already mentioned study by Ng *et al.* [17], who found gas-liquid coexistence for the dipolar hard sphere system. More than twenty years later, McGrother and Jackson [28] induced gas-liquid coexistence in a system of nonspherical hard-core dipolar molecules, i.e. they consider hard spherocylinders with central longitudinal point dipole moments. By using Monte Carlo simulations to calculate the equation of state and the free energy of dipolar hard sphere fluids at low temperatures and densities, Camp *et al.* [29] obtained

evidence in favor of an isotropic fluid-to-isotropic fluid phase transition. Pshenichnikov and Mekhonoshin [30] utilized the Monte Carlo method to simulate dipolar hard sphere with open boundaries. They applied an extra field which confines the particles to a spherical region and observed a gas-like distribution within this region, or a pronounced clustering, depending on the strength of dipolar interaction. They interpret this as an indication for phase separation in the dipolar hard sphere bulk system. Ganzenmüller and Camp [31] used a fluid of charged hard dumbbells, each made up of two oppositely charged hard spheres, separated by the distance $d$, to track the gas-liquid coexistence towards the dipolar hard sphere limit $d \to 0$. Via extrapolation of their grand-canonical Monte Carlo results obtained for finite dumbbell length, they found a gas-liquid critical point in the dipolar hard sphere limit. Almarza *et al.* [32] confirm the results of Ganzenmüller and Camp [31] using Monte Carlo to analyze a mixture of hard spheres and dipolar hard sphere. The critical parameters for the gas-liquid equilibrium, extrapolated based on their mixture results to the limit of vanishing neutral hard sphere concentration, are in accord with the extrapolation for the dumbbells approaching the dipolar hard sphere limit. Kalyuzhnyi *et al.* [33] examine the phase behaviour of the dipolar Yukawa hard sphere fluid using Monte Carlo simulations. Again the critical point may be tracked as the dipolar hard sphere limit is approached by decreasing the strength of the attractive Yukawa potential. They find a critical point for values of the Yukawa potential well depth which is used as control parameter and representing the "distance" from the dipolar hard sphere limit, which are far lower than the limit set by the earlier study by Szalai *et al.* [19]. Continuation of this work in Ref. [34], however, results in the conclusion that phase separation is not observable beyond a critical value of the Yukawa energy parameter. Similar to the aforementioned work by Stevens and Grest [18], our colleague Jia [35] tracked the critical point for the dipolar soft sphere model as a parameter of the field strength and found critical values in the limit of vanishing field. The results were also confirmed as part of this work at zero field strength. A graphical representation to summarize the results on the localization of the gas-liquid critical point on dipolar systems is shown in Figure 1.1.

Based on the above-mentioned results, the assembly of single dipolar particles into reversible dipole chains or other aggregates like rings and branched structures, has a significant effect on the gas-liquid coexistence of dipolar systems (an interesting study of gas-liquid phase separation in systems composed of rings and chains was presented by Pam *et al.* [36]). Therefore, different approaches, such as an external field or modifications to the dipolar potential, were introduced in several aforementioned studies with the main target to prevent or somehow control the assembly reversible aggregates. Also, those long chains are difficult to equilibrate in computer simulations and also hard to handle analytically. The original notion of gas-liquid phase separation of monomers is generalized to include phase separation in systems of polydisperse reversible aggregates, or even other types of transitions like the demixing of topological defects [37].

In this work, we present another attempt to track the gas-liquid critical point in a system approaching the dipolar soft sphere limit. We study a system of charged soft dumbbells using the molecular dynamics technique. The charge-to-charge separation on the dumbbell $d$ can be controlled and we start our simulations in an "easy regime", where gas-liquid phase

separation is readily observed and the assembly of chains is energetically unfavourable. The charge-to-charge separation, $d$, is systematically decreased, keeping the dumbbell dipole moment, respectively the dumbbell charges, constant. Using this procedure we can approach the dipolar soft sphere limit in such a way that difficulties like the reversible association of particles develop "slowly", which allows the extrapolation to the desired limit. Even at the smallest $d$ ($= 10^{-4}$), we do observe a transition terminating in a critical point, which suggests a gas-liquid critical point in the dipolar soft sphere limit. This result is in accordance with the previous simulation study by Ganzenmüller and Camp [31] for dipolar hard spheres. To explain our simulation results, we apply different simple models. However, neither the extension of Flory's lattice theory to reversibly aggregating polymers [38, 39], nor the defect model put forward by Tlusty and Safran [37], yields a consistent description of the simulation results. Only the developed van der Waals mean field theory provides a close to quantitative description of the critical parameters obtained from the simulation. The theory combines the Onsager approach to dipolar liquids [40] with the idea that the basic unit is not the single dipole, but rather a small reversible aggregate. To support the results for charged soft dumbbell in the dipole limit, i.e. $d \to 0$, we also conduct simulations for the dipolar soft sphere model in its pure form and with an additional parameter which controls the soft sphere repulsion. We see that the soft repulsive interaction can be used as an effective means for limiting the aggregation in the dipole limit. The resulting short reversible chains, which are easy to equilibrate, do exhibit gas-liquid phase separation. Subsequently to the investigation at the dipole limit we study the gas-liquid phase transition in the dumbbell system for $d \gg 1$ and observe critical parameters in the whole simulated range, i.e. up to $d = 7$. On the basis of the aforementioned mean field theory, we construct a qualitative description of the critical behavior in the range of $1 < d < 7$. In this range it seems likely that the charged soft dumbbell model behaves similar to an ionic system and therefore relates to the restricted primitive model of ionic liquids. The restricted primitive model is also a model whose gas-liquid transition has attracted interest both from the analytical (e.g., Refs. [41, 42]) as well as from the simulation side (e.g., Refs. [43, 44]). In order to connect to the restricted primitive model results, we simulate an ionic model, where we have eliminated the rigid dumbbell bond. Thus the dumbbell model becomes equal to the restricted primitive model, except that the hard core repulsion is replaced by soft sphere repulsion. We also observe a gas-liquid critical point for this model and discuss the relation to the charged soft dumbbell system, as well as to the numerical predictions of the Debye-Hückel theory. In addition to the investigation of the phase transition, we have a look at the cation-anion pairing in terms of Bjerrum association in our ionic model, which serves as an important basic model in the interpretation of experimental data obtained from colloidal suspensions, liquid salts, and salt solutions [45].

Finally, we make additional use of the expertise gained in the course of our work on the phase behavior of charged and dipolar systems in the context of osmotic equilibria driven by Coulomb interactions. Specifically, we extend previous Monte Carlo simulations of osmotic equilibria in Lennard-Jones systems by Schreiber in our work group [46, 47]. We employ the Monte Carlo algorithm developed by Schreiber and Hentschke and apply it

to an ionic solute in a dipolar solvent. The algorithm allows us to perform Monte Carlo simulations in the $Tp\pi$ ensemble, with the temperature $T$, the external pressure $p$, and the osmotic pressure $\pi$ across the membrane. Thus we can study the dependency of the solute concentration on osmotic pressure and vice versa, which can then be compared with experimental data. The detailed study of osmosis is also of special interest due to the multitude of technical and biological problems connected with it.
The present work is structured as follows. An introduction to the simulation techniques used here is given in chapter 2. Chapter 3 contains the description of the various model systems studied using the aforementioned techniques. In the subsequent three chapters the results of the charged soft sphere model (chapter 4), the dipolar soft sphere model (chapter 5), and the ionic soft sphere model (chapter 6) are presented and discussed. Chapter 7 is an introduction to the topic of osmotic pressure followed by our numerical results. The last chapter provides a summary of this work and is followed by the acknowledgement and appendix.

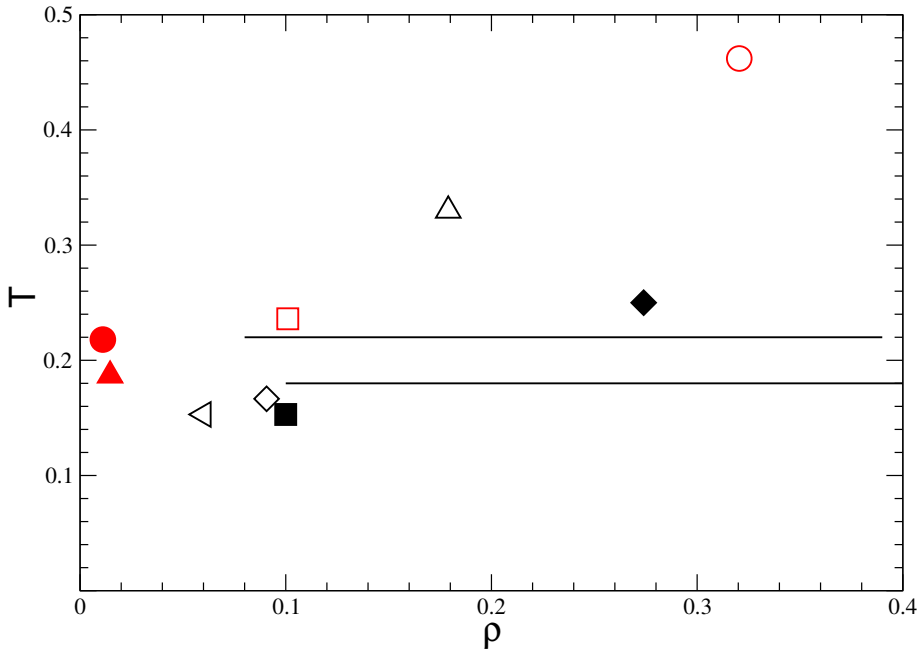


Figure 1.1.: Summarized illustration of attempts in the literature and by ourselves to locate the gas-liquid critical point in dipolar soft and hard sphere like systems. All dipolar soft sphere and dipolar soft sphere like results are mapped onto the dipolar hard sphere system using the procedure explained in section 3.5.1 (red symbols).
The symbols refer to the following sources: red solid circle: [own result for dipolar soft sphere]; red solid triangle: [own result for charged soft dumbbell]; black hollow triangle left: [32]; black hollow diamond: [34]; black solid square: [31]; red hollow square: [18]; black hollow triangle: [19]; black solid diamond: [17]; red hollow circle: [5]; black horizontal lines [16]. Filled symbols are used for results where a gas-liquid critical point is found or it is claimed to exist. Open symbols are critical values obtained for systems close to the dipolar hard sphere or dipolar soft sphere system where the dipolar limit can be modeled with a control parameter. The horizontal lines represent isotherms along which the gas-liquid transition can be precluded. The solid-diamond-result should be considered with caution due to the small system size of 32 particles in the simulation. Camp *et al.* used two different models to approach the dipolar hard sphere limit (black solid square and black hollow diamond). For the charged hard dumbbell model (solid square) it was possible to extrapolate to the dipolar hard sphere limit, but it failed for the second system (hollow diamond) where the dipolar Yukawa hard sphere fluid was used. For that, the symbol represents the simulation result for the gas-liquid critical point closest to the dipolar hard sphere limit. The limiting values of the charged hard dumbbell results have been confirmed by Almarza *et al.* (hollow triangle left), but they conclude that their result does not necessarily mean that a gas-liquid equilibria for pure dipolar systems exits.

# Bibliography


[1] J. D. Van der Waals. *Over de Continuiteit van den Gas-en Vloeistoftoestand*. AW Sijthoff, 1873.

[2] J. E. Jones. On the determination of molecular fields. II. From the equation of state of a gas. *Proceedings of the Royal Society of London. Series A*, 106(738):463, 1924.

[3] A. Z. Panagiotopoulos. Direct determination of phase coexistence properties of fluids by Monte Carlo simulation in a new ensemble. *Molecular Physics*, 61(4):813, 1987.

[4] B. Smit. Phase diagrams of Lennard-Jones fluids. *The Journal of Chemical Physics*, 96(11):8639, 1992.

[5] M. E. van Leeuwen and B. Smit. What makes a polar liquid a liquid? *Physical Review Letters*, 71(24):3991, 1993.

[6] R. Hentschke, E. M. Aydt, B. Fodi, and E. Stöckelmann. Molekulares Modellieren mit Kraftfeldern. http://constanze.materials.uni-wuppertal.de.

[7] B. J. Alder and T. E. Wainwright. Phase transition for a hard sphere system. *The Journal of Chemical Physics*, 27(5):1208, 1957.

[8] C. Holm and J. J. Weis. The structure of ferrofluids: A status report. *Current Opinion in Colloid & Interface Science*, 10(3-4):133, 2005.

[9] J. J. Weis and D. Levesque. *Advanced Computer Simulation Approaches for Soft Matter Sciences II*, volume 185 of *Advances in Polymer Science*, chapter Simple dipolar fluids as generic models for soft matter. Springer-Verlag, Berlin, 1986.

[10] S. H. L. Klapp. Dipolar fluids under external perturbations. *Journal of Physics: Condensed Matter*, 17(15):R525, 2005.

[11] B. Huke and M. Lücke. Magnetic properties of colloidal suspensions of interacting magnetic particles. *Reports on Progress in Physics*, 67:1731, 2004.

[12] R. P. Sear. Low-density fluid phase of dipolar hard spheres. *Physical Review Letters*, 76(13):2310, 1996.

[13] R. van Roij. Theory of chain association versus liquid condensation. *Physical Review Letters*, 76(18):3348, 1996.

[14] J. M. Tavares, M. M. Telo Da Gama, and M. A. Osipov. Criticality of dipolar fluids: Liquid-vapor condensation versus phase separation in systems of living polymers. *Physical Review E*, 56(6):R6252, 1997.

[15] Y. Levin. What happened to the gas-liquid transition in the system of dipolar hard spheres? *Physical Review Letters*, 83(6):1159, 1999.

[16] J. Caillol. Search of the gas–liquid transition of dipolar hard spheres. *The Journal of Chemical Physics*, 98:9835, 1993.

[17] K. Ng, J. P. Valleau, G. M. Torrie, and G. N. Patey. Liquid-vapour co-existence of dipolar hard spheres. *Molecular Physics*, 38(3):781, 1979.

[18] M. J. Stevens and G. S. Grest. Coexistence in dipolar fluids in a field. *Physical Review Letters*, 72(23):3686, 1994.

[19] I. Szalai, D. Henderson, D. Boda, and K. Chan. Thermodynamics and structural properties of the dipolar Yukawa fluid. *The Journal of Chemical Physics*, 111(1):337, 1999.

[20] J. Bartke and R. Hentschke. Phase behavior of the Stockmayer fluid via molecular dynamics simulation. *Physical Review E*, 75:061503, 2007.

[21] R. Hentschke and J. Bartke. Reply to "comment on 'equilibrium polymerization and gas-liquid critical behavior in the Stockmayer fluid'". *Physical Review E*, 77(1):013502, 2008.

[22] J. O. Sindt and P. J. Camp. Simulations of dipolar fluids using effective many-body isotropic interactions. *The Journal of Chemical Physics*, 143(2):024501, 2015.

[23] L. Rovigatti, J. Russo, and F. Sciortino. No evidence of gas-liquid coexistence in dipolar hard spheres. *Physical Review Letters*, 107(23):237801, 2011.

[24] L. Rovigatti, J. Russo, and F. Sciortino. Structural properties of the dipolar hard-sphere fluid at low temperatures and densities. *Soft Matter*, 8(23):6310, 2012.

[25] L. Rovigatti, J. M. Tavares, and F. Sciortino. Self-assembly in chains, rings, and

branches: a single component system with two critical points. *Physical Review letters*, 111(16):168302, 2013.

[26] A. O. Ivanov, S. S. Kantorovich, L. Rovigatti, J. M. Tavares, and F. Sciortino. Low temperature structural transitions in dipolar hard spheres: The influence on magnetic properties. *Journal of Magnetism and Magnetic Materials*, 383:272, 2015.

[27] S. Dussi, L. Rovigatti, and F. Sciortino. On the gas–liquid phase separation and the self-assembly of charged soft dumbbells. *Molecular Physics*, 111(22-23):3608, 2013.

[28] S. C. McGrother and G. Jackson. Island of vapor-liquid coexistence in dipolar hard-core systems. *Physical Review Letters*, 76(22):4183, 1996.

[29] P. J. Camp, J. C. Shelley, and G. N. Patey. Isotropic fluid phases of dipolar hard spheres. *Physical Review Letters*, 84(1):115, 2000.

[30] A. F. Pshenichnikov and V. V. Mekhonoshin. Cluster structure and the first-order phase transition in dipolar systems. *The European Physical Journal E*, 6(1):399, 2001.

[31] G. Ganzenmüller and P. J. Camp. Vapor-liquid coexistence in fluids of charged hard dumbbells. *Journal of Chemical Physics*, 126:191104, 2007.

[32] N. G. Almarza, E. Lomba, C. Martín, and A. Gallardo. Demixing in binary mixtures of apolar and dipolar hard spheres. *The Journal of Chemical Physics*, 129(23):234504, 2008.

[33] Y. V. Kalyuzhnyi, I. A. Protsykevytch, G. Ganzenmüller, and P. J. Camp. Liquid-vapour coexistence in the dipolar Yukawa hard-sphere fluid. *EPL (Europhysics Letters)*, 84(2):26001, 2008.

[34] G. Ganzenmüller, G. N. Patey, and P. J. Camp. Vapour–liquid phase transition of dipolar particles. *Molecular Physics*, 107(4-6):403, 2009.

[35] R. Jia, H. Braun, and R. Hentschke. Gas-liquid coexistence in a system of dipolar soft spheres. *Physical Review E*, 82(6):062501, 2010.

[36] L. S. Pam, L. L. Spell, and J. T. Kindt. Simulation and theory of flexible equilibrium polymers under poor solvent conditions. *The Journal of Chemical Physics*, 126(13):134906, 2007.

[37] T. Tlusty and S. A. Safran. Defect-induced phase separation in dipolar fluids. *Science*, 290(5495):1328, 2000.

[38] J. Dudowicz, K. F. Freed, and J. F. Douglas. Flory-Huggins model of equilibrium polymerization and phase separation in the Stockmayer fluid. *Physical Review Letters*, 92(4):045502, 2004.

[39] R. Hentschke, J. Bartke, and F. Pesth. Equilibrium polymerization and gas-liquid critical behavior in the Stockmayer fluid. *Physical Review E*, 75:011506, 2007.

[40] L. Onsager. Electric moments of molecules in liquids. *Journal of the American Chemical Society*, 58:1486, 1936.

[41] M. E. Fisher and Y. Levin. Criticality in ionic fluids: Debye-Hückel theory, Bjerrum, and beyond. *Physical Review Letters*, 71(23):3826, 1993.

[42] Y. Levin and M. E. Fisher. Criticality in the hard-sphere ionic fluid. *Physica A: Statistical Mechanics and its Applications*, 225(2):164, 1996.

[43] A. Z. Panagiotopoulos. Critical parameters of the restricted primitive model. *The Journal of Chemical Physics*, 116(7):3007, 2002.

[44] J. M. Caillol, D. Levesque, and J. J. Weis. Critical behavior of the restricted primitive model revisited. *Journal of Chemical Physics*, 116(24):10794, 2002.

[45] H. Braun and R. Hentschke. Phase coexistence for charged soft dumbbell and ionic soft sphere systems via molecular dynamics simulation. *Physical Review E*, 87(1):012311, 2013.

[46] S. Schreiber. Monte Carlo Simulationen zum osmotischen Druck. Master's thesis, Bergische Universität Wuppertal, 2011.

[47] S. Schreiber and R. Hentschke. Monte Carlo simulation of osmotic equilibria. *The Journal of Chemical Physics*, 135(13):134106, 2011.

# 2. Methods

With the help of computer simulations or molecular simulations in particular it is possible to get results, which are not measurable experimentally. Also the level of detail exceeds that of any experiment. Computer simulations give the possibility to pursue totally new physical questions or approach existing questions in an abstract way. This we do for example with our dumbbell system, in order to analyze the phase behavior of dipolar fluids. The two most common methods used for molecular modelling are the stochastic Monte Carlo (MC) method and the deterministic molecular dynamics (MD) simulation method. In this work we use the MD method mainly for the analysis of the phase transition of the charged soft dumbbell (CSD), dipolar soft sphere (DSS) and ionic model. The MC method is used for the research of the osmotic pressure, where specifically a modification of the Gibbs ensemble Monte Carlo (GEMC) method is utilized. In the following section we give an overview of those methods, and also of some techniques implemented to optimize the results in respect of computational costs.

## 2.1. Molecular dynamics simulation

The development of the MD method dates back to the late 50s [1, 2]. The MD method gives us the possibility to study a $N$ particle system for a specific period of time, i.e we can calculate the state functions of the system, and even monitor the physical trajectory of each individual particle. The latter is not possible with MC simulations, due to its stochastic approach of moving particles. This "unnatural" move of particles is also the reason, why we prefer to use the MD method for most of our investigations. We mostly deal with polar fluids, which tent to build long chain like aggregates, where the application of MC methods would require complex bias-methods to support the reversible aggregation with acceptable computational costs [3–5].
The underlying approach to the MD simulations are the equations of motion, i.e.

$$\frac{d}{dt}\vec{p}_i = \vec{F}_i \tag{2.1.1}$$

for the translation of the center of mass and

$$\frac{d}{dt}\vec{L}_i = \vec{N}_i \tag{2.1.2}$$

for the rotation of the particle $i \in N$. In the equations of motion is $\vec{p}_i$ the momentum of particle $i$ with the acting force $\vec{F}_i$ and $\vec{L}_i$ is the angular momentum with the torque $\vec{N}_i$. By solving the equations of motion numerically we get the trajectories of the particles and can gain a deep insight into the atomic processes of the simulated matter.
Most of the following sections are molecular modelling basics and thus can be found in a similar fashion in other works like this or in more detail in standard text books dealing with the topic like [6–10].

### 2.1.1. Integrating the equations of motion

To numerically solve the equations of motion (2.1.1) and (2.1.2) in MD simulations a so called integrator is necessary. There is a big variety of different integrators available and a good overview of them can be found in [6], [7] and [11]. In general the integrator should retain the mathematical and physical characteristics of the exact solution of the equations of motion. Therefore the integrator must be symplectic, time-reversible and conserve energy and momentum. In our work we use the velocity Verlet algorithm [12] for the translation and rotation of the particle. The velocity Verlet algoritm is a slightly modified version of the original Verlet algorithm [13]. A big advantage of the velocity Verlet algorithm is the computational cost, as it only requires the calculation of one force per time step, the numerical stability and the errors, which are of order $\mathcal{O}(\Delta t^4)$.

**Integrator for translation** The velocity Verlet algorithm can be derived using a Taylor expansion of the positions $\vec{r}_i(t)$ and the velocities $\dot{\vec{r}}_i(t)$. For the positions we get

$$\vec{r}_i(t+\Delta t) = \vec{r}_i(t) + \Delta t\, \dot{\vec{r}}_i(t) + \frac{1}{2}\Delta t^2\, \ddot{\vec{r}}_i(t) + \mathcal{O}(\Delta t^3)\,. \tag{2.1.3}$$

To determine the velocities at the same time as the position, i.e. $t + \Delta t$, we first need to do an expansion of the velocities for $t \pm \Delta t/2$, which yields

$$\dot{\vec{r}}_i(t+\frac{\Delta t}{2}) = \dot{\vec{r}}_i(t) + \frac{1}{2}\Delta t\, \ddot{\vec{r}}_i(t) + \mathcal{O}(\Delta t^2) \tag{2.1.4}$$

$$\dot{\vec{r}}_i(t-\frac{\Delta t}{2}) = \dot{\vec{r}}_i(t) - \frac{1}{2}\Delta t\, \ddot{\vec{r}}_i(t) + \mathcal{O}(\Delta t^2)\,. \tag{2.1.5}$$

With adding another time step $\Delta t$ to (2.1.5), we get the velocities at time $t + \Delta t$ as

$$\dot{\vec{r}}_i(t+\Delta t) = \dot{\vec{r}}_i(t+\frac{\Delta t}{2}) + \frac{1}{2}\Delta t\, \ddot{\vec{r}}_i(t+\Delta t) + \mathcal{O}(\Delta t^2)\,. \tag{2.1.6}$$

To implement the algorithm in the simulation program, and process one simulation step, the equations must be solved in the following order

$$\vec{r}_i(t+\Delta t) = \vec{r}_i(t) + \Delta t\,\dot{\vec{r}}_i(t) + \frac{1}{2}\,\Delta t^2\,\ddot{\vec{r}}_i(t) \tag{2.1.7}$$

$$\dot{\vec{r}}_i(t+\frac{\Delta t}{2}) = \dot{\vec{r}}_i(t) + \frac{1}{2}\Delta t\,\ddot{\vec{r}}_i(t) \tag{2.1.8}$$

$$\dot{\vec{r}}_i(t+\Delta t) = \dot{\vec{r}}_i(t+\frac{\Delta t}{2}) + \frac{1}{2}\Delta t\,\ddot{\vec{r}}_i(t+\Delta t)\,. \tag{2.1.9}$$

The necessary acceleration $\ddot{\vec{r}}_i(t)$ can be calculated from the forces, noted down in chapter 3, for the individual models used in this work.

**Integrator for rotation** We also use the velocity Verlet algorithm for the integration of the rotation. We describe the rotation using the unit vector $\vec{n}_i$. Treating it analogously to the translation, we get the following formulas for the implementation of the rotation

$$\vec{n}_i(t+\Delta t) = \vec{n}_i(t) + \Delta t\,\dot{\vec{n}}_i(t) + \frac{1}{2}\,\Delta t^2\,\ddot{\vec{n}}_i(t) \tag{2.1.10}$$

$$\dot{\vec{n}}_i(t+\frac{\Delta t}{2}) = \dot{\vec{n}}_i(t) + \frac{1}{2}\Delta t\,\ddot{\vec{n}}_i(t) \tag{2.1.11}$$

$$\dot{\vec{n}}_i(t+\Delta t) = \dot{\vec{n}}_i(t+\frac{\Delta t}{2}) + \frac{1}{2}\Delta t\,\ddot{\vec{n}}_i(t+\Delta t)\,. \tag{2.1.12}$$

As we have described the rotation solely as expression of the unit vector $\vec{n}_i$, we need to link the commonly known torque

$$\vec{N}_i = -\vec{r}_i \times \frac{\partial U}{\partial \vec{r}_i} \tag{2.1.13}$$

to the orientation $\vec{n}_i$. Therefore we mainly follow [14] and start with the equation of motion (2.1.2), where we write for the torque

$$\vec{N}_i = \dot{\vec{L}}_i = I\,\ddot{\vec{\phi}}_i \tag{2.1.14}$$

using the angular acceleration $\ddot{\vec{\phi}}_i$ and the moment of inertia $I$. In the next step we look at the change of the potential energy of the particle $i$

$$\delta U_i = -\sum_{j,\alpha} \vec{f}_{j_\alpha} \cdot \delta\vec{r}_{j_\alpha} = -\sum_{j,\alpha} \vec{f}_{j_\alpha} \cdot \left(\delta\vec{\phi}_i \times \vec{r}_{j_\alpha}\right) \tag{2.1.15}$$

$$= -\delta\vec{\phi}_i \cdot \sum_{j,\alpha} \vec{f}_{j_\alpha} \times \vec{r}_{j_\alpha} = -\vec{N}_i \cdot \delta\vec{\phi}_i \tag{2.1.16}$$

caused by a small rotation $\delta\vec{\phi}_i$, where the forces $\vec{f}_{j_\alpha}$ act on the particle $i$ at position $\vec{r}_{j_\alpha}$. The magnitude of the angle of rotation is given by $|\delta\vec{\phi}_i|$, and $\delta\vec{\phi}_i$ is perpendicularly to the

plane of the rotation, i.e. parallel to the axis of rotation. We can also express the change of the potential energy, caused by a small rotation of the orientation vector $\vec{n}_i$, as

$$\delta U_i = \frac{\partial U}{\partial \vec{n}_i} \cdot \delta \vec{n}_i = \frac{\partial U}{\partial \vec{n}_i} \cdot (\delta \phi_i \times \vec{n}_i) = \left( \vec{n}_i \times \frac{\partial U}{\partial \vec{n}_i} \right) \cdot \delta \phi_i \,. \tag{2.1.17}$$

By comparing this with (2.1.16), we can write for the torque

$$\vec{N}_i = -\vec{n}_i \times \frac{\partial U}{\partial \vec{n}_i} = I \, \ddot{\vec{\phi}}_i \tag{2.1.18}$$

and get it related to the orientation $\vec{n}_i$. Together with (2.1.18) and

$$\dot{\vec{n}}_i = \dot{\vec{\phi}}_i \times \vec{n}_i \tag{2.1.19}$$

we have now two first-order differential equations for the rotation of the particle. For the implementation in the MD program it is helpful to eliminate $\dot{\vec{\phi}}_i$ and describe the rotation using a second-order differential equation, which is only dependent on the orientation $\vec{n}_i$. To gain the second-order differential equation, we take the derivate of (2.1.19) with respect to time and get

$$\begin{aligned}
\ddot{\vec{n}}_i &= \ddot{\vec{\phi}}_i \times \vec{n}_i + \dot{\vec{\phi}}_i \times \dot{\vec{n}}_i && (2.1.20)\\
&= \frac{1}{I} \vec{N}_i \times \vec{n}_i + \dot{\vec{\phi}}_i \times \left( \dot{\vec{\phi}}_i \times \vec{n}_i \right) && (2.1.21)\\
&= \frac{1}{I} \left( -\vec{n}_i \times \frac{\partial U}{\partial \vec{n}_i} \right) \times \vec{n}_i + \left[ \dot{\vec{\phi}}_i \left( \dot{\vec{\phi}}_i \cdot \vec{n}_i \right) - \vec{n}_i \left( \dot{\vec{\phi}}_i \right)^2 \right] && (2.1.22)\\
&= \frac{1}{I} \left[ -\frac{\partial U}{\partial \vec{n}_i} + \vec{n}_i \left( \vec{n}_i \cdot \frac{\partial U}{\partial \vec{n}_i} \right) \right] - \vec{n}_i \cdot \dot{\vec{n}}_i^2 && (2.1.23)
\end{aligned}$$

for the acceleration of the orientation. In the last step we used $\dot{\vec{\phi}}_i \cdot \vec{n}_i = 0$, and together with $\vec{n}_i^2 = 1$ the relation

$$\dot{\vec{n}}_i^2 = \left( \dot{\vec{\phi}}_i \times \vec{n}_i \right)^2 = \dot{\vec{\phi}}_i^2 \, \vec{n}_i^2 - \left( \dot{\vec{\phi}}_i \cdot \vec{n}_i \right)^2 = \dot{\vec{\phi}}_i^2 \,. \tag{2.1.24}$$

Finally we introduce $\vec{G}_i = -I^{-1} \left( \partial U / \partial \vec{n}_i \right)$ to write the acceleration of the orientation as

$$\ddot{\vec{n}}_i = \vec{G}_i - \left( \vec{n}_i \cdot \vec{G}_i + \dot{\vec{n}}_i^2 \right) \vec{n}_i \,, \tag{2.1.25}$$

which directly can be used in the first two steps (2.1.10) and (2.1.11) of the velocity Verlet algorithm. One hitch we have to overcome, is that $\ddot{\vec{n}}_i(t+\Delta t)$ also depends on the unknown velocity $\dot{\vec{n}}_i(t + \Delta t)$. Therefore we have to approximate the calculation of (2.1.12) via

$$\dot{\vec{n}}_i(t + \Delta t) = \dot{\vec{n}}_i(t + \frac{1}{2}\Delta t) + \frac{1}{2} \Delta t \, \ddot{\vec{n}}_i(t) \,. \tag{2.1.26}$$

Herewith follows at time $t + \Delta t$ the expression for the angular acceleration (2.1.25) as

$$\begin{aligned}\ddot{\vec{n}}_i(t+\Delta t) = \vec{G}_i(t+\Delta t) - \Big[\vec{n}_i(t+\Delta t)\cdot\vec{G}_i(t+\Delta t) \\ + \left(\dot{\vec{n}}_i(t+\frac{1}{2}\Delta t) + \frac{1}{2}\Delta t\,\ddot{\vec{n}}_i(t)\right)\Big]\vec{n}_i(t+\Delta t)\,.\end{aligned} \tag{2.1.27}$$

This is the final form used in the velocity Verlet algorithm. This form of the integrator produces numerically stable results. But it seems that also without the velocity term, stable results are possible [7].
During the simulation the following two conditions have to be ensured

$$|\vec{n}_i| = 1 \qquad \text{and} \qquad \vec{n}_i \cdot \dot{\vec{n}}_i = 0\,. \tag{2.1.28}$$

Hence we normalize $\vec{n}_i$ and orthogonalize $\vec{n}_i$ as well as $\dot{\vec{n}}_i$ after each time step $\Delta t$.

## 2.2. Monte Carlo simulations

The Monte Carlo method is a stochastic method. In contrast to MD it cannot be used to calculate dynamic properties like the phase space trajectories and only allows to compute time average values. Nevertheless the MC is also heavily used in molecular simulations as it easily allows to simulate various ensembles. A lot of quantities, we are interested in, can be calculated without the knowledge of the dynamic properties. E.g. the internal energy $U$ or the force on an individual particle $\vec{F}_i$ are only dependent on the coordinates $\vec{r}_i$ of the particles. The coordinates $\{\vec{r}\}$ of the particles in a system can be determined as in the MD via an update step. But now this update step is stochastic and not deterministic anymore. In the following we want to explain, how this update step can be produced. We mainly follow the description given by Hentschke *et al.* in Ref. [6] and specifically for the $Tp\pi$ ensemble in Ref. [15].

### 2.2.1. Metropolis Monte Carlo method

Let us consider a macroscopic quantity $A$, which is only dependent on the configurations $\{\vec{r}\}$ of the system in the NVT ensemble. I.e. a thermodynamic system with constant number of particles $N$, constant volume $V$, and constant temperature $T$. For this the ensemble average (see also section 2.3.1) is given by

$$\langle A\rangle_{NVT} = \int_\Gamma \mathrm{d}\Gamma A(\Gamma) f_{NVT}(\Gamma) \tag{2.2.1}$$

where $\Gamma$ is a single point in the phase space and $f_{NVT}$ is the probability density function, which gives the probability to find a certain state in the phase space. One can show that for quantity $A$ only the probability function $f_{NVT}(\{\vec{r}\})$ is necessary which is defined as

$$f_{NVT}(\{\vec{r}\}) = \frac{\exp[-\beta U(\{\vec{r}\})]}{\int \mathrm{d}\{\vec{r}\} \exp[-\beta U(\{\vec{r}\})]} \tag{2.2.2}$$

with $\beta = 1/k_B T$. Function (2.2.2) is also known as the phase space density. In general it is not possible to solve the integral and we need a trick, which allows us to create the configurations based on the distribution $f_{NVT}$ without explicitly calculating it. Therefore we consider two different states $\{\vec{r}\}_{new}$ together with $\{\vec{r}\}_{old}$ and calculate the relative probability as the quotient of the two states

$$\frac{f_n}{f_o} = \frac{f_{NVT}(\{\vec{r}\}_{new})}{f_{NVT}(\{\vec{r}\}_{old})} = \exp[-\beta \left(U(\{\vec{r}\}_{new}) - U(\{\vec{r}\}_{old})\right)] \,. \tag{2.2.3}$$

Here the integral in equation (2.2.2) is the same for both states and drops out of equation (2.2.3). So to calculate $f_n/f_o$ we only need to know that the probability of a configuration $\{\vec{r}\}$ is proportional to its Boltzmann factor $\exp[-\beta U(\{\vec{r}\})]$. Thus we need a way to generate points in the configuration space proportional to the Boltzmann factor. In other words we have to find a suitable acceptance criteria $\beta_{no}$, which tells us, when we accept the new configuration $n$ or when we reject it and proceed with the old one $o$. The solution to this question is not unique. One popular and efficient method is the Metropolis algorithm, introduced as early as 1953 by Nicholas Metropolis *et al.* [16]. The Metropolis algorithm allows us to calculate the transition probability

$$\pi_{on} = \alpha_{no} \beta_{no} \tag{2.2.4}$$

to go from configuration $o$ to $n$ together with the acceptance criteria $\beta_{no}$. To ensure that the generated chain of configurations (Markov chain) converges to the demanded ensemble, the algorithm must fulfill several properties. The first one is the detailed balance principle and requests that the probability of the accepted transitions from state $o$ to any other state $n$ is exactly the same as for the reverse transition, i.e.

$$f_o \pi_{on} = f_n \pi_{no} \,. \tag{2.2.5}$$

The second one demands that the algorithm is ergodic, i.e. all possible points in the configuration space can be reached with a final number of MC steps. The Metropolis algorithm satisfies those conditions and defines the acceptance criteria to perform an update from configuration $o$ to $n$ as

$$\beta_{no} = \min(1, \frac{f_n}{f_o}) \geq \xi \,, \tag{2.2.6}$$

where $\xi$ is a random number between 0 and 1. If the acceptance criteria (2.2.6) is not fulfilled, the new configuration $n$ is discarded and we continue with the old configuration $o$.

### 2.2.2. The $Tp\pi$ ensemble

To perform the simulations in the $Tp\pi$ ensemble, we make use of the idea of the Gibbs ensemble [17, 18], where we study two simulation boxes simultaneously. The box $i$ $(= 1, 2)$ contains $N_{l,i}$ solvent particles and $N_{s,i}$ solute molecules, respectively. The two subsystems are not isolated and particles can be exchanged between the two boxes. But as we compute an osmotic cell, we need to construct a semi-permeable membrane between the two compartments, i.e. only the particle interchange of the solvent is allowed and we force $N_{s,1} = 0$. This means the second box contains the mixture and hence also the pressure in the box is $p + \pi$. The thermodynamic states of the two subsystems are defined by the eight quantities $T_1$, $T_2$, $p$, $p + \pi$, $N_{l,i}$ and $N_{s,i}$. The number of degrees of freedom at equilibrium is reduced from 8 to 3 due to the following five conditions $T = T_1 = T_2$, equality of the chemical potentials $\mu_l = \mu_{l,1} = \mu_{l,2}$ plus the constraints on the particle numbers $N_{l,1} + N_{l,2} = N_l = \text{const.}$, $N_{s,1} = 0$ and $N_{s,2} = \text{const}$. This leaves $T$, $p$ and $\pi$ as the remaining degrees of freedom. Before noting down the partition function, we take a look at the entropy changes, which for the two boxes are

$$T\Delta S_1 = \Delta E_1 + p\Delta V_1 - \mu_l \Delta N_{l,1} \tag{2.2.7}$$

$$T\Delta S_2 = \Delta E_2 + (p+\pi)\Delta V_2 - \mu_l \Delta N_{l,2}\,, \tag{2.2.8}$$

where the $E_i$ are the internal energies. In total we get

$$\Delta S = \frac{\Delta E_1 + \Delta E_2}{T} + \frac{p\,(\Delta V_1 + \Delta V_2)}{T} + \frac{\pi \Delta V_2}{T} \tag{2.2.9}$$

as $\Delta N_{l,1} = -\Delta N_{l,2}$. The partition function, considering also small rigid molecules like water, is given by

$$\begin{aligned} Q = \int \frac{V_1^{N_{l,1}} V_2^{N_{l,2}+N_{s,2}} \mathrm{d}^{3(\mathrm{N_1+N_{s,2}})} p_{cm} \mathrm{d}^{3(\mathrm{N_1+N_{s,2}})} s_{cm}}{h^{3(N_l+N_{s,2})} N_{l,1}! N_{l,2}! N_{s,2}!} \prod_{\alpha=1}^{3} \frac{\mathrm{d}^{(\mathrm{N_1+N_{s,2}})}\phi_\alpha \mathrm{d}^{(\mathrm{N_1+N_{s,2}})} p_\alpha}{h^{3(N_l+N_{s,2})} \sigma_l^{N_l} \sigma_s^{N_{s,2}}} \\ \times \exp\left[-\beta\left(E_1 + E_2 + pV_1 + (p+\pi)V_2 + \mu_l N_l + \mu_{s,2} N_{s,2}\right)\right] \end{aligned} \tag{2.2.10}$$

with Planck's constant $h$ and $\beta = 1/k_B T$. The integration is done over the center of mass coordinates in reduced form $\vec{r}_{cm} = V^{1/3}\vec{s}$ and their conjugate momenta $p_{cm}$ as well as the Euler angles $\phi_\alpha = (\varphi, \theta, \psi)$ and their conjugate momenta $p_\alpha$. The $\sigma$'s are the symmetry numbers of the solvent and solute molecules. After integration over all momenta using the respective (kinetic) Boltzmann-weights, equation (2.2.10) becomes

$$\begin{aligned} Q = \int \frac{V_1^{N_{l,1}} V_2^{N_{l,2}+N_{s,2}}}{\Lambda_{T,l}^{3N_l} \Lambda_{T,s}^{3N_{s,2}} N_{l,1}! N_{l,2}! N_{s,2}!} \mathrm{d}^{3(\mathrm{N_1+N_{s,2}})} s_{cm} \\ \times \prod_{\alpha=1}^{3} \frac{\sin^{N_l}\theta_l \sin^{N_{s,2}}\theta_s}{\lambda_{T,l}^{N_l} \lambda_{T,s}^{N_{s,2}}} \mathrm{d}^{(\mathrm{N_1+N_{s,2}})}\phi_\alpha \exp\left[-\beta\left(U_1 + U_2\right.\right. \\ \left.\left. + \; pV_1 + (p+\pi)V_2 + \mu_l N_l + \mu_{s,2} N_{s,2}\right)\right] \end{aligned} \tag{2.2.11}$$

where $\Lambda_T$ is the usual thermal wavelength and

$$\lambda_T = \frac{\sigma(\beta\hbar/(2\pi))^{3/2}}{I_1 I_2 I_3} \tag{2.2.12}$$

with the molecular principal moments of inertia $I_j$ ($j = 1, 2, 3$). Due to the integration over the momenta, we now only have to consider the potential energies $U_i$. With that, we can write down the probability function for our Metropolis criteria as

$$\begin{aligned} f \propto & \frac{V_1^{N_{l,1}} V_2^{N_{l,2}+N_{s,2}}}{\Lambda_{T,l}^{3N_l} \Lambda_{T,s}^{3N_{s,2}} N_{l,1}! N_{l,2}! N_{s,2}!} \frac{\sin^{N_l}\theta_l \sin^{N_{s,2}}\theta_s}{\lambda_{T,l}^{N_l} \lambda_{T,s}^{N_{s,2}}} \\ & \exp\left[-\beta\left(U_1 + U_2 + pV_1 + (p+\pi)V_2 + \mu_l N_l + \mu_{s,2} N_{s,2}\right)\right] . \end{aligned} \tag{2.2.13}$$

Now we can note down the different MC trial moves, we perform to simulate in the $Tp\pi$ ensemble. We use the phase space density in equation (2.2.13) and calculate the acceptance via (2.2.6) going from the state $o$ to $n$. This yields the following four probability ratios:

- Translation of a particle within box $i$
  The translation of a particle leads to a change of the potential energy $\Delta U_i = U_{i,n} - U_{i,o}$ of the box and hence the probability ratio for translation of a particle in box $i$ is

$$\frac{f_n}{f_o} = \exp\left[-\beta \Delta U_i\right] . \tag{2.2.14}$$

- Rotation of a particle in box $i$
  The center of mass rotation of a particle also results in a change of the potential energy $\Delta U_i = U_{i,n} - U_{i,o}$. But in addition to the translation we also have to consider the ratio of the sines in (2.2.6) and get for the center of mass rotation of a particle in compartment $i$

$$\frac{f_n}{f_o} = \frac{\sin\theta_{i,n}}{\sin\theta_{i,o}} \exp\left[-\beta \Delta U_i\right] . \tag{2.2.15}$$

- Volume Change of box $i$
  The volume of each box can change individually and the two volumes $V_1$ and $V_2$ are not correlated. This is different to the normal Gibbs ensemble and the algorithm in reference [19], where the total volume is kept constant, or as in reference [20], where the volume of each box is constant. The volume change of a box is $\Delta V_i = V_{i,n} - V_{i,o}$. This also effects the potential energy $\Delta U_i$. With the use of the Kronecker delta $\delta_{i2}$, which is 1 for $i = 2$ and zero otherwise, the ratio is

$$\frac{f_n}{f_o} = \left(\frac{V_{i,n}}{V_{i,o}}\right)^{N_{l,i}+N_{s,i}} \exp\left[-\beta\left(\Delta U_i + (p + \delta_{i2}\pi)\Delta V_i\right)\right] . \tag{2.2.16}$$

- Solvent transfer between the compartments
  As aforementioned we only allow the exchange of the solvent particles between the boxes due to the semi-permeable membrane. For a particle transfer from subsystem 1 to 2 the probability ratio is given by

$$\frac{f_n}{f_o} = \frac{V_2 N_{l,1}}{V_1(N_{l,2}+1)} \exp\left[-\beta\left(\Delta U_1 + \Delta U_2\right)\right], \tag{2.2.17}$$

  where $\Delta U_1 = U_1(N_{l,1}-1) - U_1(N_{l,1})$ and $\Delta U_2 = U_2(N_{l,2}+1) - U_2(N_{l,2})$. For the opposite transfer from box 2 to 1 it is

$$\frac{f_n}{f_o} = \frac{V_1 N_{l,2}}{V_2(N_{l,1}+1)} \exp\left[-\beta\left(\Delta U_1 + \Delta U_2\right)\right], \tag{2.2.18}$$

  where now $\Delta U_1 = U_1(N_{l,1}+1) - U_1(N_{l,1})$ and $\Delta U_2 = U_2(N_{l,2}-1) - U_2(N_{l,2})$.

In the implementation of our MC simulation we have to decide, how the different types of trial moves are selected. In the original Gibbs ensemble implementation a fixed order was used [17]. Nowadays mostly a stochastic approach is taken, where the decision which type of trial move should be performed (particle transfer, rotation, volume change or solvent transfer) is randomized. This type of implementation should be preferred and was applied in our simulation routines, as it guarantees microscopic reversibility. Thus it does not make a difference at which point in the program the measurement of the physical property is performed, as all trial moves are on average equivalent [8].

## 2.3. Calculation of thermodynamic quantities

### 2.3.1. Ensemble and time average

In statistical mechanics we have learned to calculate the macroscopic quantity $A$ of a system of $N$ particles as the ensemble average

$$\langle A \rangle = \sum_i p_i A_i \tag{2.3.1}$$

of the microscopic states. Here $p_i$ is the probability of the so called microstate $i$, defined by the probability distribution of the ensemble. Each single microstate is defined by a set of generalized coordinates $q_i$ and their conjugate momentum $p_i$, which build a single point in the phase space $\Gamma = (\vec{q_1}, ..., \vec{q_N}, \vec{p_1}, ..., \vec{p_N})$. In classical terms we can write the ensemble average (2.3.1) as integral over the phase space

$$\langle A \rangle = \frac{\int_\Gamma \mathrm{d}\Gamma A(\Gamma)\rho(\Gamma)}{\int_\Gamma \mathrm{d}\Gamma \rho(\Gamma)}, \tag{2.3.2}$$

with $\mathrm{d}\Gamma$ being a phase space element and $\rho(\Gamma)$ the phase space density. In an experiment we usually take a different approach to calculate an average quantity and build the average over multiple measurements taken over a certain period of time. This procedure is quite similar to MD where we evolve the system in time, which results in a phase space trajectory $\Gamma(t)$ and a change of the quantity $A(\Gamma(t))$. The time average can be calculated as

$$\bar{A} = \frac{1}{t}\int_0^t A(\Gamma(t'))\mathrm{d}t' = \frac{1}{M}\sum_{i=1}^{M} A(\Gamma(i\Delta t))\,. \tag{2.3.3}$$

The representation of the sum considers the fact that MD evolves only in single time steps $\Delta t$. Ideally we would build the time average over an infinite period of time. In case of an ergodic system, we then can set the time average equal to the ensemble average

$$\bar{A} = \lim_{t\to\infty}\frac{1}{t}\int_0^t A(\Gamma(t'))\mathrm{d}t' = \lim_{M\to\infty}\frac{1}{M}\sum_{i=1}^{M} A(\Gamma(i\Delta t)) = \langle A\rangle = \sum_i p_i A_i\,. \tag{2.3.4}$$

The equation (2.3.4) is referred to as the "ergodic hypothesis", which was originally stated by Ludwig Boltzmann. A system can be considered as ergodic, if the trajectory can come arbitrary close to any point $\Gamma$ of the phase space in finite time. In computer simulations it is a basic assumption to deal with an ergodic systems but in general, it is not possible to show for a real system, if it is ergodic. It is even worse, because we have to be aware that many real systems like glasses are not ergodic at all [8].

### 2.3.2. Internal energy

The internal energy of a system is given by

$$E = K + U \tag{2.3.5}$$

where $K$ stands for the kinetic energy of the particles and $U$ for the potential energy, caused by the interaction potential of the individual particles. Dependent on the particle model (see chapter 3) the term of the potential energy varies. This is not the case for the kinetic energy, where we only have to distinguish between two different types of models. On the one hand there are models with a radial symmetric potential like ions. In this case the model has three degrees of freedom with the kinetic energy caused by the translation of the particles given by

$$K = K_{trans} = \frac{1}{2}m\sum_{i=1}^{N}|\dot{\vec{r}}_i|^2 = \frac{1}{2}m\sum_{i=1}^{N}\left(\dot{r}_{x_i}^2 + \dot{r}_{y_i}^2 + \dot{r}_{z_i}^2\right)\,. \tag{2.3.6}$$

On the other hand we deal with particles with a non-radial symmetric pair potential respectively geometry. Here an additional contribution of the rotation needs to be added to the kinetic energy

$$K = K_{trans} + K_{rot} \tag{2.3.7}$$

with

$$K_{rot} = \frac{1}{2} I \sum_{i=1}^{N} |\dot{\vec{n}}_i|^2 = \frac{1}{2} I \sum_{i=1}^{N} \left( \dot{n}_{x_i}^2 + \dot{n}_{y_i}^2 + \dot{n}_{z_i}^2 \right) = \frac{1}{2} I \sum_{i=1}^{N} \left( \dot{\theta_i}^2 + \dot{\varphi_i}^2 \sin^2 \theta_i \right) . \tag{2.3.8}$$

We expressed the rotational energy by spherical coordinates. In this representation we see that the rotation has only two degrees of freedom. This is for sure not true in general, but fits for the models, we use in this work.
Finally we want to note down the Hamiltonian $\mathcal{H}$, which can be derived from a Legendre transformation of the Lagrangian $\mathcal{L} = K - U$. Using spherical coordinates for the rotation and Cartesian coordinates for the translation, the Hamilton is given by

$$\mathcal{H} = \sum_{i=1}^{N} \left[ \frac{1}{2m} \left( p_{r_{x_i}}^2 + p_{r_{y_i}}^2 + p_{r_{z_i}}^2 \right) + \frac{I}{2} \left( \dot{\theta_i}^2 + \dot{\varphi_i}^2 \sin^2 \theta_i \right) \right] + U \tag{2.3.9}$$

and also shows that $\mathcal{H} = E$.

### 2.3.3. Temperature

With knowing the Hamiltonian the temperature of the system can be calculated using the equipartition theorem, which can be formulated as

$$\left\langle x_i \frac{\partial \mathcal{H}}{\partial x_j} \right\rangle = \delta_{ij} \, k_B T \, , \tag{2.3.10}$$

where $x_i$ can express either the generalized coordinate $q_i$ or the conjugate momentum $p_i$. Using the Hamiltonian equation

$$\dot{q}_j = \frac{\partial \mathcal{H}}{\partial p_j} \tag{2.3.11}$$

with $x_j = p_j$ and $i = j$ together with the equipartition theorem (2.3.10), we get for the temperature

$$T = \frac{2}{5 N k_B} K \tag{2.3.12}$$

because of

$$\left\langle \sum_{j=1}^{5N} p_j \frac{\partial \mathcal{H}}{\partial p_j} \right\rangle = \left\langle \sum_{j=1}^{5N} p_j \, \dot{q}_j \right\rangle = 5 N k_B T \tag{2.3.13}$$

$$= \left\langle \sum_{i=1}^{N} \left( p_{r_{x_i}} \dot{r}_{x_i} + p_{r_{y_i}} \dot{r}_{y_i} + p_{r_{z_i}} \dot{r}_{z_i} + p_{\theta_i} \dot{\theta}_i + p_{\varphi_i} \dot{\varphi}_i \right) \right\rangle \tag{2.3.14}$$

$$= 2 \left\langle K \right\rangle \, . \tag{2.3.15}$$

In (2.3.12) we have not distinguished between the translational and rotational contribution, but taking a look at (2.3.14) shows that we can separately note down the translational temperature and rotational temperature as

$$T_{trans} = \frac{2}{3Nk_B} K_{trans} \tag{2.3.16}$$

$$T_{rot} = \frac{1}{Nk_B} K_{rot} \,. \tag{2.3.17}$$

Additionally we know that for an equilibrated system all the temperatures have to be the same

$$T = T_{trans} = T_{rot} \ . \tag{2.3.18}$$

### 2.3.4. Pressure

To calculate the pressure of the system, we can again make use of the equipartition theorem and set $j = i$ and $x_i = q_i$. Using the Hamiltonian equation

$$\dot{p}_j = -\frac{\partial \mathcal{H}}{\partial q_j} \tag{2.3.19}$$

the equipartition theorem (2.3.10) leads us to

$$\mathcal{V} = \left\langle \sum_{j=1}^{3N} q_j \, \dot{p}_j \right\rangle = -3Nk_B T \,. \tag{2.3.20}$$

By using Cartesian coordinates, we get the virial as

$$\mathcal{V} = \left\langle \sum_{i=1}^{N} \vec{r}_i \, \vec{F}_i^{tot} \right\rangle = -3Nk_B T \,. \tag{2.3.21}$$

To link this to the pressure $P$, we note that the force $\vec{F}_i^{tot}$ consists of two parts. The first one is the sum of internal forces $\vec{F}_i^{int}$ from the interaction between the $N$ molecules in volume $V$. The second force $\vec{F}_i^{ext}$ acts through the surface of the volume $V$ on the $N$ particles. Now we can split the virial into the internal and external parts

$$\mathcal{V} = \mathcal{V}_{int} + \mathcal{V}_{ext} \tag{2.3.22}$$

$$= \left\langle \sum_{i=1}^{N} \vec{r}_{i_s} \, \vec{F}_i^{int} \right\rangle + \left\langle \sum_{i=1}^{N} \vec{r}_{i_s} \, \vec{F}_i^{ext} \right\rangle \tag{2.3.23}$$

and additionally assume to deal with an isotropic fluid to convert the external virial into an integral over the surface $\partial V$ of the volume $V$. So we can write

$$\mathcal{V}_{ext} = -P \int_{\partial V} \mathrm{d}S \ (\vec{n} \cdot \vec{r}) \ , \tag{2.3.24}$$

where $\vec{n}$ is an unit vector perpendicular to the surface element $\mathrm{d}S$ and should not be mixed up with $\vec{n}_i$. Using Gauss's theorem we get

$$\mathcal{V}_{ext} = -P \int_V \mathrm{d}V \, \vec{\nabla}\vec{r} = -3PV \tag{2.3.25}$$

and can write for the pressure

$$P = \frac{Nk_BT}{V} + \frac{1}{3V}\mathcal{V}_{int} \tag{2.3.26}$$

$$= \frac{Nk_BT}{V} + \frac{1}{3V}\left\langle \sum_{i<j}^{N} \vec{r}_{ij}\vec{F}_{ij}^{int} \right\rangle . \tag{2.3.27}$$

In the last step we made use of the pairwise additivity of the forces. As we use different models in this work, we keep it generic at this point and refer to chapter 3, where the models are defined. The notation of the sum in equation (2.3.27) means

$$\sum_{i<j}^{N} = \sum_{i=1}^{N-1} \sum_{j=i+1}^{N} . \tag{2.3.28}$$

Now we have linked the macroscopic quantity $P$ to the microscopic coordinates of the system, which are known during the simulation.

## 2.4. Temperature control with the Berendsen thermostat

In a MD simulation the kinetic energy of the system is defined by the initial configuration and due to the correlation described in equation (2.3.12) this also defines the temperature. In presence of long-range potentials like Coulomb and the usage of a cutoff $r_{cut}$ (see section (2.5.1)) the energy conservation is not given for a MD simulation. This causes energy fluctuations [21]. To enable simulations at constant temperature in the NVT ensemble, and to get rid of those fluctuations, we need to control the temperature or rather the energy. We can do this by embedding the system in an infinite heat bath [6, 22], which allows to exchange the following heat flux

$$J_Q = \frac{\Delta Q}{\Delta t} = Nc_V \frac{\Delta T}{\Delta t} . \tag{2.4.1}$$

Hereby $\Delta Q$ stands for the heat amount exchanged in time $\Delta t$ and $c_V$ represents the heat capacity for a single particle at constant volume. As the heat flux influences the energy of the system, we can introduce the factor $\lambda^2 - 1$ and couple the exchanged heat directly

with the kinetic energy

$$\Delta Q = \Delta K = \frac{1}{2}\left(\lambda^2 - 1\right) \sum_{i=1}^{N} \left( m \left|\vec{v}_i\right|^2 + I |\dot{\vec{n}}_i|^2 \right) \tag{2.4.2}$$

$$= \frac{1}{2} \sum_{i=1}^{N} \left[ m \left|\vec{v}_i\right|^2 \left(\lambda_{trans}^2 - 1\right) + I |\dot{\vec{n}}_i|^2 \left(\lambda_{rot}^2 - 1\right) \right] \tag{2.4.3}$$

$$= \frac{3}{2} N\, T_{trans} \left(\lambda_{trans}^2 - 1\right) + N\, T_{rot} \left(\lambda_{rot}^2 - 1\right) . \tag{2.4.4}$$

To control the translational and rotational temperatures separately, we have introduced two different factors $\lambda_{trans}$ and $\lambda_{rot}$. In general it is sufficient to control just one of the temperatures as the other one is coupled and also reaches the same value. But to avoid any side effects and to reach the equilibration phase faster, it is recommended to control both temperatures individually. Nevertheless it is a good test of the simulation routines to switch off the control of one of the temperatures and verify that in equilibrium both are the same. Instead of directly scaling the velocities, it is a more physical approach to introduce a dynamical friction term [23]. Therefore we define the friction coefficient $\zeta = \frac{1-\lambda}{\Delta t}$, which we use in the acceleration, as follows

$$\ddot{\vec{r}}_i = \frac{\vec{F}_i}{m} + \zeta \dot{\vec{r}}_i \,. \tag{2.4.5}$$

To apply this in the MD simulation, we need to further specify $\zeta$ or rather $\lambda$. We do this by following the approach proposed by Berendsen *et al.* [24], where the system is coupled to the heat bath via a linear heat flux

$$J_Q = \alpha_T \left(T_B - T\right) . \tag{2.4.6}$$

Here $T_B$ is the temperature of the heat bath respectively the to be temperature of the system, $T$ the current temperature and $\alpha_T$ a constant. Using (2.4.1) we can define the constant

$$\tau_T = \frac{N c_V}{\alpha_T} = \frac{5N}{2\alpha_T} \,, \tag{2.4.7}$$

which represents also the relaxation time of the temperature. Using equation (2.4.1) and (2.4.4) we now can write for $\lambda$

$$\lambda = \sqrt{1 + \frac{\Delta t}{\tau_T} \left( \frac{T_B}{T} - 1 \right)} \tag{2.4.8}$$

$$\approx 1 + \frac{\Delta t}{2\tau_T} \left( \frac{T_B}{T} - 1 \right) = 1 + \frac{\Delta t}{2\tau_T} \left( \frac{5NT_B}{2K} - 1 \right) . \tag{2.4.9}$$

Further we need to distinguish again between the translational and rotational temperatures. Therefore we note down the relaxation time according to the degrees of freedom

as

$$\tau_T^{trans} = \frac{3N}{2\alpha_T} \tag{2.4.10}$$

$$\tau_T^{rot} = \frac{N}{\alpha_T}\,. \tag{2.4.11}$$

With that we can write for the scaling factors of the velocities

$$\lambda_{trans} \approx 1 + \frac{\Delta t}{2\tau_T}\left(\frac{3NT_B}{2K_{trans}} - 1\right) \tag{2.4.12}$$

$$\lambda_{rot} \approx 1 + \frac{\Delta t}{2\tau_T}\left(\frac{NT_B}{K_{rot}} - 1\right)\,, \tag{2.4.13}$$

and for the friction coefficients

$$\zeta_{trans} \approx \frac{1}{2\tau_T}\left(1 - \frac{3NT_B}{2K_{trans}}\right) \tag{2.4.14}$$

$$\zeta_{rot} \approx \frac{1}{2\tau_T}\left(1 - \frac{NT_B}{K_{rot}}\right)\,, \tag{2.4.15}$$

which can now be applied to the velocity Verlet algorithm. So we need to replace the acceleration in the equations (2.1.7) - (2.1.9) with the new expression

$$\ddot{\vec{r}}_i = \frac{\vec{F}_i(t)}{m} - \zeta_{trans}(t)\dot{\vec{r}}_i(t)\,. \tag{2.4.16}$$

For the rotation we can proceed analogously and write for the acceleration together with the friction

$$\ddot{\vec{n}}_i = \vec{G}_i - \left(\vec{n}_i \cdot \vec{G}_i + \dot{\vec{n}}_i^2\right)\vec{n}_i + \zeta_{rot}\dot{\vec{n}}_i\,. \tag{2.4.17}$$

It can be shown that the temperature adjustment happens exponentially over time and can be expressed as

$$T = T_B - (T_B - T_0)\exp\left[-t/\tau_T\right] \tag{2.4.18}$$

where $T_0$ is the starting temperature at time $t = 0$ and $\tau_T$ the relaxation time. In the simulations, performed for this work, the relaxation time usually was in the range $\tau_T \in [0.1, 1]$, where the bigger end means less coupling and should be preferred to keep disturbance of the system at a minimum. One drawback of the Berendsen thermostat is that it does not produce trajectories in the canonical ensemble [25]. Nevertheless the use of it is sufficient for our investigation of the phase separation of polar liquids. If one wants to generate a canonical ensemble the Nosé-Hoover [23, 26] thermostat is the right one to choose.

## 2.5. Optimization techniques

### 2.5.1. Periodic boundary conditions, cutoff radius and minimum image convention

#### Periodic boundary conditions

We usually want to limit our system to a simulation volume $V$ similar to macroscopic experiments, to prevent that the particles could diffuse into space. But simply placing the particles between solid walls of a box would introduce surface effects, we want to avoid in our simulation. To minimize those effects, the walls of the box have to be open and surrounded by a bulk of the same matter. This can be achieved, using periodic boundary conditions, which place an infinite number of identical copies of the simulation box in all directions next to each other. I.e. if a particle escapes on one side of the box, directly a periodic picture of the particle enters the box on the opposite site. With this procedure we have avoided the surface effects by allowing a particle to escape the box while keeping the density $\rho$ of the box constant. For vapour or liquid systems the shape of the box does not have any influence on the simulation results in the equilibrium [27]. This is not true for crystalline simulation volumes, where the shape of the box can be important. In our case we use a cubic box with edge length $L$. Mathematically we can express the periodic boundary conditions for an arbitrary measurable quantity as

$$A(\vec{r}) = A(\vec{r} + \vec{s}\,L) \tag{2.5.1}$$

where $\vec{s} \in \mathbb{Z}^3$. This means that for each particle $i$ at place $\vec{r}_i$ exists a set of so called image particles at position

$$\vec{r}_i + \vec{s}\,L\,. \tag{2.5.2}$$

As the periodic boundary conditions introduce translation symmetry with regard to the boxes, we get, according to Noether, conservation of the total moment of inertia [6], which reduces the degrees of freedom by three. This leads to a slight adjustment of the temperature calculation in (2.3.16) to

$$T_{trans} = \frac{2}{3(N-1)k_B} K_{trans} \quad . \tag{2.5.3}$$

For large systems this effect is negligible and we would not produce wrong results sticking to (2.3.16). As the rotational moment of inertia is not influenced by the periodic boundary conditions, there is no impact on the calculation of the rotational temperature $T_{rot}$.

### Cutoff radius and Minimum Image convention

The usage of the periodic boundary conditions generates some trouble, which we need to fix. We have now a quasi infinitive system and the calculation of the potential energy $U$ has the form

$$U = \sum_{i<j} u\left(|\vec{r}_i - \vec{r}_j|\right) + \sum_{\vec{s}\in\mathbb{Z}_0^3} \sum_{i<j} u\left(|\vec{r}_i - \vec{r}_j + \vec{s}\,L|\right) \tag{2.5.4}$$

with an infinite sum as the second term. To get rid of this infinite calculation, we have to introduce a cutoff radius $r_{cut}$, which defines the maximum length up to which we consider pair-interactions between two particles. In addition we need a mechanism, which allows us to easily calculate the distance $r_{ij}$ between the particle $i$ and particle $j$, respectively its closest image. Thus we make use of the so called *minimum image convention* which can be expressed as

$$|\vec{r}_i - \vec{r}_j| = r_{ij} = \min_{\vec{s}\in\mathbb{Z}^3} \left(|\vec{r}_i - \vec{r}_j + \vec{s}\,L|\right) . \tag{2.5.5}$$

Together with the periodic boundary conditions the minimum image convention ensures that a particle in the simulation box only interacts at maximum with the $N-1$ other particles or their images. To avoid that a particle interacts more than once with another particle or even interacts with itself the cutoff distance has to be limited to

$$r_{cut} < \frac{L}{2} . \tag{2.5.6}$$

For the direct calculation of the minimum image distance $r_{ij}$ the definition (2.5.5) is not usable. Therefore we use

$$r_{l,ij} = \left| r_{l,i} - r_{l,j} - L \cdot \mathrm{ANINT}\left(\frac{r_{l,i} - r_{l,i}}{L}\right)\right| \tag{2.5.7}$$

where $l \in \{x, y, z\}$ and the function $\mathrm{ANINT}(x)$ rounds $x$ to the next integer. With that we have ensured that we can write the potential energy as

$$U = \sum_{i<j} u\left(r_{ij}\right) . \tag{2.5.8}$$

Finally we want to have a closer look at the cutoff radius $r_{cut}$, which we introduced above without any further comment. If we neglect the pair-interaction beyond the cutoff distance, we make an error, which needs to be corrected using so called long range corrections. In general we distinguish between short and long range interaction using the following criteria

$$\int_{\mathrm{V}} \frac{1}{r^n} \mathrm{d}V = \begin{cases} < \infty & \Longleftrightarrow n > d : \text{short range} \\ \infty & \Longleftrightarrow n \leq d : \text{long range} \end{cases} \tag{2.5.9}$$

where $d$ is defined by the dimension, i.e. $d = 3$ in our case. For short range interactions the error is limited and we can apply the commonly used continuum correction as described

in section 2.5.3 in detail. For long range interactions, like the Coulomb interaction, a more sophisticated method must be used. The two most common methods are the Ewald summation [28, 29], which is a procedure that allows to build the sum over all image particles using Fourier transformation, and the reaction field method, which is going back to Onsager [30] and was first applied in simulations by Barker and Watts [31].

### Cutoff radius for dumbbells

For elongated molecules like the dumbbell model (see section 3.1) the cutoff radius is applied to each particle of the molecule. Therefore the usage of a simple cutoff can separate the molecule into two pieces, where one part is inside the cutoff radius and the other one outside. For the CSD model we would then generate a single ion inside the cutoff radius and completely ignore the other particle with opposite charge. Those ions generate a bigger contribution to the interaction than considering the whole molecule. Therefore we soften the cutoff radius and always consider the full dumbbell if

$$\min_{\alpha,\beta}\left(r_{i_\alpha j_\beta}\right) \leq r_{cut}\,. \tag{2.5.10}$$

But we only consider this type of cutoff for the Coulomb interaction of the dumbbells, because for the soft sphere repulsion, it does not matter, if the molecule is divided and it simplifies the long range correction. In figure 2.1 the cutoff for a dumbbell is illustrated. It also shows that we have for each site of the dumbbell an own cutoff sphere. So the particles within each cutoff sphere are not necessarily the same. If we want to express this in a formula, we can write for the CSD pair-potential (3.1.10)

$$\begin{aligned} u_{ij}^{CSD_{cut}} = \sum_{\alpha,\beta=1}^{2} \Bigg\{ & 4\varepsilon \left(\frac{\sigma}{r_{i_\alpha j_\beta}}\right)^{12} \Theta(r_{cut} - r_{i_\alpha j_\beta}) \\ & + \frac{1}{4\pi\varepsilon_0}\frac{q_{i_\alpha} q_{j_\beta}}{r_{i_\alpha j_\beta}}\,\Theta\left(r_{cut} - \min_{\alpha,\beta}\left[r_{i_\alpha j_\beta}\right]\right)\Bigg\} \end{aligned} \tag{2.5.11}$$

where $\Theta(x)$ is

$$\Theta(x) = \begin{cases} 0: & x < 0 \\ 1: & x \geq 0\,. \end{cases} \tag{2.5.12}$$

For sure this is not the real pair-potential, it is just an expression of the cutoff procedure applied in our simulation. The difference between (3.1.10) and (2.5.11) is eliminated by the long-range corrections. Despite the deformations of the cutoff sphere, we will speak in the following of a sphere with the volume $V_{Sp}$ with corresponding surface $\Omega = \partial V_{Sp}$. If we want to describe the cutoff sphere for an individual molecule or site at location $\vec{r}_{i_\alpha}$, we will declare the cutoff sphere as $V_{Sp}(\vec{r}_{i_\alpha})$ and the number of particles within the sphere as $N_{Sp}(\vec{r}_{i_\alpha})$.

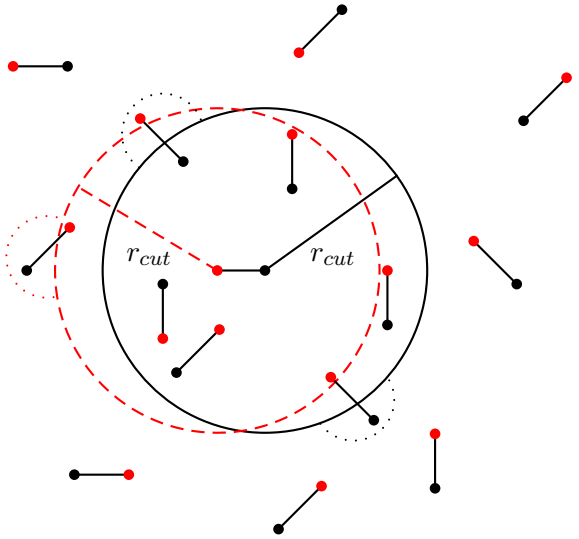


Figure 2.1.: Each interaction site of the dumbbell has its own cutoff sphere with radius $r_{cut}$. Therefore the particles in the two cutoff spheres are not necessarily the same. For the LJ-interaction dumbbells are separated if they are not completely in the cutoff sphere. For the Coulomb interaction the whole dumbbell is considered, indicated by the dotted line.

### 2.5.2. The Linked-Cell-Verlet-List algorithm

With the above introduced cutoff radius we restrict the calculation of the force or the potential energy only to those particles $N_{Sp}(\vec{r}_i) \leq N$, which are in the cutoff sphere of particle $i$. But we still need to figure out in each simulation step, which are the particles in the cutoff sphere $N_{Sp}(\vec{r}_i)$. Therefore the distance between particle $i$ with all other $N-1$ particles in the box has to be calculated using the minimum image convention. Doing this for all $N$ particles ends up in $N(N-1)/2$ calculations per simulation step. So the complexity of this problem scales with $N^2$ and makes simulations with a big number of particles very inefficient.
To reduce the complexity of the distance determination, we can use the Linked-Cell-Verlet-List algorithm, which is a combination of the later described linked-cell list and the Verlet neighbour list. The linked-cell list divides the simulation box into multiple parts, and the Verlet neighbour list makes use of the fact that at ordinary temperatures the neighbours of a particle stay almost the same for a short time period. The two methods can also be used independently and their combination to the Linked-Cell-Verlet-List algorithm was described by Auerbach *et al.* [32]. The necessary book keeping for the lists requires some more memory and computational effort. But that can be neglected as it simplifies the complexity so that the simulation time scales now linear with the number of particles $N$. A more detailed discussion on the performance impact and the optimal parameters to be

chosen can be found in [33].

### Verlet Neighbour list

As the fluctuations of surrounding interaction partners of a particle are usually very limited, Loup Verlet introduced the idea of a neighbour list [13], which allows to calculate only the distances between the particles, which are considered as neighbours. To do this we have to extend our cutoff sphere by an additional shell of depth $r_{skin}$, which leads to a list cutoff $r_{list} = r_{cut} + r_{skin}$. After the neighbour list has been built up, only for the particles within each others neighbourhood shell the distance calculation has to be done, to determine if they are within the cutoff or not. To avoid any error, we have to update the neighbour list in time. Therefore we have to find out, when a particle could have crossed the neighbour shell of thickness $r_{skin}$. We can do this, by identifying the particle with the biggest displacement at a single simulation step and summing up those maximum displacements $r_{max}(t_n)$ over all simulation steps until

$$\sum_n r_{max}(t_n) \geq \frac{r_{skin}}{2} \tag{2.5.13}$$

is reached. Afterwards a full refresh of the neighbour list must be done. For sure it does not matter if the displacement of the particle is caused by forces acting on it as in MD or by a stochastic move in MC simulations. The update has to be done as soon as $r_{skin}/2$ is reached because two particles could move towards each other. Considering a mean number $N_{list}$ of neighbours for a single particle, we need to calculate $NN_{list}/2$ interactions per simulation step. But as the number of particles $N_{list}$ is not influenced by the total number of particles $N$, the total simulation effort is of order $N$, except for those simulation steps, where the neighbour list has to be refreshed. In this case the effort is still of order $N^2$, but can be optimized to order $N$ as well using the linked-cell list, which builds the second component of the Linked-Cell-Verlet-List algorithm.

### Linked-Cell List

To reduce also the update of the neighbour list to order $N$, we make use of the Linked-Cell list algorithm, which divides the simulation box into cubic cells [34] and assigns each particle to its unique cell. For further calculations only those cells, which intersect with the neighbour list sphere, have to be screened. In theory the size of the cells is arbitrary and the smaller the chosen size is, the better the cutoff sphere can be approximated. But having too much cells negatively impacts the performance and therefore a common edge size $L_c$ is given by

$$L_c \geq r_{list} \tag{2.5.14}$$

respectively in most cases

$$L_c = r_{list}\,. \tag{2.5.15}$$

This size has also the advantage that only the cell containing the particle and the 26 direct neighbours have to be scanned. This is independent of the system size and therefore the computational effort is proportional to $N$. But even with having set $L_c = r_{list}$, we can run into the situation of high computational costs. This can happen for very thin systems, like those used in section 6.2, where with $L_c = r_{list}$ the numbers of cells is very high and slows down the computation time. In such a case $L_c \gg r_{list}$ must be chosen.
Obviously the Linked-Cell algorithm can only work if the condition $L \geq 4L_c$ is true. Otherwise we will have no advantage as the whole system needs to be scanned anyway.

## 2.5.3. Long range corrections

Our limited computational power forces us to restrict the system size to a limited number of particles, and we further reduce the computational effort through neglecting the direct pair interaction by establishing the cutoff radius $r_{cut}$. As we neglect all interactions where $r_{ij} > r_{cut}$ an error is introduced in the calculation of certain quantities like the pressure, and we need to minimize this error as much as possible, making use of the long range corrections. Dependent on the type of particles, or better their interaction potential, a different approach to correct the error can be taken. The procedures can be distinguished into two categories, on the one hand are continuum methods, like the reaction field method [30], which make use of the fact that the structure of the system is smeared out beyond the cutoff and therefore the structure in the area $r_{ij} > r_{cut}$ is not important anymore. On the other hand are methods, which explicitly calculate the particle interaction like the Ewald summation [28]. It makes use of the periodicity of the matter and was originally developed for periodic systems like polar or ionic crystals [7]. By a split of the summation into real space and Fourier space a fast convergence of the infinite sum is achieved. A drawback of the Ewald summation is the necessary computational effort and the tendency to overestimate the periodicity of the system [35]. The reaction field method works best for polar or ionic fluids, but one has to deal with the disadvantage of the *a priori* unknown dielectric constant $\epsilon$ [7]. Despite those differences it is shown in the literature [36–42] that both methods produce similar results. Especially the equivalence of both methods at the gas-liquid (g-l) transition is highlighted by Garzon *et al.* [42].

### Radial distribution function

To legitimate the continuum corrections, we want to have a look at the radial distribution function (RDF) $g_2(\vec{r}_i, \vec{r}_j)$ (also called pair correlation function), which is a measure of the spatial order, describing the density variations as a function of particle distance. The

RDF is defined using the ensemble average of a function $h(r_{ij})$ as

$$\langle h(r_{ij})\rangle = \frac{\int \mathrm{d}^3 r_i \mathrm{d}^3 r_j \mathrm{d}^{3\mathrm{N}-6}\{r\}' \mathrm{d}^{3\mathrm{N}}\{p\}\, h(r_{ij}) f(\{\vec{r}\}', \vec{r}_i, \vec{r}_j, \{\vec{p}\})}{\int \mathrm{d}^3 r_i \mathrm{d}^3 r_j \mathrm{d}^{3\mathrm{N}-6}\{r\}' \mathrm{d}^{3\mathrm{N}}\{p\}\, f(\{\vec{r}\}', \vec{r}_i, \vec{r}_j, \{\vec{p}\})} \tag{2.5.16}$$

$$= \frac{1}{V^2} \int \mathrm{d}^3 r_i \mathrm{d}^3 r_j\, h(r_{ij}) g_2(\vec{r}_i, \vec{r}_j)\,, \tag{2.5.17}$$

using the notation $\{\vec{r}\}'$, which includes all particle locations except $\vec{r}_i$ and $\vec{r}_j$. I.e. the RDF bundles the integration over all momenta and locations. To make use of the RDF in a quantity like the pressure $P$ we have to make two assumptions. The first one is that we deal with a fluid with indistinguishable particles, allowing us to write $g_2(\vec{r}_i, \vec{r}_j)$ as a function of distance

$$g_2(\vec{r}_i, \vec{r}_j) = g_2(r_{ij})\,. \tag{2.5.18}$$

Using relative coordinates, we can execute one of the remaining integrations in (2.5.17) and obtain for the ensemble average

$$\langle h(r_{ij})\rangle = \frac{1}{V} \int \mathrm{d}^3 r_{ij}\, h(r_{ij}) g_2(r_{ij})\,. \tag{2.5.19}$$

Secondly we act on the assumption that the particles are homogeneously distributed in a fluid. So we can write for the function $h(r_{ij}) = 1$

$$1 = \frac{1}{V} \int \mathrm{d}^3 r_{ij}\, g_2(r_{ij})\,. \tag{2.5.20}$$

It follows that $g_2(r_{ij}) = 1$ must be true for most of the space, which can be expressed as

$$\lim_{r\to\infty} g_2(r) = 1\,. \tag{2.5.21}$$

Now we can write for an arbitrary function $h(r_{ij})$

$$\langle h(r_{ij})\rangle = \frac{1}{V} \int \mathrm{d}^3 r_{ij}\, h(r_{ij})\,. \tag{2.5.22}$$

Additionally we can split up the calculation of the ensemble average into two parts

$$\langle h(r_{ij})\rangle = \langle h(r_{ij})\rangle_{\leq r_{cut}} + \langle h(r_{ij})\rangle_{> r_{cut}} \tag{2.5.23}$$

$$= \langle h(r_{ij})\rangle_{\leq r_{cut}} + \frac{1}{V} \int\limits_{r_{ij} > r_{cut}} \mathrm{d}^3 r_{ij}\, h(r_{ij})\,, \tag{2.5.24}$$

to treat the calculation within the cutoff sphere explicitly, e.g. as sum over the forces, and outside the cutoff sphere, we can integrate over the function. This procedure can be applied in the calculation of quantities like the pressure or internal energy, where the second term in (2.5.24) represents the continuum correction.

### Lennard-Jones Corrections

In the following we want to derive the corrections for the Lennard-Jones (LJ) potential defined in (3.3.1) with the additional parameter $\lambda$, which allows us to easily switch of the contribution of the attractive $r^{-6}$ term. Thus we can easily use the correction also for any soft sphere model like the CSD model, where only the repulsion is used. The radial symmetric nature of the LJ potential allows us to directly use the equation (2.5.19) to calculate the correction for the internal energy $U$ and the pressure $P$. We want to start with the internal energy

$$U^{LJ_\lambda} = \left\langle \sum_{i<j} u^{LJ_\lambda}(r_{rij}) \right\rangle = \frac{1}{V}\frac{N(N-1)}{2} \int \mathrm{d}^3 r \, u^{LJ_\lambda}(r) g_2(r) \tag{2.5.25}$$

$$\approx \frac{1}{2}\frac{N^2}{V} \mathrm{d}^3 r \, u^{LJ_\lambda}(r) g_2(r) \tag{2.5.26}$$

$$= U^{LJ_\lambda}_{\leq r_{cut}} + \frac{1}{2}\frac{N^2}{V} \int\limits_{r>r_{cut}} \mathrm{d}^3 r \, u^{LJ_\lambda}(r) g_2(r)\,, \tag{2.5.27}$$

which we divided into two parts, inside and outside the cutoff according to (2.5.24). Solving the integral we get

$$U^{LJ_\lambda}_{corr} = -\frac{8}{3}\pi N \rho \varepsilon \sigma^3 \left[ -\frac{1}{3}\left(\frac{\sigma}{r_{cut}}\right)^9 + \lambda \left(\frac{\sigma}{r_{cut}}\right)^3 \right] \tag{2.5.28}$$

with the particle density $\rho = N/V$ as correction to the internal energy $U^{LJ_\lambda}_{\leq r_{cut}}$ inside the cutoff sphere. In the case of $\lambda = 1$ the contribution is negative, due to the attraction of th particles and $r_{cut} \gg \sigma$. Similar we can go ahead for the calculation of the pressure in (2.3.27) where we have

$$P^{LJ_\lambda} = \frac{N k_B T}{V} + \frac{1}{3V}\left\langle \sum_{i<j} \vec{r}_{ij} F^{LJ_\lambda}(r_{ij}) \right\rangle \tag{2.5.29}$$

$$\begin{aligned} \approx \frac{N k_B T}{V} &+ \frac{1}{3V}\left\langle \sum_{i<j} \vec{r}_{ij} F^{LJ_\lambda}(r_{ij}) \right\rangle_{r_{ij}\leq r_{cut}} \\ &- \frac{1}{6}\left(\frac{N}{V}\right)^2 \int\limits_{r>r_{cut}} \mathrm{d}^3 r \, r \frac{\partial u^{LJ_\lambda}}{\partial r} g_2(r)\,. \end{aligned} \tag{2.5.30}$$

With that we get for the contribution outside the cutoff sphere the following correction term to the pressure

$$P^{LJ_\lambda}_{corr} = -\frac{16}{3}\pi \rho^2 \varepsilon \sigma^3 \left[ -\frac{2}{3}\left(\frac{\sigma}{r_{cut}}\right)^9 + \lambda \left(\frac{\sigma}{r_{cut}}\right)^3 \right]. \tag{2.5.31}$$

Again this is negative for $\lambda = 1$ as the attraction reduces the desire of the system to expand and therefore reduces the pressure.
Finally we want to have a look at two special cases, we need to deal with. The first one is the CSD system, where we have four site-site interactions per dumbbell interaction. Therefore the correction terms are four times the ones for the LJ system using $\lambda = 0$, i.e.

$$U_{corr}^{CSD} = 4U_{corr}^{LJ_{\lambda=0}} \tag{2.5.32}$$
$$P_{corr}^{CSD} = 4P_{corr}^{LJ_{\lambda=0}}\,. \tag{2.5.33}$$

The second case we need to consider is for the osmotic pressure simulations, we carry out in chapter 7. There we use two different kinds of particles, $A$ and $B$, which interact instead of $\varepsilon$ as potential depth with the parameter $\varepsilon_{AB}$. The potential is given in (7.2.1) and for this case the correction is defined as

$$U_{corr}^{LJ_{AB}} = -\frac{8}{3}\pi\sigma^3\left[-\frac{1}{3}\left(\frac{\sigma}{r_{cut}}\right)^9\frac{N^2}{V} + \left(\frac{\sigma}{r_{cut}}\right)^3\frac{\varepsilon_{AA}N_A^2 + \varepsilon_{BB}N_B^2 + 2\varepsilon_{AB}N_AN_B}{V}\right] \tag{2.5.34}$$
$$P_{corr}^{LJ_{AB}} = -\frac{16}{3}\pi\sigma^3\left[-\frac{2}{3}\left(\frac{\sigma}{r_{cut}}\right)^9\frac{N^2}{V} + \left(\frac{\sigma}{r_{cut}}\right)^3\frac{\varepsilon_{AA}N_A^2 + \varepsilon_{BB}N_B^2 + 2\varepsilon_{AB}N_AN_B}{V^2}\right]. \tag{2.5.35}$$

It needs to be applied to the simulation box, which contains the mixture of $N_A$ and $N_B$ particles. For the box which only consists of the solute particles the corrections reduce to the equations (2.5.28) and (2.5.31) as there are no solvents and therefore $N_B = 0$.

### Reaction field method

Due to the long range character, which leads to the divergence of (2.5.9) and (2.5.19) for the Coulomb and dipole interaction, the procedure we used for the LJ potential cannot be applied. Also the dependency on the orientation for the dumbbell and dipolar interaction does not allow to make use of (2.5.19). Therefore we want to outline in the following section the reaction field method as long range correction for the affected models. The reaction field method is based on the theory of dielectric continua and similar to earlier we treat the space inside the cutoff sphere and outside differently. As illustrated in figure 2.2 the electric field acting on particle $i_\alpha$ is caused by two components. First the surrounding particles inside the cutoff sphere, where the contribution is calculated exactly, and secondly the electric field outside the cutoff sphere, which is generated by the particles as well, but considered to form a dielectric continuum with dielectric constant $\epsilon_A$.

The reaction field can be determined by an analytical solution of the linearized Poisson-Boltzmann equation, which is described in detail by Tironi *et al.* [21] and shortly recapped here. We will use the notation of the CSD model, but the approach for ions and dipoles is quite similar. We start with the cutoff sphere of volume $V_{Sp}(\vec{r}_{i_\alpha})$ around the dumbbell

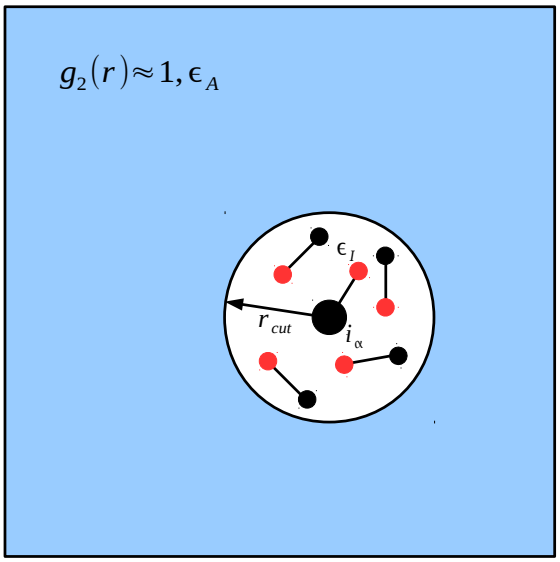


Figure 2.2.: Long range correction for charged dumbbell molecules using the reaction field method. The interaction of site $i_\alpha$ with the other dumbbells within the cutoff sphere is computed exactly. Outside of the cutoff sphere we consider a homogeneous dielectric continuum with permittivity $\epsilon_A$.

site $i_\alpha$. Within the cutoff sphere the interaction of the charge $q_{i_\alpha}$ with the other $N_{Sp}(\vec{r}_{i_\alpha})$ dipoles or $2N_{Sp}(\vec{r}_{i_\alpha})$ charges is calculated directly. For the total dipole moment of the cutoff sphere we can write

$$\vec{M}_{i_\alpha} = \sum_{j \in V_{Sp}(\vec{r}_{i_\alpha})} \vec{\mu}_j = q\, d \sum_{j \in V_{Sp}(\vec{r}_{i_\alpha})} \vec{n}_j = \sum_{j_\beta \in V_{Sp}(\vec{r}_{i_\alpha})} q_{j_\beta} \vec{r}_{j_\beta i_\alpha} \,. \tag{2.5.36}$$

The inner region of the sphere has the permittivity $\epsilon_I$ and can be expressed by the potential

$$\phi_I(\vec{r}) = \phi_C(\vec{r}) + \phi_H(\vec{r}) \qquad\qquad (r < r_{cut}) \,, \tag{2.5.37}$$

where the first potential

$$\vec{\nabla}^2 \phi_C(\vec{r}) = - \sum_{j_\beta \in V_{Sp}} \frac{q_{j_\beta}}{\epsilon_A \epsilon_I} \delta(\vec{r} - \vec{r}_{j_\beta}) \tag{2.5.38}$$

is a solution to the Poisson equation. The second potential, the harmonic function $\phi_H(r)$, corresponds to the reaction field potential of the dielectric continuum and complies with the Laplace equation

$$\vec{\nabla}^2 \phi_H(\vec{r}) = 0 \,. \tag{2.5.39}$$

Now it is clear that $\phi_I(\vec{r})$ is as well a solution to the Poisson equation. For the outside potential $\phi_A(\vec{r})$ we assume that it fulfills the linearized Poisson-Boltzmann equation

$$\vec{\nabla}^2\phi_A(\vec{r}) = \kappa^2\phi_A(\vec{r}) \qquad (r > r_{cut})\,, \tag{2.5.40}$$

where $\kappa$ is the inverse Debye screening length

$$\kappa^2 = \frac{2IF^2}{\epsilon_0\epsilon_A RT} \tag{2.5.41}$$

with Faradays constant $F$, the ionic strength $I$, the ideal gas constant $R$, and the temperature $T$. Using the following three conditions at the surface $\Omega$ of the cutoff sphere, we can calculate the potential $\phi_I(\vec{r})$.

1. On the boundary the potential is continuous

$$\phi_I(\vec{r}) = \phi_A(\vec{r})\,, \qquad \vec{r} \in \Omega\,. \tag{2.5.42}$$

2. The normal of the dielectric displacement field on any charge free surface is continuous

$$\epsilon_I\vec{\nabla}\phi_I(\vec{r}) = \epsilon_A\vec{\nabla}\phi_A(\vec{r})\,, \qquad \vec{r} \in \Omega\,. \tag{2.5.43}$$

3. The potential outside the cutoff sphere vanishes at infinitey

$$\lim_{r\to\infty}\phi_A(\vec{r}) = 0\,. \tag{2.5.44}$$

Using the moving boundary dielectric implementation [43], as done by Tironi, which means that the cutoff sphere moves along with the charged particle, we get for the potential

$$\phi_I(0) = \frac{1}{4\pi\epsilon_0\epsilon_I}\sum_{j_\beta\in V_{Sp}} q_{j_\beta}\left[\frac{1}{r_{j_\beta}} + \frac{\epsilon_I - \epsilon_A(1+\kappa r_{cut})}{\epsilon_A(1+\kappa r_{cut})}\frac{1}{r_{cut}}\right]\,, \tag{2.5.45}$$

and the corresponding electric field

$$\begin{aligned}-\vec{\nabla}_{\vec{r}}\,\phi_I(\vec{r})\Big|_{\vec{r}=0} = \frac{-1}{4\pi\epsilon_0\epsilon_I}\sum_{j_\beta\in V_{Sp}} q_{j_\beta}\Bigg[&\frac{\vec{r}_{j_\beta}}{r_{j_\beta}^3} \\ &-\frac{2(\epsilon_A-\epsilon_I)(1+\kappa r_{cut}) + \epsilon_A(\kappa r_{cut})^2}{(\epsilon_I+2\epsilon_A)(1+\kappa r_{cut}) + \epsilon_A(\kappa r_{cut})^2}\frac{\vec{r}_{j_\beta}}{r_{cut}^3}\Bigg]\,.\end{aligned} \tag{2.5.46}$$

For the force on site $i_\alpha$ we can write

$$\vec{f}(\vec{r}_{i_\alpha j_\beta}) = \frac{q_{i_\alpha}q_{j_\beta}}{4\pi\epsilon_0\epsilon_I}\left[\frac{1}{r_{i_\alpha j_\beta}^3} - \frac{1}{r_{cut}^3}\frac{2(\epsilon_A-\epsilon_I)(1+\kappa r_{cut}) + \epsilon_A(\kappa r_{cut})^2}{(\epsilon_I+2\epsilon_A)(1+\kappa r_{cut}) + \epsilon_A(\kappa r_{cut})^2}\right]\vec{r}_{i_\alpha j_\beta}\,. \tag{2.5.47}$$

For the dumbbell system the reaction field becomes more simple, due to the non existing ionic strength. Thus we get $\kappa = 0$ and therefore can write for the reaction field

$$\vec{E}_{RF}(\vec{r}_{i_\alpha}) = \frac{1}{4\pi\epsilon_0\epsilon_I}\frac{2(\epsilon_A - \epsilon_I)}{\epsilon_I + 2\epsilon_A}\frac{\vec{M}_{i_\alpha}}{r_{cut}^3} \tag{2.5.48}$$

$$= \frac{1}{4\pi\epsilon_0}\frac{2(\epsilon_A - 1)}{2\epsilon_A + 1}\frac{\vec{M}_{i_\alpha}}{r_{cut}^3} \tag{2.5.49}$$

with $\vec{r}_{i_\alpha}$ in the center of the cutoff sphere with total dipole moment $\vec{M}_{i_\alpha}$ and $\epsilon_I = 1$. This is the reaction field as already derived by Onsager [30] or by Fröhlich [44] and is valid for dipolar interactions like dipolar soft spheres or the Stockmayer model [22, 45]. As the reaction field is homogenous, there is no contribution to the pressure and dipolar forces.

**Impact of the reaction field for dumbbells** Due to the special geometry of the dumbbell system we need to determine, which quantities get a contribution from the reaction field. We start with the potential energy, for which we can write based on the potential in (2.5.45)

$$U^C = \frac{1}{2}\sum_{i=1}^{N}\sum_{\alpha=1}^{2} q_{i_\alpha}\phi_I(r_{i_\alpha}) \tag{2.5.50}$$

$$\begin{aligned} &= \frac{1}{4\pi\epsilon_0\epsilon_I}\sum_{\alpha,\beta=1}^{2}\sum_{\substack{i<j \\ j\in V_{Sp}(\vec{r}_{i_\alpha})}}\frac{q_{i_\alpha}q_{j_\beta}}{r_{i_\alpha j_\beta}} \\ &\quad + \frac{1}{4\pi\epsilon_0\epsilon_I}\frac{\epsilon_I - \epsilon_A}{2\epsilon_A\, r_{cut}}q^2\sum_{i=1}^{N}\sum_{\alpha,\beta=1}^{2}\sum_{j\in V_{Sp}(\vec{r}_{i_\alpha})}(-1)^{\alpha+\beta} \end{aligned} \tag{2.5.51}$$

$$= \frac{1}{4\pi\epsilon_0\epsilon_I}\sum_{\alpha,\beta=1}^{2}\sum_{i<j}\frac{q_{i_\alpha}q_{j_\beta}}{r_{i_\alpha j_\beta}}\,\Theta\left(r_{cut} - \min_{\alpha,\beta}\left[r_{i_\alpha j_\beta}\right]\right)\,. \tag{2.5.52}$$

As we only consider neutral cutoff spheres the second term in (2.5.51) is zero. With this we see that the reaction field has no contribution to the potential energy and we only have to consider the direct Coulomb interaction.
Starting with (2.5.47) we can write for the total Coulomb force $\vec{F}_i^C$ on the dumbbell $i$

$$\vec{F}_i^C = \frac{1}{4\pi\epsilon_0}\sum_{\alpha=1}^{2} q_{i_\alpha}\left[\sum_{j_\beta\in V_{Sp(\vec{r}_{i_\alpha})}} q_{j_\beta}\frac{\vec{r}_{i_\alpha j_\beta}}{r_{i_\alpha j_\beta}^3} + \frac{2(\epsilon_A - 1)}{2\epsilon_A + 1}\frac{\vec{M}_{i_\alpha}}{r_{cut}^3}\right]\,. \tag{2.5.53}$$

We want to take a closer look at the second term caused by the reaction field

$$\vec{F}_i^{RF} = \frac{1}{4\pi\epsilon_0}\frac{2(\epsilon_A-1)}{2\epsilon_A+1}\frac{1}{r_{cut}^3}\left[q_{i_1}\,\vec{M}_{i_1} + q_{i_2}\,\vec{M}_{i_2}\right] \tag{2.5.54}$$

$$= \frac{1}{4\pi\epsilon_0}\frac{2(\epsilon_A-1)}{2\epsilon_A+1}\frac{1}{r_{cut}^3} q_{i_1}\,\left[\vec{M}_{i_1} - \vec{M}_{i_2}\right] \tag{2.5.55}$$

$$= \vec{f}_{i_1}^{RF} + \vec{f}_{i_2}^{RF}\,. \tag{2.5.56}$$

Due to the fact that the particles in the two cutoff spheres around the sites $i_1$ and $i_2$ are not necessarily the same, i.e. $\vec{M}_{i_1} \neq \vec{M}_{i_2}$, we have to consider an additional contribution $\vec{F}_i^{RF} \neq 0$ of the reaction field also in the integration of the translational motion. So we get for the acceleration of the center of mass

$$\ddot{\vec{r}}_i = \frac{1}{m}\vec{F}_i = \frac{1}{m}\left(\vec{F}_i^{CSD} + \vec{F}_i^{RF}\right)\,. \tag{2.5.57}$$

Now let us have a look to the rotation where we start with (2.1.13) and can write for the torque

$$\vec{N}_i = \sum_{\alpha=1}^{2} \vec{r}_{i_\alpha} \times \vec{F}_{i_\alpha} \tag{2.5.58}$$

$$= \sum_{\alpha=1}^{2} \vec{r}_{i_\alpha} \times \left(\vec{f}_{i_\alpha}^{CSD} + \vec{f}_{i_\alpha}^{RF}\right) \tag{2.5.59}$$

$$= \vec{N}_i^{CSD} + \vec{N}_i^{RF}\,. \tag{2.5.60}$$

The term $\vec{N}_i^{CSD}$ is included in the equations of motion through (3.1.29). The reaction field generates the additional torque $\vec{N}_i^{RF}$ which is in detail

$$\vec{N}_i^{RF} = \frac{d}{2}\vec{n}_i \times \vec{f}_{i_1}^{RF} + (-\frac{d}{2}\vec{n}_i) \times \vec{f}_{i_2}^{RF} \tag{2.5.61}$$

$$= \frac{d}{2}\vec{n}_i \times \left(\vec{f}_{i_1}^{RF} - \vec{f}_{i_1}^{RF}\right) \tag{2.5.62}$$

$$= \frac{1}{4\pi\epsilon_0}\frac{2(\epsilon_A-1)}{2\epsilon_A+1}\frac{1}{r_{cut}^3}\,q_{i_1}\,\frac{d}{2}\,\vec{n}_i \times \left[\vec{M}_{i_1} + \vec{M}_{i_2}\right]\,. \tag{2.5.63}$$

With that we get for $\vec{G}_i$ used in equation (2.1.25) the following expression

$$\vec{G}_i = \vec{G}_i^{CSD} + I^{-1}\frac{d}{2}\left(\vec{f}_{i_1}^{RF} - \vec{f}_{i_1}^{RF}\right)\,, \tag{2.5.64}$$

and we can see that the reaction field provides an additional term not only to the translation but also to the rotation.

Finally we want to take a look at the virial respectively the pressure which is according to equation (2.3.21)

$$\mathcal{V} = \left\langle \sum_{i=1}^{N} \vec{r}_{i_s} \vec{F}_i \right\rangle = \left\langle \sum_{i=1}^{N} \vec{r}_{i_s} \left( \vec{F}_i^{CSD} + \vec{F}_i^{RF} \right) \right\rangle \tag{2.5.65}$$

$$= \left\langle \sum_{i=1}^{N} \vec{r}_{i_s} \vec{F}_i^{CSD} \right\rangle + \left\langle \sum_{i=1}^{N} \vec{r}_{i_s} \vec{F}_i^{RF} \right\rangle . \tag{2.5.66}$$

We split up again the expression for the reaction field and write for the ensemble average

$$\left\langle \sum_{i=1}^{N} \vec{r}_{i_s} \vec{F}_i^{RF} \right\rangle = \frac{1}{4\pi\epsilon_0} \frac{2(\epsilon_A - 1)}{2\epsilon_A + 1} \frac{1}{r_{cut}^3} q_{i_1} \left\langle \sum_{i=1}^{N} \vec{r}_{i_s} \left( \vec{M}_{i_1} - \vec{M}_{i_2} \right) \right\rangle \tag{2.5.67}$$

$$= \frac{1}{4\pi\epsilon_0} \frac{2(\epsilon_A - 1)}{2\epsilon_A + 1} \frac{1}{r_{cut}^3} q_{i_1} \left( \left\langle \sum_{i=1}^{N} \vec{r}_{i_s} \vec{M}_{i_1} \right\rangle - \left\langle \sum_{i=1}^{N} \vec{r}_{i_s} \vec{M}_{i_2} \right\rangle \right) . \tag{2.5.68}$$

As our system consists of indistinguishable particles we can write

$$\left\langle \sum_{i=1}^{N} \vec{r}_{i_s} \vec{M}_{i_1} \right\rangle = \left\langle \sum_{i=1}^{N} \vec{r}_{i_s} \vec{M}_{i_2} \right\rangle \tag{2.5.69}$$

and therefore

$$\left\langle \sum_{i=1}^{N} \vec{r}_{i_s} \vec{F}_i^{RF} \right\rangle = 0 . \tag{2.5.70}$$

So we do not have any effect of the reaction field on the calculation of the pressure $P$.

**Calculation of the permittivity $\epsilon_A$** For the calculation of the reaction field (2.5.49) we first need to determine the *a priori* unknown permittivity $\epsilon_A$. In the following we want to use the approach as proposed by Hentschke using a Ginzburg-Landau expansion [27] of the free energy $F$. This procedure is more generalized than the calculation done by H. Fröhlich [44]. We therefore consider an infinite dielectric with the permittivity $\epsilon_A$ with local and spontaneous oscillations of the dipole moment $\vec{p}(\vec{r})$. The free energy is defined by

$$F = \frac{1}{V} \int_V \mathrm{d}^3 r \, f\left(\vec{p}(\vec{r}), T\right) , \tag{2.5.71}$$

with the local free energy $f\left(\vec{p}(\vec{r}), T\right)$. Using the Ginzburg-Landau expansion we get for the local free energy

$$f\left(\vec{p}(\vec{r}), T\right) = f_0\left(T\right) + c_1\left(T\right) \vec{p}^{\,2}(\vec{r}) + \frac{1}{2} c_2\left(T\right) \vec{p}^{\,4}(\vec{r}) + c_3\left(T\right) \left|\nabla \vec{p}(\vec{r})\right|^2 . \tag{2.5.72}$$

As the local free energy $f$ is symmetric in $\vec{p}$ a change of the sign does not have any impact on $f$ and therefore we only get elements of equal order.
We now assume an external electric field $E$, which acts on the system. This disturbance can be reflected in the Hamiltonian as

$$\hat{H}_E = -\hat{p}E \tag{2.5.73}$$

as an operator, which is linear in $E$ and $p$. In the canonical ensemble the free energy is given by

$$F = -\beta^{-1} \ln Q_{NVT} \,, \tag{2.5.74}$$

and therefore the effect of the external electric field on the free energy $F$ or better the local free energy is given by

$$\frac{\partial f\left(\vec{p}(\vec{r}), T, E\right)}{\partial E} = -\hat{p} \,. \tag{2.5.75}$$

To ensure that the Ginzburg-Landau expansion (2.5.72) holds true for equation (2.5.75) as well, we need to add an additional term like $-\hat{p}E$ to it. With that we get for the local free energy

$$\begin{aligned} f\left(\vec{p}(\vec{r}), T, E\right) = f_0\left(T\right) + c_1\left(T\right)\vec{p}^{\,2}(\vec{r}) + \frac{1}{2}c_2\left(T\right)\vec{p}^{\,4}(\vec{r}) \\ + c_3\left(T\right)\left|\vec{\nabla}\vec{p}(\vec{r})\right|^2 \, - \vec{p}(\vec{r})\vec{E}(\vec{r}) \,. \end{aligned} \tag{2.5.76}$$

Now we want to assume a spherical volume $V$, where $\vec{p}(\vec{r}) = p \ll 1$ so that $c_2 = 0$. In the equilibrium the free energy has a minimum and it holds

$$\vec{\nabla}_{\vec{p}} \cdot \vec{f} = 0 \,. \tag{2.5.77}$$

With that and under consideration of $\vec{E} = \text{const.}$ we can now obtain $c_1\left(T\right)$ as

$$0 = c_1\left(T\right)\vec{\nabla}_{\vec{p}}\vec{p}^{\,2} - \vec{\nabla}_{\vec{p}}\left(\vec{p}\cdot\vec{E}\right) \tag{2.5.78}$$

$$\begin{aligned} &= 2\,c_1\left(T\right)\vec{p} - \Big[(\vec{p}\cdot\vec{\nabla}_{\vec{p}})\vec{E} + (\vec{E}\cdot\vec{\nabla}_{\vec{p}})\vec{p} \\ &\quad + \vec{p}\times(\vec{\nabla}_{\vec{p}}\times\vec{E}) + \vec{E}\times(\underbrace{\vec{\nabla}_{\vec{p}}\times\vec{p}}_{=0})\Big] \end{aligned} \tag{2.5.79}$$

$$= 2\,c_1\left(T\right)\vec{p} - \vec{E} \tag{2.5.80}$$

and finally

$$c_1\left(T\right) = \frac{1}{2}\frac{E}{p} \,, \tag{2.5.81}$$

because $\vec{E}$ and $\vec{p}$ are perpendicular. With the result

$$p = \frac{\epsilon_I - 1}{\epsilon_I + 2} r_{cut}^3 E \tag{2.5.82}$$

for the polarisation of a sphere with radius $r_{cut}$ in a homogenous field [46], we can write for the coefficient

$$c_1(T) = \frac{1}{2} \frac{\epsilon_I + 2}{\epsilon_I - 1} \frac{1}{r_{cut}^3} . \tag{2.5.83}$$

With that we get for the free energy $f_I$ within the volumen $V$

$$f_I \equiv f(p,T) \simeq f_0(T) + \frac{1}{2} \frac{\epsilon_I + 2}{\epsilon_I - 1} \frac{p^2}{r_{cut}^3} . \tag{2.5.84}$$

The term $-\vec{p} \cdot \vec{E}$ is not part of (2.5.84), because we omitted the electrical field, which was just introduced to get $c_1(T)$. For the whole description of the free energy we need to get hold of the contribution $f_A$ from the outside of the volume $V$, which is caused by the polarisation of the dielectric by the dipole moment $\vec{p}$. To obtain $f_A$, we follow [46] for an imbedded spherical dielectric and calculate the following integral

$$f_A = -\frac{1}{2} \int \mathrm{d}V \vec{P} \cdot \vec{E}_A^{(0)} . \tag{2.5.85}$$

Where

$$\vec{E}_A^{(0)} = -\vec{\nabla} \frac{pz}{r^3} \tag{2.5.86}$$

describes the pure electrical field outside the sphere. For the polarisation $\vec{P}$ caused by $\vec{p}$ outside the sphere we can write

$$\vec{P} = \frac{\epsilon_A - 1}{4\pi} \vec{E}_A . \tag{2.5.87}$$

To determine the electrical field $\vec{E}_A$ we use the potential

$$\varphi_A = -\frac{A_A}{r^2} \cos\Theta \tag{2.5.88}$$

whose constant $A_A$ follows from

$$\varphi_I = \left( \frac{p}{\epsilon_I r^2} - B_I r \right) \cos\Theta \tag{2.5.89}$$

together with the condition

$$\left. \frac{\partial \varphi_I}{\partial \Theta} \right|_{r=r_{cut}} = \left. \frac{\partial \varphi_A}{\partial \Theta} \right|_{r=r_{cut}} \tag{2.5.90}$$

and

$$-\epsilon_I \frac{\partial \varphi_I}{\partial r}\Big|_{r=r_{cut}} = -\epsilon_A \frac{\partial \varphi_A}{\partial r}\Big|_{r=r_{cut}} \tag{2.5.91}$$

as

$$A_A = -\frac{3}{2\epsilon_A + 1} p\,. \tag{2.5.92}$$

For the free energy $f_A$ outside the sphere we can calculate the integral (2.5.85) as

$$f_A = -\frac{1}{2}\int \mathrm{d}V \left( -\frac{3(\epsilon_A - 1)}{4\pi(2\epsilon_A + 1)}\, p \underbrace{\vec{\nabla}\frac{\cos\Theta}{r^2}}_{=\vec{\nabla}\frac{z}{r^3}} \right) \left( -\vec{\nabla}\frac{pz}{r^3} \right) \tag{2.5.93}$$

$$= -\frac{3}{8\pi}\frac{\epsilon_A - 1}{2\epsilon_A + 1} p^2 \int \mathrm{d}V \left( \vec{\nabla}\frac{z}{r^3} \right)^2 \tag{2.5.94}$$

$$= -\frac{3}{8\pi}\frac{\epsilon_A - 1}{2\epsilon_A + 1} p^2 \frac{8\pi}{3\, r_{cut}^3} \tag{2.5.95}$$

$$= -\frac{\epsilon_A - 1}{2\epsilon_A + 1}\frac{p^2}{r_{cut}^3}\,. \tag{2.5.96}$$

Together with the free energy $f_I$ inside the sphere we get for the total free energy $F$

$$F(\vec{p}, T) = f_I + f_A \tag{2.5.97}$$

$$= f_0(T) + \frac{1}{2}\frac{\epsilon_I + 2}{\epsilon_I - 1}\frac{p^2}{r_{cut}^3} - \frac{\epsilon_A - 1}{2\epsilon_A + 1}\frac{p^2}{r_{cut}^3} \tag{2.5.98}$$

$$= f_0(T) + \frac{1}{2}\frac{(2\epsilon_A + 1)(\epsilon_I + 2) - 2(\epsilon_A - 1)(\epsilon_I - 1)}{(\epsilon_I - 1)(2\epsilon_A + 1)}\frac{p^2}{r_{cut}^3} \tag{2.5.99}$$

$$= f_0(T) + \underbrace{\frac{3(2\epsilon_A + \epsilon_I)}{2(\epsilon_I - 1)(2\epsilon_A + 1)\, r_{cut}^3}}_{\equiv\kappa} p^2\,. \tag{2.5.100}$$

With this expression for the free energy we can calculate $\langle p^2 \rangle$ as well as the permittivity $\epsilon_A$ by having a look on the ensemble average (2.3.2) for $p^2$

$$\langle p^2 \rangle = \frac{\int_\Gamma \mathrm{d}\Gamma\, p^2\, e^{-\beta\mathcal{H}}}{\int_\Gamma \mathrm{d}\Gamma e^{-\beta\mathcal{H}}} \tag{2.5.101}$$

and the expression for the free energy (2.5.74)

$$F = -\beta^{-1} \ln Q_{NVT} \tag{2.5.102}$$

$$= -\beta^{-1} \ln \int_\Gamma \mathrm{d}\Gamma e^{-\beta\mathcal{H}}\,. \tag{2.5.103}$$

We take the average in (2.5.101) over a spherical volume, i.e. $\langle p^2 \rangle = \left\langle M_{Sp}^2 \right\rangle$, and can write the partition function as a sum over the not normalized probabilities of all dipole moments $\vec{p}$ as

$$Q = \sum_{\vec{p}} Q(\vec{p}) \tag{2.5.104}$$

$$= \sum_{\vec{p}} e^{-\beta F(\vec{p})} \,. \tag{2.5.105}$$

With that we get for the ensemble average

$$\left\langle p^2 \right\rangle = \frac{\sum_{\vec{p}} p^2 e^{-\beta F(\vec{p})}}{\sum_{\vec{p}} e^{-\beta F(\vec{p})}} \tag{2.5.106}$$

$$= \frac{\int \mathrm{d}^3 p \, p^2 e^{-\beta F(\vec{p})}}{\int \mathrm{d}^3 p \, e^{-\beta F(\vec{p})}} \tag{2.5.107}$$

$$= \partial_{(-\beta\kappa)} \ln \int \mathrm{d}^3 p \, e^{-\beta F(\vec{p})} \tag{2.5.108}$$

$$= \partial_{(-\beta\kappa)} \ln (\beta\kappa)^{3/2} \tag{2.5.109}$$

$$= \frac{3}{2} \partial_{(\beta\kappa)} \ln (\beta\kappa) \tag{2.5.110}$$

$$= \frac{3}{2} \frac{1}{\beta\kappa} \tag{2.5.111}$$

and finally

$$\left\langle p^2 \right\rangle = k_B T \frac{(\epsilon_I - 1)(2\epsilon_A + 1)}{2\epsilon_A + \epsilon_I} \, r_{cut}^3 \,. \tag{2.5.112}$$

Considering a homogenous fluid we can assume that the permittivity is the same inside and outside the sphere $\epsilon_A = \epsilon_I = \epsilon$ and use

$$\frac{(\epsilon - 1)(2\epsilon + 1)}{3\epsilon} = \frac{1}{k_B T} \frac{\langle p^2 \rangle}{r_{cut}^3} \tag{2.5.113}$$

for the calculation of $\epsilon$, and later usage in the reaction field (2.5.49). But within this work we want to take a slightly different approach and use instead of $\left\langle M_{Sp}^2 \right\rangle$ the value of $\left\langle \vec{M}_{Sp} \vec{M}_B \right\rangle$ as suggested by [47] and also done earlier by Bartke [22, 45]. Despite those two methods also $\left\langle \vec{M}_B \vec{M}_B \right\rangle$ would be possible and as shown by [48] the last two are equivalent for big systems. $\left\langle \vec{M}_{Sp} \vec{M}_B \right\rangle$ can be calculated for dumbbells as follows

$$\left\langle \vec{M}_{Sp} \vec{M}_B \right\rangle = \frac{1}{2N} \sum_{\alpha=1}^{2} \sum_{i=1}^{N} \vec{M}_{i_\alpha} \vec{M}_B \tag{2.5.114}$$

$$= \frac{1}{2N} \sum_{\alpha=1}^{2} \sum_{i,k=1}^{N} \sum_{j \in V_{Sp}(\vec{r}_{i_\alpha})} \vec{\mu}_j \vec{\mu}_k \,. \tag{2.5.115}$$

That means for each dumbbell site the dipole moment of the sphere $V_{Sp}$ is calculated and multiplied with the total dipole moment of the simulation box. The calculation for other systems is quite similar and only the corresponding $\vec{M}_{Sp}$ has to be calculated. For $\epsilon$ which is now given as

$$\frac{(\epsilon-1)(2\epsilon+1)}{3\epsilon} = \frac{1}{k_B T}\frac{\left\langle \vec{M}_{Sp}\vec{M}_B \right\rangle}{r_{cut}^3} \tag{2.5.116}$$

we calculate the cumulative average during the simulation, because of the big fluctuations. With that we finally can compute the reaction field.

### Ewald summation method

Another method to treat the long range character of the Coulomb interaction is the Ewald summation method. It was introduced by Paul Peter Ewald for the computation of lattices nearly hundred years ago [28]. Contrary to the reaction field method the Ewald summation allows an explicit calculation of the particle interaction using the periodicity of the matter. This explicit calculation is enabled by a split of the summation into real space and Fourier space, which results in a fast convergence of the infinite sum. Fluids we examine in this work are not periodic, but due to the periodic boundary conditions used in our simulations we can apply the Ewald method to the periodic images of the box. We have not implemented the Ewald summation in our own simulation routines, but use it in the comparison of our ionic system results with the LAMMPS (large-scale atomic/molecular massively parallel simulator) package [49]. Here an optimized implementation called PPPM (particle-particle particle-mesh) is used, which improves the order of the calculations to $N\ln(N)$ instead of $N^2$.
In the following we want to give a brief description of the method. We start with the expression of the Coulomb energy with periodic boundary conditions

$$\mathcal{U} = \frac{1}{2}\sum_{i,j}^{N}\frac{q_i q_j}{4\pi\varepsilon_0}\sum_{\substack{\vec{s}\\(i\neq j \text{ for } \vec{s}=\vec{0})}}\frac{1}{|\vec{r}_{ij}+\vec{s}|}\,. \tag{2.5.117}$$

The convergence of this sum is very slow and additionally the sum is conditionally convergent, hence the result depends on the order of the summation. Ewald rewrites the formula of the potential energy into a sum of two fast convergent expressions

$$\mathcal{U}^{\text{ewald}} = \mathcal{U}^{\text{real}} + \mathcal{U}^{\text{rec}}\,, \tag{2.5.118}$$

and introduces a Gaussian charge distribution $\rho_i = -q_i\kappa^3\exp(-\kappa^2 r^2)/\sqrt{\pi}$ to screen the charges. A graphical illustration of the procedure is shown in figure 2.3. The first sum is done in real space over the charges, as well as the Gaussian charge distribution to screen

the charge. In the second term the screening charges, which form a smooth charge density, are summed in reciprocal space. The two terms are given as

$$\mathcal{U}^{\text{real}} = \frac{1}{2}\sum_{i,j}^{N}\frac{q_i q_j}{4\pi\varepsilon_0}\sum_{\substack{\vec{s}\\(i\neq j \text{ for } \vec{s}=\vec{0})}}\frac{\operatorname{erfc}\left[\kappa\left|\vec{r}_{ij}+\vec{s}\right|\right]}{\left|\vec{r}_{ij}+\vec{s}\right|} - \sum_{i}^{N}\frac{q_i^2}{4\pi\varepsilon_0}\frac{\kappa}{\sqrt{\pi}}r \tag{2.5.119}$$

$$\mathcal{U}^{\text{rec}} = \frac{1}{2}\sum_{i,j}^{N}\frac{q_i q_j}{4\pi\varepsilon_0}\frac{4\pi}{V}\sum_{\vec{g}\neq\vec{0}} g^{-2}\exp\left[-\frac{g^2}{4\kappa^2}\right]\exp\left[i\vec{g}\cdot\vec{r}_{ij}\right] \tag{2.5.120}$$

$$\text{with}\qquad \operatorname{erfc}(x) = 1-\operatorname{erf}(x) = 1-(2/\sqrt{\pi})\int_0^x e^{-u^2}\,du\,. \tag{2.5.121}$$

For a detailed derivation of those formulas we want to refer to the book of Eastwood and Hockney [34], who also introduced the PPPM method.

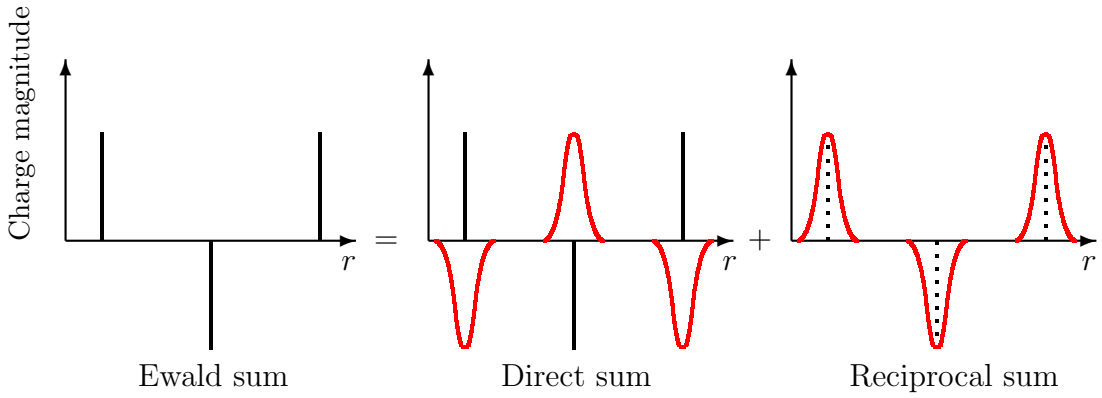


Figure 2.3.: Graphical illustration of the Ewald summation method

# Bibliography


[1] B. J. Alder and T. E. Wainwright. Studies in molecular dynamics. I. General method. *The Journal of Chemical Physics*, 31:459, 1959.

[2] A. Rahman. Correlations in the motion of atoms in liquid argon. *Physical Review*, 136(2A):A405, 1964.

[3] K. Kremer and K. Binder. Monte Carlo simulation of lattice models for macromolecules. *Computer Physics Reports*, 7(6):259, 1988.

[4] J. I. Siepmann and D. Frenkel. Configurational bias Monte Carlo: A new sampling scheme for flexible chains. *Molecular Physics*, 75(1):59, 1992.

[5] J. Caillol. Search of the gas–liquid transition of dipolar hard spheres. *The Journal of Chemical Physics*, 98:9835, 1993.

[6] R. Hentschke, E. M. Aydt, B. Fodi, and E. Stöckelmann. Molekulares Modellieren mit Kraftfeldern. http://constanze.materials.uni-wuppertal.de.

[7] M. P. Allen and D. J. Tildesley. *Computer Simulation of Liquids*. Oxford University Press, 1989.

[8] D. Frenkel and B. Smit. *Understanding molecular simulation: From algorithms to applications*. Access Online via Elsevier, 2001.

[9] D. C. Rapaport. *The art of molecular dynamics simulation*. Cambridge university press, 2004.

[10] K. Binder and G. Ciccotti, editors. *Monte Carlo and Molecular Dynamics of Condensed Matter Systems*, volume 49 of *Conference Proceedings*. Italian Physical Society, July 1995.

[11] D. W. Heermann. *Computer Simulation Methods*. Springer-Verlag, Berlin, 1986.

[12] W. C. Swope, H. C. Andersen, P. H. Berens, and K. R. Wilson. A computer simulation

method for the calculation of equilibrium constants for the formation of physical clusters of molecules: Application to small water clusters. *Journal of Chemical Physics*, 76(1):637, 1982.

[13] L. Verlet. Computer "experiments" on classical fluids. I. Thermodynamical properties of Lennard-Jones molecules. *Physical Review*, 159(1):98, 1967.

[14] W. Ouyang and R. Hentschke. From gas-liquid to liquid crystalline phase behavior via anisotropic attraction: A computer simulation study. *Journal of Chemical Physics*, 127:164501, 2007.

[15] S. Schreiber and R. Hentschke. Monte Carlo simulation of osmotic equilibria. *The Journal of Chemical Physics*, 135(13):134106, 2011.

[16] N. Metropolis, A. W. Rosenbluth, M. N. Rosenbluth, A. H. Teller, and E. Teller. Equation of state calculations by fast computing machines. *The Journal of Chemical Physics*, 21(6):1087, 1953.

[17] A. Z. Panagiotopoulos. Direct determination of phase coexistence properties of fluids by Monte Carlo simulation in a new ensemble. *Molecular Physics*, 61(4):813, 1987.

[18] A. Z. Panagiotopoulos. Direct determination of fluid phase equilibria by simulation in the Gibbs ensemble: A review. *Molecular Simulation*, 9(1):1, 1992.

[19] A. Z. Panagiotopoulos, N. Quirke, M. Stapleton, and D. J. Tildesley. Phase equilibria by simulation in the Gibbs ensemble: Alternative derivation, generalization and application to mixture and membrane equilibria. *Molecular Physics*, 63(4):527, 1988.

[20] S. Murad, J. G. Powles, and B. Holtz. Osmosis and reverse osmosis in solutions: Monte Carlo simulations and van der Waals one-fluid theory. *Molecular Physics*, 86(6):1473, 1995.

[21] I. G. Tironi, R. Sperb, P. E. Smith, and W. F. van Gunsteren. A generalized reaction field method for molecular dynamics simulations. *Journal of Chemical Physics*, 102(13):5451, 1994.

[22] J. Bartke. *Computer Simulation of the Stockmayer Fluid*. PhD thesis, Bergische Universität Wuppertal, 2008.

[23] W. G. Hoover. Canonical dynamics: Equilibrium phase-space distributions. *Physical Review A*, 31(3):1695, 1985.

[24] H. J. C. Berendsen, J. P. M. Postma, W. F. van Gunsteren, A. DiNola, and J. R.

Haak. Molecular dynamics with coupling to an external bath. *Journal of Chemical Physics*, 81(8):3684, 1984.

[25] C. Holm and K. Kremer. *Advanced computer simulation approaches for soft matter sciences I*, volume 1. Springer, 2005.

[26] S. Nosé. A molecular dynamics method for simulations in the canonical ensemble. *Molecular Physics*, 52(2):255, 1984.

[27] L. D. Landau and E. M. Lifschitz. *Statistische Physik*, volume 5. Akademie-Verlag, Berlin, 8 edition, 1991.

[28] P. P. Ewald. Die Berechnung optischer und elektrostatischer Gitterpotentiale. *Annalen der Physik*, 369(3):253, 1921.

[29] S. G. Brush, H. L. Sahlin, and E. Teller. Monte Carlo study of a one-component plasma. I. *Journal of Chemical Physics*, 45:2102, 1966.

[30] L. Onsager. Electric moments of molecules in liquids. *Journal of the American Chemical Society*, 58:1486, 1936.

[31] J. A. Barker and R. O. Watts. Monte Carlo studies of the dielectric properties of water-like models. *Molecular Physics*, 26(3):789, 1973.

[32] D. J. Auerbach, W. Paul, A. F. Bakker, C. Lutz, W. E. Rudge, and F. F. Abraham. A special purpose parallel computer for molecular dynamics: Motivation, design, implementation, and application. *Journal of Physical Chemistry*, 91:4881, 1987.

[33] G. Sutmann and V. Stegailov. Optimization of neighbor list techniques in liquid matter simulations. *Journal of Molecular Liquids*, 125(2-3):197, 2006.

[34] R. W. Hockney and J. W. Eastwood. *Computer simulation using particles*. CRC Press, 1988.

[35] J. P. Valleau. The problem of coulombic forces in computer simulation. volume 9 of *NRCC Workshop Proceedings*, page 3, 1980.

[36] C. G. Gray, Y. S. Sainger, C. G. Joslin, P. T. Cummings, and S. Goldman. Computer simulation of dipolar fluids. Dependence of the dielectric constant on system size: A comparative study of Ewald sum and reaction field approaches. *Journal of Chemical Physics*, 85(3):1502, 1986.

[37] M. Neumann and O. Steinhauser. The influence of boundary conditions used in

machine simulations on the structure of polar systems. *Molecular Physics*, 39(2):437, 1980.

[38] M. Neumann. Dipole moment fluctuation formulas in computer simulations of polar systems. *Molecular Physics*, 50(4):841, 1983.

[39] M. Neumann, O. Steinhauser, and G. S. Pawley. Consistent calculation of the static and frequency-dependent dielectric constant in computer simulations. *Molecular Physics*, 52(1):97, 1984.

[40] M. Neumann. Dielectric properties and the convergence of multipolar lattice sums. *Molecular Physics*, 60:225, 1987.

[41] C. Millot, J. Soetens, and M. T. C. Martins Costa. Static dielectric constant of the polarizable Stockmayer fluid. Comparison of the lattice summation and reaction field methods. *Molecular Simulation*, 18:367, 1997.

[42] B. Garzón, S. Lago, and C. Vega. Reaction field simulations of the vapor-liquid equilibria of dipolar fluids. Does the reaction field dielectric constant affect the coexistence properties? *Chemical Physics Letters*, 231(4-6):366, 1994.

[43] P. E. Smith and W. F. van Gunsteren. *Computer Simulation of Biomolecular Systems*, volume 2, page 182. Escom, Leiden, 1993.

[44] H. Fröhlich. *Theory of Dielectrics*. Clarendon Press, 1949.

[45] J. Bartke and R. Hentschke. Dielectric properties and the ferroelectric transition of the Stockmayer-fluid via computer simulation. *Molecular Physics*, 104(19):3057, 2006.

[46] R. Hentschke. Klassische Elektrodynamik. Skript zur Theoretischen Physik, Universität Wuppertal, 2005.

[47] S. W. De Leeuw, J. W. Perram, and E. R. Smith. Computer simulation of the static dielectric constant of systems with permanent dipoles. *Annual Review of Physical Chemistry*, 37:245, 1986.

[48] P. G. Kusalik, M. E. Mandy, and I. M. Svishchev. The dielectric constant of polar fluids and the distribution of the total dipole moment. *Journal of Chemical Physics*, 100(10):7654, 1994.

[49] S. Plimpton. Fast parallel algorithms for short-range molecular dynamics. *Journal of Computational Physics*, 117(1):1, 1995.

# 3. Models

A model chosen for molecular simulations is usually an approximation of a real world molecule or at least represents a certain characteristic (e.g. polarity) of real molecules. In the following we will describe the different models, used within this work, the CSD model, the DSS model, the Stockmayer (ST) model, and simple ions. For the first two models mainly the g-l phase transition was studied, whereas the latter two were used for the analysis of the osmotic pressure. One component common to all the models is a soft sphere repulsion, which is identical to the repulsion in the LJ (12,6) potential. Due to the generality of the LJ [1] (12,6) potential, which is in addition often used for reference and for the test of our simulation routines, we omit to detail it out here. We refer to section 7.2.1, where a modified version of it is shortly introduced. From a geometric point of view the CSD system is the most complex one, as it consists of two different charges separated by a fixed distance. Sweet and Steele [2] introduced such a dumbbell like system for the first time using LJ interaction on the individual sites. The other systems are all centered on a single point.
As we mainly concentrate on the g-l phase-transition of dipolar liquids, all our models, except the later used ions, have a dipolar character. This could be a point dipole used for DSS and ST or a dipole built of two spatially separated charges like in the CSD model.
Our basic simulation system consists of $N$ particles boxed into a volume $V$. We will also define characteristics like the dipole moment $\vec{\mu}$ and the moment of inertia $I$ for each molecule.

## 3.1. Charged soft dumbbell model

The CSD particle is a rigid linear molecule. It consists of two oppositely charged sites $i_1$ and $i_2$ of the molecule $i \in \{1, 2, ..., N\}$ separated by the fixed distance $d$. In addition to the charges with magnitude $q$ each site has a repulsive $r^{-12}$ potential, which models the short range Pauli repulsion, caused by overlapping electron orbitals. The $r^{-12}$ form of the repulsion is just an approximation quite often used for soft sphere models and established by the use of the LJ [1] (12,6) potential. Historically this was motivated by minimizing computational costs, as in the LJ model the $r^{-12}$ term can be calculated as the square of the attractive $r^{-6}$ term. The orientation of the axis is defined by the unit vector $\vec{n}_i$, which points from the negative to the positive charge. The total charge of the dumbbell

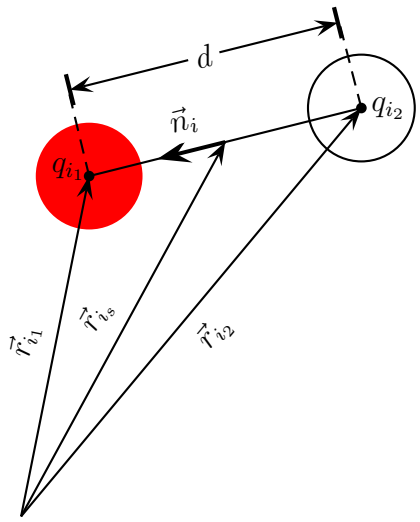


Figure 3.1.: Description of the dumbbell molecule used in this work, length $d$ with charges $q_{i_1} = -q_{i_2}$. Because of the masses being equal, we get for the center of mass coordinates $\vec{r}_{i_s} = \frac{m_{i_1}\vec{r}_{i_1}+m_{i_2}\vec{r}_{i_2}}{m_{i_1}+m_{i_2}} = \frac{1}{2}(\vec{r}_{i_1}+\vec{r}_{i_2})$.

is 0 so we can say $0 \leq q_i = q_{i_1} = -q_{i_2}$. The dumbbell mass is defined as $m$ and split for each site into $m/2$. A schematic drawing of such a molecule is presented in figure 3.1.

With the direction of the unit vector $\vec{n}_i$ and the use of the center of mass coordinate $\vec{r}_{i_s}$ the individual site coordinates $\vec{r}_{i_\alpha}$, $\alpha \in \{1, 2\}$ can be written as

$$\vec{r}_{i_1} = \vec{r}_{i_s} + \frac{d}{2}\vec{n}_i \tag{3.1.1}$$

$$\vec{r}_{i_2} = \vec{r}_{i_s} - \frac{d}{2}\vec{n}_i\,. \tag{3.1.2}$$

Obviously the CSD particle has five degrees of freedom, three for translation and two for rotation. The constraint

$$|\vec{r}_{i_1} - \vec{r}_{i_2}| = |d\vec{n}_i| = d \tag{3.1.3}$$

of a fixed axis length forbids any vibration. As the molecule can rotate around its center of mass, we will note down the moment of inertia $I$ as

$$I = \sum_{\alpha=1}^{2} m_i |\vec{r}_{i_s} - \vec{r}_{i_\alpha}|^2 = \frac{m}{2}\frac{d^2}{4}\sum_{\alpha=1}^{2}|\vec{n}_i|^2 \tag{3.1.4}$$

$$= m\frac{d^2}{4}\,. \tag{3.1.5}$$

Due to the strong $d$ dependence of the moment of inertia, which goes along with a very fast rotation for small dumbbells, we mainly keep it constant at $I = 1$.

With having the two charges at $\vec{r}_{i_\alpha}$, $\alpha \in \{1,2\}$ we finally can calculate the total dipole moment for the dumbbell

$$\vec{\mu}_i = q_i \left(\vec{r}_{i_1} - \vec{r}_{i_2}\right) = q_i \, d \, \vec{n}_i \,. \tag{3.1.6}$$

Now we have introduced all the individual characteristics of the CSD molecule and we want to take a look at the pair potential and the electric field of the dumbbell. Therefore we consider first the Coulomb potential, caused by the two charges

$$\varphi(\vec{r}_{i_s}, \vec{n}_i) = \frac{1}{4\pi\varepsilon_0} \sum_{\alpha=1}^{2} \frac{q_{i_\alpha}}{r_{i_\alpha}} \,. \tag{3.1.7}$$

This directly gives us the Coulomb pair potential for two dumbbells as

$$u_{ij}^{Coul}((\vec{r}_{i_s}, \vec{n}_i), (\vec{r}_{j_s}, \vec{n}_j)) = \frac{1}{4\pi\varepsilon_0} \sum_{\alpha=1}^{2} \sum_{\beta=1}^{2} \frac{q_{i_\alpha} q_{j_\beta}}{r_{i_\alpha j_\beta}} \,. \tag{3.1.8}$$

For the electric field we obtain via the gradient the expression

$$\vec{E}(\vec{r}_{i_s}, \vec{n}_i) = -\vec{\nabla}\varphi = \frac{1}{4\pi\varepsilon_0} \sum_{\alpha=1}^{2} \frac{q_{i_\alpha} \vec{r_{i_\alpha}}}{r_{i_\alpha}^3} \,. \tag{3.1.9}$$

Together with the aforementioned $r^{-12}$ repulsion the total pair potential is given by

$$u_{ij}^{CSD}((\vec{r}_{i_s}, \vec{n}_i), (\vec{r}_{j_s}, \vec{n}_j)) = \sum_{\alpha,\beta=1}^{2} \left[ 4\varepsilon \left( \frac{\sigma}{r_{i_\alpha j_\beta}} \right)^{12} + \frac{1}{4\pi\varepsilon_0} \frac{q_{i_\alpha} q_{j_\beta}}{r_{i_\alpha j_\beta}} \right] \,. \tag{3.1.10}$$

For all the equations above the site-site distance vector $\vec{r}_{i_\alpha j_\beta}$ is given by

$$\vec{r}_{i_\alpha j_\beta} = \vec{r}_{i_\alpha} - \vec{r}_{j_\beta} \tag{3.1.11}$$

$$= \vec{r}_{ij} - \frac{d}{2} \left[ (-1)^\alpha \, \vec{n}_i - (-1)^\beta \, \vec{n}_j \right] \tag{3.1.12}$$

with the corresponding distance $r_{i_\alpha j_\beta} = |\vec{r}_{i_\alpha} - \vec{r}_{j_\beta}|$. A typical arrangement of two interacting particles is shown in figure 3.2. The site-site interaction causes four different terms in the pair potential. This is important to keep in mind. Especially for comparison with other models, where only one interaction center is present. In such cases the repulsive $r^{-12}$ term of the CSD model is approximately four times the one of the single center particles. To be able to use the model in the velocity Verlet integrator of the MD simulation, we need to calculate the force respectively the acceleration for the translation of the particle and the angular acceleration for the rotation. We can easily calculate the force as derivate of the potential as

$$\vec{F}_{ij}^{CSD} = -\vec{\nabla}_{i_s} \, u_{ij}^{CSD} \tag{3.1.13}$$

$$= \sum_{\alpha,\beta=1}^{2} \left\{ 48 \frac{\varepsilon}{\sigma^2} \left( \frac{\sigma}{r_{i_\alpha j_\beta}} \right)^{14} + \frac{1}{4\pi\varepsilon_0} \frac{q_{i_\alpha} q_{j_\beta}}{r_{i_\alpha j_\beta}^3} \right\} \vec{r}_{i_\alpha j_\beta} \,. \tag{3.1.14}$$

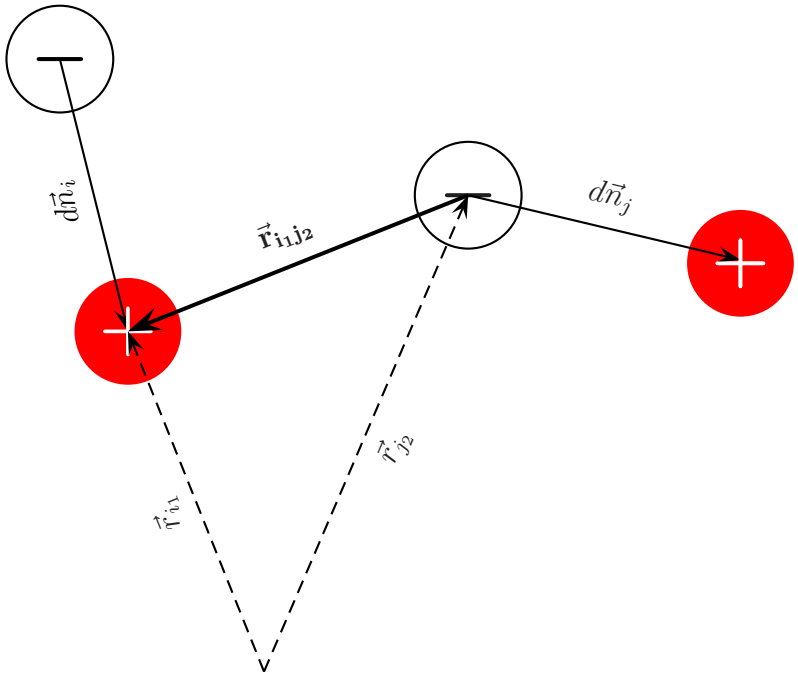


Figure 3.2.: The single sites of the molecule are described by the coordinates $\vec{r}_{i_\alpha}$. From these you get the connection vector between two sites as $\vec{r}_{i_\alpha j_\beta} = \vec{r}_{i_\alpha} - \vec{r}_{j_\beta}$.

Considering a system of $N$ particles and the pairwise additivity of the CSD model, we can write for the total potential energy of the system

$$U = \sum_{i<j} u_{ij}^{CSD}((\vec{r}_{i_s}, \vec{n}_i), (\vec{r}_{j_s}, \vec{n}_j)) \tag{3.1.15}$$

$$= \sum_{i<j} \sum_{\alpha,\beta=1}^{2} \left\{ 4\varepsilon \left( \frac{\sigma}{r_{i_\alpha j_\beta}} \right)^{12} + \frac{1}{4\pi\varepsilon_0} \frac{q_{i_\alpha} q_{j_\beta}}{r_{i_\alpha j_\beta}} \right\} . \tag{3.1.16}$$

Here we use the notation

$$\sum_{i<j} = \sum_{i=1}^{N-1} \sum_{j=i+1}^{N} \tag{3.1.17}$$

which counts pairs only once and excludes self-interaction. We can calculate the total force acting on one CSD particle caused by the remaining $N-1$ particles as

$$\vec{F}_i^{CSD} = m\ddot{\vec{r}}_{i_s} = -\frac{\partial U}{\partial \vec{r}_{i_s}} \tag{3.1.18}$$

$$= \sum_{\substack{j=1 \\ j\neq i}}^{N} \sum_{\alpha,\beta=1}^{2} \left\{ 48\frac{\varepsilon}{\sigma^2}\left(\frac{\sigma}{r_{i_\alpha j_\beta}}\right)^{14} + \frac{1}{4\pi\varepsilon_0}\frac{q_{i_\alpha}q_{j_\beta}}{r^3_{i_\alpha j_\beta}} \right\} \vec{r}_{i_\alpha j_\beta} \tag{3.1.19}$$

$$= \sum_{\substack{j=1 \\ j\neq i}}^{N} \sum_{\alpha,\beta=1}^{2} \vec{f}_{i_\alpha j_\beta}\,, \tag{3.1.20}$$

which easily gives us the acceleration to be used in the integrator (2.1.7 - 2.1.9) of the MD simulation.
We finally want to have a look at the angular acceleration, which is derived in paragraph (2.1.1) as

$$\ddot{\vec{n}}_i = \vec{G}_i - \left(\vec{n}_i \cdot \vec{G}_i + \dot{\vec{n}}_i^2\right)\vec{n}_i \tag{3.1.21}$$

with $\vec{G}_i = -I^{-1}\left(\partial U/\partial \vec{n}_i\right)$. For the CSD model we get for the derivative of the potential with respect to $\vec{n}_i$

$$\vec{G}_{ij}^{CSD} = -\frac{1}{I}\frac{\partial u_{ij}^{CSD}}{\partial \vec{n}_i} \tag{3.1.22}$$

$$= \frac{d}{2\,I}\sum_{\alpha,\beta=1}^{2} (-1)^{\alpha+1} \left\{ 48\frac{\varepsilon}{\sigma^2}\left(\frac{\sigma}{r_{i_\alpha j_\beta}}\right)^{14} + \frac{1}{4\pi\varepsilon_0}\frac{q_{i_\alpha}q_{j_\beta}}{r^3_{i_\alpha j_\beta}} \right\} \vec{r}_{i_\alpha j_\beta} \tag{3.1.23}$$

$$= \frac{d}{2\,I}\sum_{\alpha,\beta=1}^{2} (-1)^{\alpha+1}\, \vec{f}_{i_\alpha j_\beta} \tag{3.1.24}$$

but with respect to $\vec{n}_j$ we get

$$\vec{G}_{ji}^{CSD} = \frac{d}{2\,I}\sum_{\alpha,\beta=1}^{2} (-1)^{\beta} \left\{ 48\frac{\varepsilon}{\sigma^2}\left(\frac{\sigma}{r_{i_\alpha j_\beta}}\right)^{14} + \frac{1}{4\pi\varepsilon_0}\frac{q_{i_\alpha}q_{j_\beta}}{r^3_{i_\alpha j_\beta}} \right\} \vec{r}_{i_\alpha j_\beta} \tag{3.1.25}$$

$$= \frac{d}{2\,I}\sum_{\alpha,\beta=1}^{2} (-1)^{\beta}\, \vec{f}_{i_\alpha j_\beta} \tag{3.1.26}$$

and therefore obviously

$$\vec{G}_{ij}^{CSD} \neq -\vec{G}_{ji}^{CSD}\,. \tag{3.1.27}$$

Considering now the whole system, we get for our CSD model

$$\vec{G}_i^{CSD} = -\frac{1}{I}\frac{\partial U}{\partial \vec{n}_i} \tag{3.1.28}$$

$$= \frac{d}{2\,I}\sum_{\alpha,\beta=1}^{2}\sum_{\substack{j=1\\ j\neq i}}^{N}\left\{[-\Theta(j-i)]^{\alpha+1} + [-\Theta(i-j)]^{\beta}\right\}\vec{f}_{i_\alpha j_\beta} \tag{3.1.29}$$

where $\Theta(n)$ again is

$$\Theta(n) = \begin{cases} 0: & n < 0 \\ 1: & n \geq 0\,. \end{cases} \tag{3.1.30}$$

Now we can calculate the acceleration (2.1.25) as needed in the velocity Verlet algorithm.

We use the dumbbell system mainly to track the g-l critical point from a regime, where we can easily find g-l coexistence, due to the absence of long chains, to the limit of DSSs. This can be done by reducing the charge-to-charge separation $d$ step by step. Additionally we also follow the critical point for long dumbbells up to $d = 7$. We apply different theoretical approaches to our results and succeed with a description using a modified van der Waals mean field theory.

## 3.2. Charged hard dumbbell model

A similar model to CSD is the charged hard dumbbell model (CHD), which was proposed by Ganzenmüller and Camp [3] and allows us a comparison with our results for the CSD. The geometry of the hard dumbbells is the same as for soft dumbbells. The only difference is the repulsion, where each dumbbell site has the term

$$u_{ij}^{HS} = \begin{cases} 0 & \text{for} \quad r_{i_\alpha j_\beta} > \sigma \\ \infty & \text{for} \quad r_{i_\alpha j_\beta} < \sigma \end{cases} \tag{3.2.1}$$

to model the hard sphere characteristic. Together with the additional charges of magnitude $q$ the final form of the pair potential is defined as

$$u_{ij}^{CHD} = \begin{cases} \frac{1}{4\pi\varepsilon_0}\sum_{\alpha,\beta=1}^{2}\frac{q_{i_\alpha}q_{j_\beta}}{r_{i_\alpha j_\beta}} & \text{for} \quad \min_{\alpha,\beta}\left(r_{i_\alpha j_\beta}\right) > \sigma \\ \infty & \text{for} \quad \min_{\alpha,\beta}\left(r_{i_\alpha j_\beta}\right) < \sigma \end{cases} \tag{3.2.2}$$

where the parameters ($r_{i_\alpha j_\beta}$ , $q_{i_\alpha}$, ...) are the same as introduced for CSD.
We do not use the CHD model for any simulation in this work and therefore omit further

details. A more sophisticated analysis of the CHD was done by Ganzenmüller and Camp in the reference mentioned above. They observed the g-l phase transition in a range of $0.1 \leq d \leq 1.0$ using MC simulations. Due to finite-size effects it was not possible for Camp to observe the area for $d < 0.1$, but extrapolating the values gives evidence for a phase transition also in this region.

## 3.3. Stockmayer model

A famous and in computer simulations commonly used dipolar model is the ST potential. As a model for polar gas the ST potential is based on a work of Walter Hugo Stockmayer in 1941 [4]. The ST model consists of the isotropic LJ (12,6) potential

$$u_{ij}^{LJ}(r_{ij}) = 4\varepsilon \left[ \left( \frac{\sigma}{r_{ij}} \right)^{12} - \left( \frac{\sigma}{r_{ij}} \right)^{6} \right] \tag{3.3.1}$$

with an additional point dipole, whose pair interaction is given as

$$u_{ij}^{DD}(\vec{r}_{ij}, \vec{\mu}_i, \vec{\mu}_j) = \frac{1}{4\pi\epsilon_0} \left( \frac{\vec{\mu}_i \cdot \vec{\mu}_j}{r_{ij}^3} - \frac{3\,(\vec{r}_{ij} \cdot \vec{\mu}_i)\,(\vec{r}_{ij} \cdot \vec{\mu}_j)}{r_{ij}^5} \right) . \tag{3.3.2}$$

Here $\vec{r}_{ij} = \vec{r}_i - \vec{r}_j$ is the displacement vector between the interacting particles $i$ and $j$. As already mentioned above the $r^{-12}$ term is based on the Pauli exclusion for electron shells. Long-range attractions like van der Waals forces between the particles are the physical explanation of the attractive term in the LJ potential. In our final form of the ST potential, we will add an additional factor $\lambda$, introduced by van Leeuwen and Smit [5], to the attractive term. This allows to scale it or simply to turn the attraction off. So we can write:

$$\begin{aligned} u_{ij}^{vST}(\vec{r}_{ij}, \vec{\mu}_i, \vec{\mu}_j) = \quad & 4\varepsilon \left[ \left( \frac{\sigma}{r_{ij}} \right)^{12} - \lambda \left( \frac{\sigma}{r_{ij}} \right)^{6} \right] + \\ & \frac{1}{4\pi\epsilon_0} \left( \frac{\vec{\mu}_i \cdot \vec{\mu}_j}{r_{ij}^3} - \frac{3\,(\vec{r}_{ij} \cdot \vec{\mu}_i)\,(\vec{r}_{ij} \cdot \vec{\mu}_j)}{r_{ij}^5} \right) . \end{aligned} \tag{3.3.3}$$

Finally we want to note down the force $\vec{F}$ for the ST model and $\vec{G}$, which are needed for the integrator of the MD simulation. For the total force on particle $i$ caused by the

remaining $N-1$ particles we get

$$\vec{F}_i^{vST} = -\vec{\nabla}_i U^{vST} \tag{3.3.4}$$

$$= \sum_{\substack{j=1 \\ j\neq i}}^{N} \left\{ 48\frac{\varepsilon}{\sigma^2}\left[\left(\frac{\sigma}{r_{ij}}\right)^{14} - \frac{\lambda}{2}\left(\frac{\sigma}{r_{ij}}\right)^{8}\right]\vec{r}_{ij} \quad + \right.$$

$$\frac{1}{4\pi\epsilon_0}\left[\frac{(\vec{\mu}_i\cdot\vec{\mu}_j)}{r_{ij}^5} - \frac{15(\vec{\mu}_i\cdot\vec{r}_{ij})(\vec{\mu}_j\cdot\vec{r}_{ij})}{r_{ij}^7}\right]\vec{r}_{ij} \quad + \tag{3.3.5}$$

$$\left. \frac{3}{4\pi\epsilon_0}\frac{(\vec{\mu}_j\cdot\vec{r}_{ij})\vec{\mu}_i + (\vec{\mu}_i\cdot\vec{r}_{ij})\vec{\mu}_j}{r_{ij}^5} \right\}$$

where $U^{vST} = \sum_{i<j} u_{ij}^{vST}$. For the integration of the rotation we need

$$\vec{G}_i^{vST} = -\frac{1}{I}\frac{\partial U^{vST}}{\partial \vec{n}_i} \tag{3.3.6}$$

$$= \frac{\mu^2}{I}\sum_{\substack{j=1 \\ j\neq i}}^{N}\left(\frac{\vec{n}_j}{r_{ij}^3} - \frac{3\vec{r}_{ij}(\vec{r}_{ij}\cdot\vec{n}_j)}{r_{ij}^5}\right) \tag{3.3.7}$$

with $I = 1$, to calculate the acceleration of the orientation vector. This means the rotation is only dependent on the electric field

$$\vec{E}_i^{vST} = \sum_{\substack{j=1 \\ j\neq i}}^{N}\left(\frac{\vec{\mu}_i}{r_{ij}^3} - \frac{3\vec{r}_{ij}(\vec{r}_{ij}\cdot\vec{\mu}_i)}{r_{ij}^5}\right) \tag{3.3.8}$$

and we can write $\vec{G}_i^{vST}$ also as

$$\vec{G}_i^{vST} = \frac{\mu}{I}\vec{E}_i^{vST}\,. \tag{3.3.9}$$

The ST model is a thoroughly studied system in the literature including extensive studies of the critical phenomena (e.g. [5–9]). It has also led to a controversy, if the results allow to conclude that g-l coexistence exists in the limit of DSSs or not [5, 10–13]. Despite this interesting discussion we use the ST model not for any phase coexistence analysis and only make use of it for the osmotic pressure simulations. We use the ST system as solvent due to its dipolar character, which is similar to water.

## 3.4. Dipolar soft sphere model

The DSS system is commonly used in computer simulations to study dipolar fluids. With the aforementioned modified ST potential the DSS dipole-dipole interaction can be easily

obtain by setting $\lambda = 0$ as

$$u_{ij}^{DSS}(\vec{r}_{ij}, \vec{\mu}_i, \vec{\mu}_j) = 4\varepsilon \left(\frac{\sigma}{r_{ij}}\right)^{12} + \frac{1}{4\pi\epsilon_0}\left(\frac{\vec{\mu}_i \cdot \vec{\mu}_j}{r_{ij}^3} - \frac{3\,(\vec{r}_{ij} \cdot \vec{\mu}_i)\,(\vec{r}_{ij} \cdot \vec{\mu}_j)}{r_{ij}^5}\right). \tag{3.4.1}$$

With having the parameter $\lambda = 0$ and therefore also the attractive term of the LJ potential eliminated, we want to introduce again another scaling parameter $\lambda$ for the DSS system. This new scaling parameter allows us to accommodate for the fact that we have in the CSD system, due to the two dumbbell sites, in total four soft sphere interactions for each particle-particle interaction. Therefore we introduce the new $\lambda$ and write (3.4.1) as follows

$$u_{ij}^{DSS}(\vec{r}_{ij}, \vec{\mu}_i, \vec{\mu}_j) = 4\lambda\varepsilon \left(\frac{\sigma}{r_{ij}}\right)^{12} + \frac{1}{4\pi\epsilon_0}\left(\frac{\vec{\mu}_i \cdot \vec{\mu}_j}{r_{ij}^3} - \frac{3\,(\vec{r}_{ij} \cdot \vec{\mu}_i)\,(\vec{r}_{ij} \cdot \vec{\mu}_j)}{r_{ij}^5}\right). \tag{3.4.2}$$

So with setting $\lambda = 1$ we deal with the ordinary DSS system as commonly used in the literature. To model the limit $d \to 0$ of the CSD system, we need to introduce the 4-DSS model with $\lambda = 4$ to represent the increased repulsion. Analogous to the potential we can proceed for the force of the ST system in (3.3.5) and obtain

$$\vec{F}_i^{DSS} = -\vec{\nabla}_i U^{DSS} \tag{3.4.3}$$

$$\begin{aligned} = \sum_{\substack{j=1 \\ j\neq i}}^{N} \Bigg\{ & 48\lambda\frac{\varepsilon}{\sigma^2}\left(\frac{\sigma}{r_{ij}}\right)^{14}\vec{r}_{ij} \quad + \\ & \frac{1}{4\pi\epsilon_0}\left[\frac{(\vec{\mu}_i \cdot \vec{\mu}_j)}{r_{ij}^5} - \frac{15(\vec{\mu}_i \cdot \vec{r}_{ij})(\vec{\mu}_j \cdot \vec{r}_{ij})}{r_{ij}^7}\right]\vec{r}_{ij} \quad + \\ & \frac{3}{4\pi\epsilon_0}\frac{(\vec{\mu}_j \cdot \vec{r}_{ij})\vec{\mu}_i + (\vec{\mu}_i \cdot \vec{r}_{ij})\vec{\mu}_j}{r_{ij}^5}\Bigg\}. \end{aligned} \tag{3.4.4}$$

As we have seen for the ST particle, the rotation is only dependent on the electric field caused by the point dipole of the particles. Therefore the rotation is exactly the same

$$\vec{G}_i^{DSS} = \vec{G}_i^{vST} = \frac{\mu}{I}\vec{E}_i^{vST} \tag{3.4.5}$$

as in (3.3.9) for the ST model.
The DSS model is used quite frequently in computer simulations including simulations to study the phase behavior. Therefore either the DSS model is used directly or modifications were applied, which allow to reach out to the DSS limit and extrapolate the behavior for the pure dipolar model. A more detailed discussion can be found in the introduction of this work. Therefore we only want to refer to the references [5, 9, 14, 15] at this point. In our work we have introduced the DSS system to study the phase transition of purely dipolar systems and especially with the adjusted repulsion of $\lambda = 4$ to evaluate the CSD limit $d \to 0$.

## 3.5. Dipolar hard sphere model

The dipolar hard sphere system (DHS) is a well known model in the literature [16–19] and quite similar to the DSS with the difference in the repulsion to reflect the hard sphere of the particle. Therefore the DHS potential follows as

$$u_{ij}^{DHS}(\vec{r}_{ij},\vec{\mu}_i,\vec{\mu}_j) = \begin{cases} \frac{1}{4\pi\epsilon_0}\left(\frac{\vec{\mu}_i\cdot\vec{\mu}_j}{r_{ij}^3} - \frac{3(\vec{r}_{ij}\cdot\vec{\mu}_i)(\vec{r}_{ij}\cdot\vec{\mu}_j)}{r_{ij}^5}\right) & \text{for} \quad r_{ij} > \sigma \\ \infty & \text{for} \quad r_{ij} < \sigma \end{cases} . \tag{3.5.1}$$

Numerous studies have been done to settle the question, if g-l phase coexistence exists in the dipolar limit or not, by using the DHS potential directly or similar potentials allowing to extrapolate to the DHS limit [20–29]. In the present work the DHS model is not used for any simulation. But its similarity to the soft sphere potential allows to do an interesting comparison of the DHS model results with those of the soft sphere model. We therefore convert the soft sphere results to the hard sphere system, using the approach introduced previously in Ref. [14] and recapped below.

### 3.5.1. Conversion of soft sphere to hard sphere results

To connect our soft sphere model results to previous results for DHSs we compute an effective hard-core diameter

$$\sigma_{eff}(T) \tag{3.5.2}$$

using

$$B_2(T) \approx B_2(HS) = \frac{2\pi\sigma_{eff}^3}{3} . \tag{3.5.3}$$

Here $B_2(HS)$ is the second virial coefficient of hard spheres and $B_2(T)$ is the second virial coefficient of soft spheres at temperature $T$. This results in

$$\sigma_{eff}(T) = \left[\Gamma\left(\frac{3}{4}\right)\right]^{1/3} \cdot \left(\frac{4}{T}\right)^{1/12} . \tag{3.5.4}$$

Alternatively we could also make use of the Barker-Henderson formula [30] and get for the effective hard-core diameter

$$\sigma_{eff}(T) \approx 1.0555 \left(\frac{4}{T}\right)^{1/12} \tag{3.5.5}$$

which is quite similar to our approach as $\left[\Gamma\left(\frac{3}{4}\right)\right]^{1/3} \approx 1.07011$. So with that the effective hard sphere critical temperature is given by

$$T_c^{HS} = T_c\sigma_{eff}^3(T_c) \tag{3.5.6}$$

where $T_c$ stands for the soft sphere temperature. In the same way we get for the effective hard sphere critical density

$$\rho_c^{HS} = \rho_c \sigma_{eff}^3(T_c)\,. \tag{3.5.7}$$

This approach is quite beneficial and allows us to convert our soft sphere model results to the results obtained in studies of hard-core models.

## 3.6. Ionic soft sphere model

The ionic system consists of single charged particles and a soft sphere repulsion. I.e. we can consider the CSD model as ionic system with the special condition of rigidly bound oppositely charged ions. To keep the total simulation system charge neutral, we consider a fluid of charged soft spheres, where half of them carry charge $-q$ and the other half charge $+q$. The potential energy between two particles, $i$ and $j$, of charges $q_i$ and $q_j$ separated by distance $r_{ij}$ is given by

$$u_{ij}^{Ion}(r_{ij}) = 4\varepsilon \left(\frac{\sigma}{r_{ij}}\right)^{12} + \frac{1}{4\pi\epsilon_0}\frac{q_i q_j}{r_{ij}}\,. \tag{3.6.1}$$

With that we get for the force

$$F_i^{Ion} = -\vec{\nabla}_i U^{Ion} = \sum_{\substack{j=1\\ j\neq i}}^{N} \left\{ 48\frac{\varepsilon}{\sigma^2}\left(\frac{\sigma}{r_{ij}}\right)^{14} + \frac{1}{4\pi\varepsilon_0}\frac{q_i q_j}{r_{ij}^3}\right\}\vec{r}_{ij}\,. \tag{3.6.2}$$

As the ion is radial symmetric, we do not have any rotation for the ions.
The ionic system completes the investigation on the CSD model. We used the DSS model for the limit $d \to 0$ and on the other end of the spectrum the free ions can model the behavior of big charge separation $d$, where the individual dumbbell sites act more and more independently. Additionally the soft sphere ionic system is similar to the restricted primitive model (RPM), where the soft sphere repulsion is replaced by a hard sphere repulsion. The critical parameters we obtain from our simulations for the ionic system can be compared with estimations based on the Debye-Hückel theory published nearly 90 years ago [31].

# Bibliography


[1] J. E. Jones. On the determination of molecular fields. II. From the equation of state of a gas. *Proceedings of the Royal Society of London. Series A*, 106(738):463, 1924.

[2] J. R. Sweet and W. A. Steele. Statistical mechanics of linear molecules. I. Potential energy functions. *Journal of Chemical Physics*, 47:3022, 1967.

[3] G. Ganzenmüller and P. J. Camp. Vapor-liquid coexistence in fluids of charged hard dumbbells. *Journal of Chemical Physics*, 126:191104, 2007.

[4] W. H. Stockmayer. Second virial coefficients of polar gases. *Journal of Chemical Physics*, 9(5):398, May 1941.

[5] M. E. van Leeuwen and B. Smit. What makes a polar liquid a liquid? *Physical Review Letters*, 71(24):3991, 1993.

[6] M. J. Stevens and G. S. Grest. Phase coexistence of a Stockmayer fluid in an applied field. *Physical Review E*, 51(6):5976, 1995.

[7] J. Stoll, J. Vrabec, and H. Hasse. Comprehensive study of the vapour-liquid equilibria of the pure two-centre Lennard-Jones plus pointdipole fluid. *Fluid Phase Equilibria*, 209:29, 2003.

[8] L. Zhongyuan, O. Wenze, S. Zhaoyan, L. Zesheng, and A. Lijia. Computer simulations on the gas-liquid phase diagram of Stockmayer fluids. *Chinese Science Bulletin*, 50(15):1595, 2005.

[9] J. Bartke. *Computer Simulation of the Stockmayer Fluid*. PhD thesis, Bergische Universität Wuppertal, 2008.

[10] J. Bartke and R. Hentschke. Phase behavior of the Stockmayer fluid via molecular dynamics simulation. *Physical Review E*, 75:061503, 2007.

[11] R. Hentschke, J. Bartke, and F. Pesth. Equilibrium polymerization and gas-liquid critical behavior in the Stockmayer fluid. *Physical Review E*, 75:011506, 2007.

[12] A. O. Ivanov, S. S. Kantorovich, and P. J. Camp. Comment on "equilibrium polymerization and gas-liquid critical behavior in the Stockmayer fluid". *Physical Review E*, 77(1):013501, 2008.

[13] R. Hentschke and J. Bartke. Reply to "comment on 'equilibrium polymerization and gas-liquid critical behavior in the Stockmayer fluid'". *Physical Review E*, 77(1):013502, 2008.

[14] H. Braun and R. Hentschke. Tracking gas-liquid coexistence in fluids of charged soft dumbbells. *Physical Review E*, 80(4):041501, 2009.

[15] R. Jia, H. Braun, and R. Hentschke. Gas-liquid coexistence in a system of dipolar soft spheres. *Physical Review E*, 82(6):062501, 2010.

[16] B. Huke and M. Lücke. Magnetic properties of colloidal suspensions of interacting magnetic particles. *Reports on Progress in Physics*, 67:1731, 2004.

[17] J. J. Weis and D. Levesque. Ferroelectric phases of dipolar hard spheres. *Physical Review E*, 48:3728, Nov 1993.

[18] P. J. Camp, J. C. Shelley, and G. N. Patey. Isotropic fluid phases of dipolar hard spheres. *Physical Review Letters*, 84(1):115, 2000.

[19] P. I. C. Teixeira, J. M. Tavares, and M. M. Telo da Gama. The effect of dipolar forces on the structure and thermodynamics of classical fluids. *Journal of Physics: Condensed Matter*, (33):R411, 2000.

[20] K. Ng, J. P. Valleau, G. M. Torrie, and G. N. Patey. Liquid-vapour co-existence of dipolar hard spheres. *Molecular Physics*, 38(3):781, 1979.

[21] J. Caillol. Search of the gas–liquid transition of dipolar hard spheres. *The Journal of Chemical Physics*, 98:9835, 1993.

[22] S. C. McGrother and G. Jackson. Island of vapor-liquid coexistence in dipolar hard-core systems. *Physical Review Letters*, 76(22):4183, 1996.

[23] J. M. Tavares, M. M. Telo Da Gama, and M. A. Osipov. Criticality of dipolar fluids: Liquid-vapor condensation versus phase separation in systems of living polymers. *Physical Review E*, 56(6):R6252, 1997.

[24] I. Szalai, D. Henderson, D. Boda, and K. Chan. Thermodynamics and structural properties of the dipolar Yukawa fluid. *The Journal of Chemical Physics*, 111(1):337, 1999.

[25] N. G. Almarza, E. Lomba, C. Martín, and A. Gallardo. Demixing in binary mixtures of apolar and dipolar hard spheres. *The Journal of Chemical Physics*, 129(23):234504, 2008.

[26] Y. V. Kalyuzhnyi, I. A. Protsykevytch, G. Ganzenmüller, and P. J. Camp. Liquid-vapour coexistence in the dipolar Yukawa hard-sphere fluid. *EPL (Europhysics Letters)*, 84(2):26001, 2008.

[27] G. Ganzenmüller, G. N. Patey, and P. J. Camp. Vapour–liquid phase transition of dipolar particles. *Molecular Physics*, 107(4-6):403, 2009.

[28] L. Rovigatti, J. Russo, and F. Sciortino. No evidence of gas-liquid coexistence in dipolar hard spheres. *Physical Review Letters*, 107(23):237801, 2011.

[29] L. Rovigatti, J. Russo, and F. Sciortino. Structural properties of the dipolar hard-sphere fluid at low temperatures and densities. *Soft Matter*, 8(23):6310, 2012.

[30] J. A. Barker and D. Henderson. Perturbation theory and equation of state for fluids. II. A successful theory of liquids. *The Journal of Chemical Physics*, 47:4714, 1967.

[31] P. Debye and E. Hückel. De la théorie des électrolytes. i. abaissement du point de congélation et phénomènes associés. *Physikalische Zeitschrift*, 24(9):185, 1923.

# 4. Analysis of the gas-liquid transition for charged soft dumbbells using molecular dynamics simulation

## 4.1. Phase coexistence in fluids

Since the fundamental work of van der Waals [1] almost 150 years ago, the phase transition from a dilute gas to a dense liquid is qualitatively described by a modification of the ideal-gas equation of state $P = Nk_BT/V$. He modified the equation in two ways, first he considered a reduced pressure $P$, which is caused by the attraction of the intermolecular forces reflected by the parameter $a$. Secondly he took account of the fact that two particles cannot occupy the same region due to their repulsion at short distances. Therefore the volume $V$ needs to be reduced by $bN$, where $b$ is the excluded volume. With that he formulated the well known van der Waals equation of state [2]

$$P = \frac{Nk_BT}{V - Nb} - \frac{a}{V^2}\,. \tag{4.1.1}$$

Despite the physical motivation, the van der Waals equation is a mean field theory, as it only approximates the inter-particle forces and cannot reflect phase separation due to its homogenous character. This has some unphysical effects, like the van der Waals loop shown in figure 4.1, which violates the physical condition $\partial P/\partial V|_T \geq 0$ and cannot be observed in real life experiments. It also means that the Gibbs free energy is convex, which corresponds to unstable states in this region. Despite the fact that the van der Waals loop is unphysical and cannot be observed experimentally, it is a well known effect in MD simulations. This is caused by the finite size of the simulated systems, which is usually in the region of hundreds or thousands of particles and hence does not allow density fluctuations as seen in real experiments. The occurence of the van der Waals loop in the simulations gives us the possibility to make use of the Maxwell construction method, described in the following section. It allows us to identify the phase coexistence area of our systems.

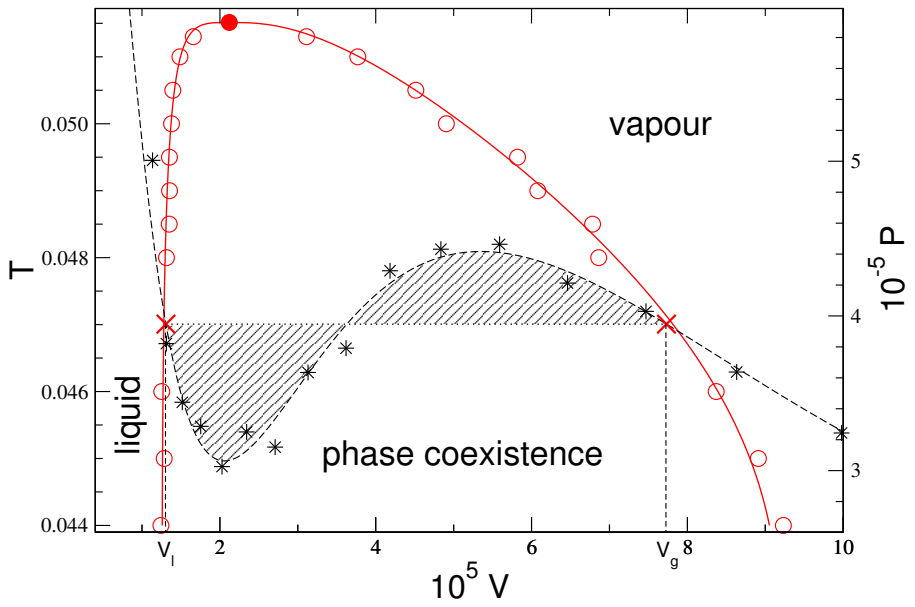


Figure 4.1.: The plot shows the Maxwell equal area construction for one simulated isotherm (stars) of the CSD system with $d = 10^{-3}$ and $T = 0.047$. An empirical equation of state is used for a fit of the isotherm (dashed line) to apply the equal area construction (shadded areas) and determine the corresponding coexistence densities (red crosses). The coexistence densities for the remaining isotherms (red hollow circles) are used to fit the envelope (red solid line) of the phase coexistence regime and to calculate the critical point (red solid circle) via the scaling relations (4.1.11) and (4.1.12).

### 4.1.1. The Maxwell construction method

The Maxwell construction method is a well established method to correct the unphysical behavior of the van der Waals loop in the phase coexistence area. The usage of the method was justified by Griffiths [3] and has been applied many times in various simulations [4–6]. Geometrically the Maxwell equal area construction method is illustrated in figure 4.1. The two points $V_g$ and $V_l$ are chosen so that the shaped regions have equal area. The two points describe the border of the g-l phase coexistence region. To legitimate this view, we follow [7] and use the fact that the pressure and the chemical potential in the g-l phase coexistence region must be identical. For the pure gas and the pure liquid at the border

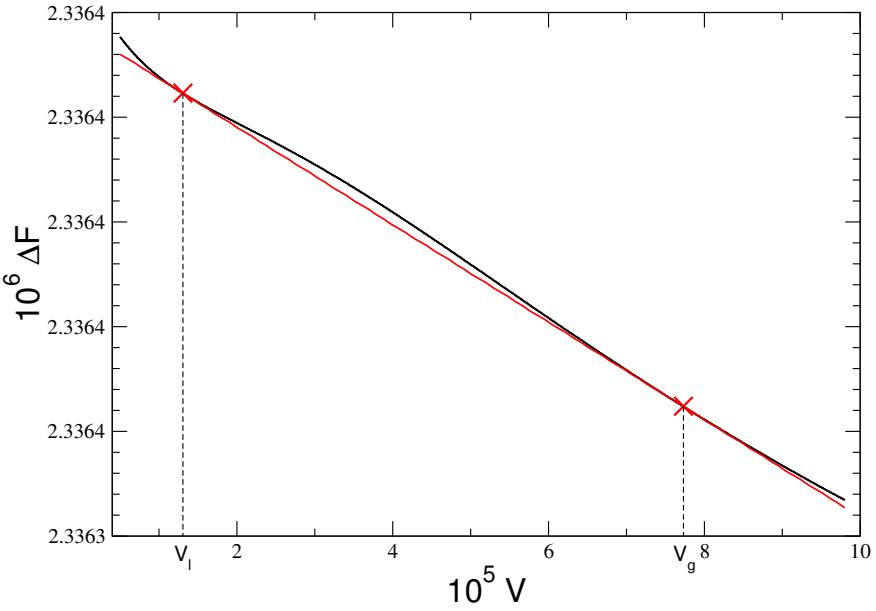


Figure 4.2.: Integrating the empirical equation of state (dashed line in figure 4.1) via $P = -\partial F/\partial V|_T$ gives the reduced free energy (black solid line). The red solid line is the common tangent on the coexistence densities.

of the phase coexistence region it holds

$$P_g = P_l \tag{4.1.2}$$

$$\mu_g = \mu_l \,. \tag{4.1.3}$$

We want to derive $V_g$ and $V_l$ from those two conditions. Therefore we use the equation of state, which describes the isotherm, and insert it into (4.1.2). For our example we use the van der Waals equation of state (4.1.1) and get

$$\frac{NT}{V_g - Nb} - \frac{a}{V_g^2} = \frac{NT}{V_l - Nb} - \frac{a}{V_l^2} \tag{4.1.4}$$

where we have set $k_B = 1$. The values for $a$ and $b$ need to be determined from the simulation data. For the second condition (4.1.3) we use the Gibbs free energy $G = N\mu = F + PV$, where $F$ stands for the free Helmholtz energy and write

$$0 = N\left(\mu_l - \mu_g\right) = F_l - F_g + P\left(V_l - V_g\right) \,. \tag{4.1.5}$$

Together with $P = -\partial F/\partial V|_T$ we get

$$\left.\frac{\partial F}{\partial V}\right|_{T,V_l} = \left.\frac{\partial F}{\partial V}\right|_{T,V_g} = \frac{F_l - F_g}{V_l - V_g} \,. \tag{4.1.6}$$

The geometrical interpretation of equation (4.1.6) is illustrated in figure 4.2 and means that the line through the points $(V_g, F_g)$ and $(V_l, F_l)$ is also the common tangent of the free energy at those two points. The difference between the Helmholtz free energies can be obtained by integrating $P = -\partial F/\partial V|_T$ along the isotherms

$$F(V_l, T) - F(V_g, T) = -\int_{V_g}^{V_l} P(V, T)\,\mathrm{d}V\,, \tag{4.1.7}$$

where $P(V, T)$ stands for the equation of state used to interpret the isotherm. Replacing the left side of (4.1.7) we can re-write it as

$$P\,(V_l - V_g) = \int_{V_l}^{V_g} P(V, T)\,\mathrm{d}V\,. \tag{4.1.8}$$

This explains the equal area approach shown in the upper picture of figure 4.1. The left side of (4.1.8) is the area in the rectangle between $V_l$ and $V_g$ with height $P$ and the right side is the area below the isotherm. It is clear that the two shaped areas are of the same size and the two volumes $V_l$ and $V_g$ can be determined by a geometrical procedure. Additionally we can interpret (4.1.6) geometrically as well, because the line through the points $(V_l, F_l)$ and $(V_g, F_g)$ is the tangent of the Helmholtz free energy on those two points. This is illustrated in the lower part of figure 4.1.
To apply the equal area construction to our simulation data, we use an equation of state like (4.1.1) as fit function to describe the isotherms, together with a small Mathematica [8] program to determine $V_l$ and $V_g$ respective $\rho_l$ and $\rho_g$. It is not necessary for the fit function to have a physical foundation. We just need a function, which describes our simulation data in the coexistence regime best. We mostly made use of the following two functions, which are derived from an equation of state for networks [9]:

$$P = \frac{T}{a_0}\left(-\frac{a_3 a_0}{V} - \frac{1}{2}\frac{a_2 a_0^2}{T\,V} - \ln\left(a_1 - \frac{a_0}{V}\right)\right) + a_4 \tag{4.1.9}$$

$$P = \frac{T}{a_0}\left(-\frac{a_3 a_5}{V} - \frac{1}{2}\frac{a_2 a_6^2}{T\,V} - \ln\left(a_1 - \frac{a_0}{V}\right)\right) + a_4\,. \tag{4.1.10}$$

Here $a_n$ are the fit parameters.

## 4.1.2. Scaling laws

The Maxwell construction gives us the possibility to identify the phase coexistence area for simulated isotherms at different temperatures below the critical point. As we get closer to the critical point, the simulation becomes more difficult due to large fluctuations particularly in the pressure. Partly this could be compensated by extensive long simulation runs. To be independent of simulations very close to the critical point, we can make use

of the scaling laws, which allow to describe the system near the critical point [10, 11]. They also enable us to derive the critical parameters $T_c$, $\rho_c$ and $P_c$ from the coexistence area, found with the Maxwell construction. The scaling laws are defined as

$$\rho_F - \rho_G \approx A_0 \mid t \mid^{\beta} + A_1 \mid t \mid^{\beta+\Delta} \tag{4.1.11}$$

$$(\rho_F + \rho_G)/2 \approx \rho_c + D_0 \mid t \mid^{1-\alpha} + D_1 \mid t \mid \tag{4.1.12}$$

$$P - P_c \approx P_0 \mid t \mid + P_1 \mid t \mid^{2-\alpha} + P_2 \mid t \mid^2 , \tag{4.1.13}$$

with $t = (T - T_c)/T_c$ and can be derived using the renormalization group theory [12, 13]. They are identical for all systems in the same universality class. For the models in this work, we use the universality class of the three dimensional Ising model. The critical exponents for the Ising model are given as $\alpha \approx 0.110$, $\beta \approx 0.326$ and $\Delta \approx 0.5$ [14]. One might ask the admittedly difficult question, whether the universality class of our systems is Ising. We cannot clearly answer this question in this work. But we can consult the literature and find for the ionic system, precisely the RPM system, in the study of Fisher and Levin a "conclusion" to the question, if long range Coulomb interaction cause mean field exponents or not. They argue that a non-Ising-like universality class seems unlikely and that the cross-over to Ising-like behavior occurs very close to $T_c$ [15]. Almost ten years later Panagiotopoulos performs a very sophisticated finite-size scaling analysis for the RPM and states, while not conclusively, the good matching of the data to the limiting Ising-class distribution is consistent with Ising-type criticality for this model [16]. We expect that a conclusive answer to this question for our systems is likewise difficult. But since evidence seems to indicate Ising behavior in the RPM, we would expect the same for our systems. This is also in line with previous works on comparable models, aimed at the critical parameters of CHDs [17] and point dipole systems [18, 19]. In the latter the mapping on the ordering parameter distribution of the 3D Ising universality class is part of the mixed-field finite size scaling employed. In general good matching of the data to the limiting Ising-class distribution is taken as a consistency check for Ising-type criticality.
A comprehensive overview of phase transitions and critical phenomena can be found in the book of the same title by Domb [6] and [20] or in [21, 22].

### 4.1.3. Parameters for the molecular dynamics simulation

Before we can use our simulation program, we first need to exercise some tests to verify that there are no errors in the implementation, which lead to wrong simulation results. Typically this is done by carrying out simulations for a simple system, where various data for comparison exists in the literature. We have passed all those tests successfully, but want to omit a lengthy discussion here and refer to [23] where this is documented for the routines used in this work. Here we only want to focus on the determination of the optimal parameters for the simulation of the isotherms.
To make use of the Maxwell construction and the scaling laws, we need to simulate several

isotherms at different temperatures in the phase coexistence region. Usually the phase coexistence region is *a priori* unknown and we need to narrow it down, by doing some test simulations in the assumed region. Once we find an isotherm showing a van der Waals loop, we can do more extensive simulations in that region. More extensive means here that we try to optimize several parameters like the number of particles $N$, the total simulation time $t_{tot}$, the cutoff radius $r_{cut}$, and the size of the time step $\Delta t$ to improve computational effort and result accuracy. The effect of the different parameters on the simulated isotherms of the CSD model are visualized in figure 4.3 for different numbers of particles and in figure 4.4 to show the influence of the cutoff radius. It turns out that the simulations with more than $N = 500$ particles and a cutoff of $r_{cut} = 9.0$ produces stable results.

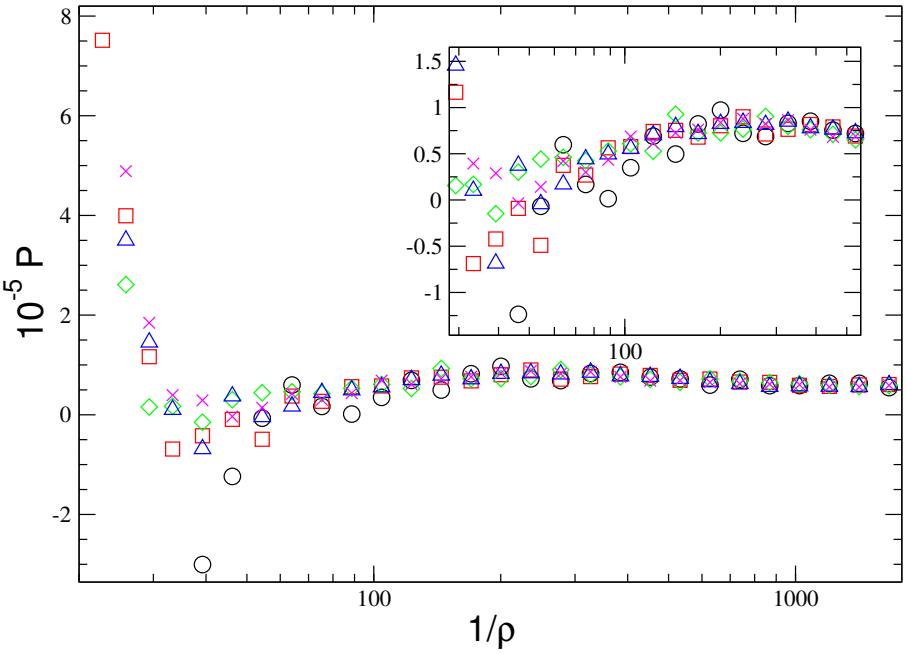


Figure 4.3.: The depicted isotherms show the influence of the system size $N$ on the pressure $P$ plotted vs. the reciprocal of the density $1/\rho$. Here the isotherms are plotted for $N = 108$ (black circles), $N = 500$ (red squares), $N = 800$ (green diamonds), $N = 1200$ (blue triangles) and $N = 1600$ (magenta stars) particles. It is apparent that above $N = 500$ particles the pressure does not change significantly. The isotherms are simulated at the temperature $T = 0.0155$, dipole moment $\mu^2 = 1$, length $d = 1$ and a cutoff $r_{cut} = 10.0$.

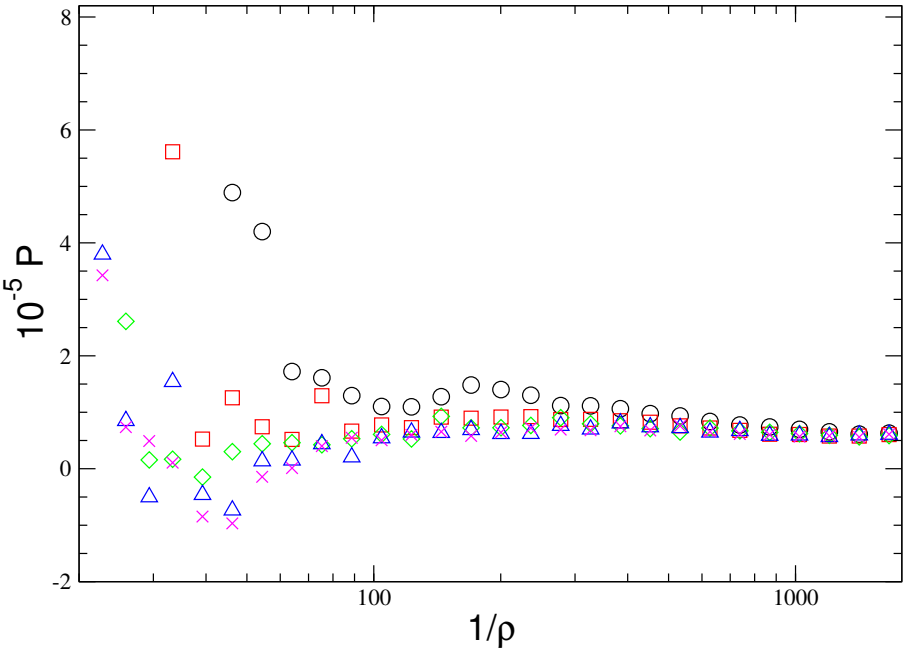


Figure 4.4.: Multiple isotherms simulated to identify the effect of the cutoff $r_{cut}$ on the pressure $P$ plotted vs. the reciprocal of the density $1/\rho$. Here the isotherms are plotted for $r_{cut} = 5.0$ (black circles), $r_{cut} = 7.0$ (red squares), $r_{cut} = 9.0$ (green diamonds), $r_{cut} = 10.0$ (blue triangles) and $r_{cut} = 12.5$ (magenta stars). For cutoffs beyond $r_{cut} = 9.0$ there is no major effect on the pressure. All of the isotherm are simulated at the temperature $T = 0.0155$, dipole moment $\mu^2 = 1$, length $d = 1$ and $N = 800$ particles.

In general most of our simulations are done with systems varying from $N = 800$ to $N = 3000$ particles and a cutoff radius between $r_{cut} = 10$ and $r_{cut} = 20$. The time step for the simulations was mostly chosen as $\Delta t = 0.001$ except for very small dumbbells of the CSD model with $d \leq 0.001$, where we decreased the time step down to $\Delta t = 2 \cdot 10^{-5}$. To avoid any systematic errors and to get better results for the isotherms, we produce for each temperature two independent isotherms. For each one a FCC (face-centered cubic) lattice with random velocities is generated as start configuration, to simulate the first state point. For all consecutive state points the previous final configuration is used as start configuration, and the density is adjusted accordingly. In total we produce for each isotherm about 30-45 individual state points. To generate one isotherm, we start at a low density and enlarge the density for each data point, i.e. the system is compressed. For the other isotherm the first data point is sampled at high density and the system is

de-compressed for all following state points. To control the temperature of the simulation, we make use of the weak coupling method of Berendsen *et al.* [24].

## 4.2. Gas-liquid transition of charged soft dumbbells

After we have verified the general correctness of our simulation program with models like the two center Lennard-Jones model (2CLJ), for which comparable data in the literature exists [23, 25], we started our investigation of the g-l transition of the CSD model. As outlined earlier the CSD model allows us to start with a large charge-to-charge separation $d$. Here we can expect a g-l phase transition due to the absence of chains, as they are energetically unprivileged as can be seen in figure 4.6. From there we can track the critical point to the limit dipolar soft sphere limit $d \to 0$. The only difference to the DSS model is due to the two sites of a dumbbell. Thus we have in total four repulsive soft sphere interactions contributing to the force, instead of a single one for the ordinary DSS model. To eliminate this difference, we have introduced a 4-DSS model (see chapter 5) to be as close as possible to the CSD model. We created a large set of simulations, which span a range of dumbbell lengths from $d = 0.0001$ to $d = 7.0$. As the absolute value of the dipole moment $\mu = qd$ depends on the dumbbell lengths the simulation series can be split into two. For the first one we sampled at constant charge $q = 1$ and the other one with constant dipolar moment $\mu^2 = 1$. To ease up the comparison with results created by other groups like [17], we note down the reduced units where the ionic temperature is defined as

$$\tau^i = \frac{k_B T D \sigma}{q^2} \tag{4.2.1}$$

and the dipolar temperature as

$$\tau^d = \frac{k_B T D \sigma^3}{\mu^2} = \frac{\tau^i \sigma^2}{d^2} \tag{4.2.2}$$

using $D = 4\pi\epsilon_0$. As usual in our simulations we set $k_B = 1$, $D = 1$, and $\sigma = 1$, which simplifies the ionic temperature for $q = 1 = const.$ to

$$\tau^i = T \tag{4.2.3}$$

and for the constant dipole moment $\mu^2 = 1 = const.$ we get

$$\tau^d = T\,. \tag{4.2.4}$$

In the following listings of critical temperatures, and in all the plots, we will always use the reduced temperature $\tau^d$ and denote it as $T$.
The critical parameters, we obtained from the isotherms using the Maxwell construction and the scaling laws, can be found in table 4.1 for constant charges $q = 1$, and in table

4.2 for constant dipole moment $\mu^2 = 1$. For the constant charge series it was not possible to observe a van der Waals loop for small dumbbells $d \leq 0.1$ even by lowering down the temperature to $\tau^i \approx 10^{-6}$. Nevertheless this does not allow to conclude that there is no critical point at all, because at such low temperatures it is difficult to reach equilibrium and simulate for sufficient long time. It is also possible that the critical temperature is in even lower regimes, where we are not able to simulate anymore due to the mentioned difficulties. Luckily the series for constant dipole moment can be continued to smaller dumbbells which we did until $d = 10^{-4}$. But there is also a drawback with this series for large dumbbells beyond $d > 4$ where it still was possible to see a van der Waals loop as shown in figure 4.7. However it was not possible to apply the Maxwell construction as only a too small regime of the phase coexistence area could be simulated. So it turns out that each of the two series has some advantages for certain dumbbell lengths $d$.
The results for the critical parameters with $\mu^2 = 1$ are plotted in figure 4.5 and for $d > 1$ also for $q = 1$. The critical parameters are stable in the range of $10^{-4} < d < 0.1$ except of some minor scattering in the critical density. This shows that the higher electric moments do not have any effect. The averages for the critical temperature, critical number density and critical pressure in this $d$ range are

$$T_c = 0.0513 \tag{4.2.5}$$
$$\rho_c = 0.004 \tag{4.2.6}$$
$$P_c = 6.6 \cdot 10^{-5}\,. \tag{4.2.7}$$

With that we can calculate the critical compressibility factor

$$Z_c = \frac{P_c}{T_c \rho_c} \tag{4.2.8}$$

as

$$Z_c = 0.33\,. \tag{4.2.9}$$

This is in very good agreement with the compressibility factor calculated using the van der Waals equation (4.1.1). To do that we can calculate the critical parameters for the van der Waals equation and get

$$P_c = \frac{1}{27}\frac{a}{b^2} \tag{4.2.10}$$
$$k_B T_c = \frac{8}{27}\frac{a}{b} \tag{4.2.11}$$
$$\rho_c = \frac{1}{3b} \tag{4.2.12}$$

which yields for the critical compressibility factor

$$Z_c = \frac{3}{8}\frac{1}{k_B}\,. \tag{4.2.13}$$

As we can see $Z_c$ is independent of the parameters $a$ and $b$, which means, in theory the critical compressibility factor is the same for all kinds of fluids. In other words "all substances obey the same equation of state in terms of reduced variables". This is called the principle of corresponding states [9]. Although the principle works very well for small dumbbells, as shown in the bottom of figure 4.5, it is not absolutely true for the full range of dumbbells we investigated. This is a known fact for dipolar fluids and was observed before [19, 26]. It seems to be related to the formation of chains and networks in polar fluids. Looking at the simulation snapshots for different dumbbell systems between $d = 1$ and $d = 0.1$ (figures 4.9 - 4.13), indicates that for $d = 1.0$ no aggregate generation exists. For the smaller dumbbells a network type structure respective chains are present. This supports that the different type of aggregation is responsible for the deviation of the principle of corresponding states. In addition, particularly the comparison between figures 4.12 and 4.13, which show the simulation above $\rho_c$ and below $\rho_c$ respectively, points out that there is a transformation from a network to chains. This allows us, to consider theories like Tlusty and Safran [27], where the type of aggregation is responsible for the phase transition.
As our system is quite similar to the CHD system studied by Ganzenmüller and Camp [17], we also did a comparison to their data. For this we converted our results into the hard sphere system using the conversion given in section 3.5.1. The comparison can be found in figure 4.8, where our critical temperatures for $q = 1$ and $\mu^2 = 1$ are plotted along with the reference data in the range $0.01 \leq d \leq 7.0$. Especially the data for $\mu^2 = 1$ is, despite some offset, in good agreement with the reference data for CHDs. The values for the critical temperature for $q = 1$ are lower, as we have not converted them into the reduced units introduced in equation (4.2.2) above.

Table 4.1.: Table with our own results for the critical parameters of the CSD system with $q = 1$.

| $d$ | $T_c$ | $\rho_c$ | $P_c \cdot 10^{-5}$ | $Z_c$ | $T_c^{DHS}$ | $\rho_c^{DHS}$ |
|---|---|---|---|---|---|---|
| 0.1500 | 0.0104 | 0.0052 | 0.0168 | 0.0031 | 0.0563 | 0.0285 |
| 0.2000 | 0.0121 | 0.0046 | 0.0062 | 0.0011 | 0.0632 | 0.0238 |
| 0.2500 | 0.0109 | 0.0062 | 0.1390 | 0.0206 | 0.0585 | 0.0331 |
| 0.5000 | 0.0195 | 0.0113 | 1.5088 | 0.0685 | 0.0903 | 0.0526 |
| 0.7500 | 0.0207 | 0.0090 | 2.7619 | 0.1485 | 0.0944 | 0.0411 |
| 1.0000 | 0.0170 | 0.0048 | 1.5640 | 0.1908 | 0.0817 | 0.0231 |
| 2.0000 | 0.0103 | 0.0048 | 3.7690 | 0.1915 | 0.0562 | 0.0259 |
| 3.0000 | 0.0057 | 0.0065 | 1.3940 | 0.0415 | 0.0361 | 0.0410 |
| 4.0000 | 0.0033 | 0.0026 | 0.6078 | 0.0458 | 0.0236 | 0.0185 |
| 5.0000 | 0.0021 | 0.0009 | 0.5305 | 0.1146 | 0.0170 | 0.0071 |
| 6.0000 | 0.0016 | 0.0014 | 0.3263 | 0.0426 | 0.0136 | 0.0118 |
| 7.0000 | 0.0012 | 0.0019 | 0.3225 | 0.0301 | 0.0110 | 0.0174 |

Table 4.2.: Table with our own results for the critical parameters of the CSD system with $\mu^2 = 1$.

| $d$ | $T_c$ | $\rho_c$ | $P_c \cdot 10^{-5}$ | $Z_c$ | $T_c^{DHS}$ | $\rho_c^{DHS}$ |
|---|---|---|---|---|---|---|
| 0.0001 | 0.0515 | 0.0046 | 7.0288 | 0.2986 | 0.1874 | 0.0166 |
| 0.0005 | 0.0516 | 0.0031 | 6.2746 | 0.3939 | 0.1875 | 0.0112 |
| 0.0010 | 0.0513 | 0.0045 | 6.3231 | 0.2770 | 0.1868 | 0.0162 |
| 0.0015 | 0.0519 | 0.0039 | 7.0521 | 0.3479 | 0.1883 | 0.0142 |
| 0.0025 | 0.0516 | 0.0037 | 6.5794 | 0.3436 | 0.1877 | 0.0135 |
| 0.0050 | 0.0522 | 0.0045 | 7.4320 | 0.3172 | 0.1892 | 0.0163 |
| 0.0075 | 0.0518 | 0.0039 | 6.9135 | 0.3412 | 0.1882 | 0.0142 |
| 0.0100 | 0.0517 | 0.0035 | 6.8934 | 0.3789 | 0.1879 | 0.0128 |
| 0.0150 | 0.0511 | 0.0039 | 6.3611 | 0.3202 | 0.1862 | 0.0142 |
| 0.0200 | 0.0518 | 0.0036 | 6.6478 | 0.3587 | 0.1881 | 0.0130 |
| 0.0350 | 0.0518 | 0.0036 | 7.0124 | 0.3813 | 0.1882 | 0.0129 |
| 0.0500 | 0.0506 | 0.0036 | 6.0740 | 0.3319 | 0.1848 | 0.0132 |
| 0.0750 | 0.0502 | 0.0043 | 6.5605 | 0.3025 | 0.1838 | 0.0158 |
| 0.1000 | 0.0487 | 0.0052 | 5.6641 | 0.2232 | 0.1797 | 0.0192 |
| 0.1500 | 0.0472 | 0.0036 | 6.1719 | 0.3675 | 0.1754 | 0.0132 |
| 0.2000 | 0.0442 | 0.0041 | 5.4273 | 0.3031 | 0.1671 | 0.0153 |
| 0.2500 | 0.0407 | 0.0045 | 3.9301 | 0.2158 | 0.1569 | 0.0173 |
| 0.3000 | 0.0374 | 0.0055 | 5.4277 | 0.2636 | 0.1475 | 0.0217 |
| 0.4000 | 0.0308 | 0.0070 | 3.6511 | 0.1687 | 0.1274 | 0.0291 |
| 0.5000 | 0.0275 | 0.0078 | 3.1222 | 0.1460 | 0.1169 | 0.0332 |
| 0.6000 | 0.0235 | 0.0066 | 2.6537 | 0.1700 | 0.1041 | 0.0293 |
| 0.7000 | 0.0221 | 0.0077 | 2.4308 | 0.1422 | 0.0994 | 0.0347 |
| 0.7500 | 0.0213 | 0.0086 | 2.4258 | 0.1330 | 0.0967 | 0.0388 |
| 0.8000 | 0.0204 | 0.0096 | 2.5155 | 0.1286 | 0.0935 | 0.0440 |
| 0.9000 | 0.0186 | 0.0084 | 2.1275 | 0.1360 | 0.0873 | 0.0395 |
| 1.0000 | 0.0170 | 0.0048 | 1.5640 | 0.1908 | 0.0817 | 0.0231 |
| 1.1000 | 0.0147 | 0.0115 | 1.1000 | 0.0653 | 0.0732 | 0.0570 |
| 1.2000 | 0.0141 | 0.0098 | 1.4000 | 0.1012 | 0.0709 | 0.0493 |
| 1.2500 | 0.0137 | 0.0113 | 1.2200 | 0.0788 | 0.0694 | 0.0572 |
| 1.3000 | 0.0136 | 0.0110 | 1.1000 | 0.0734 | 0.0690 | 0.0559 |
| 1.4000 | 0.0121 | 0.0096 | 1.2500 | 0.1078 | 0.0632 | 0.0501 |
| 1.5000 | 0.0118 | 0.0125 | 1.4962 | 0.1015 | 0.0620 | 0.0658 |
| 1.6000 | 0.0105 | 0.0091 | 0.9000 | 0.0946 | 0.0568 | 0.0491 |
| 1.7000 | 0.0097 | 0.0072 | 0.7500 | 0.1071 | 0.0536 | 0.0399 |
| 1.7500 | 0.0098 | 0.0079 | 0.9994 | 0.1298 | 0.0539 | 0.0433 |
| 1.8000 | 0.0091 | 0.0083 | 0.6000 | 0.0794 | 0.0511 | 0.0466 |

Continued on next page

Table 4.2 – continued from previous page

| $d$ | $T_c$ | $\rho_c$ | $P_c \cdot 10^{-5}$ | $Z_c$ | $T_c^{DHS}$ | $\rho_c^{DHS}$ |
|---|---|---|---|---|---|---|
| 1.9000 | 0.0084 | 0.0080 | 0.5800 | 0.0859 | 0.0481 | 0.0460 |
| 2.0000 | 0.0082 | 0.0089 | 0.8019 | 0.1097 | 0.0473 | 0.0512 |
| 2.1000 | 0.0075 | 0.0077 | 0.5800 | 0.1001 | 0.0442 | 0.0455 |
| 2.2000 | 0.0070 | 0.0070 | 0.4500 | 0.0925 | 0.0419 | 0.0417 |
| 2.3000 | 0.0068 | 0.0065 | 0.4000 | 0.0903 | 0.0410 | 0.0393 |
| 2.4000 | 0.0063 | 0.0062 | 0.4000 | 0.1023 | 0.0388 | 0.0382 |
| 2.5000 | 0.0059 | 0.0056 | 0.3800 | 0.1142 | 0.0369 | 0.0353 |
| 2.7500 | 0.0050 | 0.0052 | 0.2400 | 0.0929 | 0.0326 | 0.0337 |
| 3.0000 | 0.0041 | 0.0048 | 0.1159 | 0.0581 | 0.0282 | 0.0331 |
| 4.0000 | 0.0026 | 0.0018 | 0.0539 | 0.1125 | 0.0199 | 0.0142 |

Table 4.3.: Critical parameters for the CHD system produced by Ganzenmüller and Camp [17]

| $d$ | $\tau_c^i$ | $\tau_c^d$ | $\rho_c$ | Ref. |
|---|---|---|---|---|
| 0.10 | 0.001401(3) | 0.1401(3) | 0.0933(8) | [17] |
| 0.15 | 0.003024(4) | 0.1344(2) | 0.0958(8) | [17] |
| 0.20 | 0.005114(6) | 0.1279(1) | 0.0960(9) | [17] |
| 0.25 | 0.007585(5) | 0.12136(7) | 0.0885(9) | [17] |
| 0.50 | 0.02157(4) | 0.0863(2) | 0.0749(5) | [17] |
| 0.75 | 0.03612(4) | 0.06422(8) | 0.0655(1) | [17] |
| 1.00 | 0.04900(7) | 0.04900(7) | 0.0556(2) | [17] |

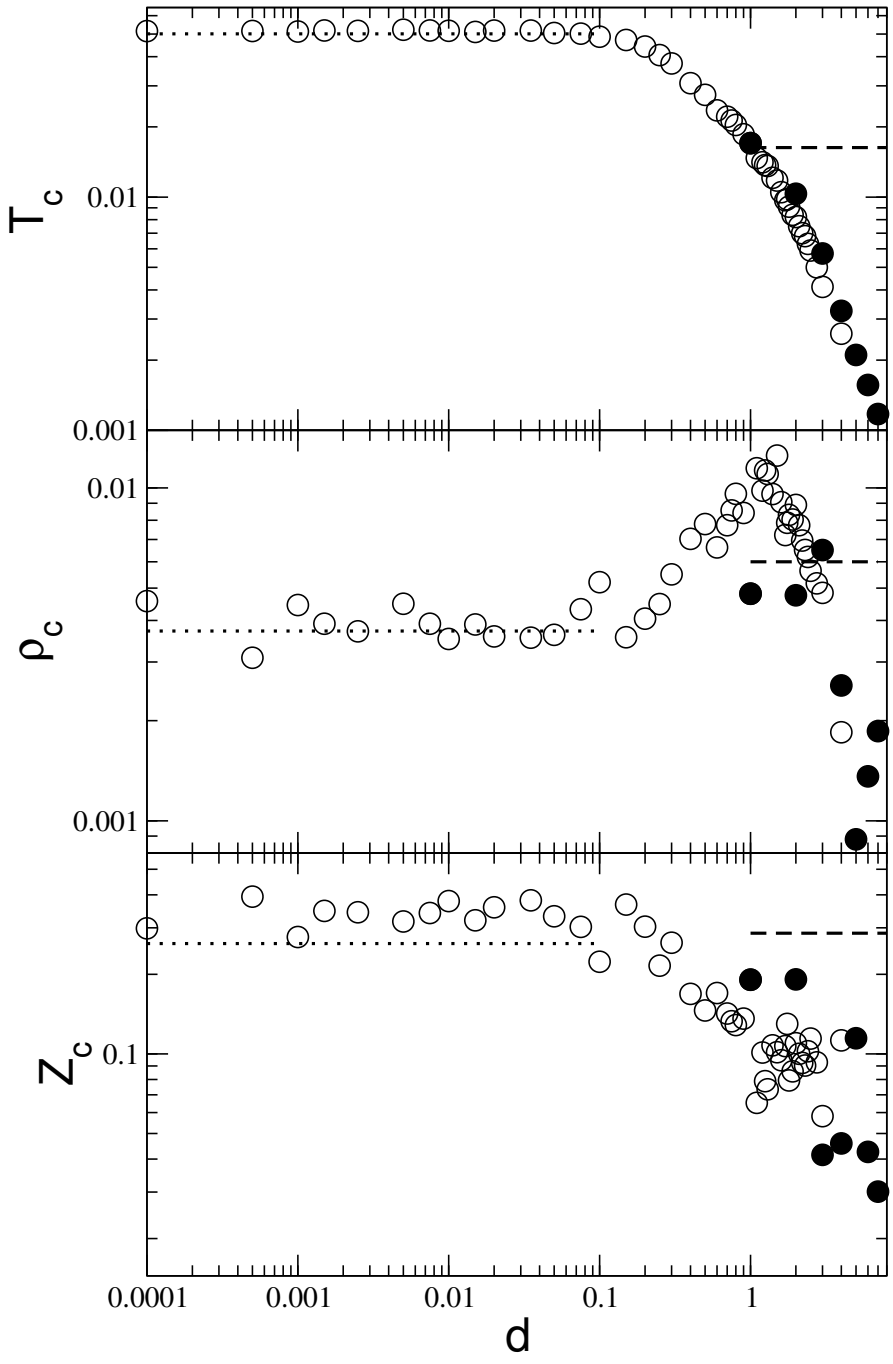


Figure 4.5.: Critical temperature, $T_c$ (top), critical density, $\rho_c$ (middle), and critical compressibility factor, $Z_c$ (bottom), for soft sphere systems vs. $d$. The simulation data is represented for CSDs and constant charge $q = 1$ via solid circles and fixed dipole moment $\mu^2 = 1$ using open circles. The horizontal lines represent $T_c$ for 4-DSS (dotted) and ions (dashed) in reduced densities.

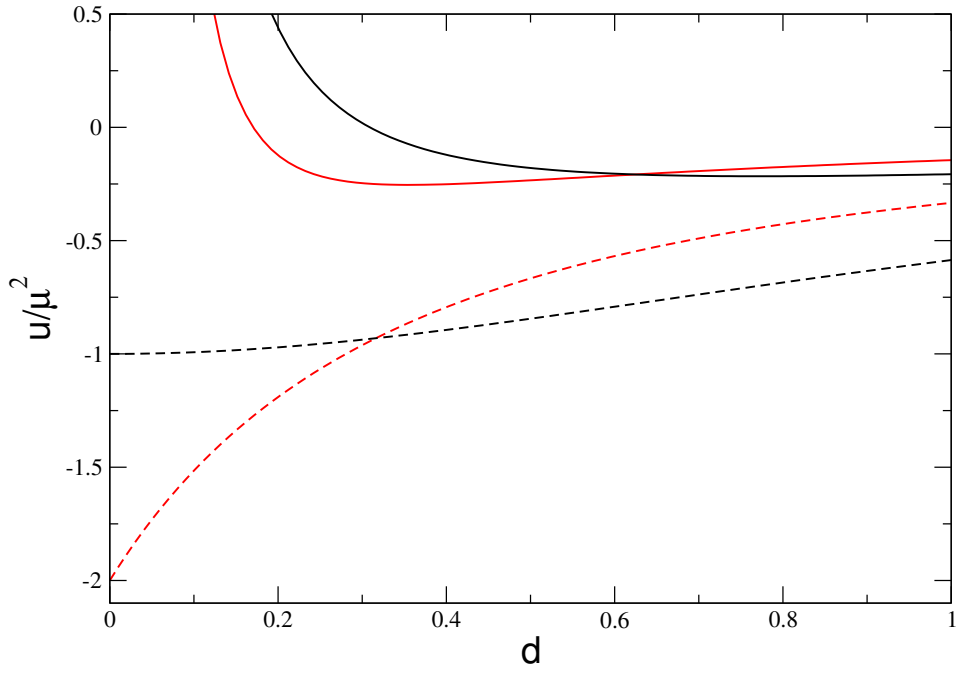


Figure 4.6.: The plot shows the cross-over energy $u/\mu^2$ for two dumbbells arranged side-by-side (black) or head to tail (red) vs. the dumbbell length $d$. We show the energy for the CSD model (continuous lines) and for the CSD model without soft sphere repulsion, i.e. two charges separated by the fixed distance $d$ (dashed lines). The head to tail formation is preferred for small $d$, i.e. the system prefers to build chains.

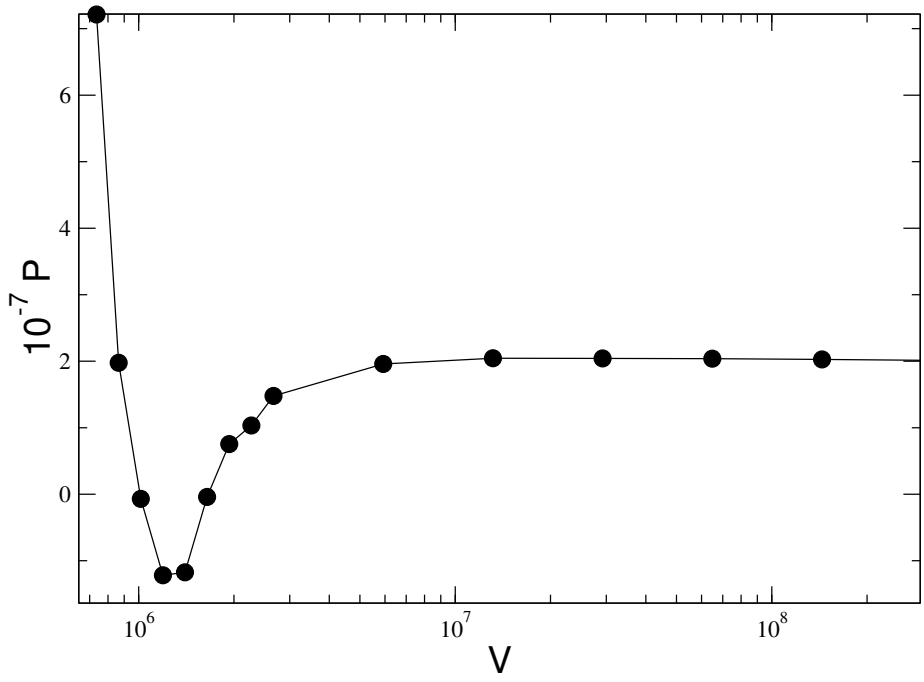


Figure 4.7.: In isotherms for dumbbells with $d = 7.0$ and $\mu^2 = 1$ still a van der Waals loop is visible, here shown for $T = 0.0025$ and $N = 1600$ particles (the drawn line just connects the dots and has no physical meaning). Nevertheless it was not possible to apply the Maxwell construction as only a too small regime of the phase coexistence area could be simulated.

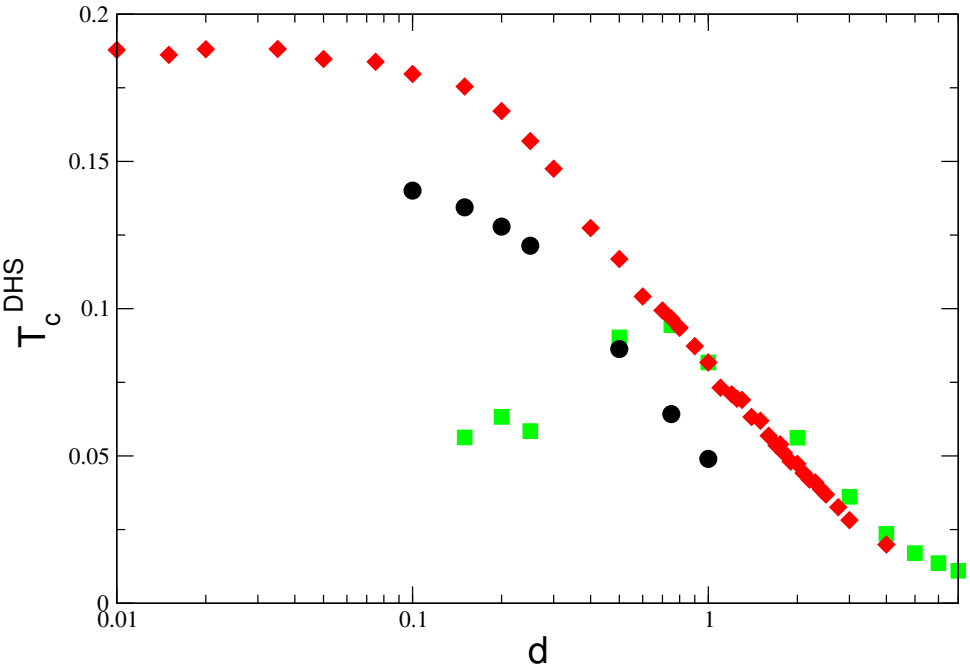


Figure 4.8.: The critical temperature $T_c^{DHS}$ as function of the dumbbell length $d$. The figure depicts the values of the CSDs with $\mu^2 = 1$ (red) and $q = 1$ (green) as well as the ones for the CHDs from Ganzenmüller *et al.* [17] (black) in the range of $0.01 \leq d \leq 7.0$.

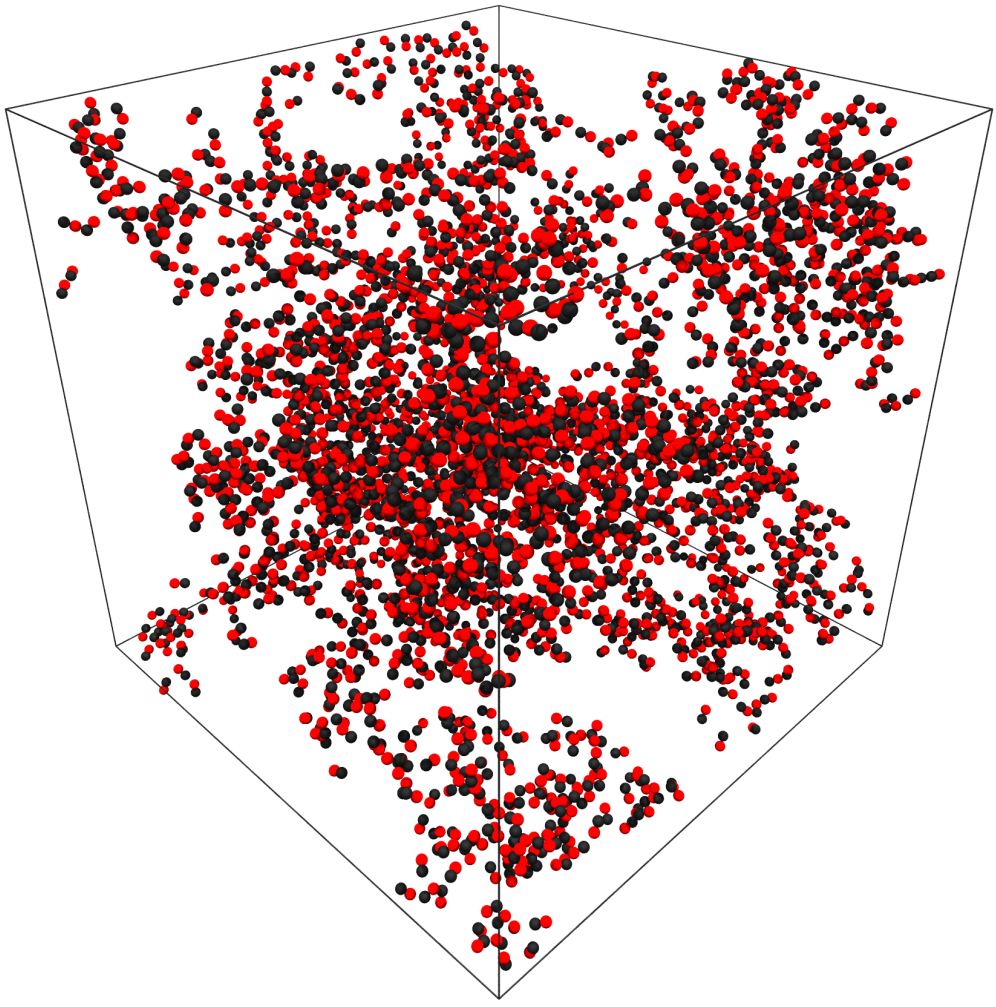

Figure 4.9.: Snapshot of the simulation for $d = 1.0$ and $\mu^2 = 1$ with $N = 2500$ particles just below the critical temperature at $T = 0.0155$ and at a density of $\rho = 0.0011$ close to $\rho_c$. There is no chain like or network type aggregation visible.

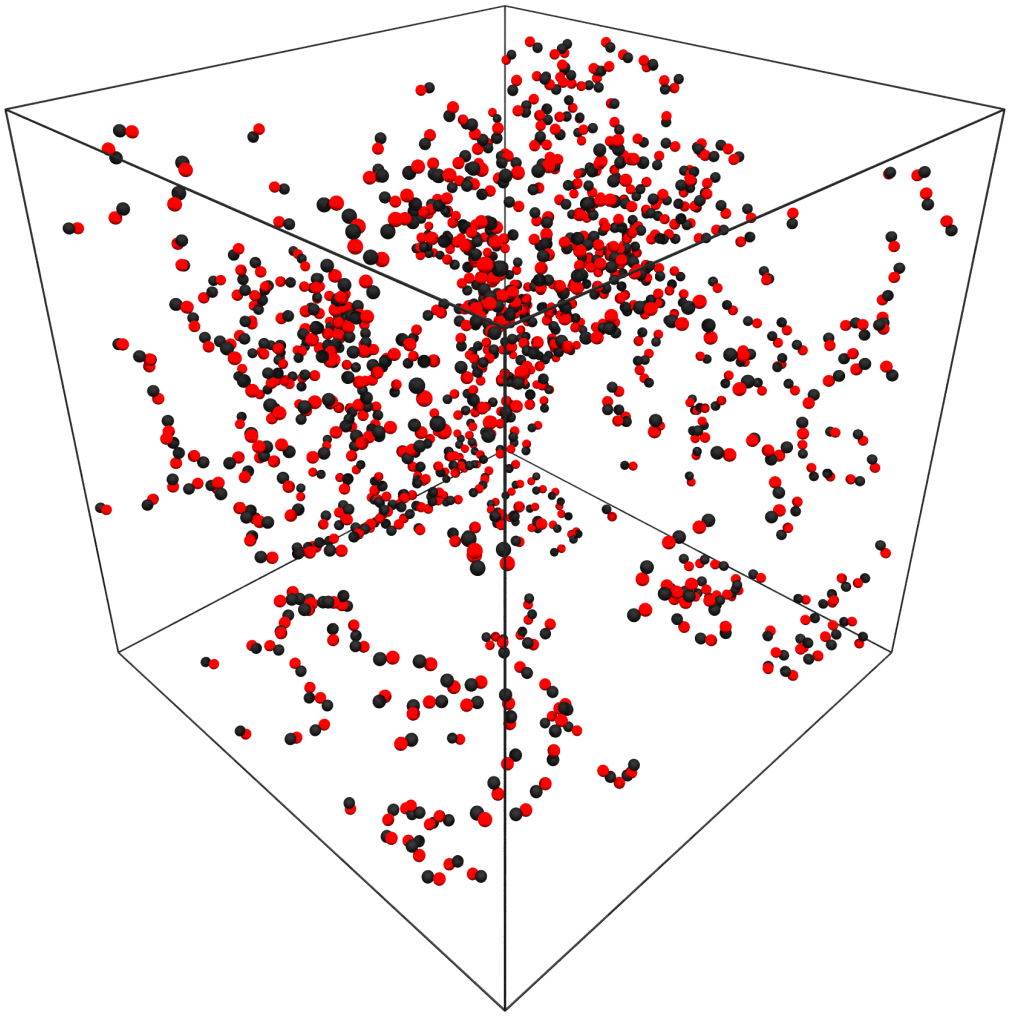

Figure 4.10.: Snapshot of the simulation for $d = 0.75$ and $\mu^2 = 1$ with $N = 800$ particles just below the critical temperature at $T = 0.0207$ and at a density of $\rho = 0.008$. A network like branching of the particles is visible.

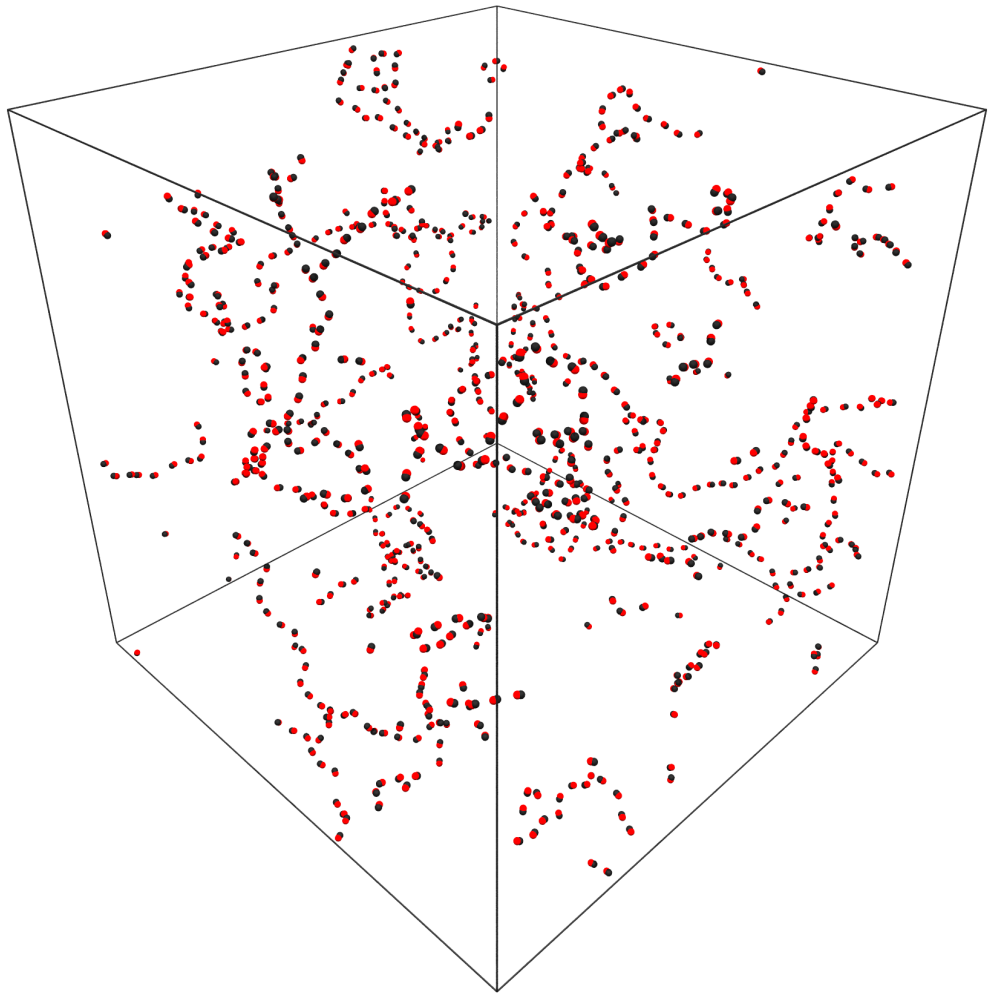

Figure 4.11.: Snapshot of the simulation for $d = 0.25$ and $\mu^2 = 1$ with $N = 800$ particles just below the critical temperature at $T = 0.04$ and at a density of $\rho = 0.0042$ close to $\rho_c$. The particles build chains, which are only rarely branched.

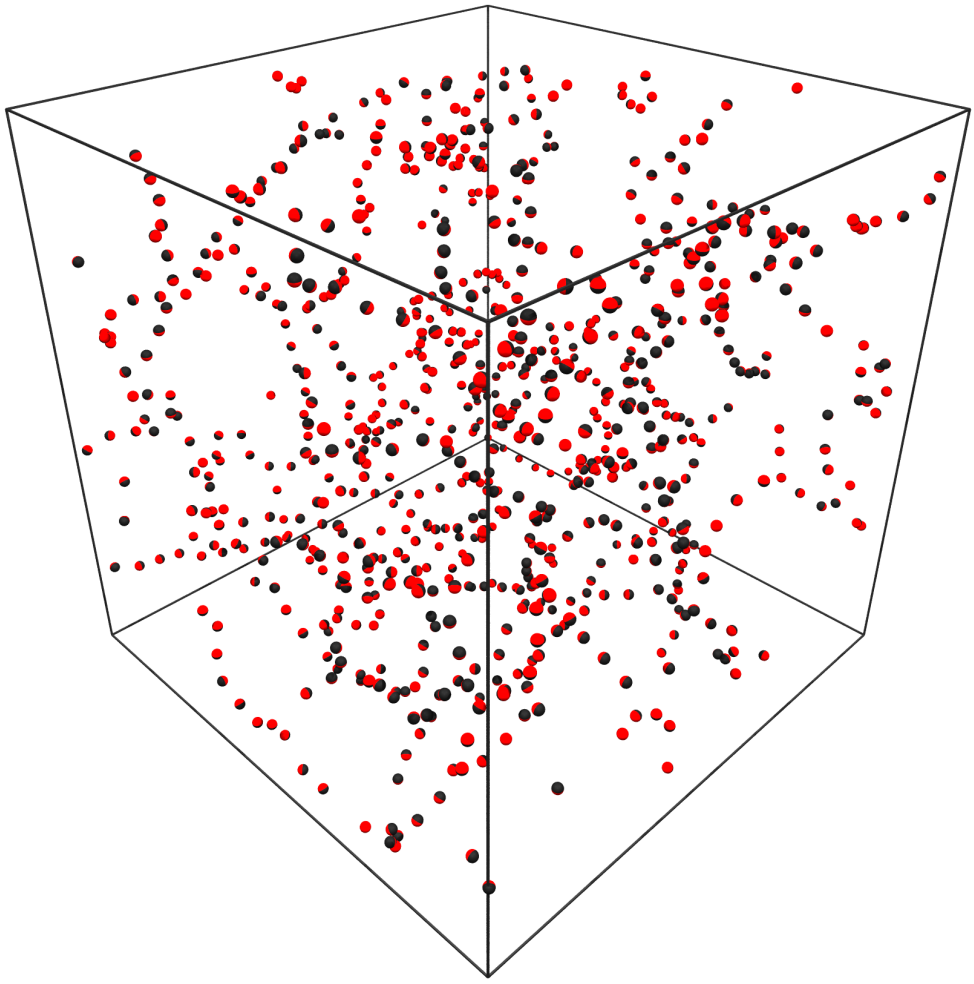

Figure 4.12.: Snapshot of the simulation for $d = 10^{-4}$ and $\mu^2 = 1$ with $N = 800$ particles just below the critical temperature at $T = 0.048$ and at a density of $\rho = 0.0194$ above $\rho_c$. A network like branching of the particles is visible.

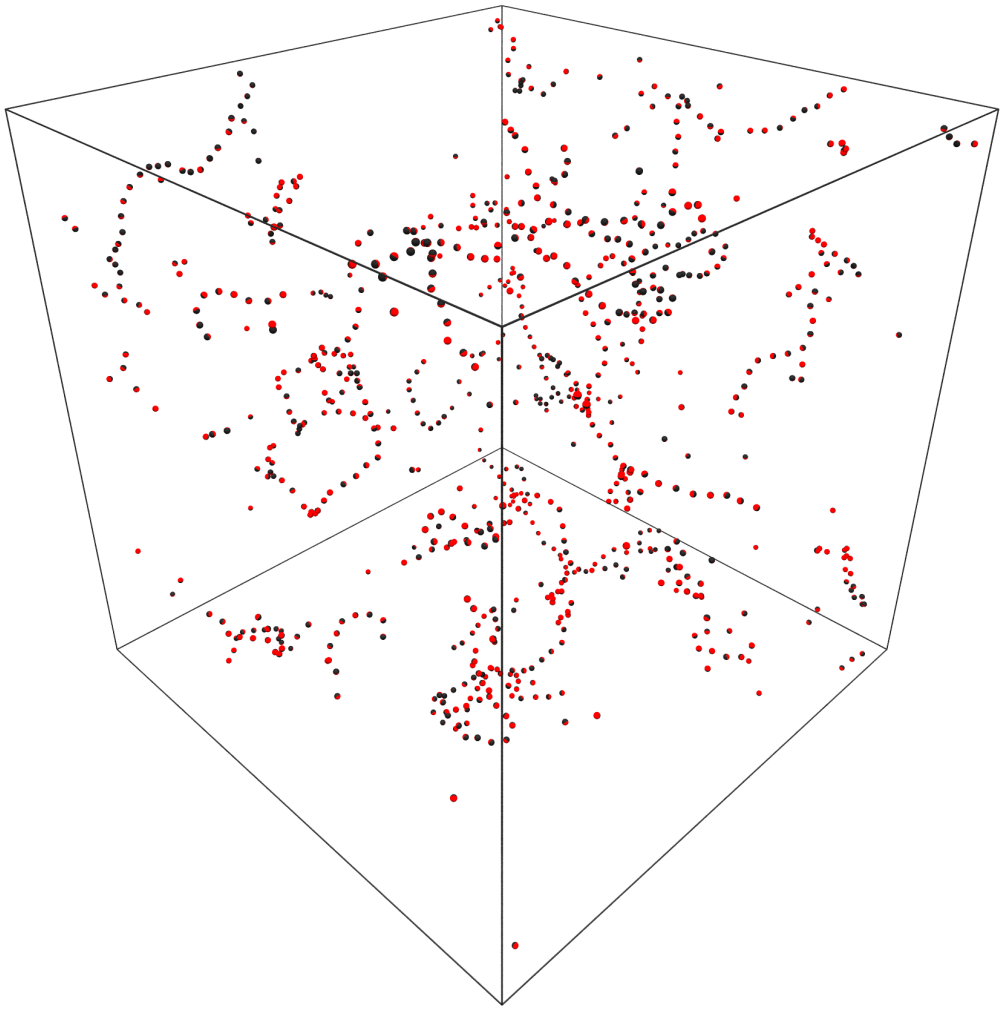

Figure 4.13.: Snapshot of the simulation of $d = 10^{-4}$ and $\mu^2 = 1$ with $N = 800$ particles just below the critical temperature at $T = 0.048$ and at a density of $\rho = 0.0030$ below $\rho_c$. The network which was visible above $\rho_c$ was replaced by chains. In addition even ring formation is visible.

### 4.2.1. Tlusty-Safran theory

With having obtained the critical parameters for a huge variety of dumbbells, we need to find an adequate theory which can explain our simulation results. The observation of chains and network like aggregates, as seen in the configuration snapshots, allows us to conclude that we do not have an ordinary g-l transition in our system. Instead another approach introduced by Tlusty and Safran in 2000 [27] could apply. In their theory they describe a defect-induced phase separation of a dilute gas with chains having two free ends and a dense liquid characterized by a branching network. The junctions as well as the free ends are considered as defects to a perfect network. To each type of defect, energetic costs are associated, $\varepsilon_1$ for the free ends and $\varepsilon_3$ for the threefold junctions. Independent of the defect type every defect contributes $-k_BT$ to the free energy. We can derive the free energy by applying the framework of self-consistent field approach to polymer systems [28] and get

$$f = -\rho_1 - \rho_3 + \frac{1}{2}\phi^2 \,. \tag{4.2.14}$$

Here the first two terms are densities for the free ends respective threefold junctions and the last term describes the excluded volume repulsion between chains proportional to the square of the monomer density $\phi$. The defect densities $\rho_1$ and $\rho_3$ can be calculated from the monomer density together with a Boltzmann factor, which accounts for the energetic costs of the defects, as

$$\rho_1 \sim \phi^{1/2} e^{-\varepsilon_1/T} \tag{4.2.15}$$

$$\rho_3 \sim \phi^{3/2} e^{-\varepsilon_3/T} \,. \tag{4.2.16}$$

This finally gives us for the free energy

$$f = -(2\phi)^{1/2} e^{-\varepsilon_1/T} - \frac{1}{3}(2\phi)^{3/2} e^{-\varepsilon_3/T} + \frac{1}{2}\phi^2 \,. \tag{4.2.17}$$

Further Tlusty and Safran discover the free ends as an additional repulsion and the junctions as attraction in the equation of state. So we get for the critical parameters of the Tlusty-Safran theory

$$T_c^{TS} = \frac{\varepsilon_1 - 3\varepsilon_3}{\ln[27/4]} \tag{4.2.18}$$

$$\ln \phi_c^{TS} = -\frac{\varepsilon_1 \ln[9/2] - \varepsilon_3 \ln[2]}{\varepsilon_1 - 3\varepsilon_3} \tag{4.2.19}$$

$$\ln P_c^{TS} = -\frac{\varepsilon_1 \ln[81/2] - \varepsilon_3 \ln[32]}{\varepsilon_1 - 3\varepsilon_3} \,. \tag{4.2.20}$$

To check if the Tlusty-Safran theory is a sound description of the phase transition in the CSD system, we need to determine $\varepsilon_1$ and $\varepsilon_3$ in dependence of $d$. Afterwards we can

calculate the critical parameters and compare them with the simulation results. Therefore we start with the pair potential (3.1.10) between two particles

$$u_{ij}^{CSD} = \sum_{\alpha,\beta=1}^{2} \left\{ 4\varepsilon \left( \frac{\sigma}{r_{i_\alpha j_\beta}} \right)^{12} + \frac{1}{4\pi\varepsilon_0} \frac{q_{i_\alpha} q_{j_\beta}}{r_{i_\alpha j_\beta}} \right\} , \tag{4.2.21}$$

which we consider to be aligned head to tail along a chain. Using the distance between two sites

$$r_{i_\alpha j_\beta} = |\vec{r}_{ij} - \frac{d}{2} \left[ (-1)^\alpha \, \vec{n}_i - (-1)^\beta \, \vec{n}_j \right]| \, , \tag{4.2.22}$$

we can write for the pair potential of two particles in a chain

$$u_{ij}^1 = 4\varepsilon \left[ \left( 2\frac{\sigma}{r_{ij}} \right)^{12} + \left( \frac{\sigma}{r_{ij} - d} \right)^{12} + \left( \frac{\sigma}{r_{ij} + d} \right)^{12} \right] \tag{4.2.23}$$

$$+ \frac{q^2}{4\pi\varepsilon_0} \left[ \frac{2}{r_{ij}} - \frac{1}{r_{ij} - d} - \frac{1}{r_{ij} - d} \right] . \tag{4.2.24}$$

We need to determine the energy minimum of two particles in a chain. Hence we calculate the distance $r_{min}$ via

$$\frac{\partial u_{ij}^1}{\partial r_{ij}} = 0 \tag{4.2.25}$$

for the corresponding dumbbell lengths $d$. With this we compute

$$u_{min}^1 = u_{ij}^1(r_{min}) \, . \tag{4.2.26}$$

For a chain with $n+1$ particles, i.e. $n$ bonds, we can write the approximate potential energy as

$$u_n^1 = n u_{min}^1 \, . \tag{4.2.27}$$

To calculate the energy $\varepsilon_1$ of free ends, we split the chain into two parts, which reduces the number of bonds by 1 and creates two additional free ends with the energy

$$2\varepsilon_1 = (n-1)u_{min}^1 - n u_{min}^1 = -u_{min}^1 \, . \tag{4.2.28}$$

We can follow a similar approach to determine the energy $\varepsilon_3$ of the threefold junctions. We consider that the three particles of the junctions form an equilateral triangle whose angles are continued by a chain. The orientation of the particles is for each along the bisecting line and therefore are at an angle of 30° respective 150° to the sites of the triangle. For this geometry we can note down the potential energy of the junction as

$$u_{ijk}^3 = 12\varepsilon \left[ \left( \frac{\sigma}{r_{ijk} - \frac{d}{2}\sqrt{3}} \right)^{12} + \left( \frac{\sigma}{r_{ijk} \frac{d}{2}\sqrt{3}} \right)^{12} + 2 \left( \frac{\sigma}{\sqrt{r_{ijk}^2 + \frac{d^2}{4}}} \right)^{12} \right]$$

$$+ \frac{q^2}{4\pi\varepsilon_0} \left[ \frac{1}{r_{ijk} - \frac{d}{2}\sqrt{3}} - \frac{1}{r_{ijk} + \frac{d}{2}\sqrt{3}} - \frac{2}{\sqrt{r_{ijk}^2 + \frac{d^2}{4}}} \right] . \tag{4.2.29}$$

Here $r_{ijk}$ is the distance of the center of mass between the particles which is obviously the same for all the particles in the triangle. As earlier we get $r_{min}$ from

$$\frac{\partial u^3_{ijk}}{\partial r_{ijk}} = 0 \tag{4.2.30}$$

to finally calculate $u^3_{min}$. To calculate $\varepsilon_3$ we consider again a large chain with $n$ bonds, and split it up twice, to re-join the three parts afterwards, in order to form the threefold junction. This yields

$$\varepsilon_3 = (n-2)u^1_{min} - nu^1_{min} + u^3_{min} = u^3_{min} - 2u^1_{min}\,. \tag{4.2.31}$$

The results for the values of $\varepsilon_1$ and $\varepsilon_3$, calculated via the potential minimum approach in equation (4.2.28) and (4.2.31), are shown in figure 4.14 as red lines. The plot also shows the results obtained from the simulation data using $T_c$ and $P_c$ as symbols. If we use $\rho_c$ instead of $P_c$ the results for $d > 1.0$ stay almost the same. But for the smaller dumbbells this increases the result quantitatively by 10 to 20% without changing it qualitatively. Comparing the theoretical derived data with the results from the simulation, shows that the general trend of the data seems to be similar, i.e. for smaller dumbbell lengths the values for $\varepsilon_1$ and $\varepsilon_3$ decrease. For $\varepsilon_1$ also the values are similar in the limit $d \to 0$, but there is a strong deviation between the data sets for $\varepsilon_3$. Here the value at the limit $d \to 0$ deviates almost by a factor 9. This deviation is most likely caused by the difficulty to find a good approximation for the junctions and their defect energies. Without having a good estimate for $\varepsilon_3$, the Tlusty-Safran theory cannot provide a sound description of the critical parameters. Another way to check, if the Tlusty-Safran theory is a valid description of our system, is to analyze the junction density $\rho_3$. We can calculate it from the critical parameters according to (4.2.16) as

$$\rho_3 \sim \rho_c^{3/2} e^{-\varepsilon_3/T_c}\,, \tag{4.2.32}$$

and do a comparison with the data from the simulation configurations close to the critical point. For the anlysis of the configurations we define that a particle forms a junction, as soon as it has more than two neighbours in a distance $r_{i_\alpha j_\beta} \leq 2$. For this criteria we ideally chose a distance in the first minimum of the pair correlation function (see figure 5.5 for CSD). Values, which deviate from our selected distance $r_{i_\alpha j_\beta} \leq 2$, will only slightly change the result quantitatively. The comparison of the junction density is shown in figure 4.15, where in the top panel the concentration of junctions is calculated from the critical parameters $\rho_c$ and $T_c$ using equation (4.2.32). We see that the concentration increases for decreasing dumbbell length $d$ and finally forms a plateau. This is in contradiction to the data we get from the simulated configurations shown in the bottom of figure 4.15, where we see a large increase of the junction density for long dumbbells.
Overall it is not possible to bring the simulation results in accordance with the predicted values of the Tlusty-Safran theory. So we have to conclude that the Tlusty-Safran theory does not provide a good phase transition description of the CSD model. The underlying partial free energy, which models a competition of free ends vs. junctions, oversimplifies

the observed phase transition. Along with the sole description of a dipolar liquid in terms of free chain ends and junctions another weak point is the neglect of higher correlations in the Tlusty-Safran theory. So we have to look for another approach to explain the phase transition of CSDs.

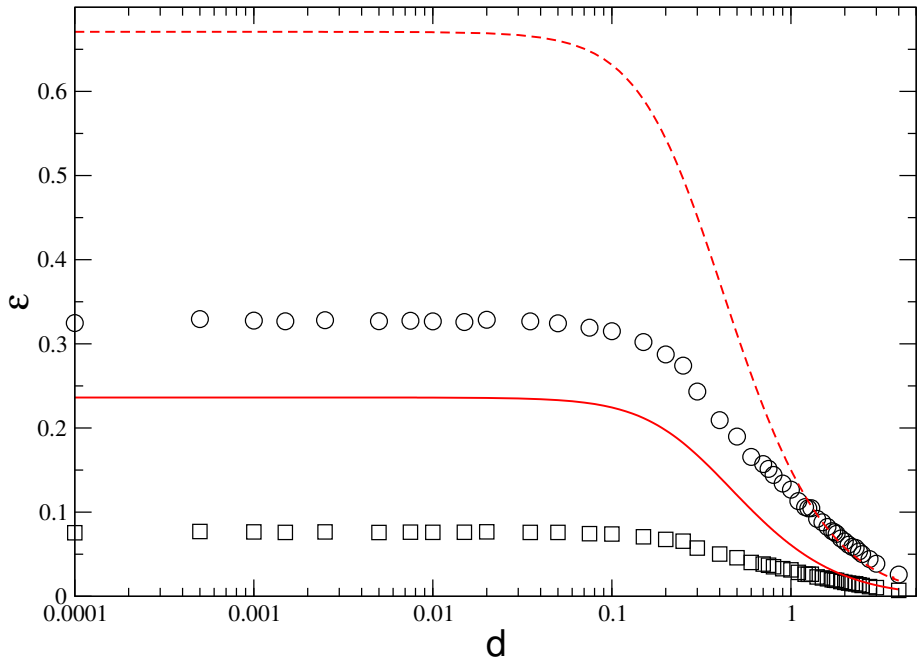


Figure 4.14.: The symbols represent the defect energies $\varepsilon_1$ (circle) and $\varepsilon_3$ (squares) calculated from the Tlusty-Safran model from our simulation results for CSD with constant dipole moment $\mu^2 = 1$ using $T_c$ and $P_c$ vs. the dumbbell length $d$. The red lines show the defect energies $\varepsilon_1$ (continuous line) and $\varepsilon_3$ (dashed line) as calculated via the potential minimum approach in equation (4.2.28) and (4.2.31).

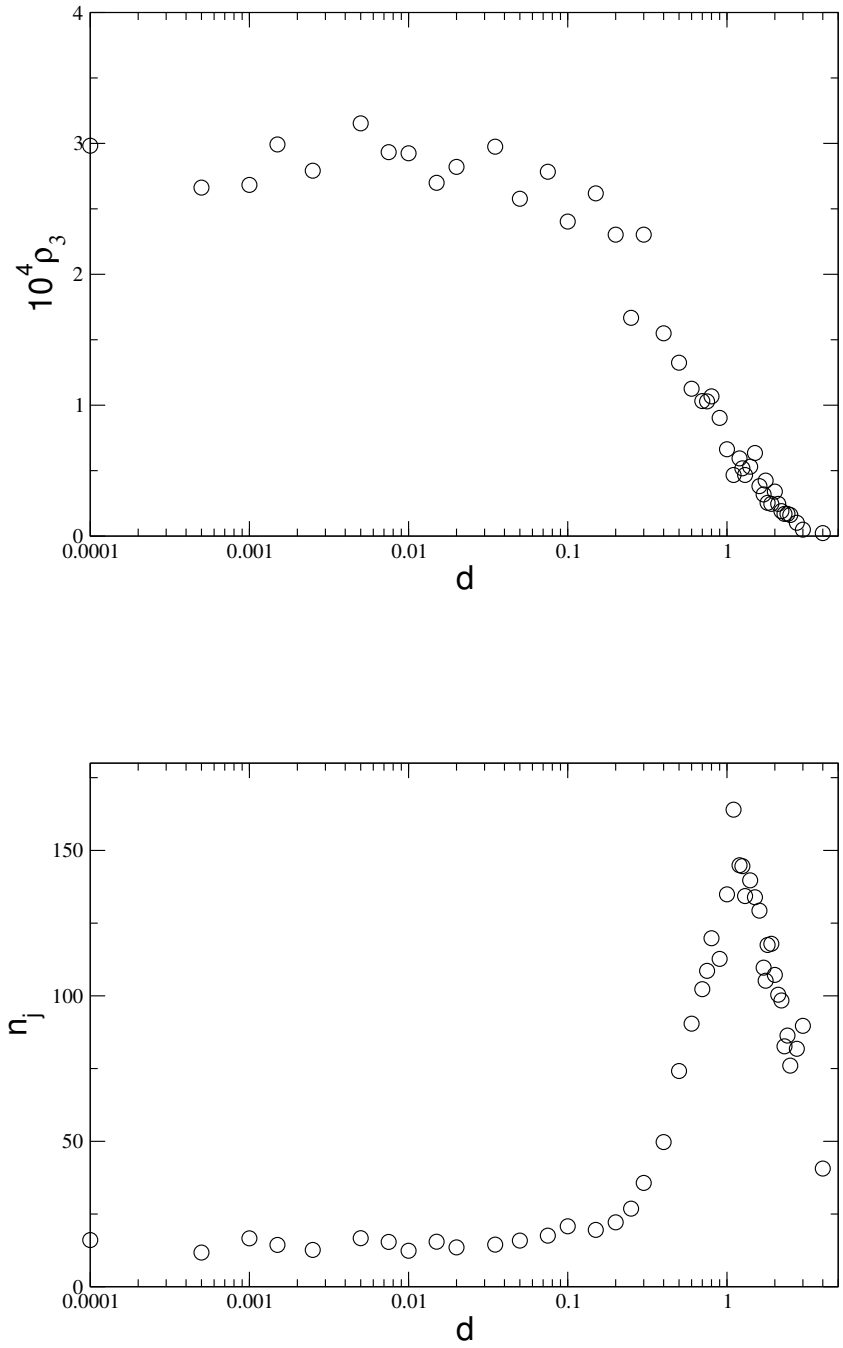


Figure 4.15.: Top: The concentration of junctions $\rho_3$ calculated via the critical parameters using the equation (4.2.32) vs. $d$. Bottom: Average number of junctions per configuration $n_j$ vs. $d$ from simulations done at $T \approx T_c$ and $\rho \approx \rho_c$.

### 4.2.2. Flory lattice theory

As we can see in the simulation snapshot figures 4.10 - 4.13 the idea of describing the g-l phase coexistence in a way, where the effect of reversible formation of chains or networks contributes to the phase transition may be a good start for a further attempt. As this kind of aggregation is very likely for dipolar fluids [29], and similar to common polymer systems in a solute, we can start with Flory's equation of state [30]

$$\frac{bP}{T} = -\left(1 - \frac{1}{n}\right)\phi - \ln\left[1-\phi\right] - \frac{q\varepsilon_0}{2T}\phi^2 \,. \tag{4.2.33}$$

This gives a theoretical description how chain formation may impact the critical behavior of the CSD model. In the equation of state $n$ represents the segments of linear chains, $q$ is the coordination number of the lattice and $\phi = b\rho$ expresses the chain volume fraction with the monomer or segment volume $b$. The above equation of state can be derived using a Flory-Huggins mean-field lattice model. Among several other applications, mainly in polymer physics, it is also commonly used to describe dipolar fluids [5, 31–33]. In this work we will omit a detailed derivation of the Flory-Huggins theory and just mention the results we need for the comparison of our simulation data with the theory. For a more detailed elaboration one can read [19, 34].
Using the equation of state (4.2.33), we can obtain the resulting critical parameters as

$$\rho_c = \frac{1}{b}\frac{1}{1+\sqrt{n}} \tag{4.2.34}$$

$$T_c = T_c^{\infty}\frac{n}{(1+\sqrt{n})^2} \,. \tag{4.2.35}$$

With the Boyle temperature $T_{Boyle}$ for monomers, i.e. $n = 1$, we can write $T_c^{\infty} = T_{Boyle} = -q\varepsilon_0$. For the monomer case the critical parameter $\rho_c$ and $T_c$ are very similar to those we obtained earlier in (4.2.12) and (4.2.11) via the van der Waals equation. This is no surprise as the consideration of an ideal gas, as done by van der Waals, also only takes monomers into account. Interesting is the behavior of the critical density, which vanishes for large chains, $n \to \infty$ due to $\rho_c \sim n^{-1/2}$, whereas the critical temperature reaches the constant value $T_c^{\infty}$. Corrections to the disappearance of the critical density for large chains are discussed for instance in ( [35, 36]).
As we do not deal with a real polymer, the chain formation in our system is a dynamic process. The dumbbells aggregate reversibly into linear chains and therefore our chain length $n$ varies. Thus we find multiple chains of different length $n$ in a single system configuration. This fact is not considered in the above equation of state (4.2.33). But luckily it still can be used, if we identify $n$ as the average chain length in terms of monomer numbers [33]. The junctions we observe in our system configuration will be ignored for the moment. In the low concentration limit, i.e. chain-chain interaction is ignored, the average chain length is given by

$$n = \frac{1}{2} + \frac{1}{2}\sqrt{1 + 4(q-1)\phi e^{-\varepsilon_i}} \,, \tag{4.2.36}$$

where the quantity $\varepsilon_i$ is an in-chain contact free energy characterizing the chain growth together with the concentration $\phi$. This formula is well known from the theory of micellar systems (see for instance Ref. [37]). By replacing $n$ in equation (4.2.33) with (4.2.36) we get for the modified critical parameters

$$\rho_c = \frac{1}{b}\left(1+\sqrt{\frac{m^3}{K}}\right)^{-1} \tag{4.2.37}$$

$$T_c = -\frac{1}{2}q\varepsilon_0\left(\frac{n}{m}+(K-n(n-1))\sqrt{\frac{1}{Km^3}}\right)^{-1}, \tag{4.2.38}$$

where $m = 2n-1$ and $K = 6n(n-1)+1$. These expressions are far more complex than the earlier ones for constant $n$. But considering large $n$ we see that the limiting $n$-dependence retains, i.e.

$$\rho_c \approx \frac{1}{b}\frac{\sqrt{3}}{2}\frac{1}{n_c^{1/2}} \tag{4.2.39}$$

$$T_c \approx -q\varepsilon_0 \tag{4.2.40}$$

$$P_c \approx -\frac{q\varepsilon_0}{b}\frac{5\sqrt{3}}{16}\frac{1}{n_c^{3/2}}, \tag{4.2.41}$$

with $n_c = n(\phi_c, \varepsilon_i(T_c))$. As we can see in figure 4.6, the chain formation becomes more and more favorable, when $d$ approaches zero. Thus we can expect the critical density to drop for $d \to 0$ respectively to vanish in case of unlimited chain growth. The critical temperature is controlled by the *a priori* unknown parameter $\varepsilon_0$ which possibly depends on $d$. As both $\rho_c$ as well as $T_c$ depend on parameters like $b$ or $\varepsilon_0$, which we do not know exactly, it is hard to calculate predictions for the critical parameters. Nevertheless it is still possible to calculate the critical compressibility factor, where all the adjustable parameters vanish as

$$P_c/(\rho_c T_c) = \frac{5}{8}n_c^{-1} \tag{4.2.42}$$

$$\sim n_c^{-1}. \tag{4.2.43}$$

At the bottom of figure 4.5 we find the critical compressibility factor plotted versus $d$. It shows an increase for decreasing $d$ until $d > 0.1$ from there $P_c/(\rho_c T_c)$ remains essentially constant. This is not in total contradiction to the expected behavior if decreased $d$ induces progressively longer average chain lengths. But it means that the aggregation at small $d$ is not as strong as one would expect and limited to rather small aggregation numbers. This fact is also supported by analyzing the number average size $n$ of the reversible aggregates from the simulation data as function of $d$, shown in figure 4.16. Here we have defined $n$ via a distance criterion, where two dumbbells are considered to belong to the same cluster or aggregate if the separation $r_{i_\alpha j_\beta}$ between any of their charge site to any of the charge sites on another dumbbell is less than a certain distance. As shown in figure 4.16, we have used

multiple distances in a range between 1.8 to 2.2 and each one produces to some extend a different $n$ (for the same $d$), but the basic dependence of $n$ on $d$ remains unaltered. We observe that the aggregates become smaller as $d$ is reduced, until a plateau value of $n \approx 5$ in the range $10^{-4} < d < 10^{-1}$ is reached.

Another interesting aspect is the mean aggregation size $s$, which has been studied based

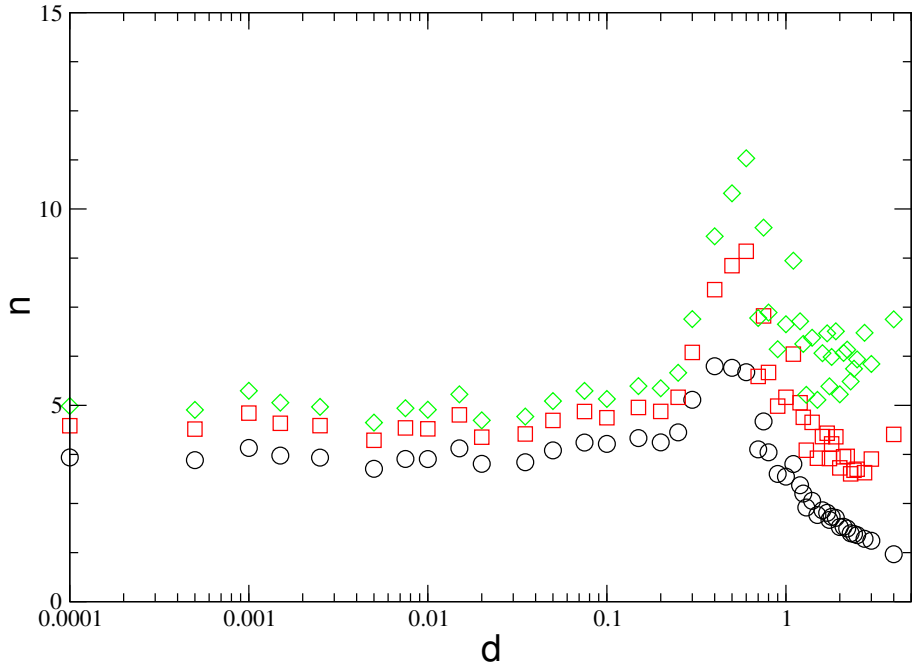


Figure 4.16.: Average aggregation number $n$ for CSDs vs. $d$ for different distance criterias $r_{i_\alpha j_\beta} < 1.8$ (circles), $r_{i_\alpha j_\beta} < 2.0$ (squares) and $r_{i_\alpha j_\beta} < 2.2$ (diamonds). The simulations were done close to the critical temperature $T \approx T_c$ and with constant density $\rho = 0.006$.

on an extended Flory-Huggins theory by [38]. It has also been analyzed in simulation studies, where a continuous growth with increasing concentration of the solute [37] is predicted. Therefore we want to have a closer look at the mean aggregate size of the CSD model. We start by exploiting the effect of reversible aggregation to the chemical potential at equilibrium, where we can write

$$\mu_s = s\mu_1 \,. \tag{4.2.44}$$

Here $\mu_s$ denotes the chemical potential of a s-aggregate or s-mer containing $s$ molecules with chemical potential $\mu_1$. In the low concentration limit of reversibly assembling molec-

ular systems we can also write for the chemical potential

$$\mu_s = \bar{\mu}_s + k_B T \ln x_s \,. \tag{4.2.45}$$

Here $x_s$ describes the mole fraction of s-mers and the quantity $\bar{\mu}_s$ sums up the remaining dependencies of the chemical potential. Following [37] we can further specify $x_s$ as

$$x_s = (x_1 \exp^{\alpha})^s \tag{4.2.46}$$

with the mole fraction of free monomers $x_1$. The exponent $\alpha$ is given as

$$\alpha = \frac{1}{k_B T}\left(\bar{\mu}_1 - \frac{\bar{\mu}_s}{s}\right) \tag{4.2.47}$$

$$= \frac{1}{k_B T}\left(\bar{\mu}_1 - \bar{\mu}_{bulk}\right) - \delta s^{-1/D} \tag{4.2.48}$$

using the space dimension $D = 1$ for chainlike aggregates and the surface free enthalpy $T\delta$. Plotting now the aggregate size distribution $h(s)$ fetched from the simulation data in a logarithmic plot vs. $s$, as done in figure 4.17, we expect

$$s \sim h(s) \,. \tag{4.2.49}$$

For small dumbbells, as shown in the bottom of figure 4.17 for $d = 0.0001$, the simulation shows a linear behavior over a wide $s$ range in accordance with the above aggregation model. As we can see in the top panel of figure 4.17 for $d = 1$, this is not true anymore for larger CSDs, where the aggregate size distribution does not behave linear anymore.
In summary the above theory, which explains the shift of the critical parameters rather well for the ST model [5, 33] and another dipolar fluid [32], where reversible aggregation of long chains occurs, does not come to bear in the present case because $n$ remains rather small. For the CSD model we observe a broad aggregate size distribution, but the average size is quite small with $n \approx 5$ for dumbbells of length $d < 0.1$. The constant behavior of the aggregate size for $d < 0.1$ can be understood by equation (4.2.36), which explains the chain growth by concentration and the in-chain contact free energy $\varepsilon_i$. For the CSD model the charges retreat into the center of the soft-repulsive core as $d$ decreases. Thus if $d \ll 1$ there is no obvious reason why $\varepsilon_i$ should increase, and therefore the average size, $n$, approaches a constant at constant particle density and constant magnitude of the dipole moment.

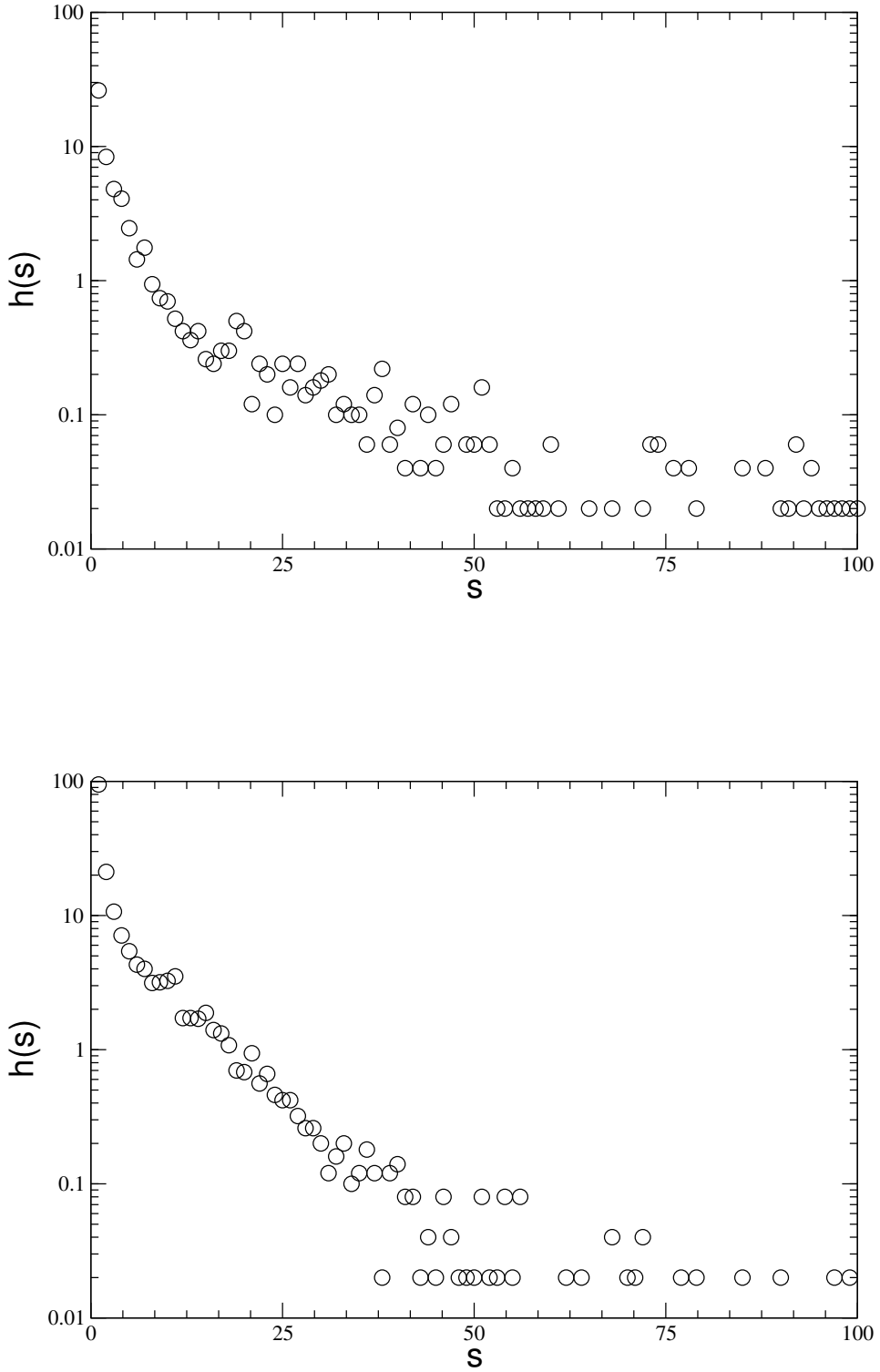


Figure 4.17.: Aggregation size distribution for CSD, frequency $h(s)$ vs $s$, at $\rho = 0.006$ for $T$ close to the respective $T_c$. Top: $d = 1$; bottom $d = 0.0001$.

### 4.2.3. Modified van der Waals mean field theory

Finally we want to take a third attempt to explain the simulation data, by constructing a mean field theory, which combines the Onsager cavity theory [39] of dipolar fluids with notions from polymer theory. We consider a modified van der Waals free energy $f = \Delta F/(NT)$ given by

$$f = \ln \frac{b\rho}{1-b\rho} - \frac{4\pi}{3}\frac{\epsilon-1}{2\epsilon+1}\frac{\mu^2}{bT}\,. \tag{4.2.50}$$

The first term in equation (4.2.50) is the usual van der Waals repulsion. The second term is the free energy of immersion of a point dipole $\mu$ in a spherical cavity with volume $b$ in a medium with dielectric constant $\epsilon$ [39]. Using the following equation the dielectric constant can be written as

$$\frac{1}{4\pi}\frac{(\epsilon-1)(2\epsilon+1)}{\epsilon} = \frac{\rho\mu^2}{T}\,. \tag{4.2.51}$$

Because we observe the critical point in the simulation at low densities, we can expand $\epsilon$ in terms of $\rho$. Keeping only the first-order terms allows us to simplify the critical parameters as follows

$$T_c \approx \frac{8\sqrt{2}\pi}{27}\frac{\mu^2}{b} \tag{4.2.52}$$

$$\rho_c \approx \frac{1}{3b} \tag{4.2.53}$$

$$P_c \approx \frac{\sqrt{2}\pi}{27}\frac{\mu^2}{b^2}\,. \tag{4.2.54}$$

From the critical parameters we can calculate the critical compressibility factor as

$$P_c/(\rho_c T_c) \approx 3/8 \tag{4.2.55}$$

which is identical to the ordinary van der Waals criticality.
Now we want to have a closer look at the parameter $b$. Without consideration of any aggregation we can estimate the value for $b$ via the second virial coefficient given by

$$B_2(T) = b - \frac{16\pi^2\mu^4}{27bT} \tag{4.2.56}$$

which ends up for $\mu = 0$ in $B_2 = b$. Focusing now on small dumbbells where $d < 0.1$, we can compute the second virial coefficient $B_2(T)$ for the $r^{-12}$-repulsive part of the

dumbbell-dumbbell interaction by solving the well known integral for radial symmetric pair-potentials

$$B_2(T) = -2\pi \int_0^\infty r^2 \left(e^{-u/T} - 1\right) \mathrm{d}r \,. \tag{4.2.57}$$

As each dumbbell has two interaction sites, we get in total a fourfold soft sphere repulsion and therefore have to use

$$u = \frac{16}{r^{12}} \tag{4.2.58}$$

to calculate (4.2.57). At the critical temperature $T_c = 0.05$, obtained from the simulation data, we get for the second virial coefficient

$$B_2(T = 0.05) \approx 11 \,. \tag{4.2.59}$$

Using this value for $b$ together with $\mu = 1$, we can calculate the critical parameters via the formulas given above as

$$\rho_c \approx 0.03 \tag{4.2.60}$$

$$T_c \approx 0.12 \tag{4.2.61}$$

$$P_c \approx 1.4 \cdot 10^{-3} \,, \tag{4.2.62}$$

which is not in-line with the simulation results. As of now we treated the particles as monomers and did not take into account the earlier observation of linear aggregates or s-mers. So by considering the linear aggregates in our expression for $b$, we can greatly improve the comparison. In the case of (long) cylinders of diameter $D$ and length $L$, we can expect

$$b = b_1 n^2 \tag{4.2.63}$$

because of $B_2 \propto DL^2$. Again we can set $b_1 = 11$ from the monomer calculation above. We also have to take into account that the density $\rho_c$, which we can calculate from our theory, is the critical aggregate number density $\rho_c^{agg}$ and not the critical monomer density $\rho_c^{mon}$, we can calculate from the simulation results. So using the equations (4.2.53) and (4.2.63) we need to introduce the conversion

$$\rho_c^{mon} = n\rho_c^{agg} = \frac{1}{3b_1 n} \tag{4.2.64}$$

to link the two different kinds of densities. The value for $n$ in this equation has to be obtained from the simulation data. In figure 4.18 we see the average aggregation number in the case that monomers are included in the calculation of $n$ and in the case that monomers are excluded. In the following we take $n \approx 6$ which corresponds to the case of excluded monomers. This makes equation (4.2.64) only an approximation, as it now underestimates the critical density. Going ahead with the value of $n \approx 6$ and $b_1 = 11$ we get for the critical density

$$\rho_c \approx 0.005 \,. \tag{4.2.65}$$

We have to apply the same mapping between the monomer and aggregate values to the

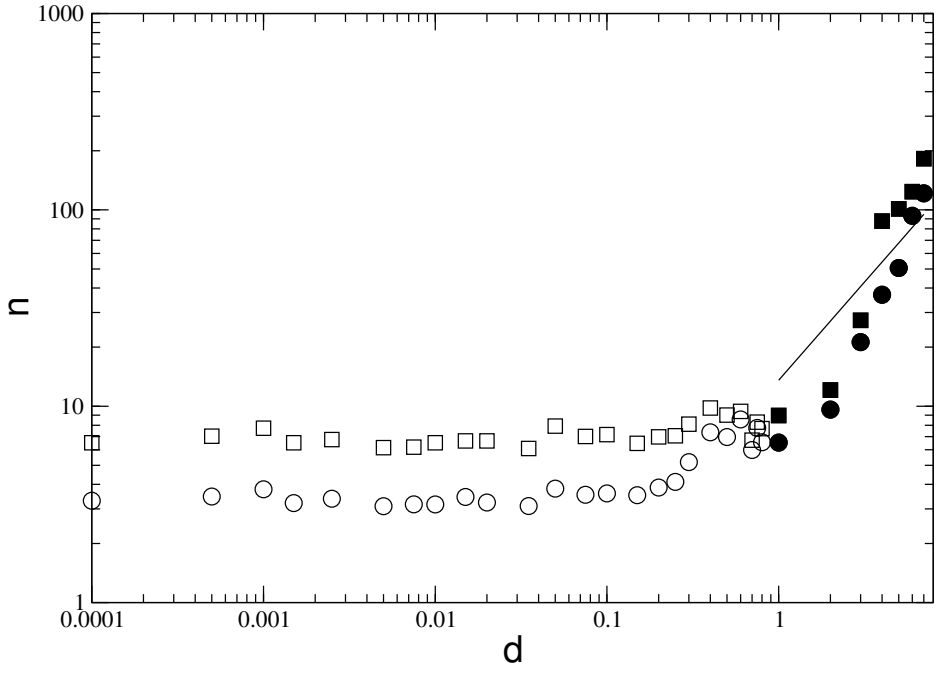


Figure 4.18.: Average aggregation number, $n$ vs. $d$ for constant $\rho = 0.004$ and $T \approx T_c$. Circles: Monomers are included in the calculation of $n$; squares: monomers are excluded. The open circles represent the results for constant dipole moment $\mu^2 = 1$ and the open symbols stand for constant charge $q = 1$. The straight line corresponds to $n \propto d$.

critical temperature. Inserting (4.2.63) into (4.2.53) and replacing the monomer dipole moment $\mu$ by the dipole moment of the $n$-mer $\mu_n$, the aggregate theory based critical temperature becomes

$$T_c = \frac{8\sqrt{2}\pi}{27} \frac{\mu_n^2}{b_1 n^2} \,. \tag{4.2.66}$$

To calculate the temperature we need a way to determine the total dipole moment $\mu_n^2$ of the $n$-mer. We can consider the CSD chains as freely-rotating chains of dipole vectors and adopt the well-known expression for the calculation of the characteristic ratio of polymer

chains as discussed in [40] and write for the dipole moment

$$\mu_n^2 = \sum_{i,j=1}^{n} \langle \vec{\mu}_i \vec{\mu}_j \rangle \tag{4.2.67}$$

$$= n\mu^2 \left\{ (\mathbf{1}+\mathbf{T})(\mathbf{1}-\mathbf{T})^{-1} - \frac{2}{n}\mathbf{T}(\mathbf{1}-\mathbf{T}^n)[(\mathbf{1}-\mathbf{T})^{-1}]^2 \right\}_{1,1} \tag{4.2.68}$$

$$= nc_n \,. \tag{4.2.69}$$

In the freely rotating chain approximation all entries in the matrix $\mathbf{T}$ are zero except the two entries $T_{1,1} = \langle \cos\theta \rangle$ and $T_{1,2} = \langle \sin\theta \rangle$. To get the value for $\theta$ we can use the order parameter

$$P_2(\theta) = \left\langle \frac{3\cos^2\theta - 1}{2} \right\rangle \tag{4.2.70}$$

$$= \frac{1}{(N-1)N} \left\langle \sum_{i<j}^{N} (3\cos^2\theta_{ij} - 1) \right\rangle \tag{4.2.71}$$

$$= \frac{1}{(N-1)N} \left\langle \sum_{i<j}^{N} [3(\vec{n}_i \cdot \vec{n}_j)^2 \theta_{ij} - 1] \right\rangle \tag{4.2.72}$$

which is also known as the nematic order parameter. $\theta_{ij}$ describes the angle between the two particles $i$ and $j$ and their orientation $\vec{n}_i$ and $\vec{n}_j$. The order parameter can take a value between 1.0 and $-0.5$. A completely ordered system, i.e. all dipoles are parallel reaches $P_2(\theta) = 1.0$ and a randomly disordered system has $P_2(\theta) = 0$. The negative branch down to $-0.5$ is also possible, but has not been observed. To get insight into the orientation of the particle chains in our system, the calculation of (4.2.72) is slightly adjusted to restrict the calculation to adjacent particles in an aggregate only. To identify those nearest neigbours we use the distance criteria $\min_{\alpha,\beta}\left(r_{i_\alpha j_\beta}\right) < 2.0$. The normalization factor $1/[(N-1)N]$ needs to be adapted accordingly. A plot of the order parameter with the simulation data for adjacent dumbbells is shown in figure 4.19. Taking the average of $P_2(\theta) \approx 0.3$ for small dumbbells, we get an average angle of $\theta = 43$ degrees between adjacent dumbbells. With the value of $\theta$ we now get $c_n = 3.58$ for $n = 6$ and with that $\mu_6^2 = 21.5$. Together with the earlier calculated critical density these numbers yield into the following theoretical critical parameters

$$T_c^{theo} \approx 0.07 \tag{4.2.73}$$

$$\rho_c^{theo} \approx 0.005 \tag{4.2.74}$$

$$P_c^{theo} \approx 2.3 \cdot 10^{-5} \,. \tag{4.2.75}$$

Comparing those values with the average simulation results for small dumbbells $d < 0.1$

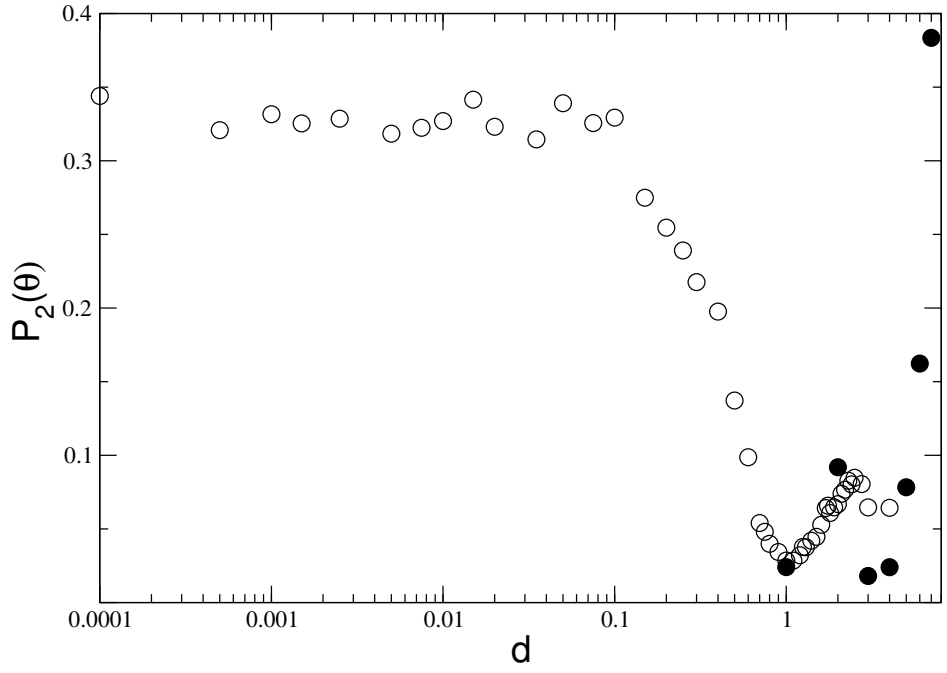


Figure 4.19.: Nearest neighbour dipole orientation coupling measured via $P_2(\theta)$ vs $d$ for CSDs at $\rho = 0.004$ and $T \approx T_c$. The open circles represent the results for constant dipole moment $\mu^2 = 1$ and the open symbols stand for constant charge $q = 1$.

which are

$$T_c^{sim} = 0.0513 \tag{4.2.76}$$

$$\rho_c^{sim} = 0.004 \tag{4.2.77}$$

$$P_c^{sim} = 6.6 \cdot 10^{-5} \tag{4.2.78}$$

we see the predicted values in reasonable agreement with our simulation results.
Having shown that the above approach works quite well for small dumbbells, we want to apply it also for large dumbbells, where $d > 0.1$. As the equations (4.2.52) - (4.2.54) are still the basis for our further discussion, we only can vary the volume $b$ to get an adequate description. In figure 4.18 we see a slight growth of the aggregate size starting at $d \approx 0.1$. It turns into a large growth beyond $d = 1$ with aggregates consisting of more than 10 to 100 monomers. In the region $0.1 < d < 1.0$ we observe a drop of the nearest neighbour order parameter (see figure 4.19), which remains small for most of the cases for $d > 1.0$. This indicates less order for the large aggregates and therefore we can consider

the aggregates as random coils below the overlap threshold. Then the volume scales as $b \sim d^2 n^{3/2}$ (note that the random coil radius scales as $n^{1/2}$) [29]. But it turns out that this form of $b$ does not produce a $n$ dependence of the critical parameters in agreement with the simulation data. Thus it is more reasonable to model the aggregates as compact clusters corresponding to $b \sim dn$. Analyzing figure 4.18 we can infer $d \sim n$ and hence write

$$\rho_c^{mon} = n\rho_c^{agg} \sim \frac{1}{n} \tag{4.2.79}$$

for the critical density. Here the quantity $\mu_n^2$ is the mean square fluctuation of the cluster dipole moment. This leads to $\mu_n^2 \sim n$ and hence

$$T_c \sim \frac{1}{n}\,. \tag{4.2.80}$$

As the critical pressure scales with $\mu_n^2/b^2$ we have in total $P_c \sim n^{-3}$ which yields

$$Z_c = \frac{P_c}{\rho_c^{mon} T_c} \sim \frac{1}{n} \tag{4.2.81}$$

for the critical compressibility factor.

As the three critical quantities $T_c$, $\rho_c$ and $Z_c$ all scale with $n^{-1}$, it is reasonable to compare this $n$ dependence in a double-logarithmic version of figure 4.5 in figure 4.20. Here we convert $d$ to $n$ on the basis of figure 4.18. The scaling for the temperature is fairly good and also for the critical density $\rho_c$ the data, despite extensive scattering, is consistent with the expected $n^{-1}$ scaling. For the critical compressibility factor the scatter makes a definite conclusion impossible.

In conclusion we found with the modified van der Waals mean field approach, expressed in equations (4.2.50) and (4.2.51), a qualitatively valid description for $d < 0.1$ and $d > 1$, if $b$ and $\mu_n$ are interpreted properly. With having now a sound explanation for the simulation data for small and large $d$, we lack an authoritative description of the $d$ range of rising critical density. The peak of the critical density indicates a change in the formation of the particles, i.e. the increase of the critical density points to a restructuring of the short linear aggregates into more compact clusters. This is supported by two observations. First the increase of the number of junctions starting from $d > 0.1$ as shown in figure 4.16, which one would suspect for more compact clusters. Secondly an inspection of the simulation snapshots, showing that the preferred head-to-tail pairing of small dumbbells becomes disfavored compared to a $\pi/2$ rotation into a side-by-side pairing, if $d$ is close to or larger than unity. We can gain further insight into the pair arrangement of dumbbells by a comparison of the CSD-CSD pair energies for the head-to-tail and side-by-side pairing, as illustrated in figure 4.6. It shows that the head-to-tail arrangement is energetically favored for small dumbbells with $d < 0.624$ and becomes disfavored for $d > 0.624$. This also supports the above observation of the more compact aggregates. In the terminology of the van der Waals theory the compact clusters decrease $b$ and lead to an increase of the critical density. The further growth of the aggregates eventually leads to a renewed increase of $b$ and a corresponding decrease of the critical density.

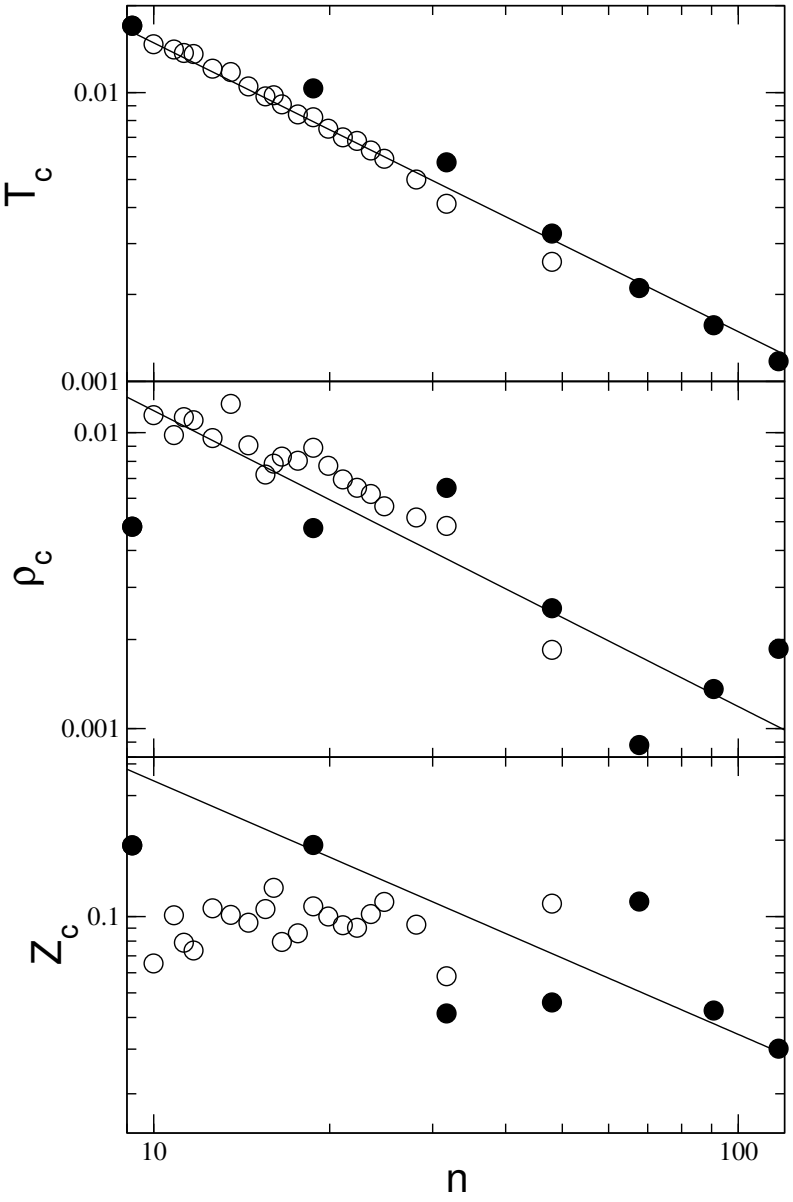


Figure 4.20.: Critical temperature, $T_c$ (top), critical density, $\rho_c$ (middle), and critical compressibility factor, $Z_c$ (bottom), for soft sphere systems vs. $n$ (converted from $d$ on the basis of figure 4.18). The simulation data is represented for CSDs and constant charge $q = 1$ via diamonds and fixed dipole moment $\mu^2 = 1$ using circles. The horizontal lines represents $T_c$ for DSS (dotted) and ions (dashed) in reduced densities. The continuous line shows the $n^{-1}$ scaling as obtained from the mean field approach.

# Bibliography


[1] J. D. Van der Waals. *Over de Continuiteit van den Gas-en Vloeistoftoestand*. AW Sijthoff, 1873.

[2] R. Hentschke. *Statistische Mechanik*. Wiley-VCH, 2004.

[3] R. B. Griffiths. Thermodynamic functions for fluids and ferromagnets near the critical point. *Physical Review*, 158(1):176, 1967.

[4] X. Shan and H. Chen. Simulation of nonideal gases and liquid-gas phase transitions by the lattice Boltzmann equation. *Physical Review E*, 49(4):2941, 1994.

[5] J. Bartke and R. Hentschke. Phase behavior of the Stockmayer fluid via molecular dynamics simulation. *Physical Review E*, 75:061503, 2007.

[6] C. Domb. *The Critical Point*. Taylor & Francis, 1996.

[7] R. Hentschke, E. M. Aydt, B. Fodi, and E. Stöckelmann. Molekulares Modellieren mit Kraftfeldern. http://constanze.materials.uni-wuppertal.de.

[8] Wolfram Research Inc. Mathematica, Champaign, Illinois. 2014.

[9] J. O. Hirschfelder, C. F. Curtiss, R. B. Bird, and M. G. Mayer. *Molecular Theory of Gases and Liquids*. John Wiley & Sons, Inc., 8 edition, 1964.

[10] J. V. Sengers and J. M. H. Sengers Levelt. Thermodynamic behavior of fluids near the critical point. *Annual Review of Physical Chemistry*, 37(1):189, 1986.

[11] J. M. H. Levelt Sengers. From Van der Waals' equation to the scaling laws. *Physica*, 73(1):73, 1974.

[12] M. Ley-Koo and M. S. Green. Consequences of the renormalization group for the thermodynamics of fluids near the critical point. *Physical Review A*, 23(5):2650, 1981.

[13] M. E. Fisher. The renormalization group in the theory of critical behavior. *Reviews*

*of Modern Physics*, 46(4):597, 1974.

[14] A. Pelissetto and E. Vicari. Critical phenomena and renormalization-group theory. *Physics Reports*, 368(6):549, 2002.

[15] M. E. Fisher and Y. Levin. Criticality in ionic fluids: Debye-Hückel theory, Bjerrum, and beyond. *Physical Review Letters*, 71(23):3826, 1993.

[16] A. Z. Panagiotopoulos. Critical parameters of the restricted primitive model. *The Journal of Chemical Physics*, 116(7):3007, 2002.

[17] G. Ganzenmüller and P. J. Camp. Vapor-liquid coexistence in fluids of charged hard dumbbells. *Journal of Chemical Physics*, 126:191104, 2007.

[18] G. Ganzenmüller, G. N. Patey, and P. J. Camp. Vapour–liquid phase transition of dipolar particles. *Molecular Physics*, 107(4-6):403, 2009.

[19] J. Bartke. *Computer Simulation of the Stockmayer Fluid*. PhD thesis, Bergische Universität Wuppertal, 2008.

[20] C. Domb. *Phase transitions and critical phenomena*, volume 19. Academic Press, 2000.

[21] W. Gebhardt and U. Krey. *Phasenübergänge und kritische Phänomene*. Friedrich Vieweg & Sohn, 1980.

[22] J. M. Yeomans. *Statistical mechanics of phase transitions*. Oxford University Press, 1992.

[23] H. Braun. Computersimulation des gas-flüssig Phasenverhaltens geladener Hantelmoleküle. Master's thesis, Bergische Universität Wuppertal, 2008.

[24] H. J. C. Berendsen, J. P. M. Postma, W. F. van Gunsteren, A. DiNola, and J. R. Haak. Molecular dynamics with coupling to an external bath. *Journal of Chemical Physics*, 81(8):3684, 1984.

[25] H. Braun and R. Hentschke. Tracking gas-liquid coexistence in fluids of charged soft dumbbells. *Physical Review E*, 80(4):041501, 2009.

[26] M. E. Van Leeuwen. Deviation from corresponding-states behaviour for polar fluids. *Molecular Physics*, 82(2):383, 1994.

[27] T. Tlusty and S. A. Safran. Defect-induced phase separation in dipolar fluids. *Science*,

290(5495):1328, 2000.

[28] P. De Gennes. *Scaling concepts in polymer physics*. Cornell university press, 1979.

[29] P. De Gennes and P. A. Pincus. Pair correlations in a ferromagnetic colloid. *Physik der kondensierten Materie*, 11(3):189, 1970.

[30] P. J. Flory. *Principles of Polymer Chemisty*. Cornell University Press, Ithaca, 1953.

[31] J. Dudowicz, K. F. Freed, and J. F. Douglas. Flory-Huggins model of equilibrium polymerization and phase separation in the Stockmayer fluid. *Physical Review Letters*, 92(4):045502, 2004.

[32] W. Ouyang and R. Hentschke. From gas-liquid to liquid crystalline phase behavior via anisotropic attraction: A computer simulation study. *Journal of Chemical Physics*, 127:164501, 2007.

[33] R. Hentschke, J. Bartke, and F. Pesth. Equilibrium polymerization and gas-liquid critical behavior in the Stockmayer fluid. *Physical Review E*, 75:011506, 2007.

[34] T. L. Hill. *An introduction to statistical thermodynamics*. Courier Dover Publications, 1960.

[35] H. Frauenkron and P. Grassberger. Critical unmixing of polymer solutions. *The Journal of Chemical Physics*, 107(22):9599, 1997.

[36] L. V. Yelash, T. Kraska, A. R. Imre, and S. J. Rzoska. Apparent exponents for the chain length dependence of the volume fraction in critical polymer solutions. *The Journal of Chemical Physics*, 118(13):6110, 2003.

[37] R. Hentschke, P. Lenz, and B. Fodi. *Supramolecular Polymers*, chapter Supramolecular Liquid Crystals: Simulation. 2nd ed., edited by A. Ciferri, Taylor & Francis, Boca Raton, 2005.

[38] J. T. Kindt and W. M. Gelbart. Chain self-assembly and phase transitions in semiflexible polymer systems. *The Journal of Chemical Physics*, 114(3):1432, 2001.

[39] L. Onsager. Electric moments of molecules in liquids. *Journal of the American Chemical Society*, 58:1486, 1936.

[40] P. J. Flory. Statistical mechanics of chain molecules, 1969. *Interscience, New York*, page 308, 1989.

# 5. Gas-liquid transition of dipolar soft spheres

We have tracked the critical point for CSDs from an elongated charge-to-charge separation to very small dumbbells $d \to 0$, in order to approximate the limit of the DSS model. Now we want to study in the following chapter a real dipolar system. Therefore we use the DSS system as described in chapter 3. We re-express the pair potential (3.4.2) here once again

$$u_{ij}^{DSS}(\vec{r}_{ij}, \vec{\mu}_i, \vec{\mu}_j) = 4\lambda\varepsilon \left(\frac{\sigma}{r_{ij}}\right)^{12} + \frac{1}{4\pi\epsilon_0}\left(\frac{\vec{\mu}_i \cdot \vec{\mu}_j}{r_{ij}^3} - \frac{3\,(\vec{r}_{ij} \cdot \vec{\mu}_i)\,(\vec{r}_{ij} \cdot \vec{\mu}_j)}{r_{ij}^5}\right). \tag{5.0.1}$$

For the ordinary DSS system the parameter $\lambda$ must be set to 1. We carry out the simulation in the same way as described in section 4.1.3, i.e. we use the NVT ensemble and simulate for each temperature two isotherms. For the dipole moment of the system we use $\mu^2 = 1$. After testing several simulation parameters, it turns out that $N = 1600$ particles and a cutoff radius $r_{cut} = 10$ with a time step of $\Delta T = 0.001$ produces accurate simulation results at acceptable simulation costs. In figure 5.1 we can see the comparison of different cutoff radii and their influence on the van der Waals loop. The isotherms, shown there, were simulated at temperature $T = 0.059$ with $N = 1600$ particles. For $r_{cut} > 8.0$, no significant difference in the van der Waals loop is apparent. This legitimates the usage of $r_{cut} = 10.0$ in our further simulations. To take care of the dipole-dipole interactions beyond the cutoff radius, we again make use of the reaction field method. It contributes to the potential energy of the particle $i$ as follows [1]

$$u_i^{RF} = -\frac{1}{4\pi\epsilon_0}\frac{2(\epsilon-1)}{2\epsilon+1}\frac{1}{r_{cut}^3}\vec{\mu}_i \sum_{j \in V_{Sp}(\vec{r}_i)} \vec{\mu}_j\,. \tag{5.0.2}$$

This then finally results in the total energy

$$U = \lambda \sum_{i<j} \frac{4}{r_{ij}^{12}} + \frac{1}{2}\sum_{i=1}^{N} \vec{\mu}_i \left[ \sum_{\substack{j \in V_{Sp}(\vec{r}_i) \\ j \neq i}} \left(\frac{\vec{\mu}_j}{r_{ij}^3} - \frac{3\vec{r}_{ij}\,(\vec{r}_{ij} \cdot \vec{\mu}_j)}{r_{ij}^5}\right) - \frac{2(\epsilon-1)}{2\epsilon+1}\frac{1}{r_{cut}^3} \sum_{j \in V_{Sp}(\vec{r}_i)} \vec{\mu}_j \right] \tag{5.0.3}$$

of the system. Here we have set $4\pi\epsilon_0 = 1$ and also $\varepsilon = \sigma = 1$.

Having tracked the critical point for the CSD system earlier to $d \to 0$, we got the starting

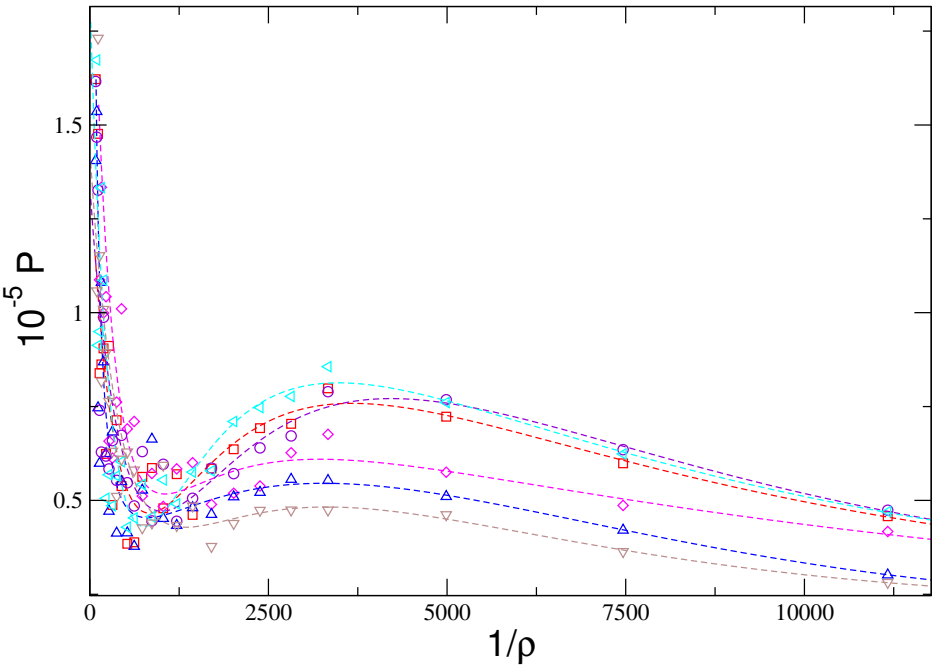


Figure 5.1.: Influence of $r_{cut}$ on isotherms for the DSS system with $N = 1600$ particles and temperature $T = 0.059$. The plot shows cutoffs from $r_{cut} = 5.0$ to $r_{cut} = 15.0$, where the colors and symbols are as follows, $r_{cut} = 5.0$ (brown triangle down), $r_{cut} = 6.0$ (blue triangle up), $r_{cut} = 8.0$ (magenta diamonds), $r_{cut} = 10.0$ (red squares), $r_{cut} = 12.5$ (cyan triangle left), and $r_{cut} = 15.0$ (violet circles). The lines are drawn with the fit function in equation (4.1.10).

region of temperature and density, which we have to analyze for the g-l phase transition of the DSS system. This is an enormous advantage, because based on earlier simulations done on DSS or comparable hard sphere systems [2–4], we would look at higher temperatures and densities. Definitely that would make the detection of the phase coexistence area more difficult. Figure 5.2 exemplifies the van der Waals loops in the DSS system for two different isotherms. Beside the clear evidence of the loop itself, we can also see that the isotherm at $T = 0.063$ seems to be very close to the critical point. Therefore the plotted line, which was constructed for all isotherms using the earlier defined fit function (4.1.10), shows almost an inflection point instead of a loop. The complete g-l phase coexistence area is shown in figure 5.3 including the critical point, which we found at temperature $T_c = 0.0632$ and critical density $\rho_c = 0.0033$. These values are in accordance with another study of the DSS system, done within our group by Jia [5]. He followed a

different approach similar to Steven and Grest [6] and tracked the critical point of the DSS in an external field to the limit of zero field, which is identical to our study.

Finally we can calculate with the critical pressure $P_c = 9.9 \cdot 10^{-6}$, the critical com-

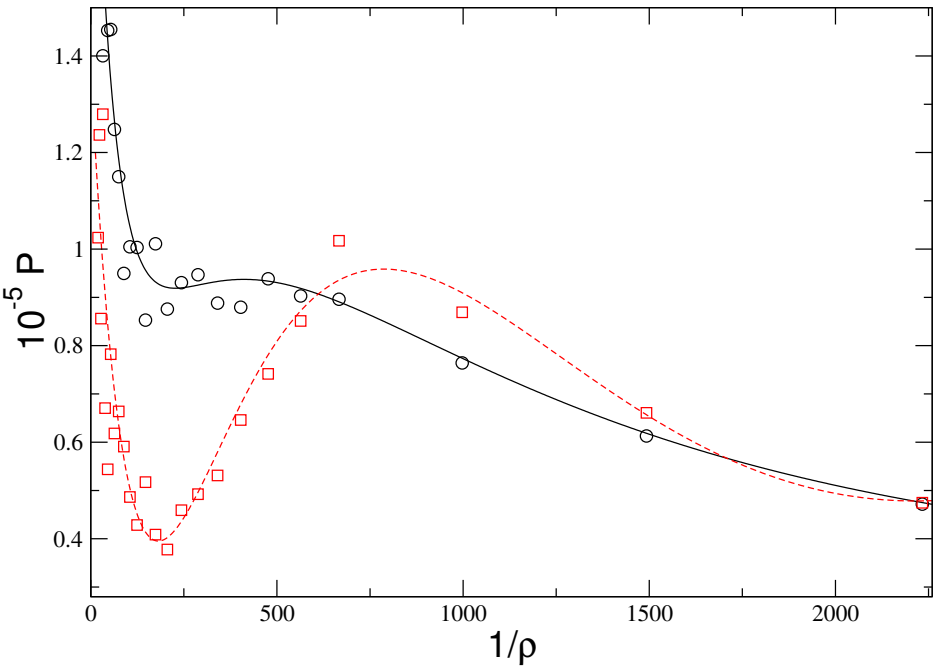


Figure 5.2.: Two exemplary van der Waals loops for DSS system with $N = 1600$ particles at temperature $T = 0.058$ (red squares) and $T = 0.063$ (black circles). The lines are drawn with the fit function in equation (4.1.10).

pressibility factor, which results in $Z_c = 0.047$ and is much lower than the one we have calculated earlier for the CSD system. To understand this difference, we have to recap the geometry of the CSD particle. It consists of two soft sphere sites, which end up in four particle-particle soft sphere interactions, whereas we have only one interaction for ordinary DSS particles. Therefore we do another study of the DSS system with $\lambda = 4$ and call this the 4-DSS system. In figure 5.4 we can see the impact of the fourfold repulsion on the structure of the system, by comparing two simulation snapshots, created at the same conditions with $T = 0.05$, $\rho = 0.003$. The ordinary DSS system forms long reversible chains including rings, whereas the additional repulsion of the 4-DSS system suppresses aggregation. Thus only small chains are formed. Taking a look at the pair correlation function in figure 5.5, shows that with the introduction of the fourfold repulsion, the structure of the 4-DSS becomes almost identical to the one of the CSD model for small

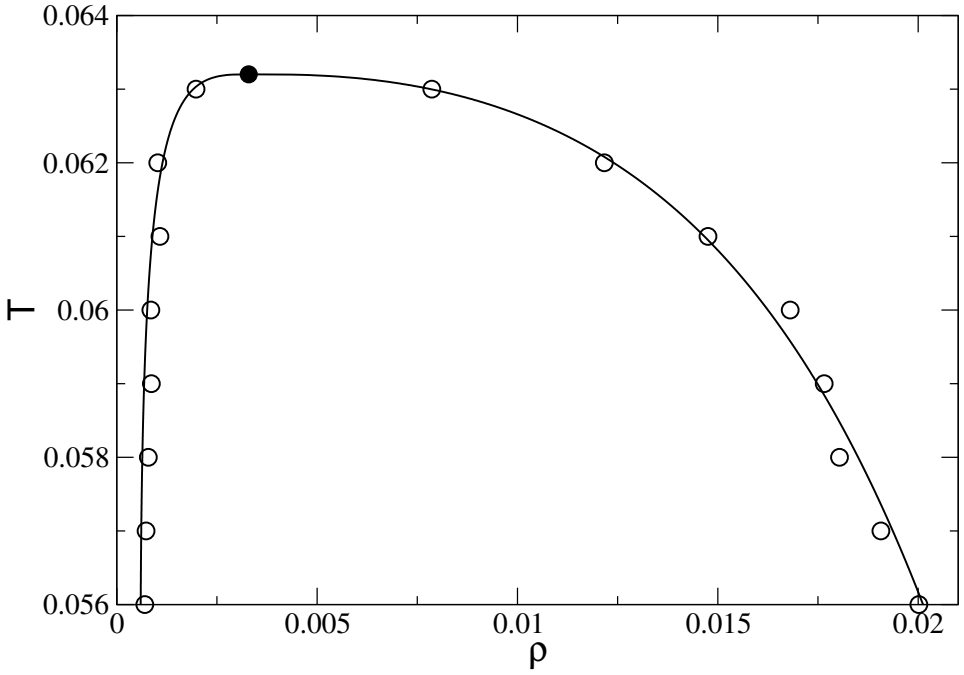


Figure 5.3.: Phase coexistence regime of the DSS system simulated for $N = 1600$ particles.

dumbbells.

Besides the fact that the fourfold repulsion allows a direct comparison to the CSD model, it also opens a new aspect in the effort to analyze purely dipolar systems. Due to the increased repulsion the 4-DSS system is much easier to equilibrate. Following the idea to avoid excessive chain formation, numerous functional forms for the interaction potential (e.g. [4, 7, 8]) have been proposed to study the g-l criticality. They are characterized by a control parameter, allowing to approach the ordinary DSS (or DHS) interaction. Tuning the potential towards the DSS (or DHS potential), one hopes to collect sufficient data, permitting extrapolation to the critical parameters of the limiting systems, before excessive aggregation renders equilibration prohibitively time consuming. However, to the best of our knowledge, no such study has controlled aggregation via scaled repulsion. Increased repulsion, however, appears to be the easiest approach to a model potential with purely dipolar attraction and easy access to its g-l critical point [9].

The critical parameters for the 4-DSS, which we have determined via NVT MD simulations in the same way as for the ordinary DSS system are $\rho_c = 0.0037$, $T_c = 0.0501$ and $P_c = 4.9 \cdot 10^{-5}$. The critical compressibility factor is $Z_c = 0.262$, which is slightly lower than the value $Z_c = 3/8$ obtained from simple liquid mean field theories like van

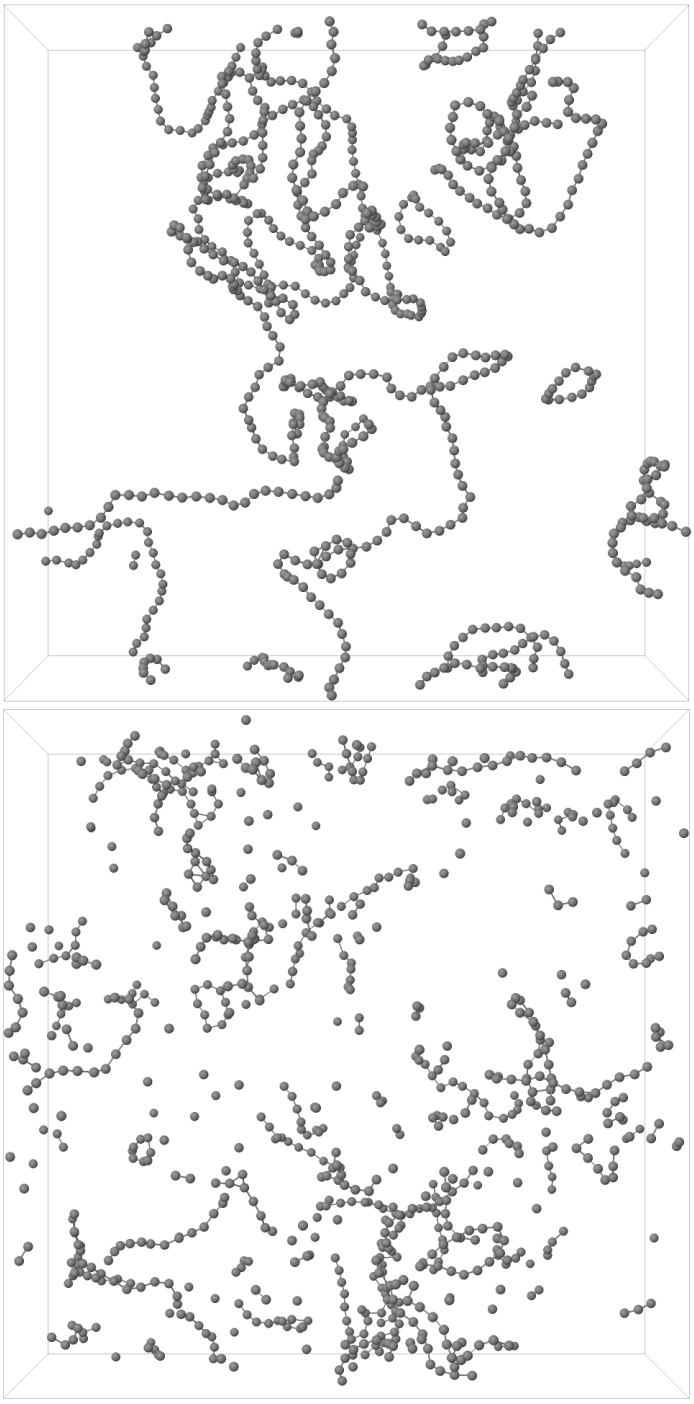

Figure 5.4.: Top: Ordinary DSS at $T = 0.05$, $\rho = 0.003$; bottom: 4-DSS with fourfold repulsive interaction at the same conditions. Lines connecting particles indicate reversible bonds based on a distance criteria.

der Waals. All critical parameters can be found in table 5.1. Thus both DSS systems can be compared with the average values for the CSD system for $d < 0.1$, where the influence of $d$ is very limited. The 4-DSS system is in very good agreement with the average values for CSD below $d < 0.1$ and shows that the limit of $d \to 0$ of the dumbbell system indeed can be considered for the g-l phase transition of the dipolar system.

Table 5.1.: Critical parameters for the DSS systems and the average CSD values for $d < 0.1$ noted as $\langle \text{CSD} \rangle$

| System | $T_c$ | $\rho_c$ | $P_c$ | $Z_c$ |
|---|---|---|---|---|
| DSS | 0.0632 | 0.0033 | $9.88 \cdot 10^{-6}$ | 0.047 |
| 4-DSS | 0.0501 | 0.0037 | $4.85 \cdot 10^{-5}$ | 0.262 |
| $\langle \text{CSD} \rangle$ | 0.0513 | 0.0040 | $6.74 \cdot 10^{-5}$ | 0.330 |

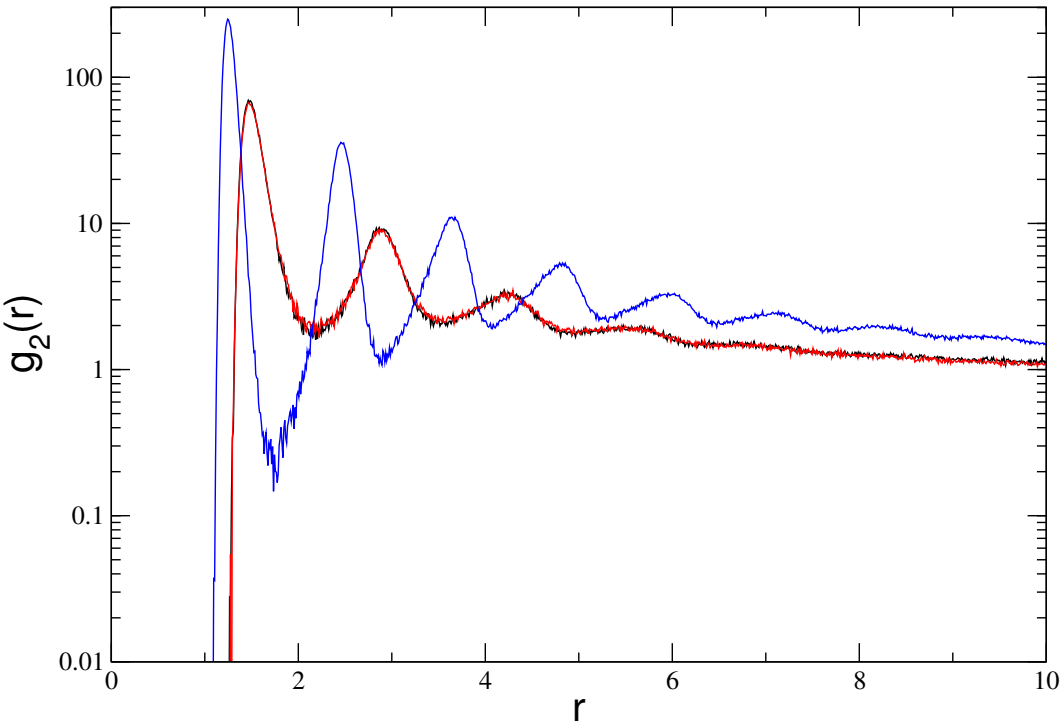


Figure 5.5.: Pair correlation functions for the CSD, DSS and 4-DSS model at $T = 0.05$, $\rho = 0.003$ and dumbbell length $d = 0.0001$. The black continuous line shows the pair correlation function $g_2(r)$ for the dumbbells. The red line presents the same for the 4-DSS model and the blue line for the ordinary DSS model. It is obvious that the structure of the CSD and 4-DSS model are almost identical.

# Bibliography


[1] R. Jia and R. Hentschke. Dipolar particles in an external field: Molecular dynamics simulation and mean field theory. *Physical Review E*, 80(5):051502, 2009.

[2] J. Bartke. *Computer Simulation of the Stockmayer Fluid*. PhD thesis, Bergische Universität Wuppertal, 2008.

[3] P. J. Camp, J. C. Shelley, and G. N. Patey. Isotropic fluid phases of dipolar hard spheres. *Physical Review Letters*, 84(1):115, 2000.

[4] G. Ganzenmüller and P. J. Camp. Vapor-liquid coexistence in fluids of charged hard dumbbells. *Journal of Chemical Physics*, 126:191104, 2007.

[5] R. Jia. *Computer-Simulationen polarer Flüssigkeiten in einem äußeren elektrischen Feld*. PhD thesis, Bergische Universität Wuppertal, 2011.

[6] M. J. Stevens and G. S. Grest. Coexistence in dipolar fluids in a field. *Physical Review Letters*, 72(23):3686, 1994.

[7] G. Ganzenmüller, G. N. Patey, and P. J. Camp. Vapour–liquid phase transition of dipolar particles. *Molecular Physics*, 107(4-6):403, 2009.

[8] R. Jia, H. Braun, and R. Hentschke. Gas-liquid coexistence in a system of dipolar soft spheres. *Physical Review E*, 82(6):062501, 2010.

[9] H. Braun and R. Hentschke. Phase coexistence for charged soft dumbbell and ionic soft sphere systems via molecular dynamics simulation. *Physical Review E*, 87(1):012311, 2013.

# 6. Simulation results for the ionic system

In the previous chapters we studied the phase behavior of CSDs and their limit for $d \to 0$ to DSS [1, 2] using MD simulations. With extending the analysis of the CSD model to $d \gg 1$ up to $d = 7$, we crossed the line, where one would expect that the CSD model behaves similar to an ionic fluid. So with eliminating the rigid dumbbell bond of the CSD, we get an ionic fluid. This soft sphere ionic fluid is similar to the commonly used RPM, which has a hard core repulsion instead of a soft sphere repulsion. In the following chapter we want to analyze the phase coexistence of the soft sphere ionic system and compare it with the literature results of the RPM, as well as the theoretical predictions of the Debye Hückel theory. In addition we want to compare the results with the CSD model, because a detailed theoretical study of the g-l phase separation in the RPM [3, 4] shows that its critical parameters are governed by the formation of (primarily) dimers. Our dumbbells are akin to these dimers, at least for certain values of $d$. To substantiate our results and investigate the impact of the long-range correction, we compare our simulation with the results of the LAMMPS MD simulator [5], which makes use of the Ewald [6] correction instead of the reaction-field method applied in our own MD simulation package. In addition we also analyzed the structural information of the systems in the regime of the critical point and for a broad range of densities from $10^{-10}$ to $10^{-1}$. A similar work was done recently by Valeriani *et al.* [7] for the RPM. We also compare our results with the theoretical approach for ion-pairing.

## 6.1. Gas-liquid transition of ionic soft spheres

In the following we want to analyze the g-l transition of an ionic system. This corresponds to the earlier studied dumbbells in case the charge is not rigidly bound. We therefore consider a fluid of charged soft spheres, i.e. a $r^{-12}$ repulsion. Half of them carry charge $-q$ and the other half charge $+q$. We already defined the potential energy between two particles in (3.6.1) by

$$u_{ij}(r_{ij}) = \frac{4}{r_{ij}^{12}} + \frac{1}{4\pi\epsilon_0}\frac{q_i q_j}{r_{ij}}\,. \tag{6.1.1}$$

As we usually set the LJ parameters $\epsilon$ and $\sigma$ to one, we omitted them in the equation above. Whereas we keep $4\pi\epsilon_0$, which also equals one in our units, for easier comparison with the formulas below. The interaction potential is applied to a system of $N$ particles in NVT MD simulation. As we use a cutoff radius $r_{cut}$ for the interaction potential, we apply a long-range correction method for the Coulomb interaction. As for the other models we rely on the reaction field method as introduced in section (2.5.3) and derived from Tironi *et al.* [8]. In contrast to the dumbbells, for which the cutoff sphere is charge neutral, we get for the ionic system the following contribution from the reaction field to the total Coulomb energy

$$u_i^{RF} = \frac{1}{4\pi\epsilon_0\epsilon_I}\frac{\epsilon_I - \epsilon}{\epsilon\, r_{cut}} \sum_{j\in V_{Sp}(\vec{r}_i)} q_i q_j \,. \tag{6.1.2}$$

This results in a total Coulomb energy of the system given by

$$\begin{aligned} U^C &= \frac{1}{2}\sum_{i=1}^{N} \frac{q_i}{4\pi\epsilon_0\epsilon_I}\phi_I(r_i) && (6.1.3)\\ &= \frac{1}{4\pi\epsilon_0\epsilon_I} \sum_{\substack{i<j \\ j\in V_{Sp}(\vec{r}_i)}} \frac{q_i q_j}{r_{ij}} \\ &\quad + \frac{1}{4\pi\epsilon_0\epsilon_I}\frac{\epsilon_I - \epsilon}{2\epsilon\, r_{cut}} \sum_{i=1}^{N} \sum_{j\in V_{Sp}(\vec{r}_i)} q_i q_j \,. && (6.1.4) \end{aligned}$$

Here $V_{Sp}(\vec{r}_i)$ describes the cutoff sphere of the particle at position $r_i$ with radius $r_{cut}$ and $\epsilon$ corresponds to the dielectric constant of the fluid. The dielectric constant of the inner part of the cutoff sphere can be set to $\epsilon_I = 1$.
The total Coulomb force on charge $q_i$ caused by another particle $j$ including the reaction field can be expressed via

$$\vec{F}^C(\vec{r}_{ij}) = \frac{q_i q_j}{4\pi\epsilon_0}\left(\frac{1}{r_{ij}^3} - \frac{2(\epsilon-1)}{2\epsilon+1}\frac{1}{r_{cut}^3}\right)\vec{r}_{ij} \,. \tag{6.1.5}$$

The last term in equation (6.1.5) is the force $\vec{F}^{RF}(\vec{r}_{ij})$ based on the reaction field. It contributes also to the pressure as follows

$$\left\langle \sum_{i=1}^{N} \vec{r}_i \vec{F}^{RF}(\vec{r}_{ij}) \right\rangle = \frac{1}{4\pi\epsilon_0}\frac{2(\epsilon-1)}{2\epsilon+1}\frac{1}{r_{cut}^3}\left\langle \sum_{i<j}^{N} r_{ij}^2 q_i q_j \right\rangle \quad . \tag{6.1.6}$$

The unknown dielectric constant $\epsilon$ can be obtained via

$$\frac{(\epsilon-1)(2\epsilon+1)}{3\epsilon} = \frac{\left\langle \vec{M}_{Sp}\cdot\vec{M}_B \right\rangle}{T r_{cut}^3} \tag{6.1.7}$$

with the dipole moment $\vec{M}_{Sp}$ of a cutoff sphere and the total dipole moment of the simulation box $\vec{M}_B$. Equation (6.1.7) is evaluated in each simulation step. To calculate the reaction field contribution to the force and torque the cumulative average of $\epsilon$ is used. With our own software package we carry out MD simulations in the NVT ensemble. The temperature is controlled via the weak coupling method of Berendsen *et al.* [9]. One isotherm consists of 30-45 state points. The initial configuration for the first state point is based on particles arranged on a fcc lattice with random velocities. Along a single isotherm the final configuration of the preceding density is used for the new density. For each state point we equilibrated the system for 1000 time units before collecting the results over 800 time units using a time step of 0.003. Depending on density these times are extended up to 100-fold if necessary. The simulations to obtain the critical parameters were performed for a system containing $N = 1000$ particles with a cutoff $r_{cut} = 10.0$. Variation of the cutoff up to $r_{cut} = 20.0$ and the number of particles up to $N = 3000$ showed that the chosen values are sufficient to calculate reliable results.

For comparison we used the LAMMPS package, which delivers several pair styles out of the box. For our purpose we chose one standard pair style, which is based on a LJ potential in combination with Coulomb interaction and the PPPM [10, 11] long range correction. To be in accordance with the potential given by (6.1.1) the attractive $r^{-6}$ term in the LJ force was removed from the standard pair style. To reduce the computation time, we used the final configuration of an individual state point of our own package as initial configuration for the LAMMPS run to construct the corresponding state point. We further equilibrated the start configuration for LAMMPS for 750 time units before we took the results over further 800 time units. Similar to our own package those times were extended if necessary. In our LAMMPS simulation the temperature is controlled using a Nosé-Hoover thermostat [12]. To determine the critical parameter, we again make use of the Maxwell construction (see 4.1.1) and the scaling laws introduced in section 4.1.2.

The critical parameters calculated with the isotherms of our own software package were $T_C = 0.0163$ and $\rho_c = 0.006$, this is in good agreement with the results produced via LAMMPS, which are $T_C = 0.0152$ and $\rho_c = 0.007$. All critical parameters can be found in table 6.1. The phase coexistence area produced from both packages is shown in figure 6.1 in critical units. As expected there is a good agreement between the two results. This accordance of the two software packages also shows that the different methods used for the long-range correction of the Coulomb interaction produce similar results in the g-l phase of the ionic system. This is also in concordance with [13–16], who studied dipolar systems (ST fluid or water) to compare the two long-range correction methods. Even though the closeness of the above results does already indicate that our reaction field method and the Ewald summation do yield the same results, we do a further simple test of both methods in section 6.3 below.

As our model is quite similar to the restrictive primitive model, we want to compare simulation results from literature with ours. But before we can do this, we have to cover the influence of the different repulsions on the critical parameters. We follow the same approximation as done previously (see section 3.5.1) to convert the results between the soft ions (si) and the hard sphere (hs) ions of the RPM. For the temperature conversion

we use

$$\frac{T_{eff}^{hs}}{q^2/\sigma^{hs}} = \frac{T^{si}}{q^2/\sigma^{si}} \quad , \tag{6.1.8}$$

where $T_{eff}^{hs}$ is the temperature in the soft sphere ionic system converted to a hard sphere system. Analogous we proceed for the density, i.e.,

$$(\sigma^{hs})^3 \rho_{eff}^{hs} = (\sigma^{si})^3 \rho^{si} \quad . \tag{6.1.9}$$

Here $\sigma^{si}$ follows via $B_2^{si}(T_c^{si}; \sigma^{si}) = B_2^{hs}(\sigma^{hs} = 1)$, where $B_2$ refers to the second virial coefficient of the respective model. With that we get

$$\sigma^{si}(T) = \Gamma(3/4)^{1/3}(4/T)^{1/12} \tag{6.1.10}$$

where $\Gamma(3/4)^{1/3} \approx 1.07011$. With the critical temperature $T_c = 0.0163$, calculated by our own package, and the above introduced conversion we arrive at $T_c^{hs} = 0.028$ and $\rho_c^{hs} = 0.029$. Historically the studies of the RPM system used mostly MC methods to determine the critical parameters arriving at a wide range of results. Valleau calculated $T_c = 0.070$ and $\rho_c = 0.07$ in 1991 [17] and an early work by Panagiotopoulos in 1992 [18] found the critical point at $T_c = 0.057$ and $\rho_c = 0.030$. But latest simulations for the RPM done by Panagiotopoulos [19] reveal $T_c = 0.0489$ and $\rho_c = 0.076$ for the critical parameters, which is almost identical to the results of Caillol *et al.* [20], which are $T_c = 0.049$ and $\rho_c = 0.080$. Those values differ approximately a factor of two from our converted results. But without the conversion the critical temperature of the soft ions differs from the same quantity in the RPM by a factor of about three. In the case of the critical density the respective factor is about 12.

Table 6.1.: Critical parameters for the ionic system produced with our own software package and LAMMPS.

| Package | $T_c$ | $\rho_c$ | $P_c$ | $Z_c$ | $T_c^{hs}$ | $\rho_c^{hs}$ |
|---|---|---|---|---|---|---|
| Own | 0.0163 | 0.006 | $2.8 \cdot 10^{-6}$ | 0.286 | 0.028 | 0.029 |
| LAMMPS | 0.0152 | 0.007 | $3.1 \cdot 10^{-6}$ | 0.291 | 0.026 | 0.035 |

In addition to the comparison with simulation data, we can use the estimations for the RPM system based on the Debye-Hückel theory published nearly 90 years ago [21]. The Debye-Hückel theory predicts the critical parameters of the RPM at $T_c = 1/16$ and $\rho_c = 1/64\pi$. A further improvement of the Debye-Hückel theory was done by Levin and Fisher [3, 4], who encouraged the idea that the basic unit is not the ion but the neutral ion pair. This leads to the Debye-Hückel Bjerrum plus Dipole Ionic coupling theory. Therefore we get $T_c = 0.0574$ and $\rho_c = 0.0277$ for the critical parameters of the RPM, which is again a factor of two away from our result for the critical temperature but does

very good correspond to our critical density.
As our earlier studied CSD model can be considered as neutral ion pairs with infinite coupling, we want to see how good the results of the ionic system fit into this. The figure 6.2 presents the recent results for the ionic system along with those obtained earlier for CSDs and DSS. For $T_c$ and $\rho_c$ the results are in accord with the above idea; i.e., for $T_c$ the results intersect at $d \approx 1$ and for $\rho_c$ at $d \approx 2$. Only in case of the critical compressibility factor the intercept appears at a too small $d$. We note that Daub *et al.* [22] have studied the critical behavior of the hard core variant of the dumbbell model and find rather good agreement between their system, in which the dumbbell length is equal to the diameter of the repulsive cores, and the RPM critical parameters. On the other hand a recent study by Nikoubashman *et al.* [23] shows that the details of the ion-ion interaction have a strong influence on the values of the critical parameters. In this analysis the point charges were replaced by extended charge distributions. Additional information can be gained from the pair correlation functions shown in figure 6.3. The first peak is very sharp for $g_2^{+-}$and totally missing for $g_2^{++,--}$. Indeed this is a very good indicator of having cation-anion pairs in the system and therefore a valid explanation of the closeness of the ion critical parameters to the dumbbells with length $d \approx 1-2$ as they are similar to ion pairs. In the following we want to do some further analysis of the pairing in ionic systems.

## 6.2. Ion pairing in the soft sphere ionic system

We want to continue our study with an analysis of the cation-anion pairing of ions in terms of Bjerrum association in our system. A similar work was done recently by Valeriani *et al.* [7] for the RPM at low concentrations and low temperatures, where a substantial ion pairing is expected [24]. They did a detailed comparison between theory, simulations and experimental data. We want to shortly recap the theoretical approach based on the ideal Bjerrum dipoles [25], to derive an approximation for the ion degree of association $\alpha$. More details also can be found in Ref. [4, 26]. We start with the quasi-chemical equilibrium

$$cation - anion \quad pair \rightleftharpoons cation + anion \quad , \tag{6.2.1}$$

and go ahead with the number density for (reversible) cation-anion pairs, defined as $\rho_\pm = \alpha\rho/2$ and the density of cations and anions $\rho_+ = \rho_- = (1-\alpha)\rho/2$. The association $\alpha$ can be derived by considering chemical equilibrium $\mu_\pm = \mu_+ + \mu_-$ of the three types of components, cations, anions and neutral pairs. For an ideal gas of free charged particles and neutral ion pairs the chemical potentials are

$$\mu_+ = k_B T \ln\left[\frac{(1-\alpha)\rho}{2}\Lambda_+^3\right] = k_B T \ln(\rho_+\Lambda_+^3) \tag{6.2.2}$$

$$\mu_- = k_B T \ln\left[\frac{(1-\alpha)\rho}{2}\Lambda_-^3\right] = k_B T \ln(\rho_+\Lambda_+^3) \tag{6.2.3}$$

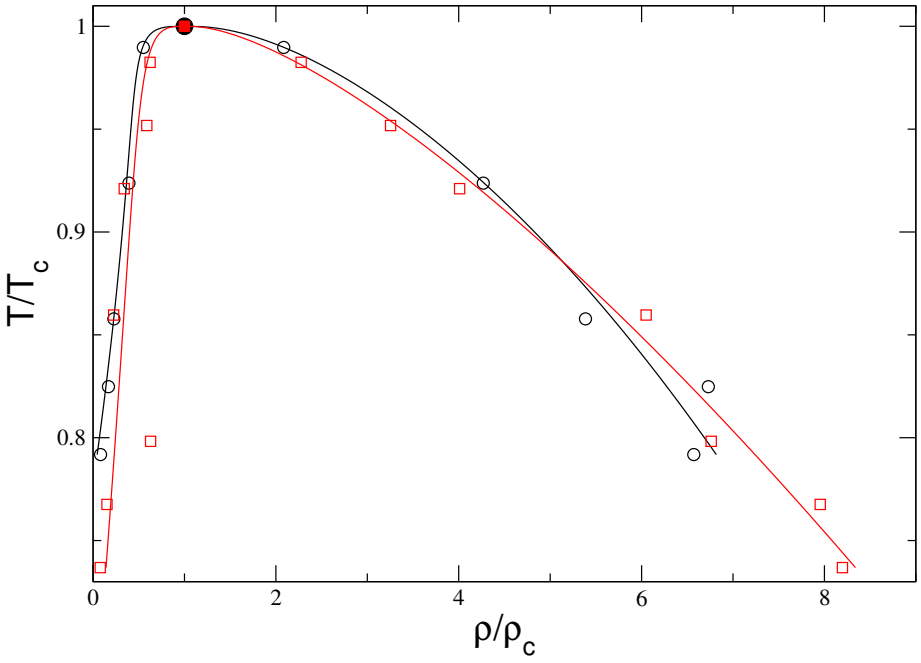


Figure 6.1.: Phase coexistence area of the ionic fluid based on the results produced with our own software package (red) and LAMMPS (black) in critical units.

$$\mu_{\pm} = k_B T \ln(\alpha\rho\Lambda_+^3\Lambda_-^3/2K) = k_B T \ln(\rho_{\pm}\Lambda_+^3\Lambda_-^3/K)\,. \tag{6.2.4}$$

Here we use the de Broglie thermal wavelengths $\Lambda_+$ and $\Lambda_-$ of the corresponding particles. With that we get

$$\frac{\alpha}{(1-\alpha)^2} = \frac{\alpha\rho}{2}\,. \tag{6.2.5}$$

This we can solve for $\alpha$, which is between 0 and 1, to arrive at

$$\alpha = 1 - \frac{1}{K\rho}\left(\sqrt{1+2K\rho} - 1\right) \quad . \tag{6.2.6}$$

The quantity $K$ is an "equilibrium constant" and named association constant. It is described via the pair configuration integral

$$K(T) = 4\pi \int_{R_<}^{R_>} \mathrm{d}r r^2 \exp\left[\frac{-u_{\pm}}{T}\right] \mathrm{d}r \quad , \tag{6.2.7}$$

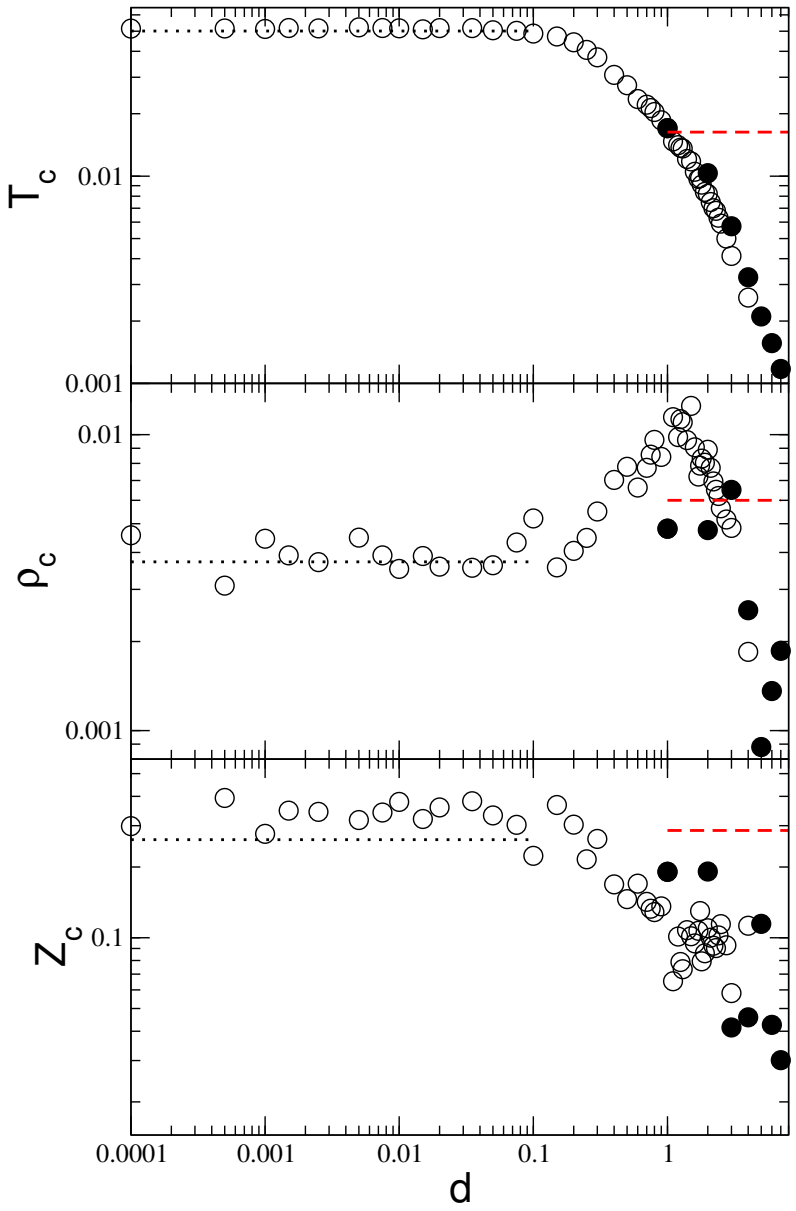


Figure 6.2.: Critical temperature, $T_c$ (top), critical density, $\rho_c$ (middle), and critical compressibility factor, $Z_c$ (bottom), for soft sphere systems vs. $d$. The simulation data is represented for CSDs and constant charge $q = 1$ via diamonds and fixed dipole moment $\mu^2 = 1$ using circles. The horizontal lines represent $T_c$ for DSS (dotted) and ions (dashed) in reduced densities.

where $u_{\pm}$ is the intrapair potential. As described in [4] there are also other expressions available to calculate the association constant. But for very low temperatures the devia-

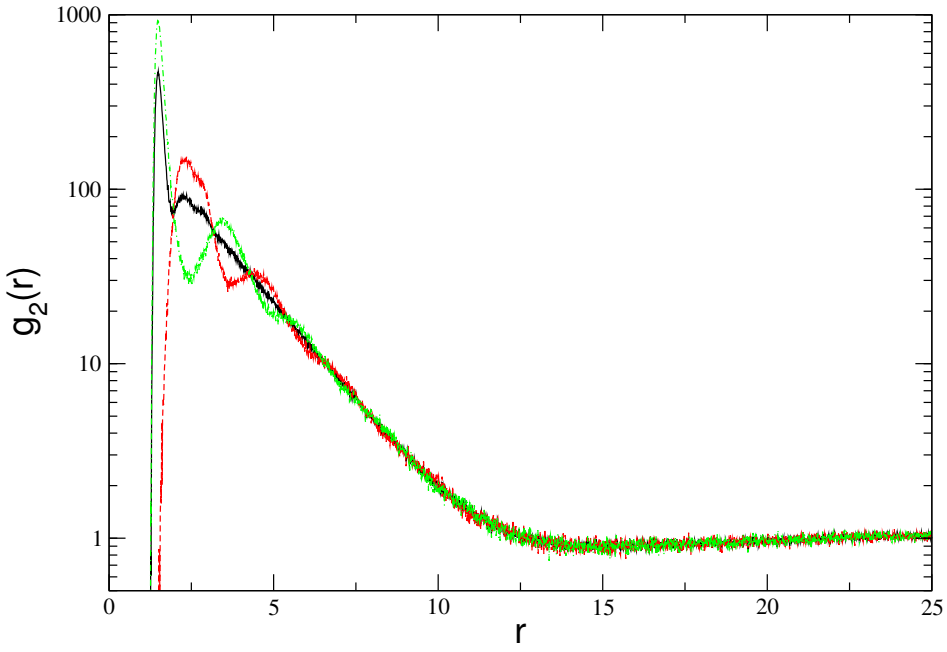


Figure 6.3.: Pair correlation functions for the ionic systems. The black continuous line shows the pair correlation function $g_2(r)$ ignoring the charge of the particles. The red dashed line presents $g_2^{++,--}(r)$, the result for identical charged particles, and the green doted $g_2^{+-}(r)$ is the result for oppositely charged particles. The results are taken from simulations close to the critical point at $T = 0.0163$ and $\rho = 0.006$.

tions are only minor. In the case of the RPM $u_\pm$ is a $-r^{-1}$-Coulomb potential and $R_>$ is given by the hard core repulsion. For the soft ions $u_\pm = 4r^{-12} - r^{-1}$ and $R_< = 0$. As the integral in eqn 6.2.7 does not converge for $R_> \to \infty$ a suitable upper limit for the integral needs to be identified. For the RPM we could approximate it as

$$K \approx 4\pi\sigma^3 \exp(1/T) \left[T + 2(T)^2 + 2(T)^3\right] \quad . \tag{6.2.8}$$

Here we use the fact that the particle distance for cation-anion pairs at low temperatures will be only slightly more than $\sigma$. We can use a similar approach for our soft sphere ions. We set the upper limit of the integral with the same criteria, we used to define two particles as paired. We can take a value close to the first minimum of the pair correlation function in figure 6.3. In our case we consider two ions as paired, if their separation is less than $R_< = 3.2$ and use the same value as upper limit for the calculation of $K$ in (6.2.7). In general it turns out that there are multiple options for the upper limit of the integrand. Using for instance the minimum of the integrand, i.e. $R_< \approx (2T)^{-1}$ as originally proposed

by Bjerrum, yields almost identical results. A discussion of the cutoff ambiguity can be found in Ref. [26].
To compare the theoretical results with our simulation for the soft sphere ions, we created several independent simulation runs for different temperatures and varied the density from $\rho = 10^{-10} - 10^{-1}$. All simulations were performed for $N = 800$ particles and $t^* = 5.25 \cdot 10^4$ LJ-time units for the high densities and up to $t^* = 5.25 \cdot 10^7$ for the very low densities. We also used different cutoffs from $r_{cut} = 10.0$ for high densities up to $r_{cut} = 200.0$ for the lowest ones. With the above mentioned distance criteria we considered two ions as paired if their separation is less than $r < 3.2$. The herewith calculated association $\alpha$ is plotted in figure 6.4 versus ion number density $\rho$ for temperatures between 0.04 to 0.08. We also included the theoretical results. We use equations 6.2.6 and (6.2.7) for the numerical computation of $K(T)$. Notice that $\alpha$, following an S-shaped curve, increases for increasing density. The threshold density, at which the steepest rise occurs, becomes lower with decreasing temperature, as expected. The comparison is not as good as for instance found in Ref. [7] for the RPM, following up on an earlier simulation study by Shelley and Patey [27]. But overall it supports the basic idea of ion pairing as a central ingredient for the understanding of this type of system.

## 6.3. Comparison between Ewald summation and the reaction-field method

Even though our comparison between the Lammps package and our own simulations does already indicate that the reaction field method and Ewald summation do yield the same results, we briefly want to double check the equivalence of the two methods in our system. The most common Coulomb long range methods used in computer simulations fall into two principal categories, the direct particle-particle calculation based on the Ewald summation technique [6, 28] and the continuum description established via the reaction-field method [8, 29–31]. The Ewald summation approach makes use of the periodicity of the system, which is established via the periodic boundary conditions and works perfectly on periodic systems. The reaction field method calculates the long-range interactions by embedding the particles into a structureless dielectric continuum. This requires the knowledge of the dielectric constant $\epsilon$ of the surrounding. The dielectric constant is *a priori* unknown, but luckily it can be calculated directly from the system [32].
As noted above, the two different ways to treat the long-range character of the Coulomb force had no big impact on the critical parameters of the ionic system. But for a detailed investigation of those two methods, we lower the temperature of our ionic model to the solid phase. Here the Ewald summation can be taken as reference, as this is the area for which it was developed. We calculate the Coulomb energy including the long-range correction for a system of particles with unit charge $\pm 1$ placed on a perfect NaCl lattice with the nearest neighbour spacing between ions equal to one. After a small random displacement,

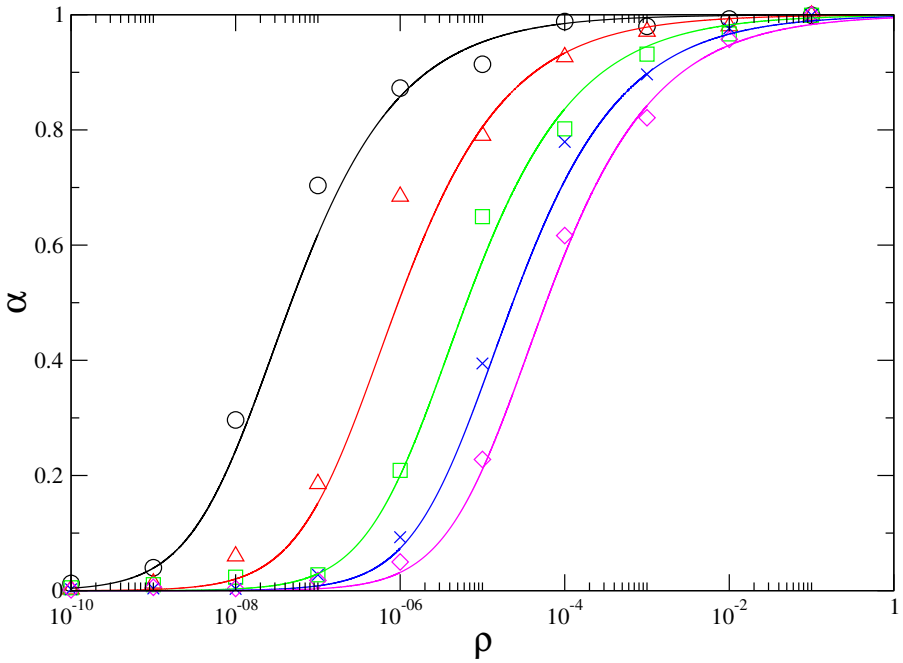


Figure 6.4.: Degree of association for the ionic fluid. The symbols show the simulation results taken for different temperatures along with the continuous lines in the same color calculated by the theoretical approach for $K$ given by 6.2.8. The temperatures correspond to $T = 0.04$ (circles), $T = 0.05$ (triangles), $T = 0.06$ (squares), $T = 0.07$ (crosses), $T = 0.08$ (diamonds).

$r$, of the individual particles we calculate the Coulomb energy per ion, $u_c$, of the system using both methods, i.e., reaction field and Ewald summation. In figure 6.5 the results of the two methods are shown as function of $r$. As expected the two methods do not correspond for small $r$ when the system is close to a perfect grid, whereas agreement improves for larger displacements, when the original lattice is completely randomized. Additionally we get similar results, if we apply the different methods on arbitrary simulation snapshots produced by our earlier simulation runs, which are not related to any lattice structure at all. This shows that for our computer simulations both techniques can be used to treat the long range contribution of the Coulomb force. This is also in compliance with other comparisons found in literature. Especially Neumann *et al.* did several studies of the reaction field method for dipolar systems using a lattice approach [31, 33] and also the Ewald summation method [34]. He showed that both methods produce similar results. The results of Benavides *et al.* [35], who extended the comparison of dipolar fluids to

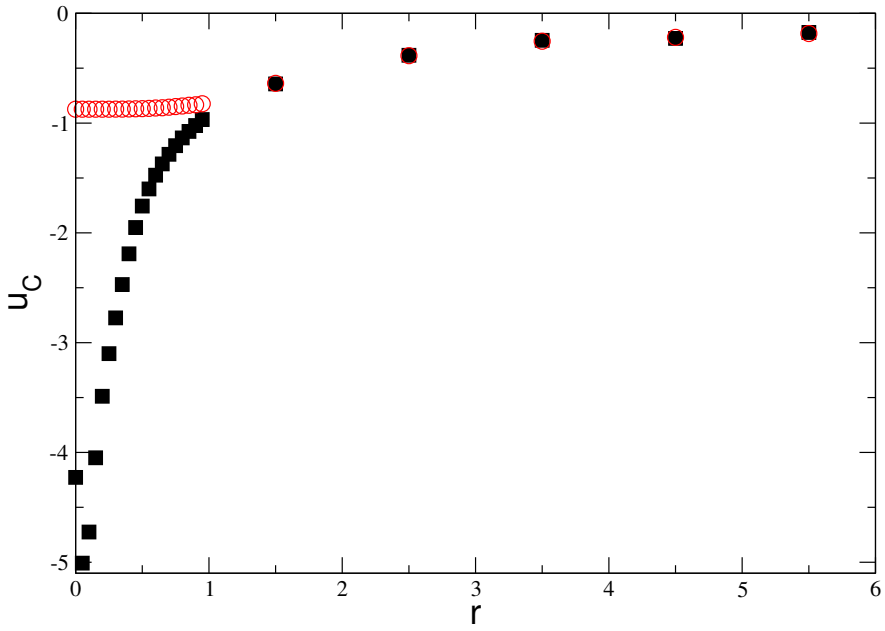


Figure 6.5.: Total Coulomb energy for a FCC lattice over the displacement of the particles $r$ to the lattice for the Ewald summation technique (circles) and reaction field method (squares)

consider also the quadrupole interactions, and Nymand *et al.* [15], who used also charged particles, strengthen the view, that both methods produce consistent results.

# Bibliography


[1] H. Braun and R. Hentschke. Tracking gas-liquid coexistence in fluids of charged soft dumbbells. *Physical Review E*, 80(4):041501, 2009.

[2] R. Jia, H. Braun, and R. Hentschke. Gas-liquid coexistence in a system of dipolar soft spheres. *Physical Review E*, 82(6):062501, 2010.

[3] M. E. Fisher and Y. Levin. Criticality in ionic fluids: Debye-Hückel theory, Bjerrum, and beyond. *Physical Review Letters*, 71(23):3826, 1993.

[4] Y. Levin and M. E. Fisher. Criticality in the hard-sphere ionic fluid. *Physica A: Statistical Mechanics and its Applications*, 225(2):164, 1996.

[5] S. Plimpton. Fast parallel algorithms for short-range molecular dynamics. *Journal of Computational Physics*, 117(1):1, 1995.

[6] P. P. Ewald. Die Berechnung optischer und elektrostatischer Gitterpotentiale. *Annalen der Physik*, 369(3):253, 1921.

[7] C. Valeriani, P. J. Camp, J. W. Zwanikken, R. van Roij, and M. Dijkstra. Ion association in low-polarity solvents: Comparisons between theory, simulation, and experiment. *Soft Matter*, 6(12):2793, 2010.

[8] I. G. Tironi, R. Sperb, P. E. Smith, and W. F. van Gunsteren. A generalized reaction field method for molecular dynamics simulations. *Journal of Chemical Physics*, 102(13):5451, 1994.

[9] H. J. C. Berendsen, J. P. M. Postma, W. F. van Gunsteren, A. DiNola, and J. R. Haak. Molecular dynamics with coupling to an external bath. *Journal of Chemical Physics*, 81(8):3684, 1984.

[10] R. W. Hockney and J. W. Eastwood. *Computer simulation using particles*. CRC Press, 1988.

[11] S. Plimpton, R. Pollock, and M. Stevens. Particle-mesh Ewald and rRESPA for

parallel molecular dynamics simulations. In *PPSC*. Citeseer, 1997.

[12] W. G. Hoover. Canonical dynamics: Equilibrium phase-space distributions. *Physical Review A*, 31(3):1695, 1985.

[13] C. G. Gray, Y. S. Sainger, C. G. Joslin, P. T. Cummings, and S. Goldman. Computer simulation of dipolar fluids. Dependence of the dielectric constant on system size: A comparative study of Ewald sum and reaction field approaches. *Journal of Chemical Physics*, 85(3):1502, 1986.

[14] C. Millot, J. Soetens, and M. T. C. Martins Costa. Static dielectric constant of the polarizable Stockmayer fluid. Comparison of the lattice summation and reaction field methods. *Molecular Simulation*, 18:367, 1997.

[15] T. M. Nymand and P. Linse. Ewald summation and reaction field methods for potentials with atomic charges, dipoles, and polarizabilities. *The Journal of Chemical Physics*, 112(14):6152, 2000.

[16] T. M. Nymand and P. Linse. Molecular dynamics simulations of polarizable water at different boundary conditions. *The Journal of Chemical Physics*, 112(14):6386, 2000.

[17] J. P. Valleau. The coulombic phase transition: Density-scaling Monte Carlo. *The Journal of Chemical Physics*, 95:584, 1991.

[18] A. Z. Panagiotopoulos. Molecular simulation of phase equilibria: Simple, ionic and polymeric fluids. *Fluid Phase Equilibria*, 76:97, 1992.

[19] A. Z. Panagiotopoulos. Critical parameters of the restricted primitive model. *The Journal of Chemical Physics*, 116(7):3007, 2002.

[20] J. M. Caillol, D. Levesque, and J. J. Weis. Critical behavior of the restricted primitive model revisited. *Journal of Chemical Physics*, 116(24):10794, 2002.

[21] P. Debye and E. Hückel. De la théorie des électrolytes. i. abaissement du point de congélation et phénomènes associés. *Physikalische Zeitschrift*, 24(9):185, 1923.

[22] C. D. Daub, G. N. Patey, and P. J. Camp. Liquid–vapor criticality in a fluid of charged hard dumbbells. *The Journal of Chemical Physics*, 119(15):7952, 2003.

[23] A. Nikoubashman, J. Hansen, and G. Kahl. Mean-field theory of the phase diagram of ultrasoft, oppositely charged polyions in solution. *The Journal of Chemical Physics*, 137(9):094905, 2012.

[24] C. Valeriani, P. J. Camp, J. W. Zwanikken, R. Van Roij, and M. Dijkstra. Computer simulations of the restricted primitive model at very low temperature and density. *Journal of Physics: Condensed Matter*, 22(10):104122, 2010.

[25] N. Bjerrum. Analysis of ionic association. *Kongelige Danske Videnskabernes Selskab Mathematisk-Fysiske Meddelelser*, 7:1, 1926.

[26] M. E. Fisher. The story of coulombic critiality. *Journal of Statistical Physics*, 75(1-2):1, 1994.

[27] J. C. Shelley and G. N. Patey. A comparison of liquid–vapor coexistence in charged hard sphere and charged hard dumbbell fluids. *The Journal of Chemical Physics*, 103(18):8299, 1995.

[28] M. P. Allen and D. J. Tildesley. *Computer Simulation of Liquids*. Oxford University Press, 1989.

[29] J. G. Kirkwood. Theory of solutions of molecules containing widely separated charges with special application to zwitterions. *The Journal of Chemical Physics*, 2:351, 1934.

[30] L. Onsager. Electric moments of molecules in liquids. *Journal of the American Chemical Society*, 58:1486, 1936.

[31] M. Neumann. Dipole moment fluctuation formulas in computer simulations of polar systems. *Molecular Physics*, 50(4):841, 1983.

[32] P. E. Smith and W. F. van Gunsteren. Consistent dielectric properties of the simple point charge and extended simple point charge water models at 277 and 300 K. *The Journal of Chemical Physics*, 100:3169, 1994.

[33] M. Neumann, O. Steinhauser, and G. S. Pawley. Consistent calculation of the static and frequency-dependent dielectric constant in computer simulations. *Molecular Physics*, 52(1):97, 1984.

[34] M. Neumann. Dielectric properties and the convergence of multipolar lattice sums. *Molecular Physics*, 60:225, 1987.

[35] A. L. Benavides, Y. Guevara, and F. Del Río. Vapor-liquid equilibrium of a multipolar square-well fluid: I. Effect of multipolar strengths. *Physica A: Statistical Mechanics and its Applications*, 202(3):420, 1994.

# 7. Osmotic pressure of charged systems

In the first section of this chapter we explain osmosis and the osmotic pressure including a derivation of the van't Hoff equation following Ref. [1]. In the second section we document the results of our simulations and compare them to the van't Hoff equation as well as experimental results.

## 7.1. Osmosis and osmotic pressure

We consider a system which consists of two subsystems containing two types of particles. The first subsystem contains the solvent particles and the second one a mixture of the solvent and solute. The two subsystems can exchange particles through a semi-permeable membrane which confines the solute particles in the second subsystem but allows the solvent to pass the membrane in both directions. If we now start to monitor this kind of system as it is illustrated in figure 7.1, we observe that the solvent particles are exchanged between the two subsystems until chemical equilibrium of the solvent between the two subsystems is reached. Thus

$$\mu^*_{l,1}(T,p) = \mu_{l,2}(T,p+\pi,x_{l,2}) \tag{7.1.1}$$

where the left side is the chemical potential of the pure solvent in the beaker and the right side is the chemical potential of the solvent in the mixture inside the tube. Here we use the nominations that the index $l$ denominates the solvent and $s$ the solute. The beaker containing the pure solvent represents the first subsystem using index 1 and the tube the second one using index 2. In addition the asterisk $*$ indicates a pure substance. The temperature $T$ in both subsystems is identical, and $x_{l,2}$ is the solvent mole fraction inside the tube. The difference between the pressure $p+\pi$ in the tube and the external pressure $p$ is called osmotic pressure $\pi$. It is caused by the semi-permeable membrane which only allows the chemical equilibration of the solvent and not the solute. Comparing the setup shown in figure 7.1 together with the initial setup when the two surfaces are on the same level, and the tube only contains solute particles, the osmotic pressure $\pi$ can be calculated from the height of the liquid column inside the tube $h$ at equilibrium. With that it seems to be easy to measure the osmotic pressure. But as the effect is large, e.g. a one molar solution of sucrose has an osmotic pressure of about 27 atm. at 25°C [2], it is not as easy

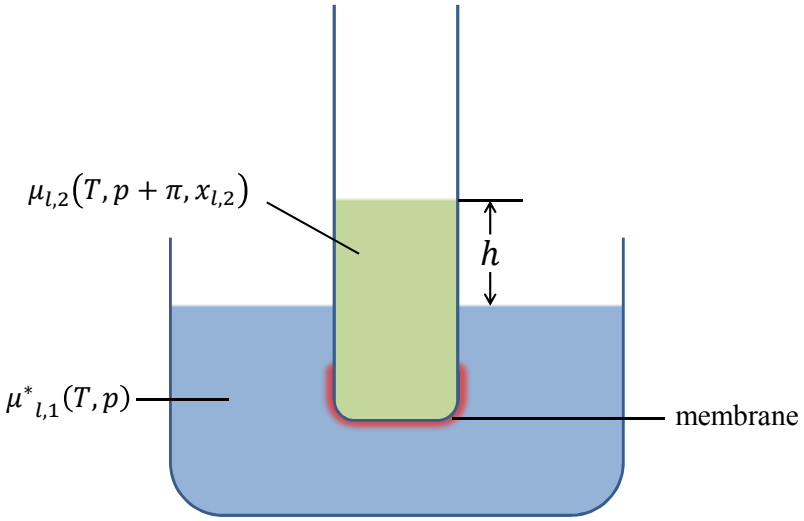


Figure 7.1.: A simple osmosis experiment is illustrated where a semi-permeable membrane separates the solution inside the tube from the solvent in the beaker. The solvent flows through the membrane increasing the amount of liquid and thus the height of the meniscus in the tube. This continues until the pressure generated by the liquid column is equal to the osmotic pressure of the solute.

as it seems. A special difficulty is the manufacturing of appropriate membranes which are truly semi-permeable.

In the following we want to derive the van't Hoff equation which is an expression for the osmotic pressure in an ideal solution. We start from the Gibbs-Duhem equation given by

$$-S\mathrm{d}T + V\mathrm{d}p + \ldots - \sum_{i=1}^{K} n_i \mathrm{d}\mu_i = 0 \tag{7.1.2}$$

where $K$ gives the number of components in the mixture and ... stands for other intensive variables in addition to $T$ and $p$. As in our case only the pressure $p$ and the chemical potential $\mu_l$ vary we can simplify it to

$$V^*(p)\mathrm{d}p - n_l^*\mathrm{d}\mu_l^* = 0\,. \tag{7.1.3}$$

Assuming incompressibility of the liquid, i.e. $V^*(p) = \text{const.}$, the integration of equation (7.1.3) yields

$$V^*(p)(p+\pi-p) \approx n_l{}^*\left[\mu_l{}^*(T, p+\pi) - \mu_l{}^*(T, p)\right]. \tag{7.1.4}$$

$l$

Replacing $\mu_l^*(T,p)$ via equation (7.1.1) in (7.1.4) yields

$$\mu_l^*(T,p+\pi) - \frac{1}{n_l^*}V^*(p)\pi \approx \mu_l(T,p+\pi,x_l) \tag{7.1.5}$$

with the chemical potential of the solvent in the mixture with the solute on the right side. With $x_l \gg x_{s,2}$ the effect of the solute on the chemical potential is given in the following equation [1, 3]

$$\mu_l(T,p+\pi,x_l) = \mu_l(T,p+\pi) + RT\ln x_l \tag{7.1.6}$$

and we can write

$$\mu_l^*(T,p+\pi) - \frac{1}{n_l^*}V^*(p)\pi \approx \mu_l(T,p+\pi) + RT\ln x_l\,. \tag{7.1.7}$$

With this we can finally write down the expression for the osmotic pressure

$$\pi \approx -\frac{RT}{V^*(p)/n_l^*}\ln x_l \tag{7.1.8}$$

$$\pi \approx \frac{RT}{V_{l,\mathrm{mol}}}x_{s,2} \tag{7.1.9}$$

where we have used the molar volume $V_{l,\mathrm{mol}} = V^*(p)/n_l^*$ of the solute at pressure $p$ and temperature $T$ and the approximation $\ln x_l = \ln(1-x_{s,2}) \approx -x_{s,2}$. This equation is obviously proportional to $x_{s,2}$. Here we already see some resemblance of the osmotic pressure in equation (7.1.9) to the pressure of the ideal gas. It becomes even more apparent with introducing another transformation

$$x_{s,2} = \frac{N_{s,2}}{N_{s,2}+N_{l,2}} \approx \frac{N_{s,2}}{N_{l,2}} \tag{7.1.10}$$

which yields together with $V_2 \approx V_{l,\mathrm{mol}}n_{l,2}$ the final van't Hoff equation

$$\pi \approx \frac{N_{s,2}k_BT}{V_2}\,. \tag{7.1.11}$$

This is no longer proportional to $x_{s,2}$ as it depends on the molar concentration $N_{s,2}/V_2 = x_{s,2}\cdot\rho_2$, where $\rho_2$, the density of the mixture, will change with increasing osmotic pressure. The equation is named after Jacobus van't Hoff, who in 1901 received the first Nobel prize in chemistry for his work on chemical dynamics and osmotic pressure in solutions. This result shows also that the osmotic pressure is a colligative quantity under the approximations we have made in the derivation as it only depends on the molar concentration $N_{s,2}/V_2$ of the solute and the temperature $T$.

## 7.2. Simulation results for osmotic pressure

In the following sections we first explain the details of the systems which we have studied. Then we present the results of a LJ model which we used to confirm the correctness of our simulation routines. Finally we discuss our results for the osmotic pressure in solutions of ions in a dipolar solvent.

### 7.2.1. The modified simulation models

We analyze the osmotic pressure for a mixture between dipolar particles as solvent and simple ions as solute. In addition we test our program routines using the LJ model. All three models have been already introduced in chapter 3. However in the following we use a slightly modified LJ pair potential given as

$$u_{ab}^{LJ}(r_{ij}) = 4\left[\left(\frac{\sigma_{ab}}{r_{ij}}\right)^{12} - \varepsilon_{ab}\left(\frac{\sigma_{ab}}{r_{ij}}\right)^{6}\right] \tag{7.2.1}$$

which allows us to introduce different attractive interactions between the particles using the parameter $\varepsilon_{ab}$ to model the solute and solvent particles for the LJ system. The adjustments to the long range corrections of the potential energy and pressure are defined in (2.5.34) and (2.5.35). Due to the importance of the potential energy for our MC simulation we express the energy correction again

$$U_{corr}^{LJ_{AB}} = -\frac{8}{3}\pi\sigma^3\left[-\frac{1}{3}\left(\frac{\sigma}{r_{cut}}\right)^9\frac{N^2}{V} + \left(\frac{\sigma}{r_{cut}}\right)^3\frac{\varepsilon_{AA}N_A^2 + \varepsilon_{BB}N_B^2 + 2\varepsilon_{AB}N_AN_{s,2}}{V}\right]. \tag{7.2.2}$$

Obviously we do not only have to deal with the parameter $\varepsilon_{ab}$ in the correction but also need to consider the mixture of solute and solvent particles.
For the pure systems of ST particles and ions we already have noted down in chapter 3 the interactions between the same kind of particles. But for the mixture we still have to treat the cross interactions between different kind of particles. For the non coulombic part of the interaction we use the modified LJ pair potential defined in equation (7.2.1) with the parameter

$$\varepsilon_{SI} = 0 \tag{7.2.3}$$

for the cross interaction between the Stockmayer(S) particles and the ions (I). For the interaction between the same particles we have

$$\varepsilon_{SS} = 1 \tag{7.2.4}$$

for the ST particles and

$$\varepsilon_{II} = 0 \tag{7.2.5}$$

for the ions. The charge-dipole pair potential, which is a monopole-dipole potential, between the particles $i$ and $j$ can be defined as [4]

$$u_{ij}^{CD}(\vec{r}_{ij}, \vec{\mu}_j) = \frac{q_i}{r_{ij}^3} \left(\vec{\mu}_j \cdot \vec{r}_{ij}\right) \tag{7.2.6}$$

where $q_i$ is the charge on the ion and $\vec{\mu}_j$ is the dipole moment vector of the ST particle. For the simulation we need to apply a cutoff distance $r_{cut}$ and therefore we have to take care of the contribution to the potential energy caused by the particles outside the cutoff sphere. As done previously, for the case of pure fluids, we make use of the reaction field method to describe the long range interaction of ions and dipolar ST particles beyond the cutoff radius. In equation (5.0.2) and (6.1.2) we have already taken care of the long range interaction for the dipole-dipole and the charge-charge interaction. Now we want to note down the terms for the charge-dipole interaction, which have to be considered in the calculation of the potential energy [5] for an ionic particle $i$ and the surrounding dipolar particles $j$

$$u_i^{C^{RF}} = -\frac{1}{4\pi\epsilon_0} \frac{2(\epsilon - 1)}{2\epsilon + 1} \frac{1}{r_{cut}^3} \sum_{j_\mu \in V_{Sp}(\vec{r}_i)} q_i \, \vec{\mu}_j \cdot \vec{r}_{ij} \tag{7.2.7}$$

and

$$u_i^{D^{RF}} = -\frac{1}{4\pi\epsilon_0} \frac{2(\epsilon - 1)}{2\epsilon + 1} \frac{1}{r_{cut}^3} \sum_{j_q \in V_{Sp}(\vec{r}_i)} q_j \, \vec{\mu}_i \cdot \vec{r}_{ij} \tag{7.2.8}$$

for the energy of a dipolar particle $i$ and an ionic particle $j$. The summation in the terms above includes all particles in the cutoff sphere $V_{Sp}(\vec{r}_i)$ of particle $i$. However, only the particles of different type to $i$ are considered noted by $j_q$ for ions and $j_\mu$ for dipoles. With these additional terms we can write for the total energy for an ion $i$ in the ion-dipole mixture

$$u_i^{Ion} = q_i \left[ \sum_{\substack{j_q \in V_{Sp}(\vec{r}_i) \\ j \neq i}} \left( \frac{q_j}{r_{ij}} - \frac{\epsilon - 1}{\epsilon} \frac{q_j}{r_{cut}} \right) - \frac{2(\epsilon - 1)}{2\epsilon + 1} \frac{1}{r_{cut}^3} \sum_{j_\mu \in V_{Sp}(\vec{r}_i)} \vec{\mu}_j \cdot \vec{r}_{ij} \right], \tag{7.2.9}$$

and in the same system for the dipole

$$\begin{aligned} u_i^{DP} = \vec{\mu}_i \Bigg[ & \sum_{\substack{j_\mu \in V_{Sp}(\vec{r}_i) \\ j \neq i}} \left( \frac{\vec{\mu}_j}{r_{ij}^3} - \frac{3\vec{r}_{ij} \left(\vec{r}_{ij} \cdot \vec{\mu}_j\right)}{r_{ij}^5} \right) \\ & - \frac{2(\epsilon - 1)}{2\epsilon + 1} \frac{1}{r_{cut}^3} \left( \sum_{\substack{j_\mu \in V_{Sp}(\vec{r}_i) \\ j \neq i}} \vec{\mu}_j + \sum_{j_q \in V_{Sp}(\vec{r}_i)} q_j \vec{r}_{ij} \right) \Bigg] \end{aligned} \tag{7.2.10}$$

where we have used $4\pi\epsilon_0 = 1$. So with these two expressions we can consider the reaction field in the calculation of the Metropolis criteria. From the existing literature we know that the reaction field method generates results which are in accordance with the Ewald summation technique. Amongst others the equivalence between the two methods was shown by Neumann [6] for dipolar systems. Bandura *et al.* [7] studied for ion solutions in dipolar solvent the thermodynamics and structure using the reaction field method and concludes that the method works well for mixtures of ions and dipoles for moderate values of dipole moments and charges.

### 7.2.2. Test of the simulation routines for a Lennard-Jones system

To verify that our simulation program produces reliable results we carried out simulations which allow us to compare our data with those published in the literature. The first test of our program routines continues the earlier discussion on g-l transition which we can analyze using the GEMC technique. We therefore use the ST system as we will use this model later on also for the analysis of the osmotic pressure in charged systems. In addition we also determine the critical parameters for the LJ system, which is as a special case of the ST system when $\mu^2 = 0$. Studying the LJ system is useful, because we will make use of it in our second test where we try to reproduce previous osmotic pressure results in the literature. Table 7.1 compiles our simulation results and compares them to data from the literature. As it turns out, the agreement is very good. A visual representation of

Table 7.1.: Critical parameters for the LJ, i.e. $\mu^2 = 0$, and ST system in comparison with results from the literature

| $\mu^2$ | $T_c$ | $\rho_c$ | $T_c^{lit}$ | $\rho_c^{lit}$ | Ref. |
|---|---|---|---|---|---|
| 0 | 1.310 | 0.296 | 1.316 | 0.304 | [8] |
| 1 | 1.402 | 0.303 | 1.41 | 0.30 | [9] |
| 2 | 1.601 | 0.312 | 1.60 | 0.31 | [9] |
| 3 | 1.815 | 0.308 | 1.82 | 0.312 | [10] |

the g-l phase coexistence area in critical units produced with our program can be found in figure 7.2. Corresponding coexistence curves can be found in Ref. [8–11]. Again, the good overall agreement confirms the proper performance of our program routines. The simulations for the LJ system were created using $N = N_1 + N_2 = 1000$ particles and $r^{cut} = 5.0$. In the case of the ST system we used $N = N_1 + N_2 = 4096$ with a cutoff $r_{cut} = 7.5$. In both cases the simulation was started at the density $\rho = 0.3$ in each box.

Having shown that our simulation program produces results in accordance with the literature, we can continue with the second test. We now apply the modified MC algorithm to the calculation of osmotic pressure. As done previously in our work group by Schreiber

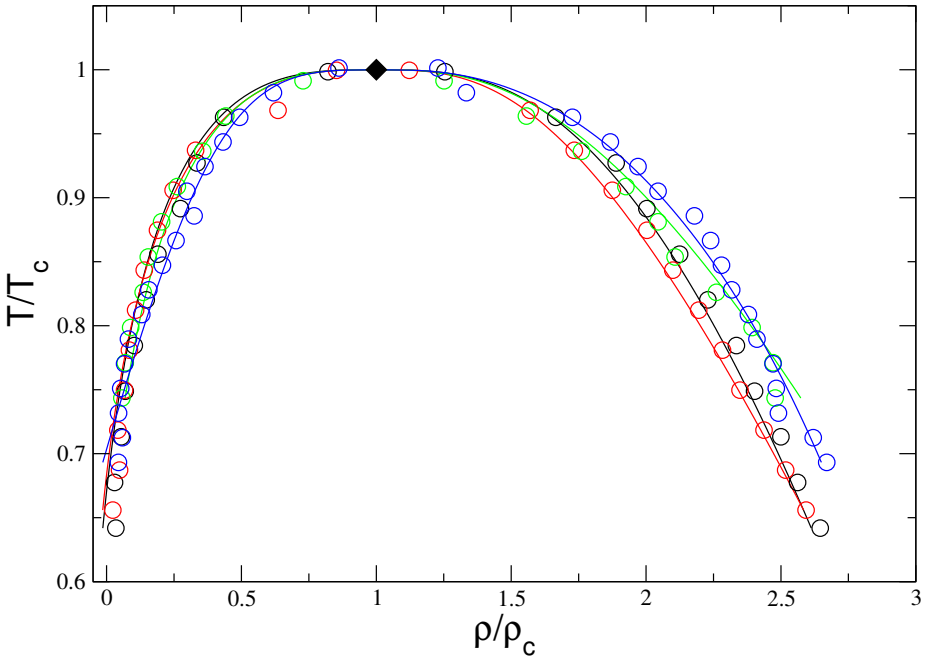


Figure 7.2.: Phase coexistence area in critical units for the LJ and ST model. The LJ model is shown in blue and the other colors are for the ST system with $\mu^2 = 1$ (black), $\mu^2 = 2$ (red) and $\mu^2 = 3$ (green). The black diamond shows the critical point.

[12, 13] we use the LJ model described in (7.2.1) which allows us a direct comparison to his results. We perform our first simulations in a system where all components interact with the same potential, i.e.

$$\varepsilon_{ab} = \varepsilon_{aa} = \varepsilon_{bb} \tag{7.2.11}$$

using $N_l = 500$ particles as solvent and either $N_{s,2} = 108$ or $N_{s,2} = 32$ (for $T = 3.418$) particles as solute. We analyze the solute mole fraction $x_{s,2}$ at fixed temperatures $T = 2.0$, $T = 3.418$ and $T = 6.0$ with different values of $\pi$ and a constant external pressure $p = 0.2$. The result is plotted in figure 7.3 where we show the osmotic pressure $\pi$ vs. the solute mole fraction $x_{s,2}$ for our simulations together with the data from Schreiber. In addition to the comparison with Schreiber we also included in figure 7.4 the comparison to the van't Hoff equation (7.2.12). It turns out that our data is in very good agreement with Schreiber as well as with the van't Hoff equation for the considered temperatures. Notice that the dependence of $\pi$ on $x_{s,2}$ is not strictly linear for the reason mentioned following equation (7.1.11). Notice also that the compressibility of the system, at the thermodynamic conditions used here, is much greater than that of a real liquid. We note

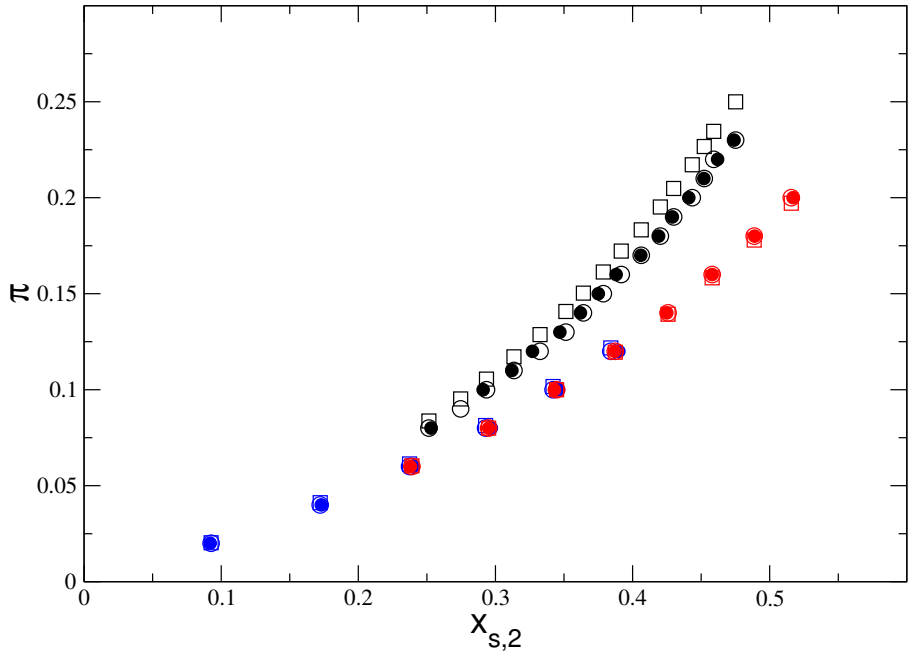


Figure 7.3.: Osmotic pressure $\pi$ of the LJ-fluid vs. the solute mole fraction $x_{s,2}$ for different temperatures and constant external pressure $p = 0.2$ in comparison to the results from Schreiber and the van't Hoff equation. The color coding represents the temperatures $T = 2.0$ (black), $T = 3.418$ (blue) and $T = 6.0$ (red). The open circles show our own data, filled circles the result from Schreiber and the open squares the values from the van't Hoff equation.

that we have not included in the plot the simulation results obtained for $T = 1.0$, which is below the critical point of the LJ system, because the box containing the solvent often runs empty and no stable state could be found. This also seemed to be a problem for Schreiber and therefore we can still trust the correctness of our simulation program and continue our further analysis without alterations.

Finally we want to study a mixture of different particles, i.e. with different interaction parameters $\varepsilon_{ab}$ in the LJ potential (7.2.1). Analogous to [13] we study the dependence of the solute mole fraction $x_{s,2}$ to the external pressure $p$ for different temperatures, osmotic pressures and in our case the interaction parameters $\varepsilon_{ss} = 0.5$ and $\varepsilon_{ll} = 1.0$. The results of our simulations which were performed with $N_l = 500$ and $N_{s,2} = 32$ for the temperatures $T = 1.0$ and $T = 2.0$ can be found in figure 7.4. As seen before our data is in very good agreement with Schreiber for the considered temperatures and interaction parameters.

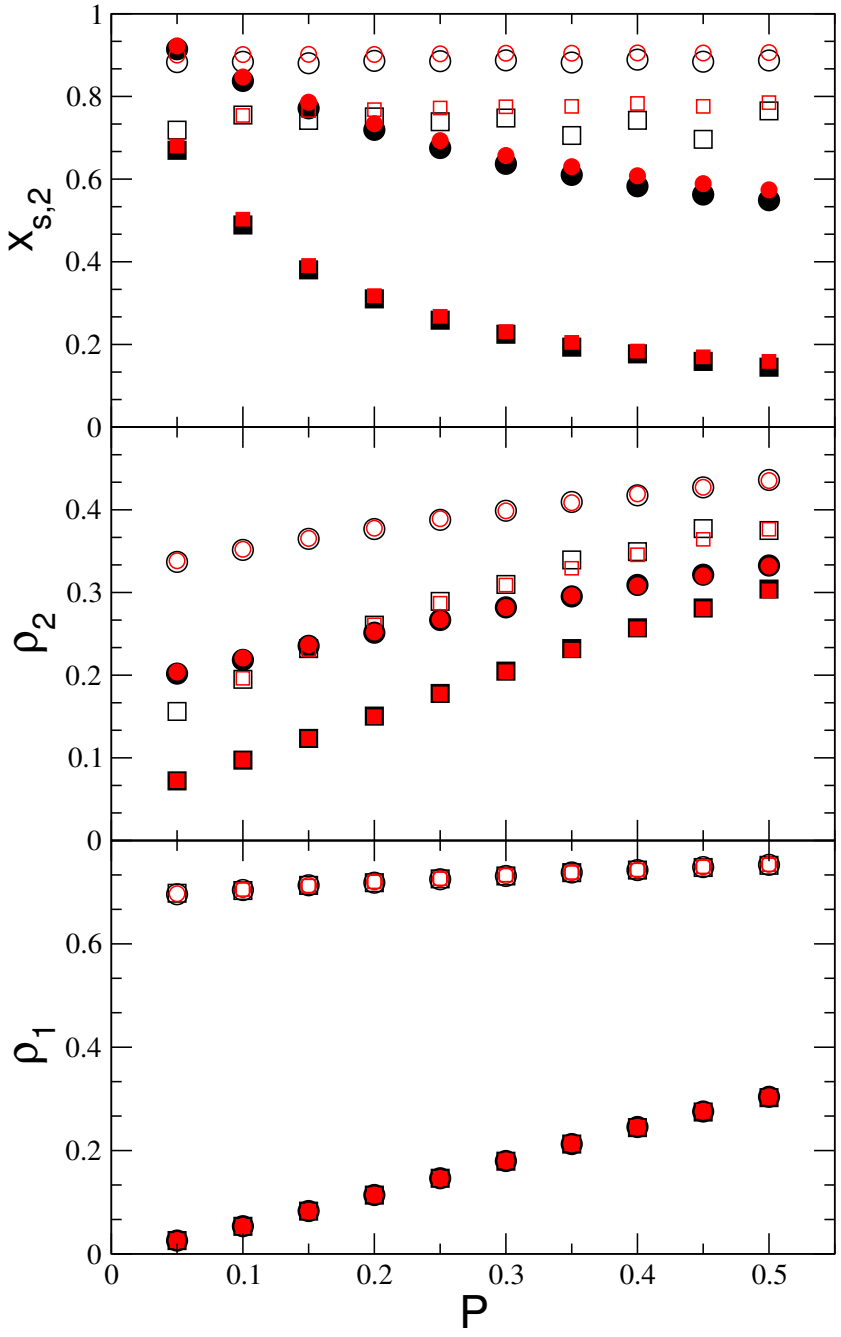


Figure 7.4.: Top: Solute mole fraction $x_{s,2}$ vs. the external pressure $p$. Middle: Total number density $\rho_2$ in box 2 containing the mixture vs. $p$. Bottom: Total number density $\rho_1$ in box 1 containing the solvent vs. $p$.
In all three panels the symbols represent $T = 1.0$, $\pi = 0.1$ (open squares); $T = 1.0$, $\pi = 0.5$ (open circles); $T = 2.0$, $\pi = 0.1$ (solid squares) and $T = 2.0$, $\pi = 0.5$ (solid circles). The black symbols show the data produced in this work and the red ones the results from Schreiber.

### 7.2.3. Results for charged systems

Now we extend our model of pure LJ molecules to consider also coulombic interactions and use ions as the solute and ST particles as the solvent. In addition to the fact that this type of mixture is more close to real compounds of salt and water it also allows us to see if the osmotic pressure is a colligative property, i.e. the type of particles we use in our simulation should not matter and the osmotic pressure only depends on the fraction of solute and solvent particles in box 2. Therefore also the van't Hoff equation

$$\pi_{vH} = \frac{N_{s,2}}{V_2} k_B T \tag{7.2.12}$$

should hold true to calculate the osmotic pressure for our mixture. To see if this is the case we first study the dependency of the solute mole fraction and the osmotic pressure for different temperatures $T$ in the range from $T = 2$ to $T = 6$. In addition we consider different combinations of ion charge $q$ and dipole strength $\mu^2$. We performed all our simulations with $N_l = 2000$ dipolar ST particles as the solvent together with $N_{s,2} = 108$ ion particles, i.e. 64 ion pairs, as solute. The external pressure of the system is set to $p = 0.2$ and the cutoff in our simulations is $r_{cut} = 10$. The results of our simulations is shown in figure 7.5 - 7.8, where we have plotted the osmotic pressure versus the solute mole fraction $x_{s,2}$. In addition to the simulation data the plots also show the osmotic pressure calculated via the van't Hoff equation (7.2.12) and another approximation of the osmotic pressure used during the deviation of the van't Hoff equation

$$\pi \approx -\frac{k_B T}{v_l(T,p)} \ln x_{l,2}(T,p)\,. \tag{7.2.13}$$

Here $v_l(T,p) = \langle V_1/N_{l,1} \rangle$ is the solvent partial mole volume and the solvent mole fraction is $x_{l,2}(T,p)$, both quantities are measured in $V_2$. For all temperatures the van't Hoff equation is in agreement with the simulation results for small solute mole fractions but the deviation to the simulation data increases with increasing solute mole fraction $x_{s,2}$. This increased deviation is no surprise as the approximations for the van't Hoff equation have been done under the assumption of a dilute system, i.e. small $x_{s,2}$. For the higher values of $x_{s,2}$ the van't Hoff equation is not linear anymore. Again this can be explained by one of the assumptions made for the van't Hoff equation which is the incompressibility of the fluid. For the condition we used the system is not necessary in its liquid state and therefore compressible. So the increased pressure affects the density $\rho_2$ in box 2 which leads to a change of the volume $V_2$. The additional approximation given in equation (7.2.13) does in general not provide a better estimate for the simulation data.
An interesting behavior can be seen due to the influence of the charge. In almost all cases the van't Hoff equation provides a too low value for the osmotic pressure except for the ion strength $q = 5.0$ and dipole moment $\mu^2 = 5.0$ where the calculated pressures are above the simulation data. This is caused by the strengthened tendency to form ion pairs and will be discussed again in the next section (7.2.4) where we compare the

data to experimental results. In addition to the increase for larger $x_{s,2}$ there is also a temperature dependence present for the deviation between the calculated values of the van't Hoff equation and our simulation results. This dependency is due to the fact that the simulated system behaves more and more like an ideal solution for high temperatures and therefore the deviations become smaller for bigger temperatures. To all this there is one outlier for $T = 2$ and $\mu^2 = 5$ where few solvent particles join the solute in box 2 and therefore the solute mole fraction $x_{s,2}$ reaches higher values with a larger gradient in comparison to the other results.

Similar to the LJ system we study in the following the dependency of our model on the external pressure $p$. Therefore we simulate different combinations of the osmotic pressure, temperature, dipole strength and ionic charge to analyze for various situations the influence of the external pressure on the solute mole fraction $x_{s,2}$ and the total number densities $\rho_1$, $\rho_2$ in the two simulation boxes. All the simulations are performed with $N_{s,2} = 108$ ionic solute particles and $N_l = 500$ ST particles as the solvent. For the sake of illustration we have selected some of our results and plotted the solute mole fraction $x_{s,2}$, the total number densities $\rho_1$ and $\rho_2$ vs. the external pressure $p$ in the figures 7.9 - 7.12. For the lowest temperature $T = 1.0$ there is no pressure dependence apparent for the solute mole fraction and only a few solvent particles make it into box 2, i.e. $x_{s,2} \approx 1$ over the examined pressure interval. The density $\rho_1$ can be considered as rather constant and for $\rho_2$ we have an increase of the density at higher pressures. The gradient of the pressure dependency is influenced by the strength of the solute-solute interaction. For weak interaction $q = 1$ the increase is higher than for strong ion charges $q = 5$. This can be seen comparing figures 7.9 and 7.10 or 7.11 and 7.12. All this is true for both osmotic pressures applied, i.e. $\pi = 0.1$ and $\pi = 0.5$. Overall the densities at $T = 1.0$ are the highest compared to the other temperatures. On increasing the temperature to $T = 2.0$ an effect of the pressure on the solute mole fraction is still not present in the case of high solute-solute interaction, i.e. $q = 5.0$. But for the weaker interaction with $q = 1.0$ the pressure dependence becomes obvious in combination with the dipoles of strength $\mu^2 = 1$. For $\mu^2 = 5$ and the high osmotic pressure $\pi = 0.5$ it is again not observable. Whereas for $\pi = 0.1$ the dependency is still apparent (see figure 7.11) but in contradiction to the other results the solute mole fraction rises for higher external pressures $p$. Looking at the highest temperature $T = 3.0$ we find a distinct relationship between the external pressure and $x_{s,2}$ for almost all results except for $\mu^2 = 1$, $q = 5.0$ and $\pi = 0.5$ where the solute mole fraction is more or less constant. For all the cases where a pressure dependency is apparent the higher osmotic pressure leads to a higher solute mole fraction as expected. In general the influence of the solute-solute interaction strength is similar to the findings from Schreiber [13] who has studied LJ fluid mixtures. There it was also observed that for stronger solute-solute interactions higher temperatures were necessary to observe an effect of the external pressure to the solute mole fraction $x_{s,2}$. Again as for the LJ system in our case the box containing the solvent is not influenced by the characteristics of the solute as can be seen in figure 7.9 and 7.10 respectively 7.11 and 7.12, where the density $\rho_1$ is almost

identical for the same dipole strength. To evaluate finite size effects for our simulation results we performed, at selected thermodynamic conditions, additional simulations with $N_{s,2} = 256$ ions and $N_l = 1200$ ST particles. The results are indicated by the crosses in the figures 7.9 - 7.12. Overall they are very close to the values for the smaller system and we can preclude the existence of finite size effects sufficiently pronounced to obscure the present results..

As mentioned above the figures 7.9 - 7.12 are chosen exemplarily. The results of the remaining simulations are added for the sake of completeness to the appendix and can be found in the figures B.1 - B.8.

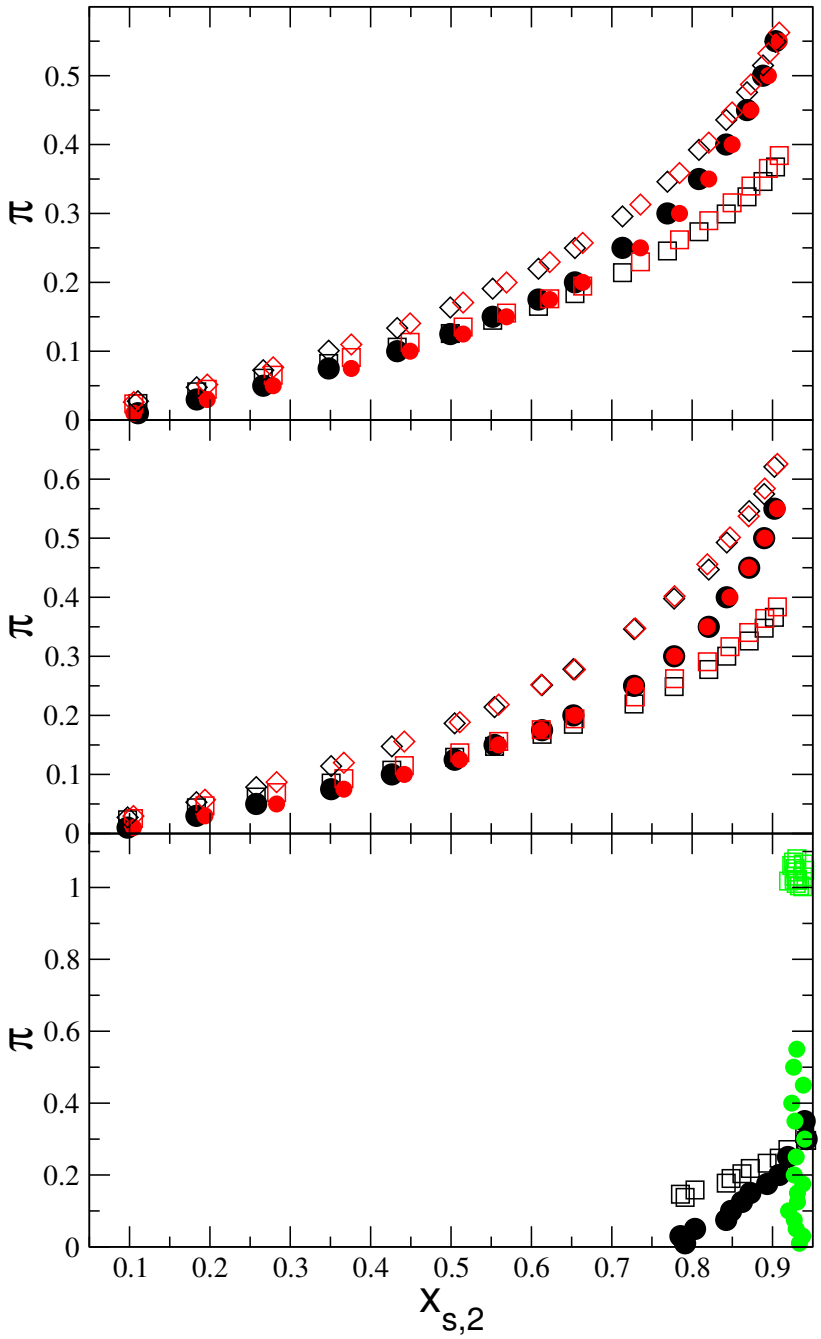


Figure 7.5.: In all three panels the osmotic pressure $\pi$ of the ion-dipole mixture vs. the solute mole fraction $x_{s,2}$ is plotted for the temperature $T = 2.0$ with constant external pressure $p = 0.2$ in comparison to the approximations of the osmotic pressure. The solid circles show our own data, the open squares the values from the van't Hoff equation (7.2.12) and the open diamonds the approximation in equation (7.2.13).
Top: Solvent $\mu^2 = 1.0$ with solute $q = 1.0$ (black) and $q = 2.0$ (red)
Middle: Solvent $\mu^2 = 2.0$ with solute $q = 1.0$ (black) and $q = 2.0$ (red)
Bottom: Solvent $\mu^2 = 5.0$ with solute $q = 1.0$ (black) and $q = 5.0$ (green)

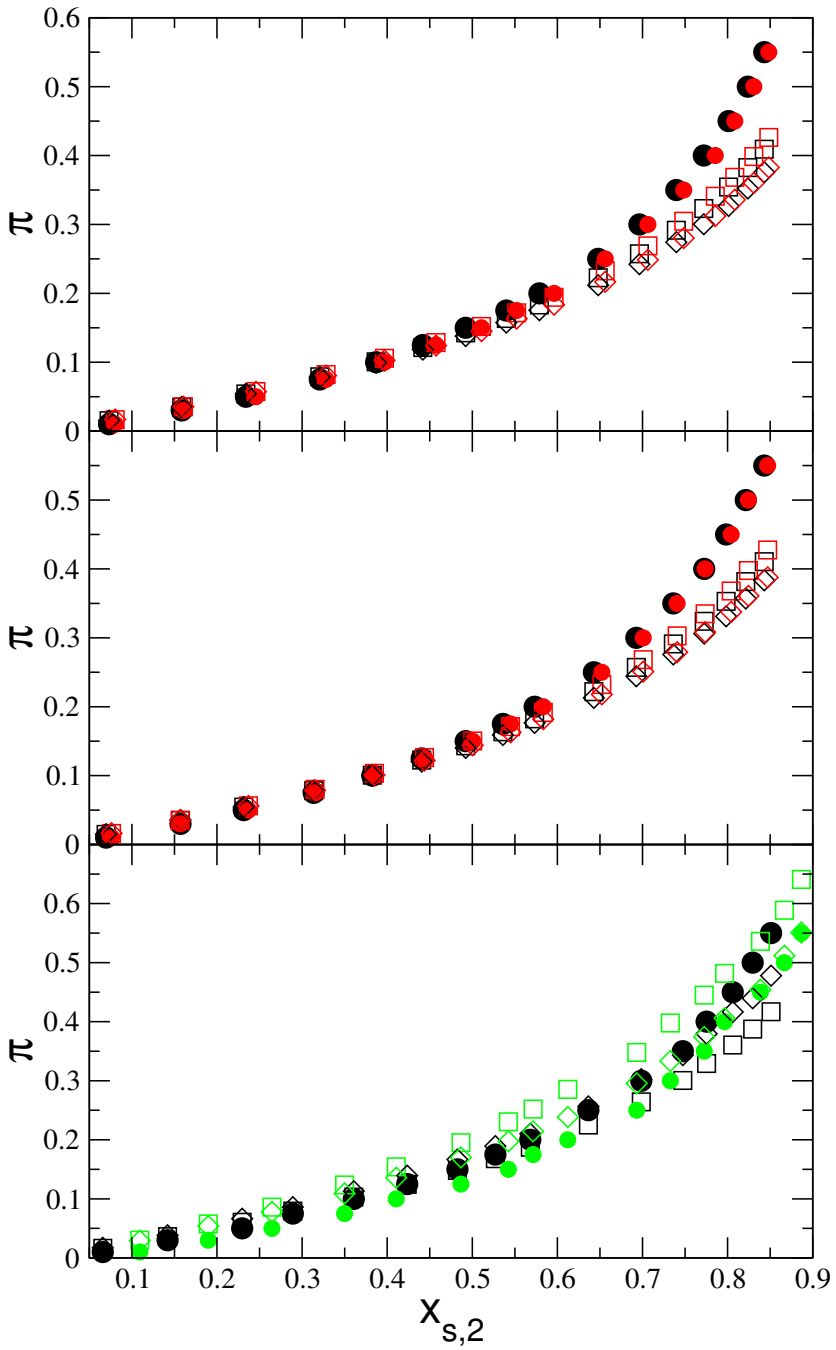


Figure 7.6.: In all three panels the osmotic pressure $\pi$ of the ion-dipole mixture vs. the solute mole fraction $x_{s,2}$ is plotted for the temperature $T = 3.0$ with constant external pressure $p = 0.2$ in comparison to the approximations of the osmotic pressure. The solid circles show our own data, the open squares the values from the van't Hoff equation (7.2.12) and the open diamonds the approximation in equation (7.2.13).
Top: Solvent $\mu^2 = 1.0$ with solute $q = 1.0$ (black) and $q = 2.0$ (red)
Middle: Solvent $\mu^2 = 2.0$ with solute $q = 1.0$ (black) and $q = 2.0$ (red)
Bottom: Solvent $\mu^2 = 5.0$ with solute $q = 1.0$ (black) and $q = 5.0$ (green)

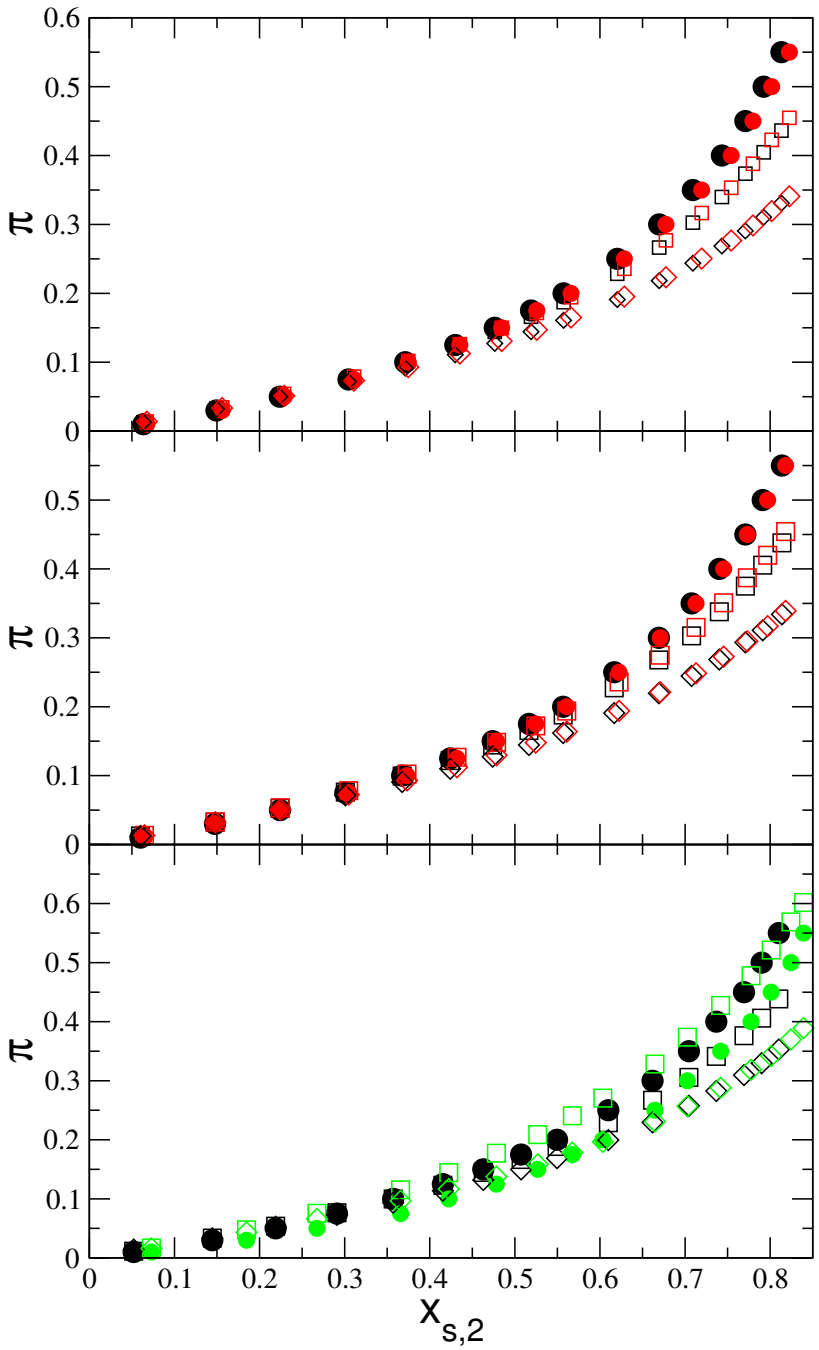


Figure 7.7.: In all three panels the osmotic pressure $\pi$ of the ion-dipole mixture vs. the solute mole fraction $x_{s,2}$ is plotted for the temperature $T = 4.0$ with constant external pressure $p = 0.2$ in comparison to the approximations of the osmotic pressure. The solid circles show our own data, the open squares the values from the van't Hoff equation (7.2.12) and the open diamonds the approximation in equation (7.2.13).
Top: Solvent $\mu^2 = 1.0$ with solute $q = 1.0$ (black) and $q = 2.0$ (red)
Middle: Solvent $\mu^2 = 2.0$ with solute $q = 1.0$ (black) and $q = 2.0$ (red)
Bottom: Solvent $\mu^2 = 5.0$ with solute $q = 1.0$ (black) and $q = 5.0$ (green)

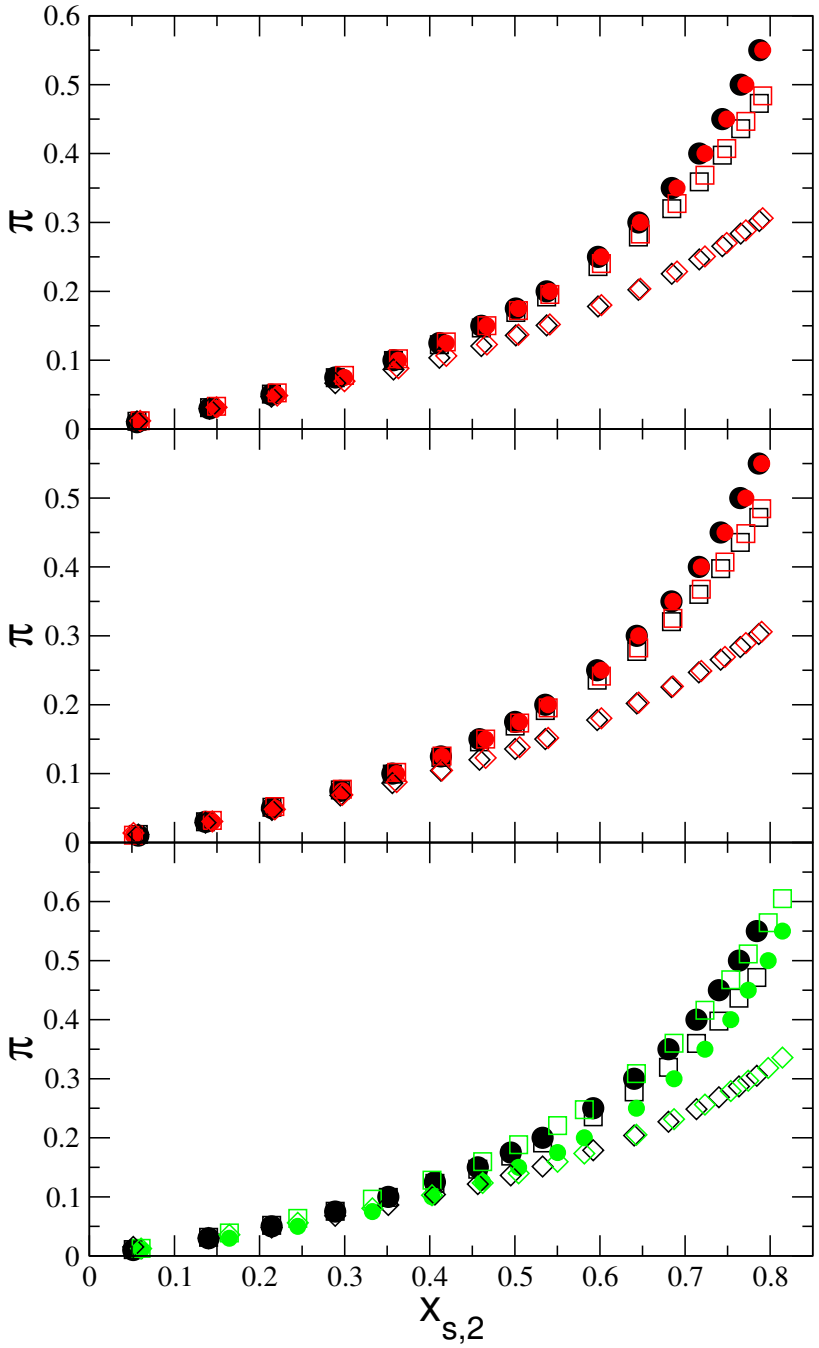


Figure 7.8.: In all three panels the osmotic pressure $\pi$ of the ion-dipole mixture vs. the solute mole fraction $x_{s,2}$ is plotted for the temperature $T = 6.0$ with constant external pressure $p = 0.2$ in comparison to the approximations of the osmotic pressure. The solid circles show our own data, the open squares the values from the van't Hoff equation (7.2.12) and the open diamonds the approximation in equation (7.2.13).
Top: Solvent $\mu^2 = 1.0$ with solute $q = 1.0$ (black) and $q = 2.0$ (red)
Middle: Solvent $\mu^2 = 2.0$ with solute $q = 1.0$ (black) and $q = 2.0$ (red)
Bottom: Solvent $\mu^2 = 5.0$ with solute $q = 1.0$ (black) and $q = 5.0$ (green)

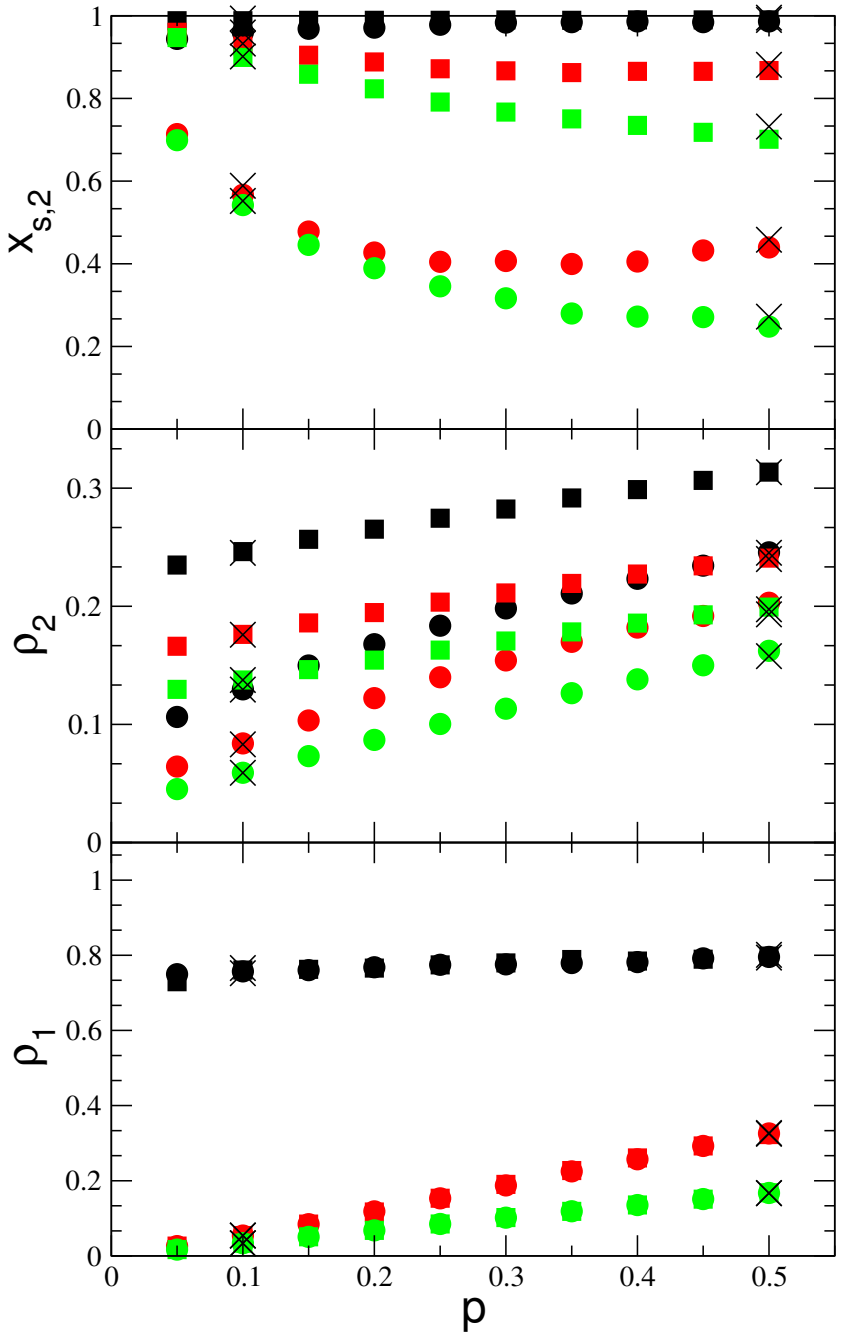


Figure 7.9.: Pressure dependency of the coulombic mixture for dipole strength $\mu^2 = 1$ and ion charge $q = 1$. Top: Solute mole fraction $x_{s,2}$ vs. the external pressure $p$. Middle: Total number density $\rho_2$ in box 2 containing the mixture vs. $p$. Bottom: Total number density $\rho_1$ in box 1 containing the solvent vs. $p$. In all three panels the colors represent $T = 1.0$ (black), $T = 2.0$ (red) and $T = 3.0$ (green). The shape of the symbols stand for $\pi = 0.1$ (circles) and $\pi = 0.5$ (squares).

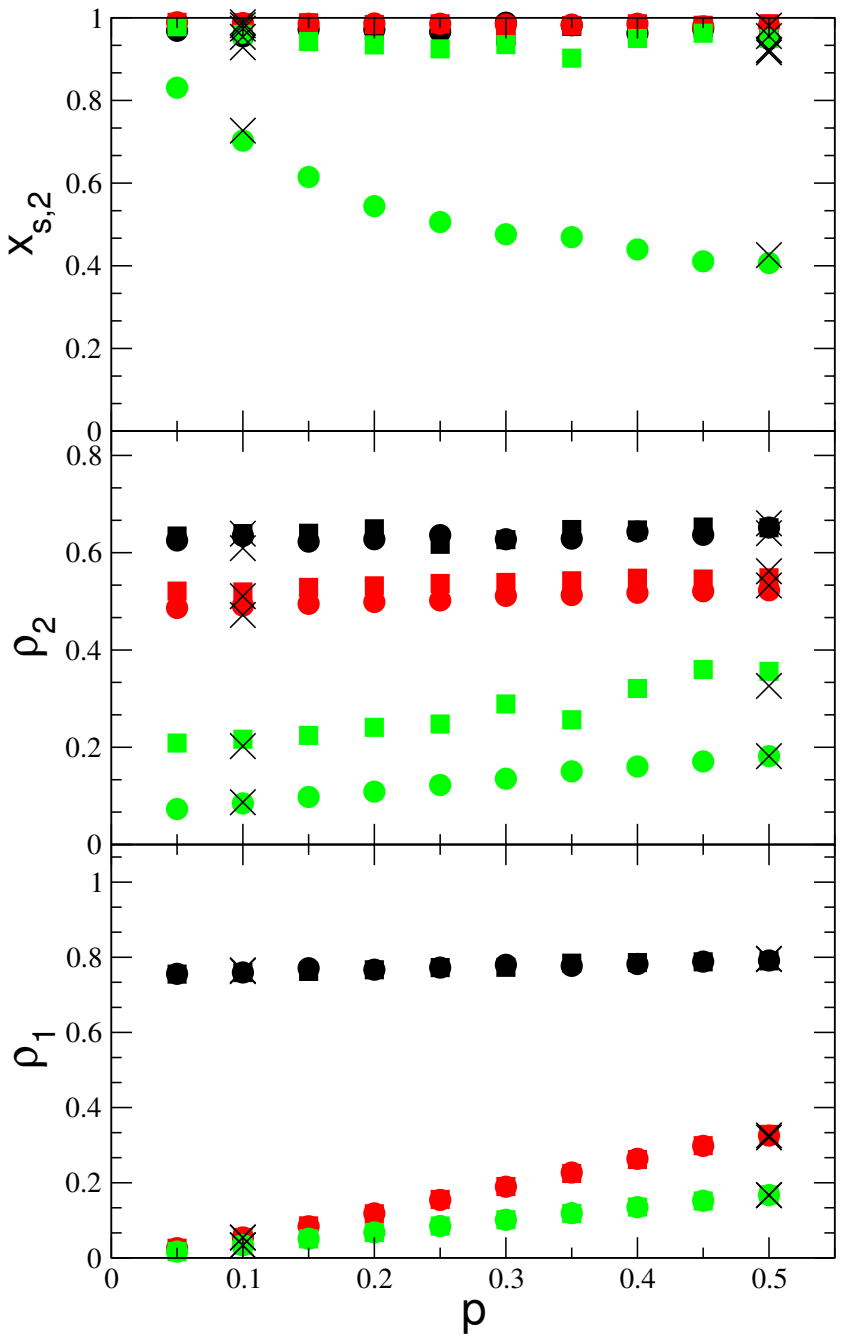


Figure 7.10.: Pressure dependency of the coulombic mixture for dipole strength $\mu^2 = 1$ and ion charge $q = 5$. Top: Solute mole fraction $x_{s,2}$ vs. the external pressure $p$. Middle: Total number density $\rho_2$ in box 2 containing the mixture vs. $p$. Bottom: Total number density $\rho_1$ in box 1 containing the solvent vs. $p$. In all three panels the colors represent $T = 1.0$ (black), $T = 2.0$ (red) and $T = 3.0$ (green). The shape of the symbols stand for $\pi = 0.1$ (circles) and $\pi = 0.5$ (squares).

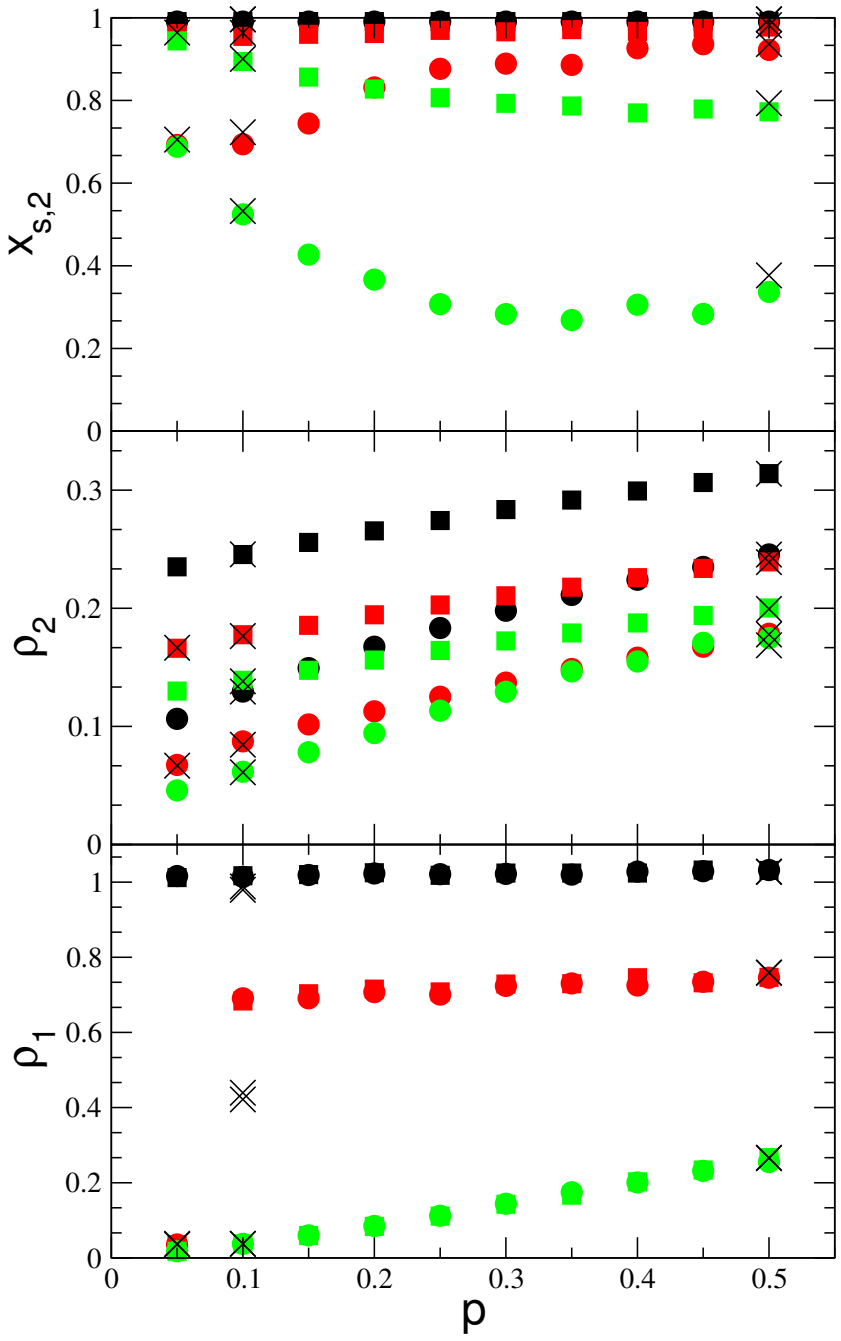


Figure 7.11.: Pressure dependency of the coulombic mixture for dipole strength $\mu^2 = 5$ and ion charge $q = 1$. Top: Solute mole fraction $x_{s,2}$ vs. the external pressure $p$. Middle: Total number density $\rho_2$ in box 2 containing the mixture vs. $p$. Bottom: Total number density $\rho_1$ in box 1 containing the solvent vs. $p$. In all three panels the colors represent $T = 1.0$ (black), $T = 2.0$ (red) and $T = 3.0$ (green). The shape of the symbols stand for $\pi = 0.1$ (circles) and $\pi = 0.5$ (squares).

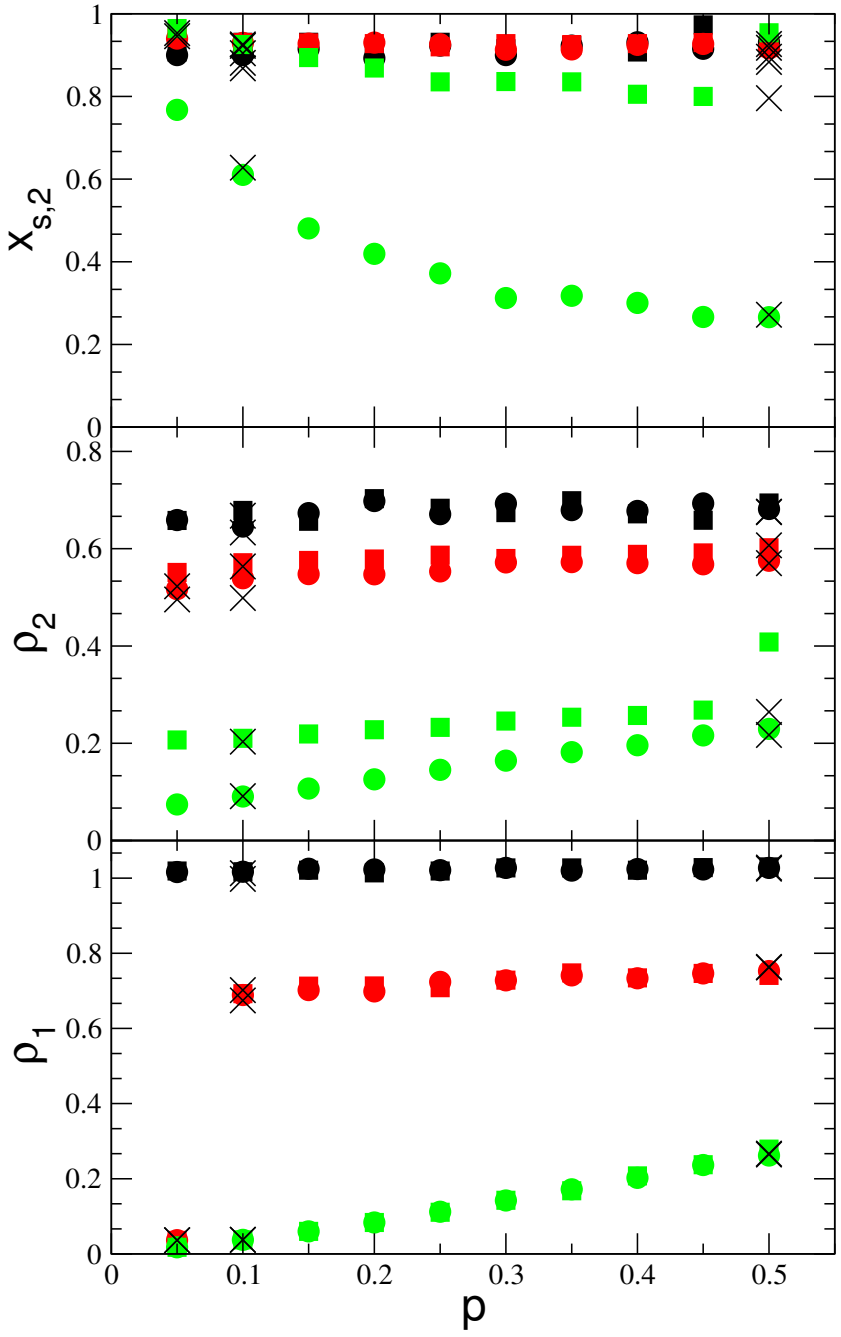


Figure 7.12.: Pressure dependency of the coulombic mixture for dipole strength $\mu^2 = 5$ and ion charge $q = 5$. Top: Solute mole fraction $x_{s,2}$ vs. the external pressure $p$. Middle: Total number density $\rho_2$ in box 2 containing the mixture vs. $p$. Bottom: Total number density $\rho_1$ in box 1 containing the solvent vs. $p$. In all three panels the colors represent $T = 1.0$ (black), $T = 2.0$ (red) and $T = 3.0$ (green). The shape of the symbols stand for $\pi = 0.1$ (circles) and $\pi = 0.5$ (squares).

### 7.2.4. Comparison with experimental results

We use the experimental data given in [14] to compare the simulation results with the experiment. Here the osmotic coefficient $\phi$ of electrolytes in water is expressed in dependence on the molality $m$, which is defined as the number of moles of solute per kilogram of solvent. The osmotic coefficient describes the deviation of the osmotic pressure $\pi$ from the van't Hoff approximation $\pi_{vH}$ in equation (7.2.12). It is a useful definition for the purpose of the comparison, as it is unitless. To convert the molality into $x_{s,2}$ we use the following formulas

$$x_{s,2} = \frac{N_{s,2}}{N_{l,2}+N_{s,2}} = \left[\frac{N_{l,2}}{N_{s,2}}+1\right]^{-1} = \left[\frac{1}{m\cdot\nu\cdot M_W}+1\right]^{-1} = \frac{m\cdot\nu\cdot M_W}{1+m\cdot\nu\cdot M_W} \tag{7.2.14}$$

with the molar mass of water given by $M_W = 0.01801528$ kg/mol and $\nu$ the number of moles of ions formed from 1 mole of electrolytes, e.g. $\nu = 1$ for ions, $\nu = 2$ for NaCl.
The osmotic coefficient is related to the osmotic pressure $\pi$ via the following expression [2]

$$\pi = \frac{\nu R T M_W}{V_{l,\mathrm{mol}}}\cdot\phi\cdot m = \frac{N_{s,2}}{n_{l,2}}k_B T\frac{1}{V_{l,\mathrm{mol}}}\phi \approx \frac{N_{s,2}}{V_2}k_B T\phi = \pi_{vH}\phi \tag{7.2.15}$$

$$\phi = \frac{\pi}{\pi_{vH}}\,. \tag{7.2.16}$$

Here again the approximation $V_2 \approx n_{l,2}\cdot V_{l,\mathrm{mol}}$, which is valid for small concentrations, is used. Experimentally three kinds of behavior can be recognized as described in [2]. Very high osmotic coefficients are taken as evidence for extensive hydration of the ions, while low osmotic coefficients are explained by ion-pair formation. In case of complex ion formation the osmotic coefficient can become very low.
As can be seen in figure 7.13 the simulated osmotic coefficient does not deviate from the ideal behavior as much as some of the experimental curves. This may be due to the differences between a simple ST fluid as solvent in comparison to the more complex water. To compare the simulation results more thoroughly with the experimental data, we use the LJ parameters of TIP4P/2005 (transferable intermolecular potential 4 point) water (see appendix A) to compare temperatures, dipole moments and charges of our results with those of [14]. We see in table 7.2 that the largest dipole moment used in our simulation is still smaller than the one of TIP4P/2005 water ($\mu = 2.305$ Debye). Also the ion charges used are quite small and only reaching 0.20987 $e$. While all experimental data was measured at 25 °C, the simulations span the region of 6 to 286 °C. Looking at experimental data from 0 to 100 °C presented in [2] the temperature dependence of the osmotic coefficient is not very large. This can also be found looking into the simulation results in figure 7.13. Here the osmotic coefficient is slowly approaching the ideal value of 1 with increasing temperature.

The experimental results all show a decreasing osmotic coefficient for small $x_{s,2}$. Unfortunately we do not have any data for such small concentrations as the size of our simulation systems was not large enough for this. KF, $HNO_3$ and CsCl are then rising

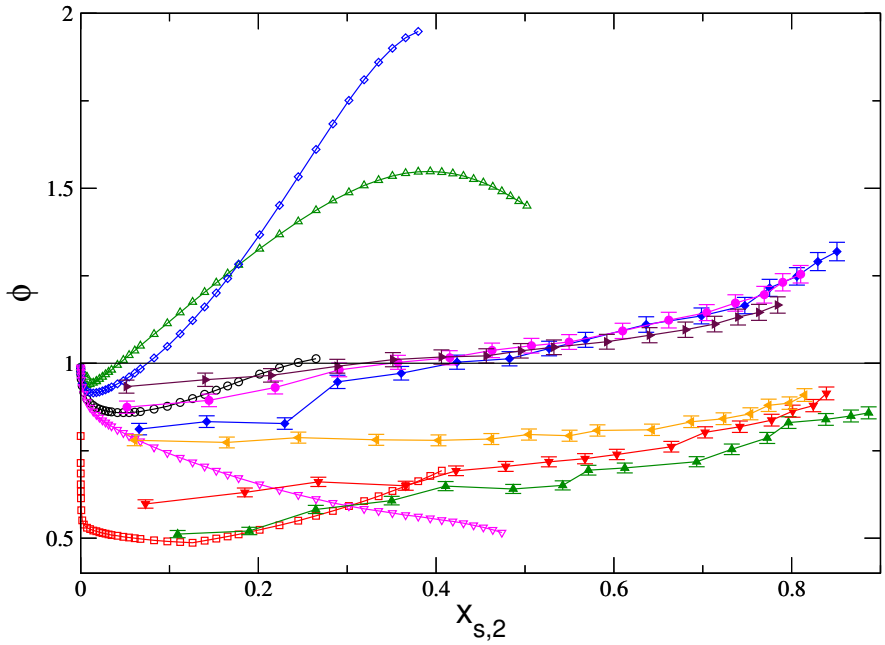


Figure 7.13.: Experimental [14] and simulated osmotic coefficient $\phi$ against $x_{s,2}$: Experimental values are for KF (blue open diamonds), $HNO_3$ (green open triangles), CsCl (black open circles), HF (red open squares) and $NH_4NO_3$ (mangenta open triangles). Simulation results are for $\mu^2 = 5$ and ion charge $q = 1$ at $T = 3$ (blue filled diamonds), $T = 4$ (mangenta filled circles), $T = 6$ (brown filled triangles) as well as $\mu^2 = 5$ and charge $q = 5$ at $T = 3$ (green filled triangles), $T = 4$ (red filled triangles), $T = 6$ (yellow filled triangles).

quickly to values of $\phi > 1$, which points to a good hydration of these ions. We see the same behaviour in our simulation results except for $\mu^2 = 5$ and $q = 5$. Here the general form of the curves remain the same, but $\phi$ is shifted to much lower values below 1 similar to the experimental data for HF and $NH_4NO_3$. As described in [2] this indicates the formation of ion pairs. To verify this assumption we can look at the pair correlation functions for $T = 3$, $\mu^2 = 5$ and $\pi = 0.1$ in figures 7.15 and 7.16. For $q = 5$ a strong ion-ion correlation for ions with unequal charge can be observed while the correlation for ions with equal charge is strongly suppressed in the first shell. For $q = 1$ only a very weak correlation can be seen. To analyze the structural development with increasing osmotic pressure, we also take a look at the pair correlation functions for $\pi = 0.25$ and $\pi = 0.7$ (figures 7.17 to 7.20). For small charges e.g. $q = 1$ the correlation does only slightly increase with growing osmotic pressure. For higher charge values e.g. $q = 5$ the correlation extends to higher

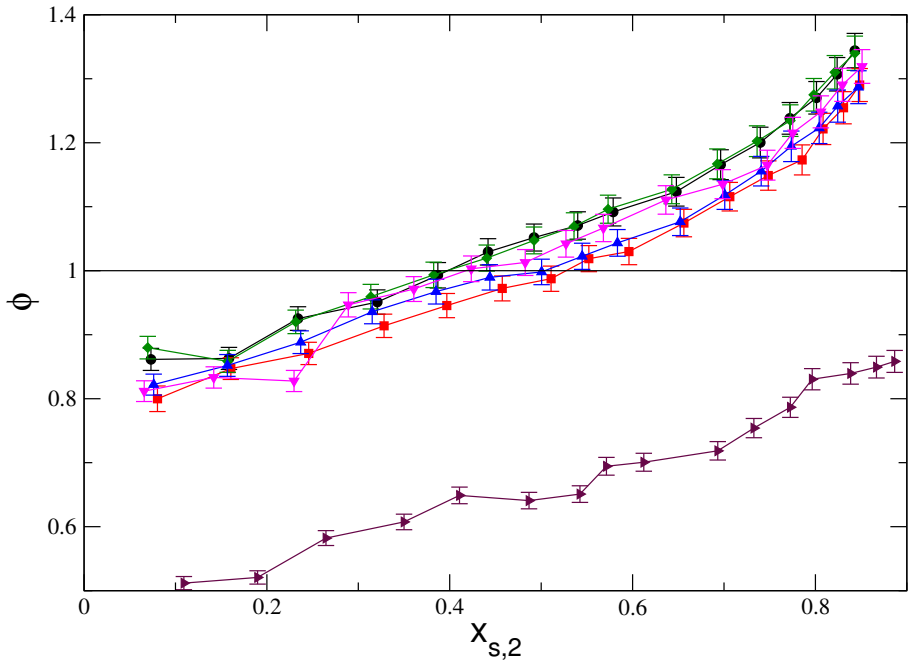


Figure 7.14.: Simulated osmotic coefficient $\phi$ against $x_{s,2}$: Simulation results are shown for $T = 3$ and ion charge $q = 1$ with $\mu^2 = 1$ (black filled circles), $\mu^2 = 2$ (green filled diamonds), $\mu^2 = 5$ (mangenta filled triangles) as well as for $T = 3$ and charge $q = 2$ with $\mu^2 = 1$ (red filled squares), $\mu^2 = 2$ (blue filled triangles) and finally $T = 3$ with $q = 5$ and $\mu^2 = 5$ (brown filled triangles).

distances. For $\pi = 0.7$ longer chains of ion pairs develop, leading to a strong correlation with maxima of equal and unequal charge pair correlations alternating with the distance $r$. Looking at some sample configurations (figures 7.21 and 7.22) we see that the ions form pairs and short chains for $q = 5$, while for smaller charges the ions are part of small chains that consist of ions and ST particles in turn. In case of ion pair and ion chain formation not the single ions but larger structures are hydrated by the solvent leading to a lower osmotic pressure.

In summary we can note that in line with the experiments, we can distinguish between an osmotic coefficient rising above 1, which occurs due to a good hydration of the ions, and an osmotic coefficient below 1, which is related to ion pair formation. In our simulations we observe that for $\mu^2 = 5$ and smaller ion charges, $q = 1$ and $q = 2$, the osmotic coefficient rises above 1, corresponding to a weak correlation with the formation of chains consisting of ions as well as ST particles. For $\mu^2 = 5$ and an ion charge of $q = 5$ the

Table 7.2.: Table converting the used temperatures, dipole moments and charges into physical units using the LJ parameters of the TIP4P/2005 water (see appendix A).

| T | red. LJ units | physical units |
|---|---|---|
| | 3 | 279.6 K |
| | 4 | 372.8 K |
| | 6 | 559.2 K |
| $\mu$ | | |
| | 1 | 0.6369 Debye |
| | 1.4142 | 0.9007 Debye |
| | 2.2361 | 1.4241 Debye |
| $q$ | | |
| | 1 | 0.04197 $e$ |
| | 2 | 0.08395 $e$ |
| | 5 | 0.20987 $e$ |

picture changes significantly. Here the osmotic coefficient lies below 1, corresponding to a strong correlation between the ions with the formation of chains of ion pairs.

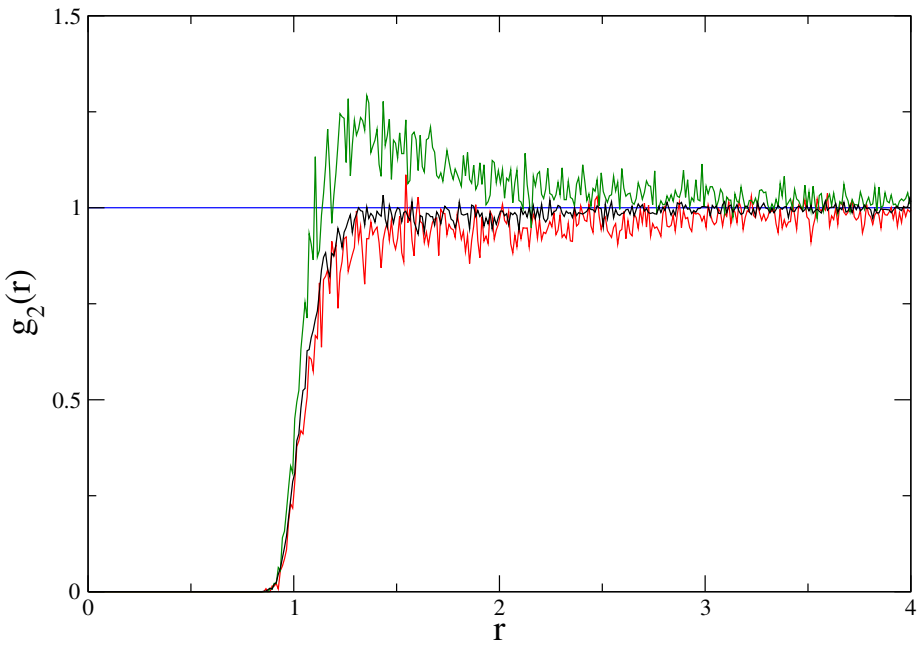


Figure 7.15.: Pair correlation functions for $T = 3$, $\pi = 0.1$, $\mu^2 = 5$ and $q = 1$. Ion-ST correlation (black), ion-ion correlation for equal charged ions (red) and ion-ion correlation for unequal charged ions (green).

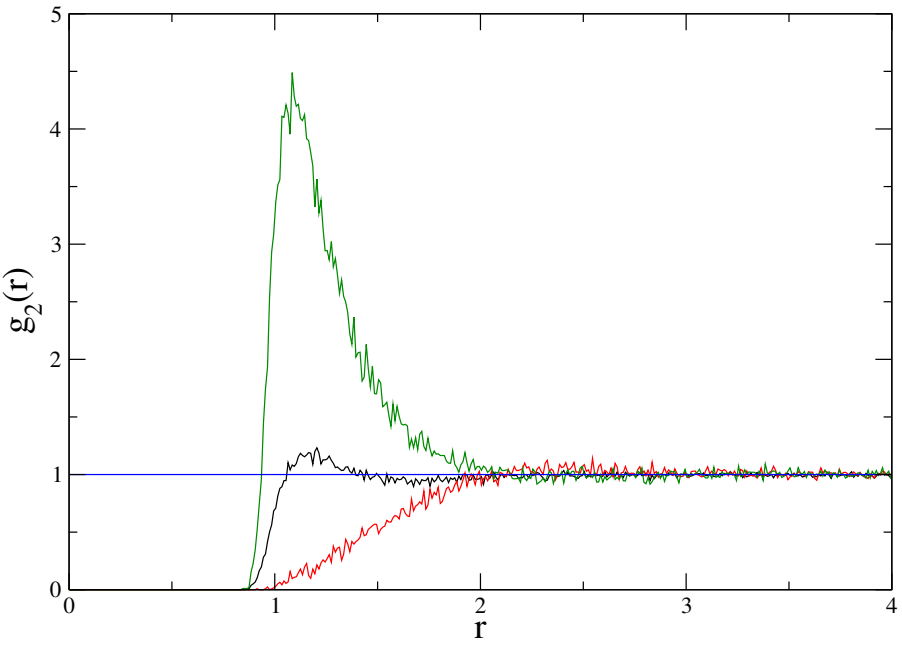


Figure 7.16.: Pair correlation functions for $T = 3$, $\pi = 0.1$, $\mu^2 = 5$ and $q = 5$. Ion-ST correlation (black), ion-ion correlation for equal charged ions (red) and ion-ion correlation for unequal charged ions (green).

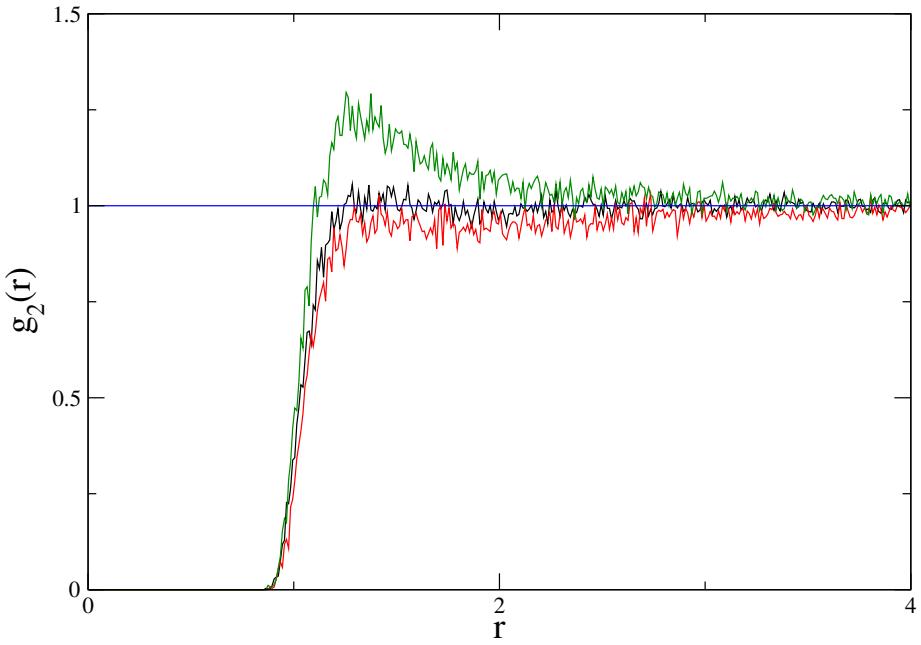


Figure 7.17.: Pair correlation functions for $T = 3$, $\pi = 0.25$, $\mu^2 = 5$ and $q = 1$. Ion-ST correlation (black), ion-ion correlation for equal charged ions (red) and ion-ion correlation for unequal charged ions (green).

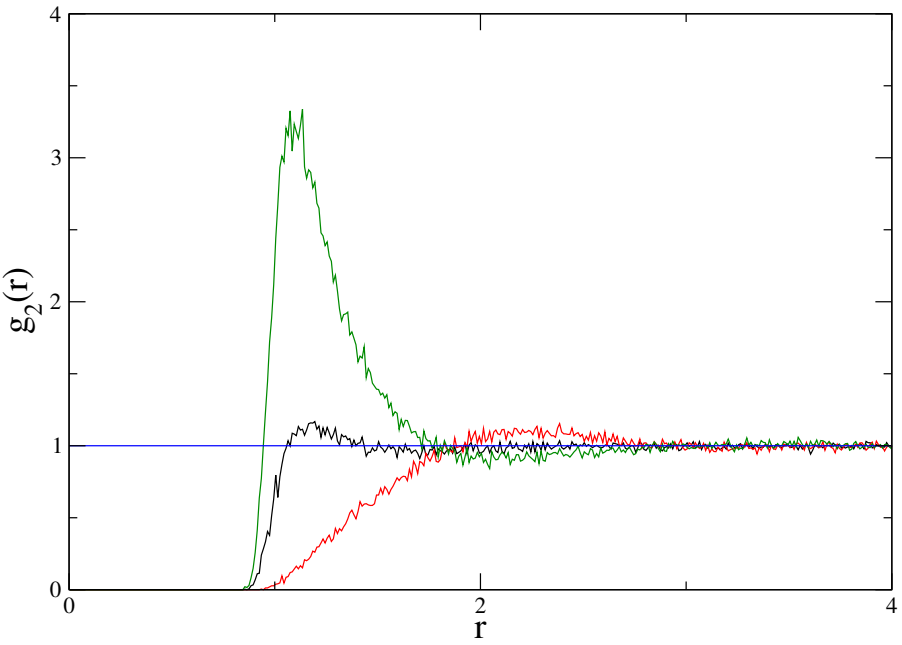


Figure 7.18.: Pair correlation functions for $T = 3$, $\pi = 0.25$, $\mu^2 = 5$ and $q = 5$. Ion-ST correlation (black), ion-ion correlation for equal charged ions (red) and ion-ion correlation for unequal charged ions (green).

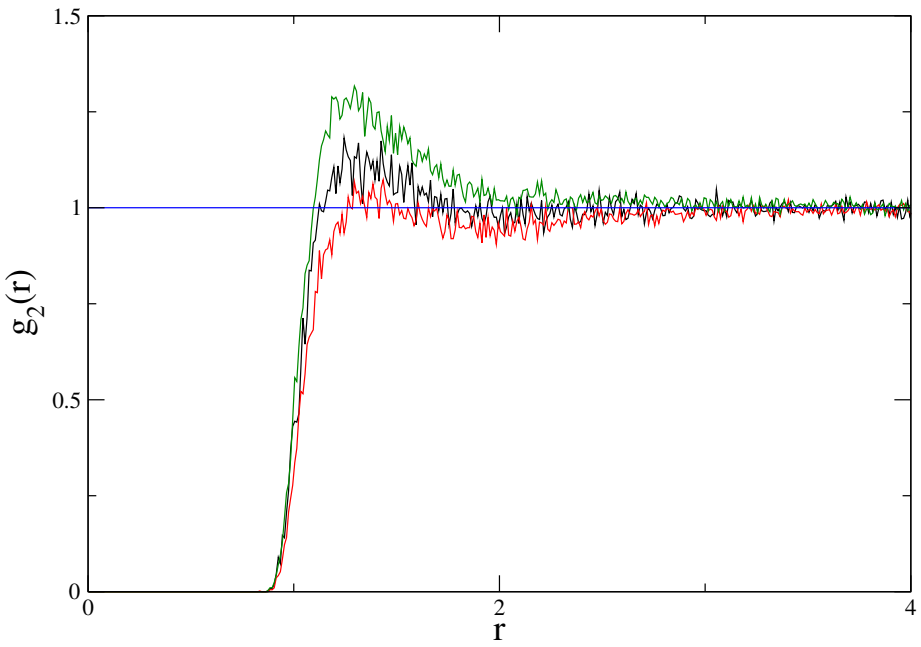


Figure 7.19.: Pair correlation functions for $T = 3$, $\pi = 0.7$, $\mu^2 = 5$ and $q = 1$. Ion-ST correlation (black), ion-ion correlation for equal charged ions (red) and ion-ion correlation for unequal charged ions (green).

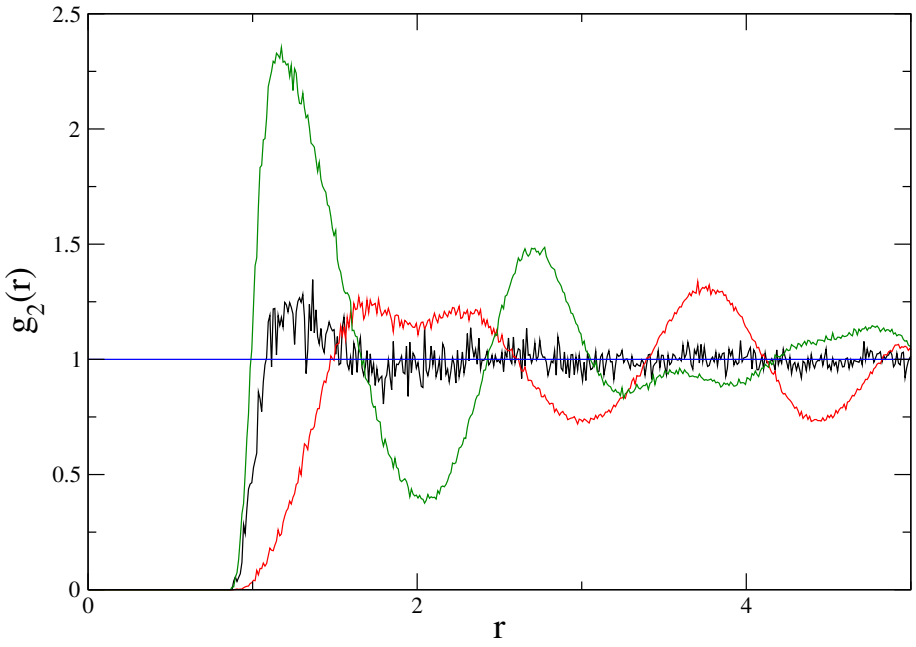


Figure 7.20.: Pair correlation functions for $T = 3$, $\pi = 0.7$, $\mu^2 = 5$ and $q = 5$. Ion-ST correlation (black), ion-ion correlation for equal charged ions (red) and ion-ion correlation for unequal charged ions (green).

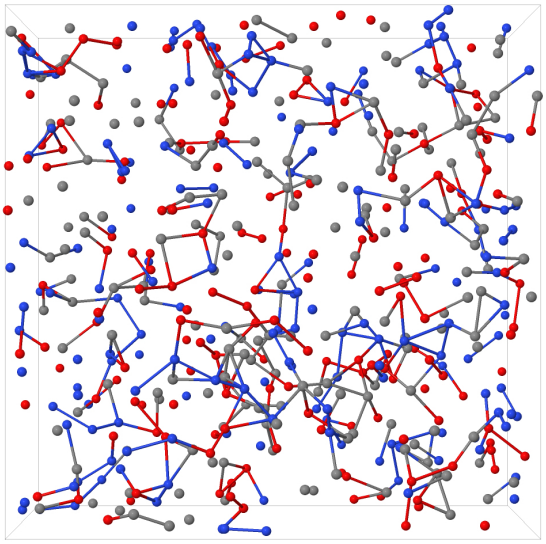

Figure 7.21.: Configuration snapshot for $T = 3$, $\pi = 0.25$, $\mu^2 = 5$ and $q = 1$. Blue balls denote ST particles, black balls negatively charged ions and red balls positively charged ions. Lines connecting particles indicate reversible bonds based on a distance criteria.

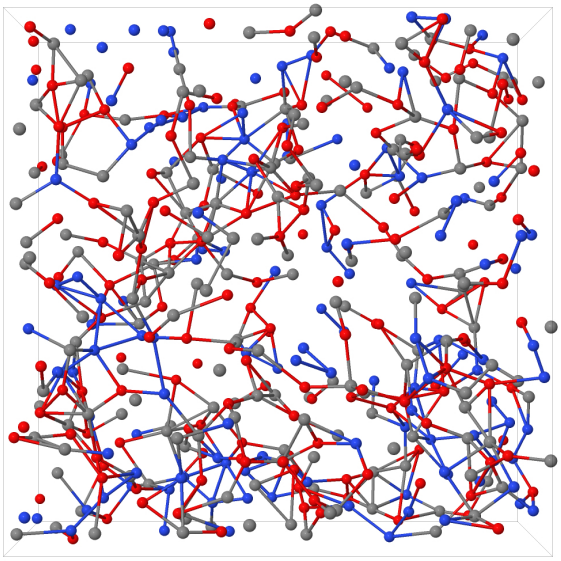

Figure 7.22.: Configuration snapshot for $T = 3$, $\pi = 0.25$, $\mu^2 = 5$ and $q = 5$. Blue balls denote ST particles, black balls negatively charged ions and red balls positively charged ions. Lines connecting particles indicate reversible bonds based on a distance criteria.

# Bibliography


[1] R. Hentschke. *Thermodynamics: For physicists, chemists and materials scientists*. Springer Science & Business Media, 2013.

[2] R. A. Robinson and R. H. Stokes. *Electrolyte solutions*. Courier Corporation, 2002.

[3] P. Atkins and J. De Paula. *Elements of physical chemistry*. Oxford University Press, 2013.

[4] M. P. Allen and D. J. Tildesley. *Computer Simulation of Liquids*. Oxford University Press, 1989.

[5] J. A. Barker. Reaction field, screening, and long-range interactions in simulations of ionic and dipolar systems. *Molecular Physics*, 83(6):1057, 1994.

[6] M. Neumann. Dielectric properties and the convergence of multipolar lattice sums. *Molecular Physics*, 60:225, 1987.

[7] A. V. Bandura, S. N. Lvov, and D. D. Macdonald. Thermodynamics of ion solvation in dipolar solvent using Monte Carlo mean reaction field simulation. *Journal of the Chemical Society, Faraday Transactions*, 94(8):1063, 1998.

[8] B. Smit. Phase diagrams of Lennard-Jones fluids. *The Journal of Chemical Physics*, 96(11):8639, 1992.

[9] B. Smit, C. P. Williams, E. M. Hendriks, and S. W. De Leeuw. Vapour-liquid equilibria for Stockmayer fluids. *Molecular Physics*, 68(3):765, 1989.

[10] M. E. Van Leeuwen, B. Smit, and E. M. Hendriks. Vapour-liquid equilibria of Stockmayer fluids: Computer simulations and perturbation theory. *Molecular Physics*, 78(2):271, 1993.

[11] J. Bartke and R. Hentschke. Phase behavior of the Stockmayer fluid via molecular dynamics simulation. *Physical Review E*, 75:061503, 2007.

[12] S. Schreiber. Monte Carlo Simulationen zum osmotischen Druck. Master's thesis, Bergische Universität Wuppertal, 2011.

[13] S. Schreiber and R. Hentschke. Monte Carlo simulation of osmotic equilibria. *The Journal of Chemical Physics*, 135(13):134106, 2011.

[14] W. J. Hamer and Y. Wu. Osmotic coefficients and mean activity coefficients of uni-univalent electrolytes in water at 25 C. *Journal of Physical and Chemical Reference Data*, 1(4):1047, 1972.

# 8. Conclusion

The original motivation for this work was the question whether or not dipole-dipole attraction is sufficient to cause g-l phase separation. Based on the work presented here, the answer is yes - or at least a very probable yes. As an aside, the expertise needed to model systems governed by long-range electrostatic forces was elaborated. It was thus both possible and useful to include an application of this "technology" to the study of osmotic pressure in electrolyte solutions. In the following we summarize the results obtained in the two distinct but related parts of this thesis.

By performing NVT-MD simulations for the CSD model, we were able to locate the critical parameters in an area around $d \approx 1$, where g-l phase separation is expected due to energetically disfavored formation of chains. Based on this starting point, we were able to track the critical point along the path of reduced charge-to-charge separation $d$ and fixed dipole moment $\mu^2$, down to the dumbbell length $d = 10^{-4}$, which suggests a g-l critical point in the DSS limit. Extrapolation of these results to the dipolar limit $d \to 0$, yields for the critical temperature $T_c = 0.051$ and the critical density $\rho_c = 0.004$. Qualitatively, these results are in accord with the work on CHD by Ganzenmüller *et al.* [1], including the extrapolation to the dipolar limit. Down to $d = 0.6$ they are also in line with Dussi *et al.* [2], who also studied the CSD model. For still smaller dumbbell elongations, Dussi *et al.* did not observe g-l phase separation in the analyzed temperature ranges. This deviation from our results can be attributed to the different methods used, i.e. MD using the reaction field method on our side, and MC simulations with the Ewald summation on their end, or alternatively to finite size effects observed in the simulations performed by Dussi. So to figure out the root cause of this deviation, some more analysis is needed, especially in comparison of the simulation methods including the long range correction for the Coulomb potential.

To interpret the $d$ dependence of our simulation results, we apply three different simple models. The first two fail to describe the observed behavior. The extension of Flory's lattice theory to reversibly aggregating polymers [3, 4], where the fixed chain length is replaced by an average chain length of equilibrium polymeric chains, does not succeed because the reversible aggregates remain rather small. Likewise, the attempt to correlate the observed behavior with the defect model introduced by Tlusty and Safran [5] also fails, because the number of network nodes, which should increase for $d \to 0$, decreases instead. But finally, the developed van der Waals mean field theory, which combines the Onsager cavity theory of dipolar fluids [6] with the idea that the basic unit is not the single dipole, but rather a small reversible aggregate, gives us a suitable theory. In the range of small

dumbbells, i.e. $d < 0.1$, where the reversible dipole-dipole aggregation produces predominantly short aggregates, the theory demonstrates a rather good quantitative description of our simulation results.
Now equipped with good evidence for the existence of g-l phase separation for dipolar systems based on the CSD results, we considered the pure DSS model to see to which extent it is possible to reproduce the extrapolation of the CSD model to the dipolar limit. In order to enable a direct comparison with the CSD model, we introduced the 4-DSS model which has a fourfold repulsion and therefore mimics the repulsion of the CSD model caused by its geometry. This change of the repulsion opened a new aspect in the effort to analyze purely dipolar systems. Besides the fact that the increased repulsion of the 4-DSS system is much easier to equilibrate, it also allowed us to overcome the obstacle of excessive chain formation with a new approach. Usually a control parameter in the interaction potential is used (e.g. [1, 7, 8]) to approach the ordinary DSS (or DHS) interaction. Tuning the potential towards the DSS (or DHS potential), one hopes to collect sufficient data permitting extrapolation to the critical parameters of the limiting systems, before excessive aggregation renders equilibration prohibitively time consuming. However, to the best of our knowledge, no such study has controlled aggregation via scaled repulsion. Increased repulsion, however, appears to be the easiest approach to a model potential with purely dipolar attraction and easy access to its g-l critical point [9]. Our comparison on the formation of reversible aggregates for the 4-DSS and DSS model showed that the higher repulsion does indeed avoid the creation of long chains. We also found very good agreement of the 4-DSS critical parameters compared to the average values for the CSD model below $d < 0.1$. The critical parameters for the 4-DSS model are $\rho_c = 0.0037$, $T_c = 0.0501$ and $P_c = 4.9 \cdot 10^{-5}$, and can be interpreted as g-l critical parameters as we were able to track the g-l critical point from the dumbbells with large elongation to the DSS limit. In subsequent work it may be interesting to explore in more detail the influence of the repulsion on the formation of reversible chains and rings and their effect on the critical parameters, and see to what extent this can be covered by theory.
In the continuation of the analysis of the dipolar limit, we extended the study on the CSD model for charge-to-charge distances $d \gg 1$ up to $d = 7$. For $d$ above one, the aggregate lengths grow and the aggregates are more flexible. In this $d$ range, the mean field theory earlier applied for small dumbbells can again be used, and it yields a valid qualitative description of our data. In the interpretation of the dumbbell data, there is only an explanation of the peak in the density missing which we have not solved in this work. By increasing the dumbbell length, we crossed the line where one can expect that the CSD model behaves similar to an ionic fluid forming ion pairs. So with the elimination of the rigid dumbbell bond of the CSD, we get an ionic fluid which is similar to the RPM which has a hard core repulsion instead of a soft sphere repulsion, and is quite often used in simulations and theoretical calculations. In our simulations of the soft sphere ions, we were able to locate the critical point at $T_c = 0.0163$ and $\rho_c = 0.006$, which is close to the results of the CSD for $d$ values consistent with the ion-ion separations in the near critical fluid. This supports the idea that the pairing of ions is a key ingredient to the quantitative description of critical parameters in ionic liquids. The critical parameters

we determined for the ionic system with our own simulation routines using the reaction field method can be reproduced independently with the LAMMPS MD simulator [10], which makes use of the Ewald summation. In contrast, the comparison of our results with simulation data for the RPM from the literature and theoretical calculations using the Debye-Hückel theory provides a mixed picture. Compared to the RPM simulation data [11, 12], our critical temperature and density is approximately a factor 2 smaller and the Debye-Hückel Bjerrum plus Dipole Ionic coupling theory [13, 14] confirms our critical density, but is again a factor 2 higher for the critical temperature.
In the last section of this work, we left the field of phase coexistence analysis and turned towards the study of the osmotic pressure for charged systems. A MC algorithm was implemented, which permits simulations in the $Tp\pi$ ensemble, developed by Schreiber and Hentschke [15, 16]. We successfully reproduced selected results obtained by these authors with the LJ system to check the correctness of our simulation routines. For the charged systems, the van't Hoff equation provides a good approximation of our simulation routines and our results do not vary very much if the charge or the dipole moment is changed. Only for the highest charge $q = 5.0$ the situation changes, and the van't Hoff equation leads to an overestimation of the simulation data. This corresponds to a strong correlation between the ions with the formation of ion pairs. Comparing the results to experimental data, the van't Hoff equation provides a good approximation for our results, but not for the experimental data chosen. This holds true even for dilute concentrations where the van't Hoff equation is supposed to be valid. Quantitatively, the experimental data does not comply with our data, but qualitatively some similarities in the behavior of the osmotic pressure for different solute mole fractions can be seen. In particular, we see agreement as far as the general relation between the osmotic coefficient and short range structural ordering is concerned. To improve the comparison to the experimental data, one could use a more realistic model like the TIP4P/2005 water for the solvent which can cater for the more complex properties of real water.

# Bibliography


[1] G. Ganzenmüller and P. J. Camp. Vapor-liquid coexistence in fluids of charged hard dumbbells. *Journal of Chemical Physics*, 126:191104, 2007.

[2] S. Dussi, L. Rovigatti, and F. Sciortino. On the gas–liquid phase separation and the self-assembly of charged soft dumbbells. *Molecular Physics*, 111(22-23):3608, 2013.

[3] J. Dudowicz, K. F. Freed, and J. F. Douglas. Flory-Huggins model of equilibrium polymerization and phase separation in the Stockmayer fluid. *Physical Review Letters*, 92(4):045502, 2004.

[4] R. Hentschke, J. Bartke, and F. Pesth. Equilibrium polymerization and gas-liquid critical behavior in the Stockmayer fluid. *Physical Review E*, 75:011506, 2007.

[5] T. Tlusty and S. A. Safran. Defect-induced phase separation in dipolar fluids. *Science*, 290(5495):1328, 2000.

[6] L. Onsager. Electric moments of molecules in liquids. *Journal of the American Chemical Society*, 58:1486, 1936.

[7] G. Ganzenmüller, G. N. Patey, and P. J. Camp. Vapour–liquid phase transition of dipolar particles. *Molecular Physics*, 107(4-6):403, 2009.

[8] R. Jia, H. Braun, and R. Hentschke. Gas-liquid coexistence in a system of dipolar soft spheres. *Physical Review E*, 82(6):062501, 2010.

[9] H. Braun and R. Hentschke. Phase coexistence for charged soft dumbbell and ionic soft sphere systems via molecular dynamics simulation. *Physical Review E*, 87(1):012311, 2013.

[10] S. Plimpton. Fast parallel algorithms for short-range molecular dynamics. *Journal of Computational Physics*, 117(1):1, 1995.

[11] A. Z. Panagiotopoulos. Critical parameters of the restricted primitive model. *The Journal of Chemical Physics*, 116(7):3007, 2002.

[12] J. M. Caillol, D. Levesque, and J. J. Weis. Critical behavior of the restricted primitive model revisited. *Journal of Chemical Physics*, 116(24):10794, 2002.

[13] M. E. Fisher and Y. Levin. Criticality in ionic fluids: Debye-Hückel theory, Bjerrum, and beyond. *Physical Review Letters*, 71(23):3826, 1993.

[14] Y. Levin and M. E. Fisher. Criticality in the hard-sphere ionic fluid. *Physica A: Statistical Mechanics and its Applications*, 225(2):164, 1996.

[15] S. Schreiber. Monte Carlo Simulationen zum osmotischen Druck. Master's thesis, Bergische Universität Wuppertal, 2011.

[16] S. Schreiber and R. Hentschke. Monte Carlo simulation of osmotic equilibria. *The Journal of Chemical Physics*, 135(13):134106, 2011.

# Acknowledgments

First, I would like to thank Prof. Dr. Reinhard Hentschke for giving me the chance to create this thesis in his work group, the great support as well as guidance during the course of this research and finally also for his patience and flexibility which allowed me to do my study in part time.
Many thanks go to my work group members Dr. Jörg Bartke, Dr. Ran Jia, Dr. Henning Hörstermann, Dr. Enno Oyen, Sebastian Schreiber and especially to Dr. Nils Hojdis for their valuable discussions, assistance and friendship. I also offer thanks to the office mates Dr. Jonathan Hager, Johannes Fischer and Sven Engelmann who administered our server farm and helped me out remotly.
I'm very grateful for the support of my family especially my parents. Finally I am deeply indebted to my wife Christa for her valuable input, support, companionship and encouragement as well as to my daughter Mina who had to spend quite some time without her dad.
This research was supported, in part, by the German Science Foundation through DFG-Grant No. HE 1545/17-1 and HE 1545/17-2.

# A. Reduced Lennard-Jones units

Simulation results are mostly presented in reduced LJ units, see e.g. [1]. These are given by:

$$\begin{aligned}
\text{Length} \quad l^* &= \frac{l}{\sigma} \\
\text{Energy} \quad E^* &= \frac{E}{\varepsilon} \\
\text{Time} \quad t^* &= \frac{t}{\tau} \\
\text{Temperature} \quad T^* &= T \cdot \frac{k_B}{\varepsilon} \\
\text{Pressure} \quad P^* &= P \cdot \frac{\sigma^3}{\varepsilon} \\
\text{Dipole moment} \quad \mu^* &= \mu \cdot \sqrt{\frac{1}{4\pi\epsilon_0} \cdot \frac{1}{\sigma^3 \varepsilon}} \\
\text{Charge} \quad q^* &= q \cdot \sqrt{\frac{1}{4\pi\epsilon_0} \cdot \frac{1}{\sigma\varepsilon}}
\end{aligned}$$

To compare the simulation results for the osmotic pressure with the experimental data of water solutions, we use the LJ parameters of the TIP4P/2005 water model [2] as example values.

$$\begin{aligned}
\sigma &= 3.1589\,\text{Å} \\
\varepsilon &= 93.2 \cdot k_B \\
q_H &= 0.5563 \cdot e \\
q_M &= -2 \cdot q_H \\
\mu &= 2.305\,\text{Debye}
\end{aligned}$$

# B. Additional figures for osmotic pressure

In the following we have added the additional results for further dipole strengths and ionic charges produced for the analysis of the influence of the external pressure on the solute mole fraction $x_{s,2}$ and the total number densities $\rho_1$, $\rho_2$ in the simulation boxes.

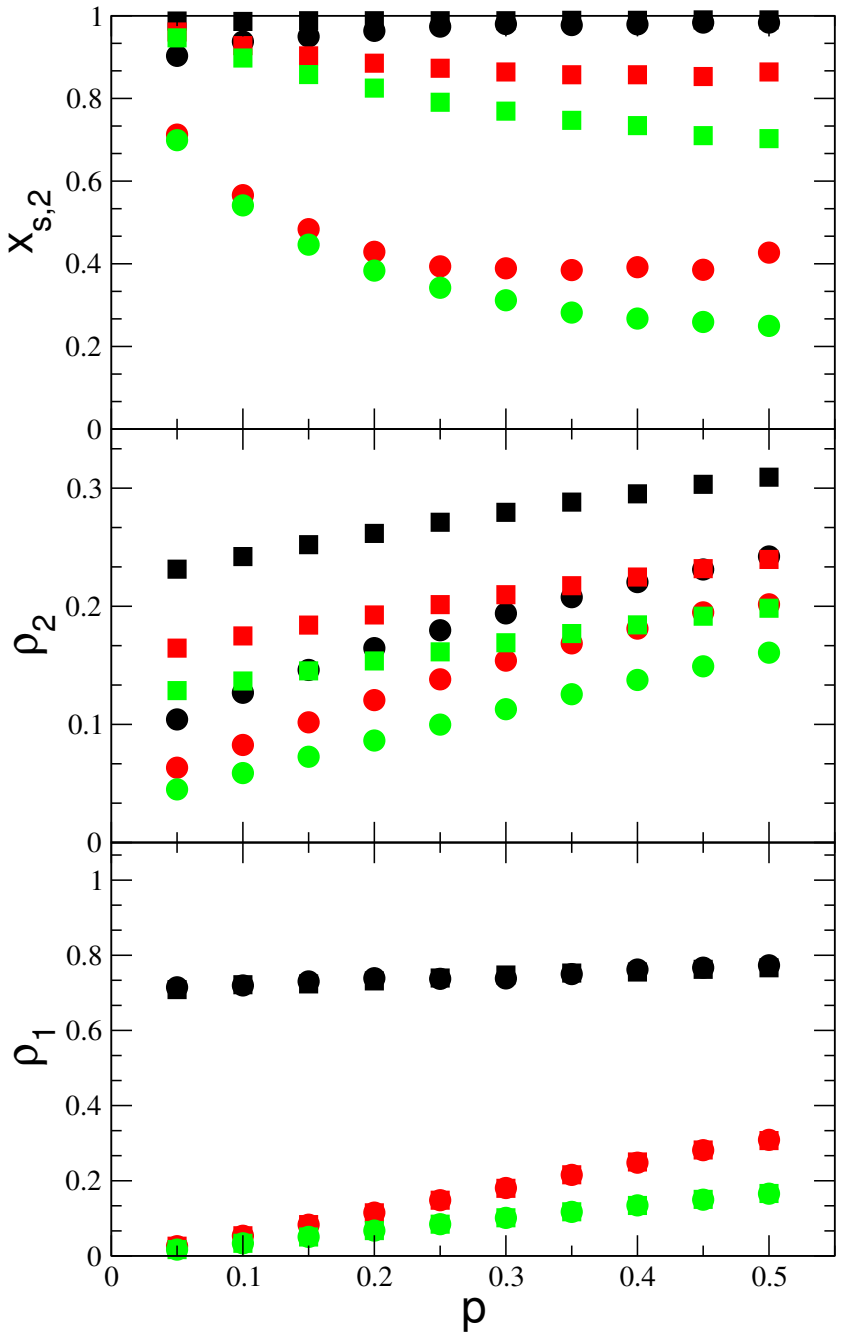


Figure B.1.: Pressure dependency of the coulombic mixture for dipole strength $\mu^2 = 0.5$ and ion charge $q = 0.5$. Top: Solute mole fraction $x_{s,2}$ vs. the external pressure $p$. Middle: Total number density $\rho_2$ in box 2 containing the mixture vs. $p$. Bottom: Total number density $\rho_1$ in box 1 containing the solvent vs. $p$. In all three panels the colors represent $T = 1.0$ (black), $T = 2.0$ (red) and $T = 3.0$ (green). The shape of the symbols stand for $\pi = 0.1$ (circles) and $\pi = 0.5$ (squares).

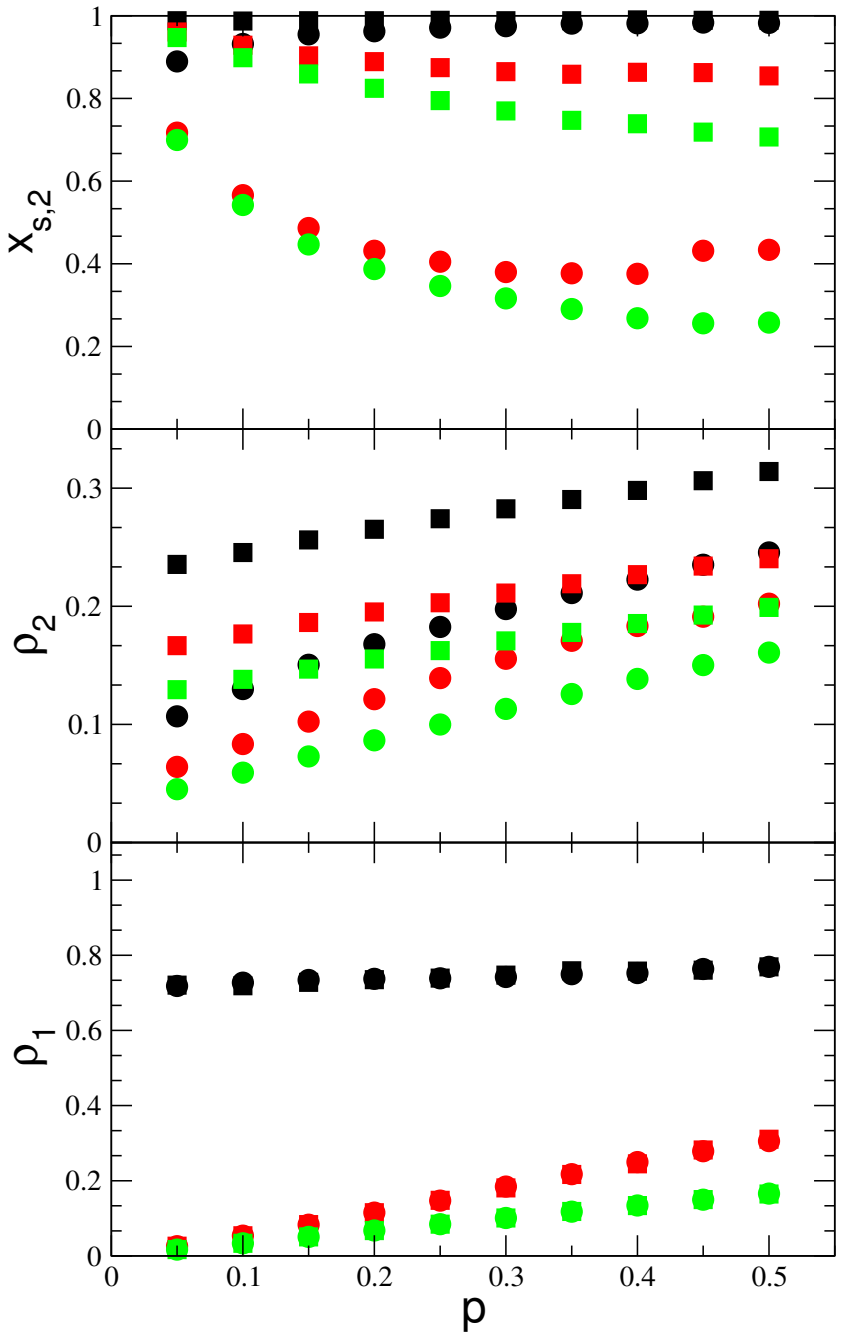


Figure B.2.: Pressure dependency of the coulombic mixture for dipole strength $\mu^2 = 0.5$ and ion charge $q = 1$. Top: Solute mole fraction $x_{s,2}$ vs. the external pressure $p$. Middle: Total number density $\rho_2$ in box 2 containing the mixture vs. $p$. Bottom: Total number density $\rho_1$ in box 1 containing the solvent vs. $p$. In all three panels the colors represent $T = 1.0$ (black), $T = 2.0$ (red) and $T = 3.0$ (green). The shape of the symbols stand for $\pi = 0.1$ (circles) and $\pi = 0.5$ (squares).

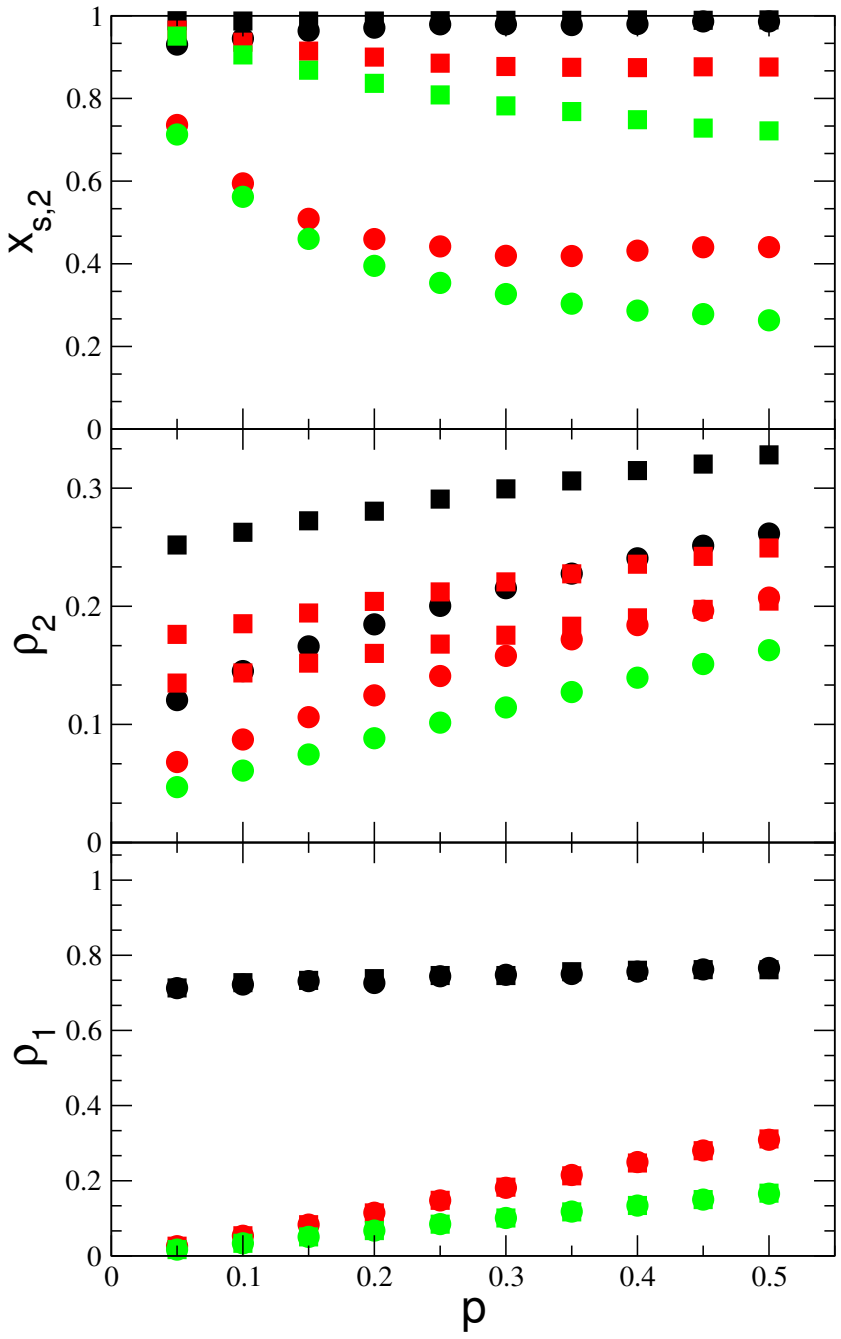


Figure B.3.: Pressure dependency of the coulombic mixture for dipole strength $\mu^2 = 0.5$ and ion charge $q = 2$. Top: Solute mole fraction $x_{s,2}$ vs. the external pressure $p$. Middle: Total number density $\rho_2$ in box 2 containing the mixture vs. $p$. Bottom: Total number density $\rho_1$ in box 1 containing the solvent vs. $p$. In all three panels the colors represent $T = 1.0$ (black), $T = 2.0$ (red) and $T = 3.0$ (green). The shape of the symbols stand for $\pi = 0.1$ (circles) and $\pi = 0.5$ (squares).

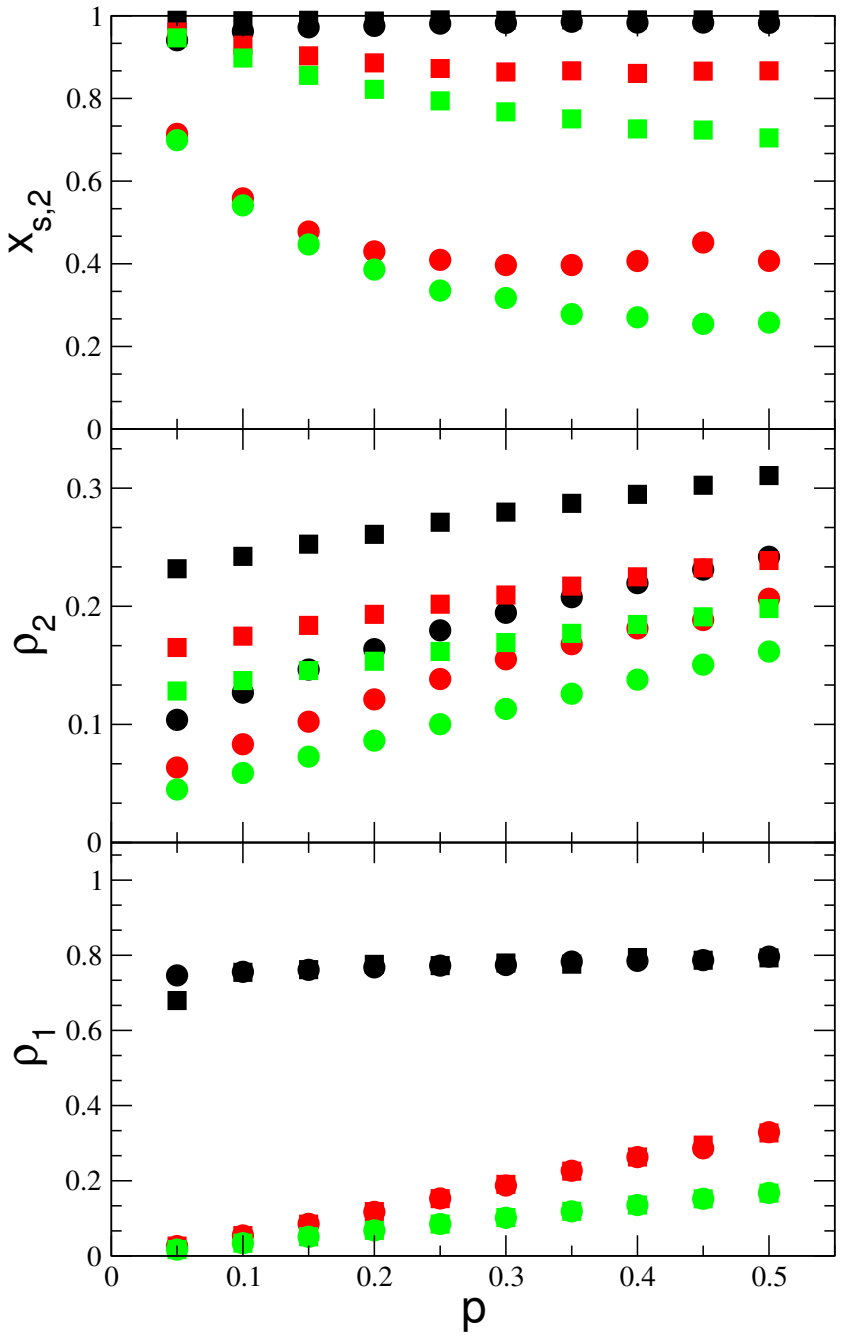


Figure B.4.: Pressure dependency of the coulombic mixture for dipole strength $\mu^2 = 1$ and ion charge $q = 0.5$. Top: Solute mole fraction $x_{s,2}$ vs. the external pressure $p$. Middle: Total number density $\rho_2$ in box 2 containing the mixture vs. $p$. Bottom: Total number density $\rho_1$ in box 1 containing the solvent vs. $p$. In all three panels the colors represent $T = 1.0$ (black), $T = 2.0$ (red) and $T = 3.0$ (green). The shape of the symbols stand for $\pi = 0.1$ (circles) and $\pi = 0.5$ (squares).

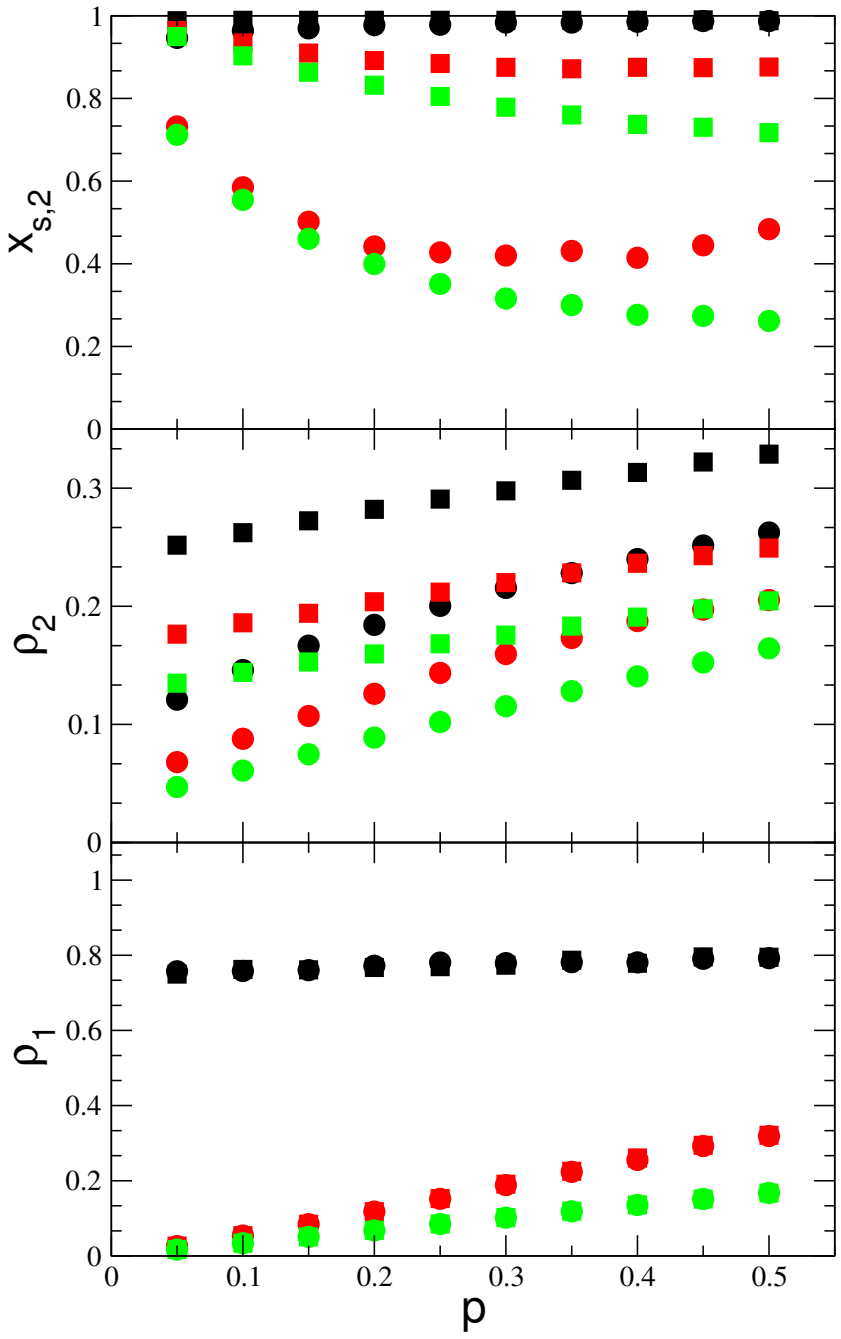


Figure B.5.: Pressure dependency of the coulombic mixture for dipole strength $\mu^2 = 1$ and ion charge $q = 2$. Top: Solute mole fraction $x_{s,2}$ vs. the external pressure $p$. Middle: Total number density $\rho_2$ in box 2 containing the mixture vs. $p$. Bottom: Total number density $\rho_1$ in box 1 containing the solvent vs. $p$. In all three panels the colors represent $T = 1.0$ (black), $T = 2.0$ (red) and $T = 3.0$ (green). The shape of the symbols stand for $\pi = 0.1$ (circles) and $\pi = 0.5$ (squares).

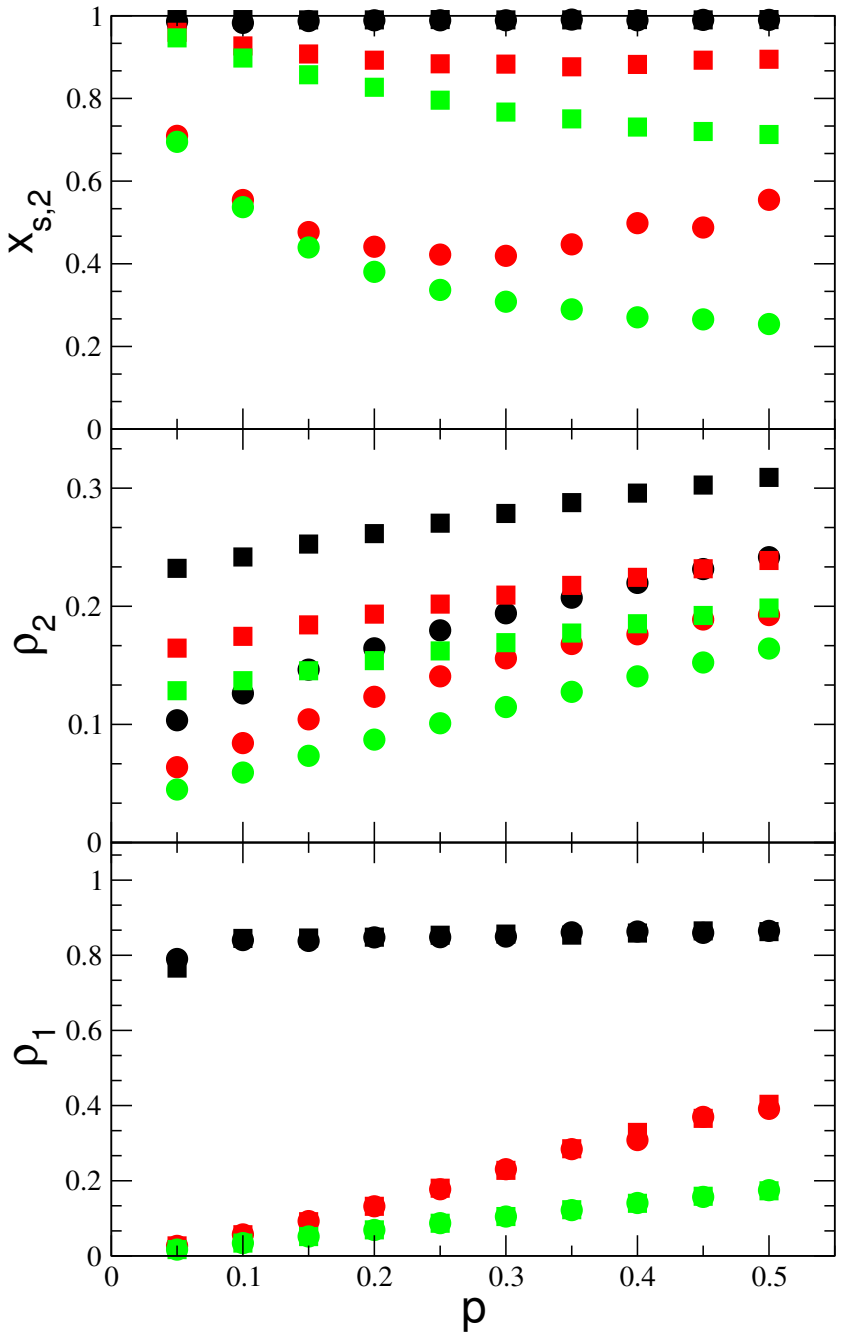


Figure B.6.: Pressure dependency of the coulombic mixture for dipole strength $\mu^2 = 2$ and ion charge $q = 0.5$. Top: Solute mole fraction $x_{s,2}$ vs. the external pressure $p$. Middle: Total number density $\rho_2$ in box 2 containing the mixture vs. $p$. Bottom: Total number density $\rho_1$ in box 1 containing the solvent vs. $p$. In all three panels the colors represent $T = 1.0$ (black), $T = 2.0$ (red) and $T = 3.0$ (green). The shape of the symbols stand for $\pi = 0.1$ (circles) and $\pi = 0.5$ (squares).

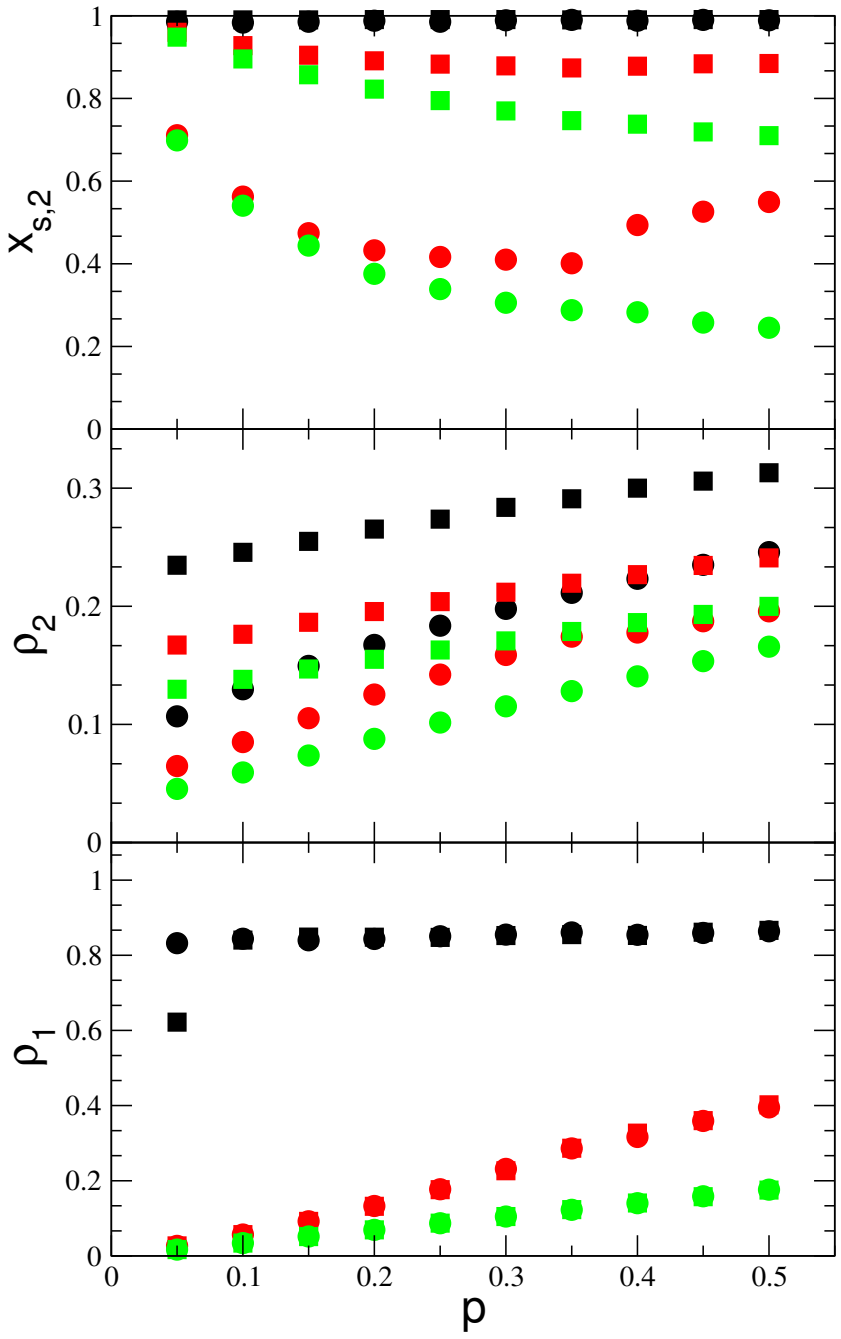


Figure B.7.: Pressure dependency of the coulombic mixture for dipole strength $\mu^2 = 2$ and ion charge $q = 1$. Top: Solute mole fraction $x_{s,2}$ vs. the external pressure $p$. Middle: Total number density $\rho_2$ in box 2 containing the mixture vs. $p$. Bottom: Total number density $\rho_1$ in box 1 containing the solvent vs. $p$. In all three panels the colors represent $T = 1.0$ (black), $T = 2.0$ (red) and $T = 3.0$ (green). The shape of the symbols stand for $\pi = 0.1$ (circles) and $\pi = 0.5$ (squares).

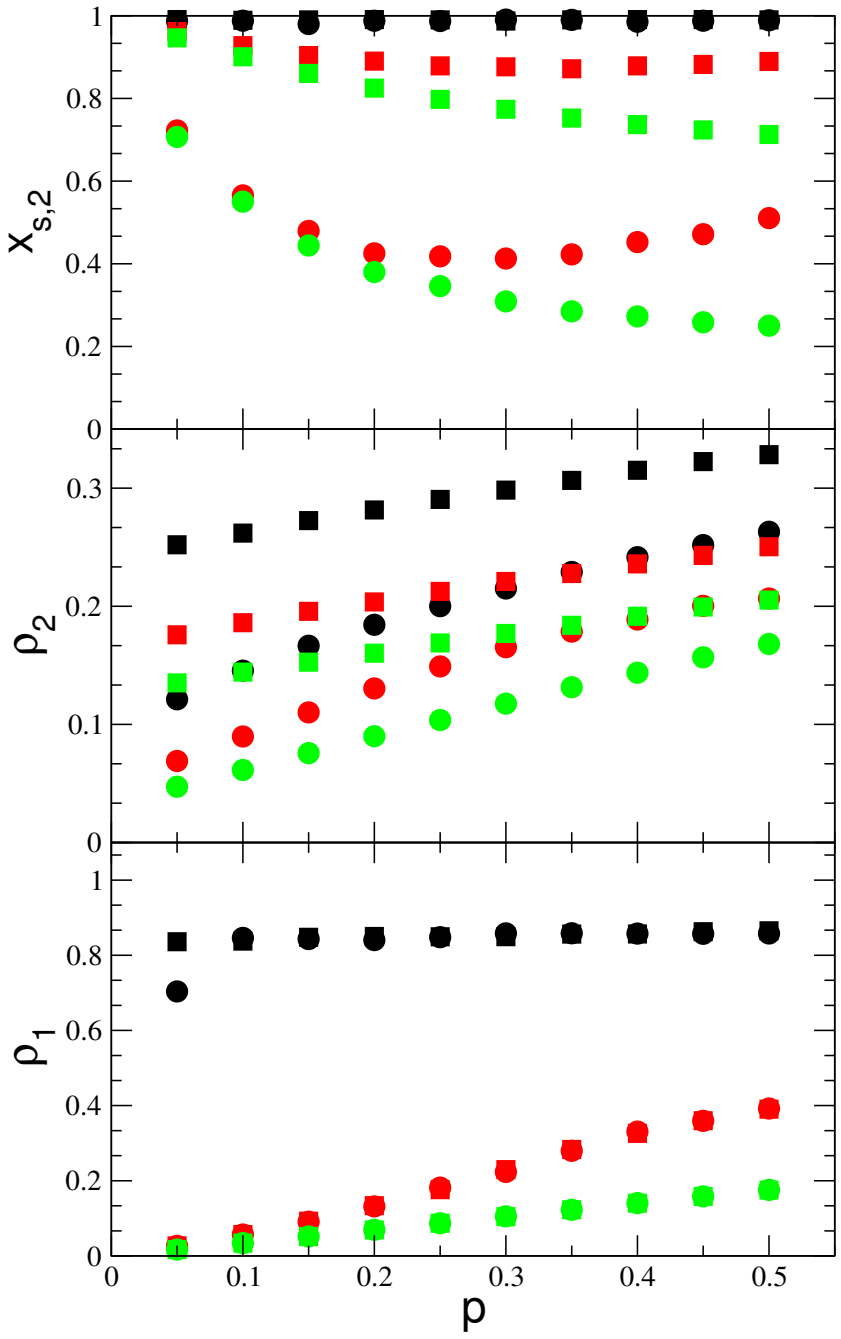


Figure B.8.: Pressure dependency of the coulombic mixture for dipole strength $\mu^2 = 2$ and ion charge $q = 2$. Top: Solute mole fraction $x_{s,2}$ vs. the external pressure $p$. Middle: Total number density $\rho_2$ in box 2 containing the mixture vs. $p$. Bottom: Total number density $\rho_1$ in box 1 containing the solvent vs. $p$. In all three panels the colors represent $T = 1.0$ (black), $T = 2.0$ (red) and $T = 3.0$ (green). The shape of the symbols stand for $\pi = 0.1$ (circles) and $\pi = 0.5$ (squares).

# Bibliography

[1] R. Hentschke, E. M. Aydt, B. Fodi, and E. Stöckelmann. Molekulares Modellieren mit Kraftfeldern. http://constanze.materials.uni-wuppertal.de.

[2] J. L. F. Abascal and C. Vega. A general purpose model for the condensed phases of water: TIP4P/2005. *The Journal of Chemical Physics*, 123(23):234505, 2005.

# Index